NEUTRAL AND CATIONIC ORGANOANTIMONY COMPOUNDS AS LEWIS ACID CATALYSTS

A Dissertation

by

MENGXI YANG

Submitted to the Office of Graduate and Professional Studies of
Texas A&M University
in partial fulfillment of the requirements for the degree of

DOCTOR OF PHILOSOPHY

Chair of Committee,	François P. Gabbaï
Committee Members,	Michael B. Hall
	Michael Nippe
	Jodie L. Lutkenhaus
Head of Department,	Simon W. North

December 2018

Major Subject: Chemistry

ABSTRACT

Organoantimony(V) compounds are potent Lewis acids which have been used for the complexation of anions or for the catalysis of organic reactions. Inspired by the broad range of applications developed for the stable Group 13 Lewis acid $B(C_6F_5)_3$, as well as the fact that SbF_5 is more acidic than BF_3, we set out to investigate organoantimony compounds in the context of Lewis acid catalysis. To this end, we synthesized electrophilic Sb(III) and Sb(V) complexes featuring electron-withdrawing halogenated ligands, cationic charges, and/or ancillary donor ligands, and tested these compounds in a number of organic transformations. Computational studies of their electronic structures provided us with insights into their unusual properties.

We compared a series of triarylstibines with their tetrachlorocatecholate stiborane analogs, and demonstrated that the Lewis acidity of organoantimony(III) species can be readily enhanced by oxidation to the +V state, a phenomenon that is rationalized by the lowering of the antimony-based accepting σ* orbital and a "deepening" of the associated σ-hole upon oxidation. We also reported the synthesis of triarylfluoro- and triarylchloro-stibonium cations, among which the trimesitylchlorostibonium hexachloroantimonate is free from direct cation-anion interactions due to the steric shielding provided by the mesityl substituents. However, this cation is not as reactive as its phenyl derivative in the catalytic polymerization of THF and the Friedel-Craft dimerization of 1,1-diphenlyethylene. Additionally, we evaluated a series of tetraarylstibonium cations as catalysts for the cycloaddition of isocyanates to oxiranes. While all stibonium cations

favor the 3,4-oxazolidinone products, the bulkier cations are found to be the most selective. Furthermore, we compared a series of *ortho*-phenylene based pnictogen cations and dications with their monofunctional derivatives as catalysts for the transfer hydrogenation of quinone derivatives with Hantzsch ester, and found that their catalytic reactivity follows the Lewis acidity trend in the order Sb dication > Sb monocation > P monocation. Lastly, this dissertation also investigates the electronic structures of selected organoantimony(V) compounds with the view to understand how coordination events at the antimony center affect the photophysical properties of these compounds.

DEDICATION

For YYG and DYX

ACKNOWLEDGEMENTS

First and foremost, I would like to express my sincere gratitude and appreciation to my research advisor, Dr. François P. Gabbaï, for his guidance and support throughout my career in graduate school. His expertise, dedication to science, kindness, patience and great humor make him a fantastic mentor. I am very fortunate to have the opportunity to pursue my Ph. D. degree in his research group, and I could sense my tremendous growth as a scientist during my time at Texas A&M University. Thank you very much, François!

I would like to acknowledge my collaborators: Dr. Ming Hyung Lee and his students Ajay Kumar and Minji Kim at the University of Ulsan, who contributed to the fluoride sensor project described in Chapter VI; Ms. Nilanjana Pati, who is an awesome undergraduate researcher and worked closely with me on the catalytic cycloadditions project described in Chapter IV. I would like to thank my committee members: Dr. Michael B. Hall, who taught me the very helpful course of Structure and Bonding and have been a constant source of encouragement and constructive criticism; Dr. Michael Nippe and Dr. Jodie Lutkenhaus, who both shared with me insightful comments and are very inspiring figures in research.

I am very thankful to the members of the Gabbaï group, past and present, who have been both friends and wonderful colleagues: Dr. Baofei Pan, Dr. Sikun Cheng, Dr. Mitsukimi Tsunoda, Dr. Kewei Huang, Dr. Boris Vabre, Dr. Daniel Tofan, Dr. Guillaume Bélanger-Chabot, Dr. Sumit Sahu, Dr. Rosmita Borthakur, Dr. Rajendra Kumar, Dr. Lewis Wilkins, Dr. Kantapat Chansaenpak, Dr. Masato Hirai, Dr. J. Stuart Jones, Dr.

Haifeng Yang, Dr. Anna M. Christianson, Dr. Srobona Sen, Ahmed Ali, Dr. Chang-Hong Chen, Elham Tabei, Ying-Hao Lo, Di You, Gregory S. Day, Christina T. Lollar, Kevin M. Jack, L. Chase Elrod, Mohammadjavad Karimi, and Gyeong-Jin Park, among whom Dan, Guillaume, Masato, Chang-Hong, and Kevin collaborated with me on various projects. Very special thanks to Baofei, Haifeng, Masato, and Stuart for their mentorship during my earlier years in the lab.

I would also want to thank the professors and staff at the chemistry department of Texas A&M. I thank Dr. Oleg V. Ozerov for his Organometallics Chemistry course, constructive comments on chemistry, and career advice. I thank Dr. Kim R. Dunbar and Dr. Timothy R. Hughbanks for their graduate courses on Physical Methods and Group Theory. I thank Dr. Lisa M. Pérez, Dr. Joseph H. Reibenspies, Dr. Nattamai Bhuvanesh, Dr. Gregory P. Wylie, Dr. Vladimir Bakhmoutov and Dr. Doug Elliott for maintaining the instruments and facilities as well as patiently answering my questions. I thank Dr. Gabbai's assistants, first Angie Wilson then later Andrezza Antonio, for taking care of the errands and making our lives easier in the lab.

On the personal side, I would like to thank my close friends, Xiaohan, Xiaoting, and Kangning, whose perspectives, understanding, supports, and companionship are beyond valuable to me. Thanks also go to my imaginary friends whose stories happen in different space times. Thank you all for inspiring me with the courage to take on challenges and to overcome difficulties. May our adventures never end.

Finally, I deeply thank my mother and father, my cousin Zheming, my grandparents, and my loving significant other for their encouragement, support, and love.

CONTRIBUTORS AND FUNDING SOURCES

Contributors

This work was supervised by a dissertation committee consisting of Professor François Gabbaï (advisor), Professors Michael Hall and Michael Nippe of the Department of Chemistry, and Professor Jodie Lutkenhaus of the Department of Chemical Engineering.

In Chapter II, the synthesis and structure of compound **62** was reported by Dr. Daniel Tofan, the Ritter-like catalysis was performed by Dr. Chang-Hong Chen, and Mr. Kevin Jack helped in synthesis and collecting preliminary experiments of small molecule complexations. In Chapter IV, the syntheses and structures of compounds [**75**][OTf] and [**2**][$SbCl_6$] were reported by Dr. Masato Hirai and Dr. Guillaume Bélanger-Chabot, respectively, and Ms. Nilanjana Pati helped in synthesis and collecting catalysis data. Dr. Masato Hirai also reported the syntheses and structures of **81**-Br, and the triflate salts [**81**][OTf] and [**82**][OTf] in Chapter V. In Chapter VI, the synthesis of compound [**85**][OTf] - [**87**][OTf] and the photophysical measurements of their response upon formation of the corresponding fluorostiboranes **85**-F - **87**-F, were carried out by Ajay Kumar and Minji Kim of Dr. Min Hyung Lee's group at University of Ulsan. The software and computational resources for computational studies were supported by the Laboratory for Molecular Simulation at Texas A&M University.

All other work conducted for the dissertation was completed by the student, under the advisement of Professor François Gabbaï of the Department of Chemistry

Funding Sources

This work was supported by the American Chemical Society Petroleum Research Fund (Grant 56871-ND3), the National Science Foundation (CHE-1566474), the Welch Foundation (Grant A-1423) and Texas A&M University (Arthur E. Martell Chair of Chemistry). The views expressed in this dissertation are those of the author and do not necessarily reflect those of the abovementioned funding agencies.

NOMENCLATURE

BINOL	1,1'-Bi-2-naphthol
BODIPY	Boron dipyrromethene
CTAB	Cetyltrimethylammonium bromide
DFT	Density functional theory
DMF	N,N-Dimethylformamide
DMSO	Dimethylsulfoxide
ee	Enantiomeric excess
HOMO	Highest occupied molecular orbital
LUMO	Lowest unoccupied molecular orbital
NBO	Natural bond orbital
NMR	Nuclear magnetic resonance
OTf	Triflate/Trifluoromethanesulfonate
PCM	Polarizable continuum model
TBA	Tetrabutylammonium
TD-DFT	Time-dependent density functional theory
THF	Tetrahydrofuran
TMS	Trimethylsilyl
TOF	Turnover frequency
TON	Turnover number
VSEPR	Valence shell electron pair repulsion

TABLE OF CONTENTS

Page

LIST OF FIGURES

Page

LIST OF TABLES

Page

CHAPTER I

INTRODUCTION TO GROUP 15 LEWIS ACIDS: SYNTHESIS AND CATALYTIC APPLICATIONS

1.1 Introduction to Group 15 Lewis acids

1.1.1 Group 15 Lewis acids: bonding and properties

Heavy main group elements have continuously attracted attention in the past decade. Owing to their potent Lewis acidity and flexible redox-activity, heavy main group elements are strong candidates for applications such as small molecule activation and Lewis acidic catalysis.[1] A common main-group Lewis acid, $B(C_6F_5)$ (**1**), which is often viewed as the economically-affordable alternative to transition metal Lewis acids, has over 2500 citations in the field of Lewis acid catalysis. Many of these citations concern industrially important reactions, such as the catalytic polymerization of olefins. The acidity of these Group 13 Lewis acids originates from their empty p orbitals and the resulting electronic and coordinative unsaturation. In contrast, heavy main group species, especially Group 15 compounds, can expend their valence shell to exceed the octet rule and form hypervalent compounds. For example, the acidity of the inorganic "magic acid" HF-SbF_5 can be partially attributed to the high stability of its conjugated anion $[SbF_6]^-$. Computational work by Krossing has shown that the gas phase fluoride ion affinity (FIA) of SbF_5 (489 kJ/mol) exceeds that of BF_3 (338 kJ/mol) by ~150 kJ/mol,[2] attesting to the strong Lewis acidity of Group 15 compounds. Similar to the related Group 13 species, the use of Group 15 halides is usually restricted by their highly reactive and corrosive nature.

The increased stability of **1** in comparison to the inorganic halide BF_3 suggests that in order to develop applications of Group 15 Lewis acids, it is critical to introduce organic substituents that allow for a retention of the Lewis acidic character.[3]

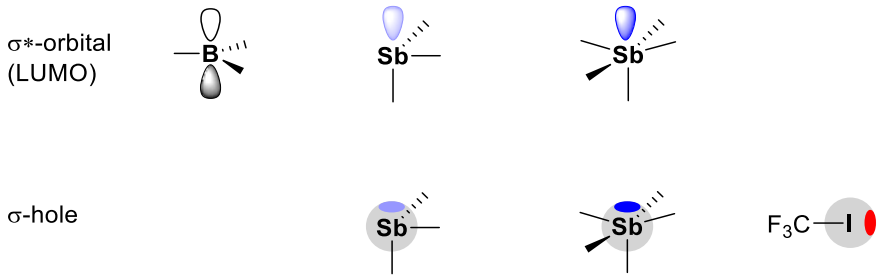

Figure 1. Illustration of the σ* orbitals in boranes, stibines, stiboranes, and the σ-hole in halogen bonding and pnictogen bonding.

The origin of the Lewis acidity in Group 15 compounds is illustrated in Figure 1. On one hand, a molecular orbital argument suggests that the acidity of Group 15 compounds is derived from low-lying σ* orbitals at the central atom – ligand bonds, which stands in contrast to Group 13 compounds and Group 14 onium species whose electrophilic nature comes from a vacant p orbital. Interactions between electron donors and σ* orbitals have been evidenced computationally in numerous reports.[4-7] Another argument used to explain the acidity of Group 15 compounds is based on the concept of σ-hole or pnictogen bond, which is parallel to the concepts of chalcogen bonding and halogen bonding for Group 16 and 17 derivatives.[8-9] The concept of σ-hole was first described by Clark *et al.* in a computational study on the series of CF_3X (X = F, Cl, Br

and I). In this study, the authors explained that CF_3I is predicted to be acidic at the iodine atom because of a positive charge (or σ-hole) developed on the electrostatic potential surface opposite to the C-I bond.[10] Murray *et al.* further applied the σ-hole concept to Group 15 derivatives by examining the electrostatic potential surfaces of species of general formula PnR_3 (Pn = N, P, As).[11] Altogether, the Lewis acidity of Group 15 compounds can be described by either the σ* orbital argument of the σ-hole argument which reflects the continuum connecting the covalent and ionic bonding schemes.

The Gabbaï group has explored a number of Lewis acidic pentavalent organoantimony(V) compounds in the past few years. Previous efforts have highlighted the ability of stibonium cations and spirocyclic stiboranes to serve as water-compatible fluoride sensors.[12] We have also isolated a Lewis acidic, yet air stable stibonium salt $[Sb(C_6F_5)_4][B(C_6F_5)_4]$ ([**2**][$B(C_6F_5)_4$]), which has been shown to be active in both the catalytic ring opening of cyclic ethers and the hydrodefluorination of alkyl fluorides.[13] Meanwhile, in a study of F^- sensing in aqueous media, we have observed the following trend in Lewis acidity of tetraphenylpnictonium ions $[Ph_4Sb]^+ >> [Ph_4As]^+ \approx [Ph_4P]^+$, thus suggesting that the Sb(V) species are the most acidic among pnictogen onium cations.[14] In the next few sections, background will be provided for each type of antimony compounds. Applications in catalysis will also be discussed.

1.1.2 Neutral organoantimony(III) Lewis acids

Neutral triarylstibines SbR_3, with an electron lone pair on the Sb center, are often referred to as Lewis bases and are often found as L-type donor ligands in metal-stibine

complexes.[15-16] An example of such behavior is provided by $SbPh_3$ in the tungsten pentacarbonyl complex $W(CO)_5(SbPh_3)$.[17] While it might be counterintuitive that three-coordinated Sb(III) compounds may function as Lewis acids, it has long been known that they may possess moderate Lewis acidity, as illustrated by the following series of inorganic chlorides, ranked in order of measured Lewis acidity. [18]:

$SbCl_5 > SnCl_4 > SnCl_4 > ZnCl_2 > SbCl_3 > PCl_5$

The fact that $SbCl_3$ is shown to be more acidic than PCl_5 demonstrates that while stabilization of conjugated inorganic anions plays an important role, the acidity of the P(V) center could be hindered by the steric factors associated with its higher coordination number. As for the acidity of Sb(III), early experimental work showed inorganic Sb(III) halides could form molecular complexes with phosphine oxide bases.[19] The Cozzolino group has reported the bis-antimony(III) compound **3** as a chloride reporter, and studied the secondary binding interactions which involves the σ* orbitals of the antimony-oxygen bonds (Figure 2).[20]

When highly electron-withdrawing ligands are incorporated in Sb(III) compounds, the Lewis acidity will drastically increase despite the presence of an electron lone pair. An example of this phenomenon is provided by tris(pentafluorophenyl)stibine (**58**), which was reported by Matile *et al.* to act as a chloride reporter (Figure 2).[9] Our group has also previously reported the organochlorostibine (*o*-$(Ph_2P)C_6H_4)_2SbCl$ (**4**), an analogue of Ph_2SbCl, which behaves as a σ-acceptor ligand towards late transition metals.[21] A similar example is the phosphinylstibine (*o*-$(PPh_2)C_6H_4)SbCl_2$ (**5**) whose antimony center was shown to assist in the activation of a pendent gold center by facilitating halide abstraction

(Figure 2).[22] In addition, when the antimony element is incorporated into a heterocycle, as in the case of the 1-chloro-2,3-diphenylstibaindole (**6**), the σ* orbital of the Sb-Cl bond will participate in the conjugation of the π* system of the indole backbone, resulting in interesting anion dependent photophysical properties (Figure 2).

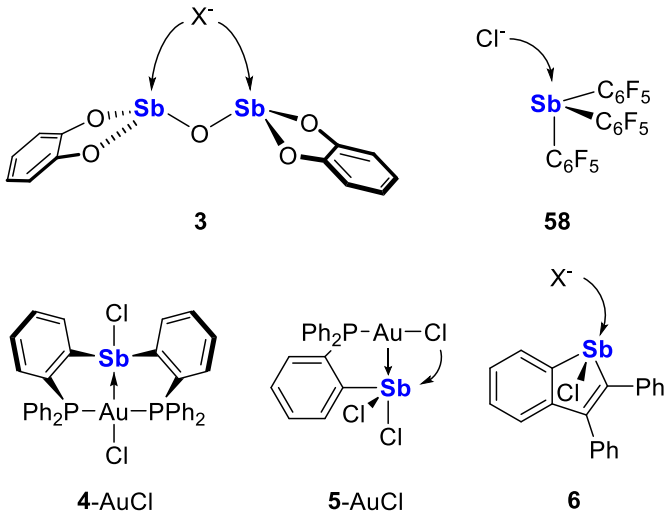

Figure 2. Organoantimony (III) Lewis acids.

1.1.3 Neutral organoantimony(V) Lewis acids

Organoantimony(V) compounds, also known as stiboranes, feature a more electron deficient center compared to the stibines due to their higher oxidation state. George Olah *et al.* began to explore the extreme acidity of antimony(V) compounds in the 1960s, and developed antimony-based super acid systems such as FSO_3H-SbF_5.[23-24] Gutmann *et al.* have determined that $SbCl_5$ is the strongest of the binary antimony halides using Et_3PO as the base.[18] The organometallic derivatives $SbPh_5$ (**7**) and $Sb(C_6F_5)_5$ (**8**), although

homoleptic, do not have a perfect trigonal bipyrimidal geometry predicted by the VSEPR theory. Cotton *et al.* re-examined the structure of compound **7** in the crystal structure that was originally reported by Wheatley,[25] and described the structure as a distorted square pyramid. They also suggested a possible pseudo-rotation in between the square pyramidal and the trigonal bipyramidal structures in the solution (Figure 3).[26] This pseudo-rotation was examined in the case of **8** by Menjón *et al.* These workers found that the perfluorinated derivative **8** prefers to adopt the distorted trigonal bipyramidal geometry both in the solid state and in solution.[27]

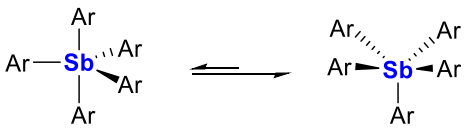

Figure 3. The geometrical interconversion of the organoantimony(V) Lewis acids.

Because the antimony atom can be six-coordinated, organoantimony(V) derivatives have been reported to bind basic anions such as chloride.[28] Our group in particular is interested in these derivatives for fluoride sensing. A common method to construct such electron-deficient organoantimony(V) compounds is by oxidizing the organoantimony(III) compounds with *ortho*-quinones, resulting in stiborane catecholates such as **9**-**11**. The spirocyclic compound phenyl(2,2'-biphenylene)(tetrachlorocatecholate)stiborane (**9**)[28] readily complexes with fluoride in a 7/3 THF/water solution with a binding constant *K* of 13500 (± 1400) M^{-1}. The fluoride

adduct [**9**-F]$^-$ was also isolated and characterized crystallographically (Figure 4).[12] The tetrachlorocatecholate substituent was replaced by an alizarin red chromophore. The resulting stiborane (**10**) features a comparable electron deficiency to **9** and displays a binding constant *K* of 16 100 (±1100) M^{-1} with fluoride in the same medium (Figure 4). Moreover, stiborane **10** shows a significant colorimetric response upon complexation with fluoride. TD-DFT analysis reveals that the fluorescence originates from the π–π* transition of the chromophore and the π*orbital is in conjugation with the antimony-centered σ* orbitals. Upon complexation with fluoride, the σ*-π* conjugation of antimony and the chromophore is perturbed, resulting in a narrower HOMO-LUMO gap and a red-shift of the fluorescence.[12] The detail of this fluorescence sensing mechanism will be further discussed in section 1.3. Besides this pendent-chromophore design, our group has also ventured into incorporating the heavy Group 15 element directly into the framework of an organic dye structure. Taking inspiration from the work by Rivard *et al*. on luminescent tellurium-incorporated heterocycles, our group prepared a series of benzostiboles featuring an antimony (V) center and a direct σ*-π conjugated system. An example of such a complex is the phenyl-substituted benzostibole tetrachlorocatecholate (**11**), which was proven to be a luminescence turn-off fluoride sensor with a binding constant *K* of 6.2 (± 0.7) × 10^5 M^{-1} in chloroform (Figure 4).[29]

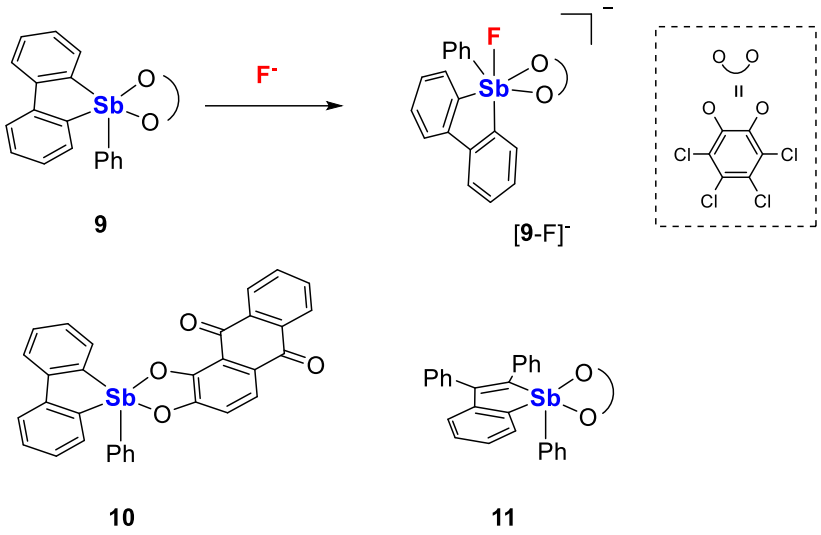

Figure 4. Neutral monofunctional organoantimony (V) fluoride sensors.

Another strategy that is frequently used in the field of small molecule activation is to introduce two Lewis acidic sites in close proximity, thus improving the host-guest interaction via chelation. The commercially available 9,9-dimethylxanthene was explored as a scaffold to construct bidentate antimony(V) systems and explore the phenomenon of chelation in fluoride complexation. Similar to synthesizing monofunctional stiboranes, oxidation of 4,5-bis(diphenylstibino)-9,9-dimethylxanthene with *o*-chloranil affords the corresponding distiborane (**12**). Compound **13** efficiently binds fluoride anion with a binding constant *K* of 700 (± 30) M^{-1} in a water/THF (v/v = 0.95/0.05) mixture, a medium with much higher water content compared with the conditions used for compounds **9** and **10**. This contesting behavior shows the advantage of the chelation effect. The presence of a Sb–F–Sb bridge in [**12**-F]$^-$ was corroborated by crystallography (Figure 5, top). Taking a step forward, a similar distiborane was constructed on the 1,8-triptycenediyl backbone

(**13**). Compared to dimethylxanthene, the triptycene backbone is more flexible during the event of anion chelation, as evidenced by the Sb-Sb separation decreasing from 5.203(2) Å in compound **13** to 4.404(1) Å in [**13**-F]$^-$. Additionally, instead of a Lewis basic electron-rich oxygen site at the central position of xanthene, the triptycene backbone offers a C-H group to provide stabilization of the fluoride anion *via* hydrogen bonding. Both of these effects contribute to a stronger complexation of the fluoride anion by **13**, as corroborated by the reaction of **13** with [**12**-F]$^-$, which readily affords free **12** and [**13**-F]$^-$ in CH_2Cl_2 (Figure 5, bottom).[30]

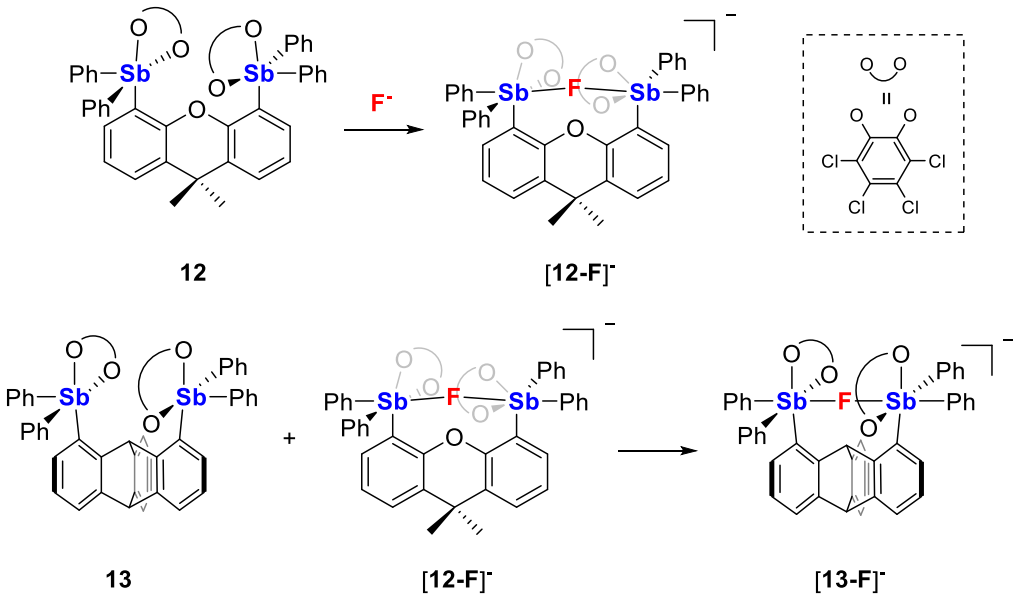

Figure 5. Neutral bidentate organoantimony(V) Lewis acids as fluoride sensors.

Besides fluoride, these five-coordinated antimony compounds have also been used for small molecule activation. Abakumov *et al.* first reported the reversible binding of

dioxygen by non-transition-metal compounds. They synthesized *o*-amidophenolatotriphenylantimony(V) (**14**) by oxidation of $SbPh_3$ with 4,6-di-tert-butyl-*N*-(2,6-diisopropylphenyl)-*o*-iminobenzoquinone.[31] Compound **14** is air-stable in the solid state yet it binds molecular oxygen in an acetone-d_6 solution after exposure to afford **14**-O_2 for 2 h. This reaction can be reversed by treating the acetone-d_6 solution of **14**-O_2 with repeated freeze-pump-thaw cycle for 1 hour (Figure 6). The O-O distance in the crystal structure of **14**-O_2 (1.416(3) Å) is comparable to an antimony endoperoxide (1.468 Å).[32] The authors suggested that a key step of the mechanism is the initiation step of a one-electron oxidation of the dianionic *o*-amidophenolate ligand to a radical-anion, resulting a cationic antimony center, while the triplet dioxygen turned into superoxide.[31] This mechanism was confirmed after the authors explored a variety of substituted catecholates and *o*-amidophenolates and concluded that the redox potential of the ligand in the antimony(V) complex plays a crucial role in the ability of the complex to bind and release O_2.[33-34] For example, (4,5-di-methoxy-3,6-di-*tert*-butyl-catecholato)triphenylantimony(V) (**15**) reversibly binds dioxygen to form **15**-O_2 in a similar fashion as **14** (Figure 6). However, when the electron-donating methoxy groups on the catecholate are substituted by hydrogens, the resultant (3,6-di-*tert*-butyl-catecholato)triphenylantimony(V) (**16**) has a higher redox potential for the first anodic process, and is inert to dioxygen both in the solid state and in solution (Figure 6).[34-35]

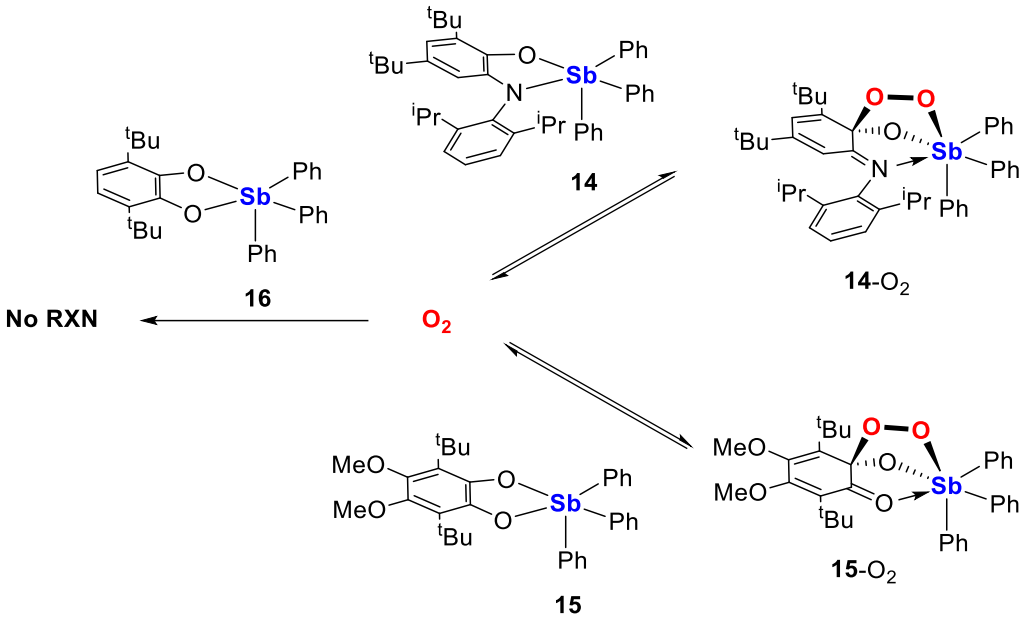

Figure 6. Complexation of organoantimony (V) Lewis acids with dioxygen.

Inspired by the Gutmann-Beckett protocol in which the Lewis acidity of an electron-deficient compound is correlated to the ^{31}P NMR shift of a triethylphosphine oxide reporter upon formation of the acid-base adduct, our group invested the abilities of organoantimony(V) compounds to complex neutral donors such as phosphine oxides. The treatment of **58** with *o*-chloranil results in the stiborane $Sb(C_6F_5)_3(O_2C_6Cl_4)$ (**61**), an air and moisture stable compound whose acidity was determined to be comparable with borane **1**. Compound **61** displays quantitative complexation with Et_3PO (Figure 7). This particular interaction was also examined in an intramolecular version, with the phosphine installed *ortho* to the stiborane center, as in *o*-$C_6H_4(PPh_2)(SbPh_2(O_2C_6Cl_4)$ (**17**). The phosphorous (III) to antimony (V) interaction is compatible with the concept of the

frustrated Lewis pair, and was used in the sensing of formaldehyde in aqueous solution (Figure 7).[36]

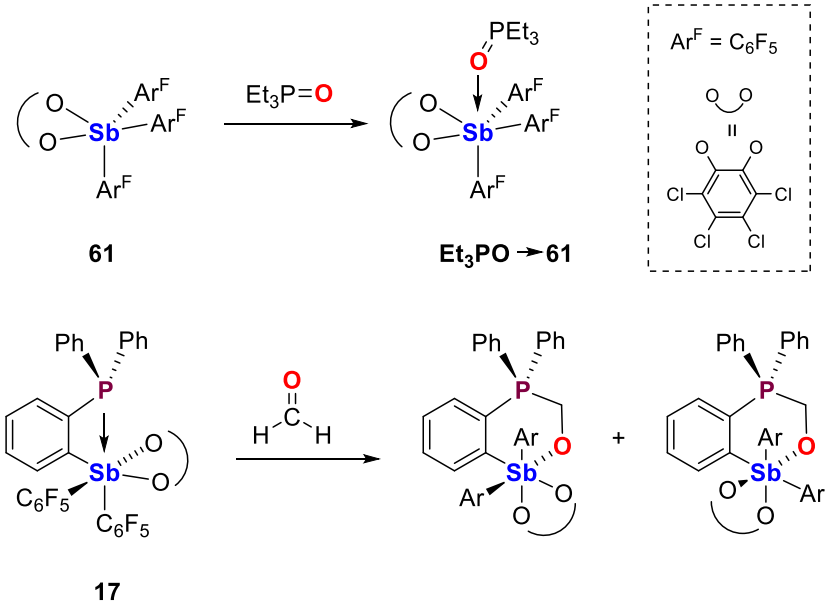

Figure 7. Complexation of organoantimony (V) Lewis acids phosphine oxide, and complexation of formaldehyde with the intramolecular frustrated Lewis pair of phosphine-stiborane in aqueous solution.

Lastly, the coordination chemistry of antimony(V) complexes allows them to be ideal Z-ligands when placed in the proximity of late-transition metals. Oxidation of compound **4** followed by ligand exchange of fluoride affords ((*o*-$(Ph_2P)C_6H_4)_2SbF_3$)AuCl (**18**-AuCl, Figure 8).[37] The strong Au→Sb donor-acceptor interaction in compound **18**-AuCl is evident by the large stabilization energy of 59 kcal/mol determined by Natural Bond Orbital (NBO) analysis of the Density Functional Theory (DFT) for the Au→Sb

interaction. The enhanced activation of the gold center by the stronger Z-ligand is also reflected in the carbophilic properties of the gold center.[37] Similar organoantimony(V) based Z-type ligands include the triaryldihalides (*o*-$(Ph_2P)C_6H_4)_3SbCl_2$(**19**)[38], (*o*-$(Ph_2P)C_6H_4)_3SbF_2$(**20**)[39], and (*o*-(^{i}Pr$_2$P)$C_6H_4)_2PhSbCl_2$ (**21**)[40] which have been complexed to different molecules. Organoantimony(V) based Z-type ligands featuring catecholate groups include (*o*-$(Ph_2P)C_6H_4)_3$(*o*-$C_6H_4O_2$)Sb (**22**)[41] as well as the tetrachlorocatecholates (*o*-$(Ph_2P)C_6H_4)_2$(*o*-$C_6Cl_4O_2$)SbPh (**23**)[42-44] and (*o*-(^{i}Pr$_2$P)$C_6H_4)_2$(*o*-$C_6Cl_4O_2$)SbPh (**24**)[42-44] which have been assembled in the coordination sphere of various transitional metals (Figure 8).[45]

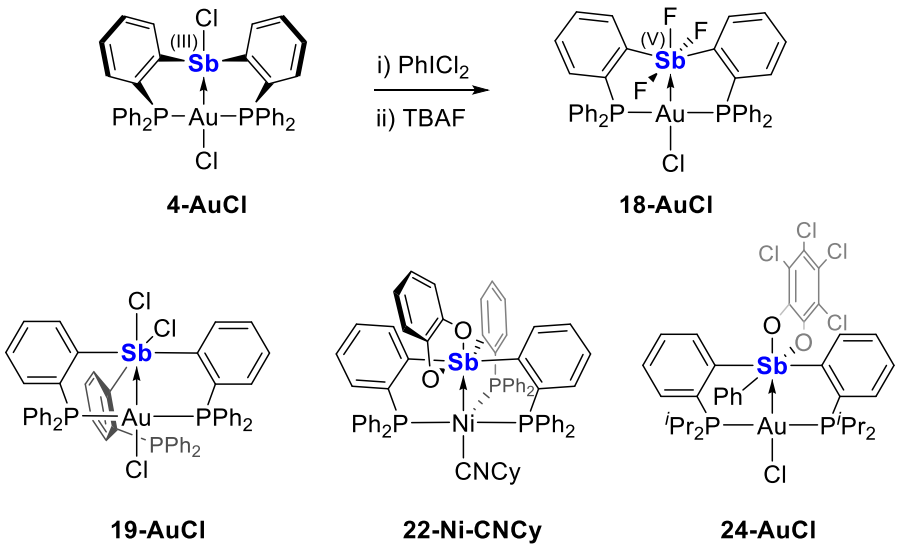

Figure 8. Organoantimony(V) compounds as Z-ligands of transition metals.

1.1.4 Cationic organoantimony Lewis acids

1.1.4.1 Organoantimony(III) cations

Another logical step to further enhance the acidity of organoantimony compounds is to introduce a cationic charge on the Group 15 element. Due to the large atom size of antimony and its tendency to have coordination numbers of six or higher, cationic species often form polymeric solids through intermolecular donor-acceptor interactions. Consequently, bulky ligands or additional neutral coordinating ligands are essential in isolating molecular complexes of such heavy main-group elements. Holeček *et al.* reported the organoantimony (III) cations supported by O,C,O pincer type ligands. Treatment of the neutral complex (2,6-($MeOCH_2$)C_6H_3)$SbCl_2$ (**25**-Cl_2) with one or two equivalents of silver triflate affords (2,6-($MeOCH_2$)C_6H_3)SbCl(OTf) (**25**Cl(OTf)) or (2,6-($MeOCH_2$)C_6H_3)$Sb(OTf)_2$ (**25**$(OTf)_2$), both with the triflate group(s) bound covalently to the central antimony atom (Figure 9).[46] When the weakly coordinating carba-closo-dodecaborate anion ($[CB_{11}H_{12}]^-$) was introduced instead of the triflate, a separate ion pair consisting of the free [**25**-Cl]$^+$ cation and the carborane anion can be isolated from a THF solution. A solvent THF molecule was found bound to the cationic antimony center in the solid state structure of [**25**-Cl(THF)]$[CB_{11}H_{12}]$ (Figure 9). VT NMR in THF revealed that the antimony center is symmetrically substituted, suggesting a fast exchange of the coordinated THF.[46] The same research group also reported similar synthetic protocols starting with an N,C,N pincer type ligand supported organoantimony(III) derivative (2,6-(Me_2NCH_2)C_6H_3)$SbCl_2$ (not shown), and once again the triflate anions were found to be bound to the central atom whereas the carborane anion co-exists with a free cationic

chloroantimony center.[47] Both structural studies addressed the importance of the non-coordinating anion in the isolation of these compounds.

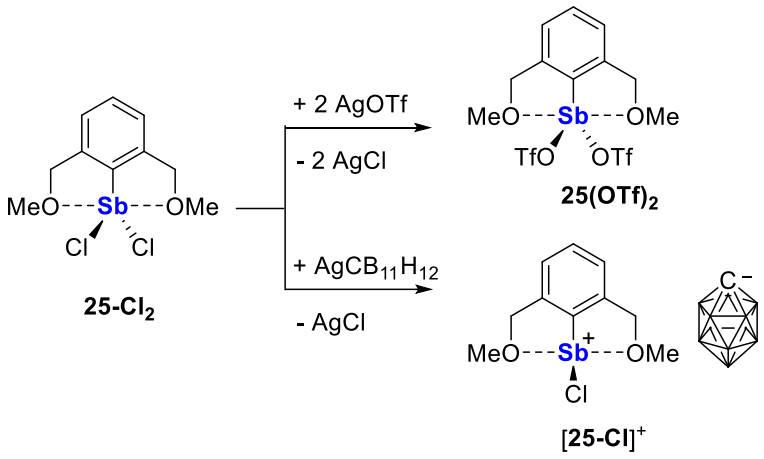

Figure 9. Organoantimony(III) cations supported by pincer type ligands.

Burford *et al.* used a different strategy of introducing a neutral ligand during the process of halide abstraction. By controlling the stoichiometry of antimony trifluoride, the fluoride abstractor trimethylsilyl triflate (TMSOTf), and the neutral ligand 2,2'-bipyridine (bipy), they were able to isolate a series of mono-, di-, and trications $[(bipy)_nSbF_{(3-m)}][OTf]_m$ (**26**: n = m = 1, **27**: n = m = 2, **28**: n =2, m = 3) (Figure 10).[48] Thermodynamic computations showed that the elimination of gaseous TMSF largely benefitted the formation of these cationic compounds. The substantial acidity of these compounds is evident by their extreme sensitivity to moisture and the presence of weak interactions between the cationic center and the triflates in the solid-state structures of **26** and **28**. The antimony center in compound **28** adopts a see-saw geometry in both single crystal

structure and a gas-phase geometry calculation, suggesting a large p contribution to these dative bonds and a stereochemically active lone pair on the antimony atom. Alternatively, compound **28** can be obtained by treating SbCl3 with AgOTf.[48] Computational work suggested the N-Sb interaction was more ionic compared with the lighter Group 15 element derivatives such as P and As. NMR measurements revealed that the mobility of bipy group is higher in Sb compared to the rest of the series as well .[48]

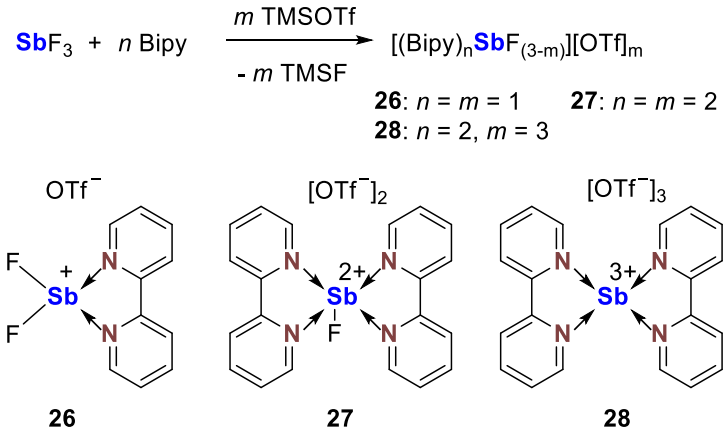

Figure 10. Organoantimony(III) cations supported by bipyridines.

1.1.4.2 Organoantimony(IV) radical cations

Despite the diversity of Group 15 cations overall, there are not so many appearances of antimony radical cations, but the general strategy of stabilizing such reactive radical cations with bulky substituents remain the same.[49-51] Recently, Wang *et al.* isolated a pair of antimony radical cations, namely $[Ar_3Sb]^{\bullet+}$ (Ar = 2,6-^{i}Pr$_2$-4-OMe-C_6H_2 for **29**$^{\bullet+}$ and 2,4,6-^{i}Pr$_3$-C_6H_2 for **30**$^{\bullet+}$) by one-electron oxidation of the triaryl

organoantimony(III) species with $AgSbF_6$ as the oxidant and $NaBAr^F_4$ (Ar^F = 3,5-$(CF_3)_2C_6H_3$) as the source of the counteranion (Figure 11).[52] The formation of these radicals was first observed transiently in the cyclic voltammograms of the corresponding stibine Ar_3Sb in CH_2Cl_2 using $^nBu_4N[BAr^F_4]$ as the supporting electrolyte. Both of the $[BAr^F_4]^-$ salts were then isolated and fully characterized. Salt [**29**]$^{\bullet+}[BAr^F_4]^-$ and [**30**]$^{\bullet+}[BAr^F_4]^-$ are thermally stable in anaerobic conditions. The structure of radical cation **29**$^{\bullet+}$ adopts a trigonal pyramidal geometry, yet is more "flattened" compared to the corresponding stibine, as evident by the increase of average $\angle C_{ipso}$-Sb-C_{ipso} angle from 107.3° to 115.75°, resulting a higher 5s-5p hybridization in the radical which is corroborated by the calculated singly occupied molecular orbital. It is interesting to note that the phosphorus analogue of the radical cation $[Ar_3P]^{\bullet+}$ (Ar = 2,4,6-$^iPr_3$-C_6H_2), due to the smaller size of the central atom, is more sensitive to ligand sterics and adopts a perfect planar geometry whose sp hybridization is even higher.[53] Compound [**30**]$^{\bullet+}[BAr^F_4]^-$ was also tested with organic radical traps such as *p*-benzoquinone. Upon reaction with the radical trap, the distinctive purple color of **30**$^{\bullet+}$ disappears, resulting in a colorless solution and the formation of a dicationic salt of the product over the course of 12h (Figure 11).

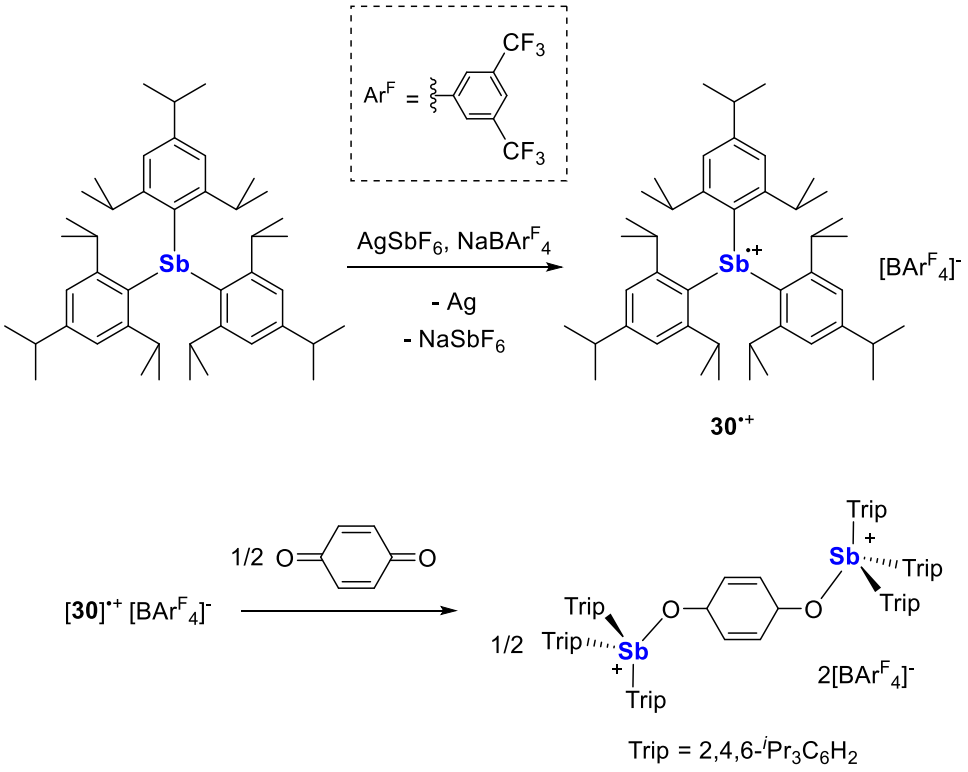

Figure 11. Organoantimony(IV) radical cation stabilized by bulky ligands and the reaction with *p*-benzoquinone.

1.1.4.3 Organoantimony(V) cations

Compared with five-coordinated neutral stiboranes, four-coordinated stibonium monocations with the general formula $[SbR_4]^+$ are expected to be more acidic due to the electron deficiency associated with their cationic charge. Given their coordinative unsaturation, these cationic species are largely stabilized by the steric bulk provided by the organic substituents or the donation from solvent molecules or other labile anions. The simple organoantimony(V) cation, $[Ph_4Sb]^+$ (**70**$^+$), which is stable to air and moisture, has versatile binding properties. In the polar solvent nitromethane, conductivity measurements

showed that **70**$^+$ co-exist with anions such as bromide, chloride, nitrate and trifluoroacetate as ion pairs, but forms tightly bound, monomeric molecules with more basic anions such as fluoride, hydroxide, trichloroacetate and acetate.[54] In terms of application, an early attempt in the 1960s described the ability of [**70**][Br] to extract fluoride in biphasic water/CCl_4 mixtures.[55] A subsequent study reported a linear response in the UV spectrum of **70**$^+$ to the concentration of fluoride, pointing to its ability to act as a photophysical fluoride sensor.[56] Attaching a fluorophore on the central antimony atom of such species results in a photophysical response in the visible range, which facilitates the practical applications of organoantimony(V) compounds as fluoride sensors. For instance, the 9-anthryl substituted tetracoordinated antimony(V) cation 9-anthryltriphenylstibonium (**72**$^+$) was synthesized as a triflate salt, and shows a faint fluorescence emission (Φ = 2.2%) in a 90% aqueous medium (9:1 H_2O:DMSO, with a pyridine buffer at pH 4.8 and 10 mM CTAB). Under this particular condition, compound [**72**][OTf] reacts with fluoride strongly to form the five-coordinated compound **72-F** (Figure 12). The binding constant *K* was measured to be 12000 ± 1100 M^{-1}, allowing for the sensing of fluoride ions at ppm levels. The fluoride adduct **72-F** features a fluorescence quantum yield of 14.1%, almost 7-fold higher than the unbound stibonium, resulting a significant turn-on response.[14] The synthetic protocol of [**72**][OTf] can be extended to prepare the triflate salts of 1-pyrenyl (**31**$^+$) and 3-perylenyl (**32**$^+$) substituted tetra-coordinate stiboniums. Comparable to **72**$^+$, both **31**$^+$ and **32**$^+$ are fluorescence turn-on sensors, and have large binding constants *K* of 10000 ± 800 M^{-1} and 10000 ± 500 M^{-1}, respectively, in the same 90% aqueous medium as mentioned above. Unlike **72-F** which is excited by UV-light (λ_{ex} = 375 nm), **32-F** has

an excitation that is shifted into the visible region (λ_{ex} = 423 nm), and the quantum yield of **32-F** reaches to a remarkable 59.2%, an 8-fold increase from the free stibonium **32**$^+$ (Φ = 7.3%), making compound **32**$^+$ a better practical fluoride sensor.[57] A dimethyl BODIPY derivative of stibonium (**33**$^+$) can also be obtained as a triflate salt, and can selectively bind fluoride ($K > 10^7$ M^{-1}) and cyanide (K = 1.6 (± 0.1) × 10^6 M^{-1}) with a turn-on response in CH_3CN. Detailed theoretical studies on the mechanism of the turn-on fluorescence will be discussed in section 1.3. In addition to applications in fluoride sensing, more tetraarylstibonium monocations have been synthesized as catalysts for organic transformations and will be discussed in section 1.2.

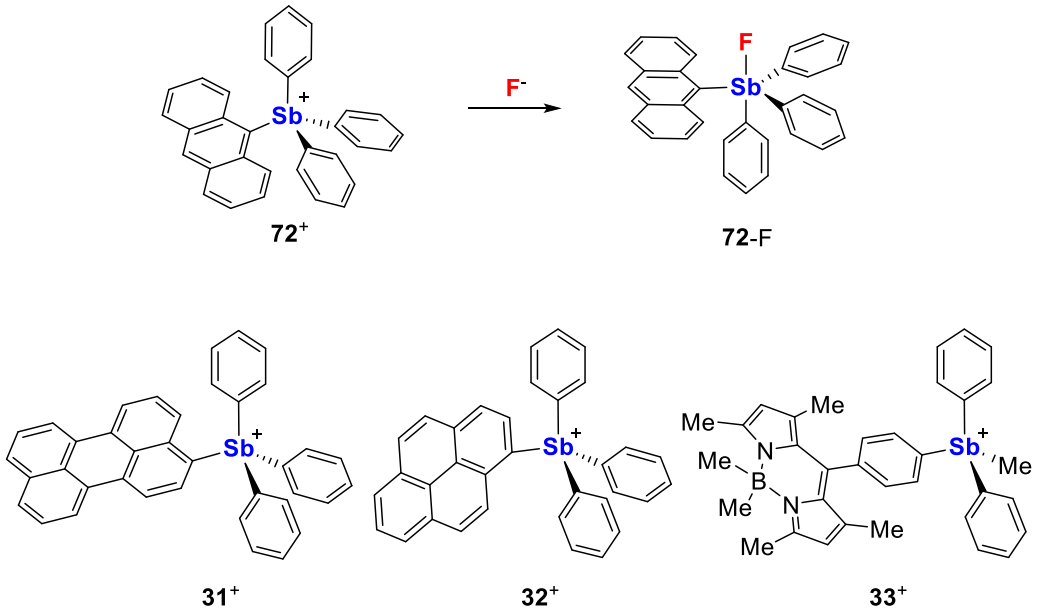

Figure 12. Fluorescence turn-on fluoride sensors based on organoantimony(V) compounds.

Organoantimony(V) dications have also attracted attention from a synthetic and coordination chemistry point of view. Owing to the intensified acidity the results from coulombic effects, these dications are highly acidic and often require additional stabilization from coordinating anions or L-type donor ligands. Early attempts by Sharutin *et al.* have reported a handful of these anion-stabilized cations such as triphenylantimony organosulfonates[58] by ligand redistribution starting from Ph_5Sb, or triphenylantimony dioximates[59-60] by oxidation of Ph_3Sb. Compounds of general formula R_3SbX_2 (X = Cl, Br, R = aryl) are another common Sb(V) source in generating antimony-centered cations, particularly dications. Burford *et al.* reported the isolation of $Ph_3Sb(OTf)_2$ (**63**), which is essentially a $[Ph_3Sb]^{2+}$ dication stabilized by two triflate anion donors, from reacting Ph_3SbCl_2 with two equivalents of AgOTf. Compared with the air-stable monocation $[Ph_4Sb]^+$ (**70**$^+$), the $[Ph_3Sb]^{2+}$ moiety in complex **63** is less sterically protected and rapidly reacts with water to form a μ-oxo-bis(tetraphenylantimony) cation (**34**).[61-62] Complex **63** also participates in coordination reaction with neutral donors such as Ph_3PO, 4-(dimethylamino)pyridine (dmap) to form the adducts $[Ph_3Sb(OPPh_3)_2][OTf]_2$ (**35**) and $[Ph_3Sb(dmap)_2(OTf)][OTf]$ (**36**), respectively. Reaction with the bidentate donor 1,10-phenanthroline (phen) was found to form $[Ph_3Sb(phen)(OTf)][OTf]$ (**37**, Figure 13).[63-64] While the antimony center in the adduct **35** adopts a trigonal bipyramidal geometry and is free from the two anions, both centers of the adducts **36** and **37** adopt distorted octahedral geometries with an additional short contact with a triflate anion. The high coordination number in **36** and **37** is rationalized with the lower steric pressure of the planar nitrogen donors compared to the conical phosphine oxide. It is interesting to note that adduct **35**

can undergo ligand exchange reaction with two equivalents of dmap to form adduct **36** together with the release of two equivalents of Ph_3PO, demonstrating the rich coordination chemistry of the dication as a synthon to diverse coordination complexes.[63] Recently, several ligand exchange reactions are reported between different anion-donor supported $[Ph_3Sb]^{2+}$ dications with a stoichiometric amount of a triphenylantimony dihalide to from two equivalents of the corresponding halostibonium.[65-66] These precedents and strategies have inspired our work that is described in chapter III.

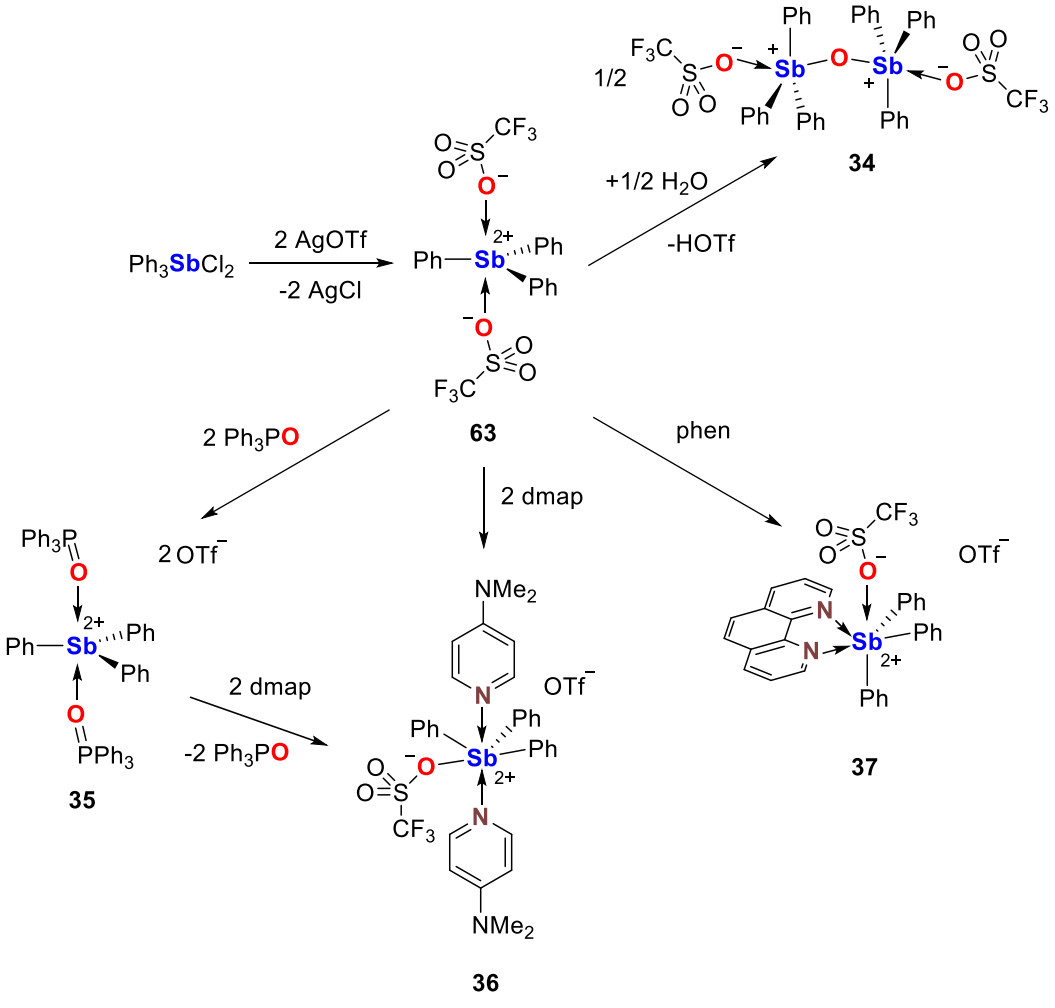

Figure 13. Synthesis and coordination reactivity of $[Ph_3Sb]^{2+}$.

1.2 Applications of the Group 15 Lewis acids in catalysis

1.2.1 Introduction to main group compounds as catalysts

Many important organic reactions are catalyzed by Lewis acidic main-group compounds. Historically, the vast majority of these catalyses involve Group 13 species such as organoboron compounds, and in some occasions these main-group compounds serve as activators or co-catalysts of transition metal catalysts. One prominent example of such organoboron compounds is $B(C_6F_5)_3$ (**1**) which has been reported with applications in the Ziegler-Natta polymerization of α-olefins,[67-68] the hydrosilylation of aldehydes,[69-70] Diels-Alder reactions,[71-72] among others. A number of comprehensive reviews have covered the developing efforts on boron-based Lewis acid catalysts.[3, 73-76] Group 14 Lewis acids such as silicon cations have also been reported as active catalysts for Diels-alder reactions[77-79] and hydrosilylations.[80-81] The application of Group 15 compounds in catalysis, by contrast, remained relatively undeveloped until the past decade when extensive explorations began. Another important aspect of catalysis involving Group 13 Lewis acids is the concept of Frustrated Lewis Pairs (FLP) where a Group 15 Lewis base is sterically prevented to interact with a Group 13 Lewis acid. The resulting Lewis acid-base pair may show cooperative effects in activating small molecules such as dihydrogen in the catalytic hydrogenation of imines[82] or carbon dioxide in the catalytic reduction to methanol in the presence of hydroboranes.[83] The concept of FLP has been extended in a wide range of catalytic applications.[84-85] This chapter, however, will exclusively discuss the instances where the Group 15 compound is the sole acting Lewis acid catalyst.

1.2.2 Phosphorus-based Lewis acids in organic catalysis

The acidity of organophosphorus compounds is overshadowed in the literature by the widely exploited nucleophilicity of P(III) Lewis bases, which are common L-type ligands of transition metals and the active Lewis bases in FLP chemistry. However, organophosphorus cations, both in the +III and +V states of the central atom, have been reported to possess a noteworthy electrophilicity. For example, a phosphonium(V) moiety, used as the acidic functionality and paired with a basic amido group (**38**) captures carbon dioxide stoichiometrically in a FLP manner.[86] Our group has also reported a phosphorous(V) cation (**39**$^+$) as a fluoride receptor in cooperation with a borane.[5] In the field of catalysis, organophosphonium(V) species such as **40**$^+$ - **42**$^+$ have demonstrated their reactivity in catalytic Mukaiyama-aldol additions ([**40**][OTf]$_2$, [**41**][B(C$_6$F$_5$)$_4$]),[87-89] Diels-Alder reactions ([**42**][OTf]),[90] or in the cyanosilylation of aldehydes and ketones ([**79**]I, Figure 14).[91]

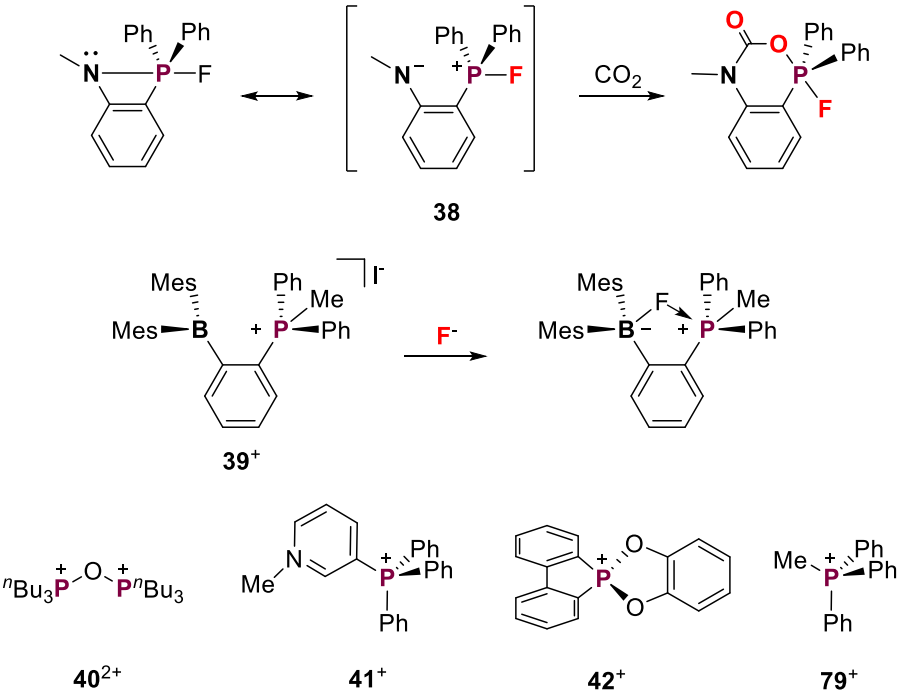

Figure 14. Selected examples of phosphorus-based Lewis acids and Lewis acid catalysts.

In 2013, Stephan *et al*. reported a highly electrophilic organophosphonium $[(C_6F_5)_3PF]^+$ (**43** $^+$) as a tetrakis(pentafluorophenyl)borate ($[B(C_6F_5)_4]^-$) salt.[7] The pentafluorophenyl substituents provide the steric bulk that kinetically stabilize the cation, and their highly electron-withdrawing nature enhances the electrophilicity of the phosphorus center. DFT analysis reveals that the LUMO of cation **43**$^+$ resides largely on the σ* orbital of the P-F bond which is more polar compared to the P-C bonds. The acidity of cation **43**$^+$ was demonstrated by its complexation with neutral donors such as DMF and Et_3PO, and more noteworthily, by its ability to cleave the strong C-F bond in a number of fluoroalkanes and to abstract a fluoride from Ph_3CF to afford the trityl cation and the phosphorus difluoride species **43**-F. Salt [**43**][$B(C_6F_5)_4$] was tested as a catalyst in

hydrodefluorination reactions. The authors found that when combined with the sacrificial silane Et_3SiH, 1-fluoroadamantane, 1-fluoropentane, fluorocyclohexane, and α,α,α-trifluorotoluene are catalytically converted into the corresponding hydrocarbons within 3 hours under 1% of catalyst loading. The proposed mechanism involves the reaction of **43**$^+$ with the fluoroalkane substrate to form **43**-F and a transient carbocation, which is quenched by the silane to afford the product alkane and a silylium cation. The silylium cation then reacts with **43**-F to regenerate the catalyst **43**$^+$ (Figure 15). Inspired by this work, a dicationic fluorophosphonium salt $[(SIMes)PFPh_2][B(C_6F_5)_4]_2$ (**44**$[B(C_6F_5)_4]_2$, SIMes = 1,3-dimesitylimidazolidin-2-ylidene) featuring a cationic imidazolium substituent was subsequently synthesized and was proven to be an effective hydrodefluorination catalyst as well (Figure 15).[92] The strong fluorophilic properties of **43**$^+$ were further exploited in the catalytic C-C coupling reaction of benzyl halides with arenes and allylic silanes, and **43**$^+$ was found to selectively activate benzyl fluorides compared with benzyl chlorides and bromides.[93] Taking advantage of its high acidity alone, cation **43**$^+$ has been established as an efficient catalyst for a variety of reactions including transfer hydrogenation and hydrosilylation of alkenes and alkynes,[94-96] polymerization of isobutylene,[94] the Friedel-Crafts type dimerization of 1,1-diphenylethylene,[94, 97] and deoxygenation of ketones.[98] Efforts have also been made in developing new phosphorus-based cations as catalysts for these transformations. Interestingly, the fluorophosphonium with the 3,5-CF_3-phenyl derivative (**45**$^+$) is not as acidic in terms of reactivity despite the phosphorus center in **45**$^+$ being kinetically more accessible than **43**$^+$ (Figure 15).[97] Recently, an air- and moisture- stable derivative,

$[Ph_3P(CF_3)]^+$ (**46** $^+$), was reported to catalyze the hydrodefluorination of 1-fluoroadamantane with Et_3SiH under elevated temperature conditions.[99]

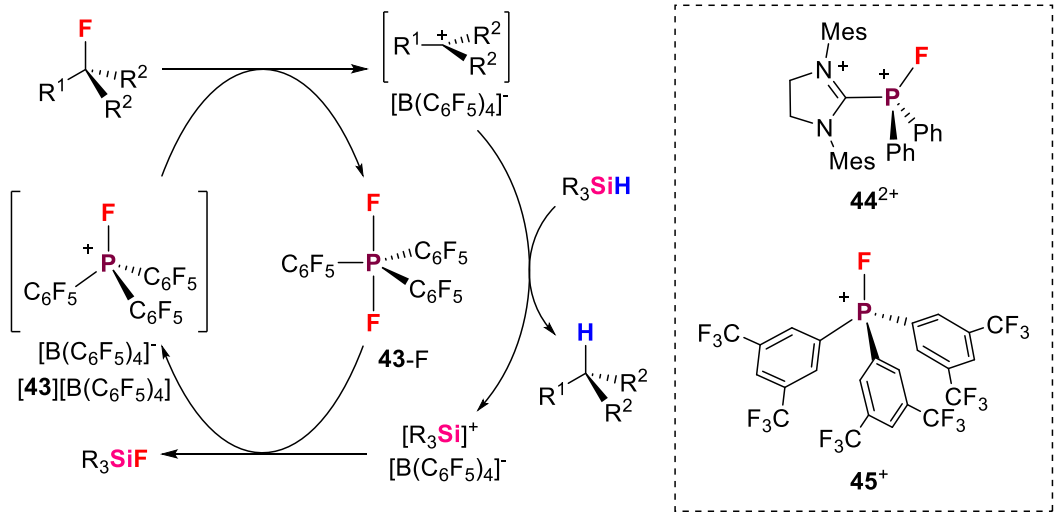

Figure 15. Proposed mechanism of the hydrodefluorination of fluoroalkanes catalyzed by [**43**][$B(C_6F_5)_4$]. The the phosphonium Lewis acid catalysts **44**$^{2+}$ and **45**$^+$ are also shown.

1.2.3 Antimony-based Lewis acids in organic catalysis

As mentioned in section 1.2.1, studies on Group 15 compounds as remained scarce until the recent decade, and the applications of antimony compounds as Lewis acids remain quite uncharted. An early example by Nomura *et al*. from 1992 describes that triphenylstibine oxide (Ph_3SbO) with assistance from tetraphosphorus decasulfide (P_4S_{10}) effectively catalyzes the fixation of carbon dioxide with diamines to form cyclic ureas (Figure 16).[100] The reaction condition was milder compared with urea formation from carbamic acids. In another example, Yin *et al*. in 2010 reported the organoantimony(III)

cation supported by a C,N,C pincer ligand and coordinated by a triflate anion (**47**(OTf)). Compound **47**(OTf) displays high catalytic efficiency towards one-pot Mannich-type reactions in a variety of solvents including water, and was able to be recycled for 10 times from aqueous catalytic systems without significant deactivation (Figure 16).[101] Interestingly, the organobismuth(III) derivative of $\mathbf{47}^{+}$ catalyzed the same reaction in high yield but required longer reaction time (24 h) and showed no diastereoselectivity in the products,[102] whilst the reaction with **47**(OTf) as catalyst selectively resulted in the *anti*-isomer in 4 hours. The difference in catalytic reactivity between these two Group 15 element-containing compounds directly reflects the difference in Lewis acidity where antimony is stronger than bismuth. These differences have shown how the strong oxophilicity of antimony affects the stereochemical outcome of the reaction.

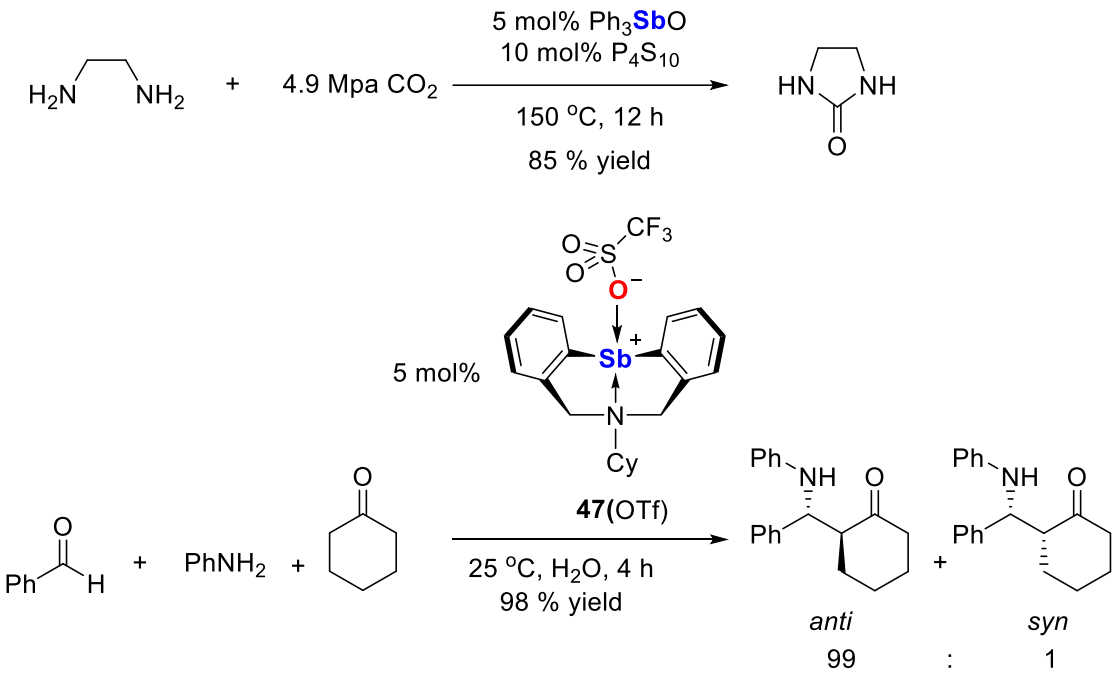

Figure 16. Top: Triphenylstibine oxide catalyzed synthesis of cyclic urea from diamine and carbon dioxide; Bottom: Direct diastereoselective Mannich reactions catalyzed by an organoantimony(III) cation in water.

The majority of the examples of antimony-containing compounds as Lewis acid catalysts involves organoantimony(V) cations as the active catalytic center. In the late 1980s to early 1990s, Baba *et al*. demonstrated that tetraphenylstibonium (**70**$^{+}$) activates oxiranes to form the unique α-cleavage products. This specific ring-opening pattern suggests a dominant S_N1 pathway meditated by the Lewis acid. When paired with bases such as iodide or triflate, the acid-base pair catalyze the cycloaddition of oxiranes with various trinuclear nucleophiles. [103-106] In particular, [**70**]I catalyzes the fixation of CO_2 with oxetane to form trimethylene carbonate in near quantitative yield under moderate

conditions (Figure 17, A). In another work from the same authors, they studied the cycloaddition of propylene oxide with phenyl isocyanates, and found that the regioselective 4,5-isomer was favored in the presence of [**70**]I (Figure 17, B). These results inspired our work described in chapter IV in which we investigated the structure-reactivity relationship among different stibonium derivatives.

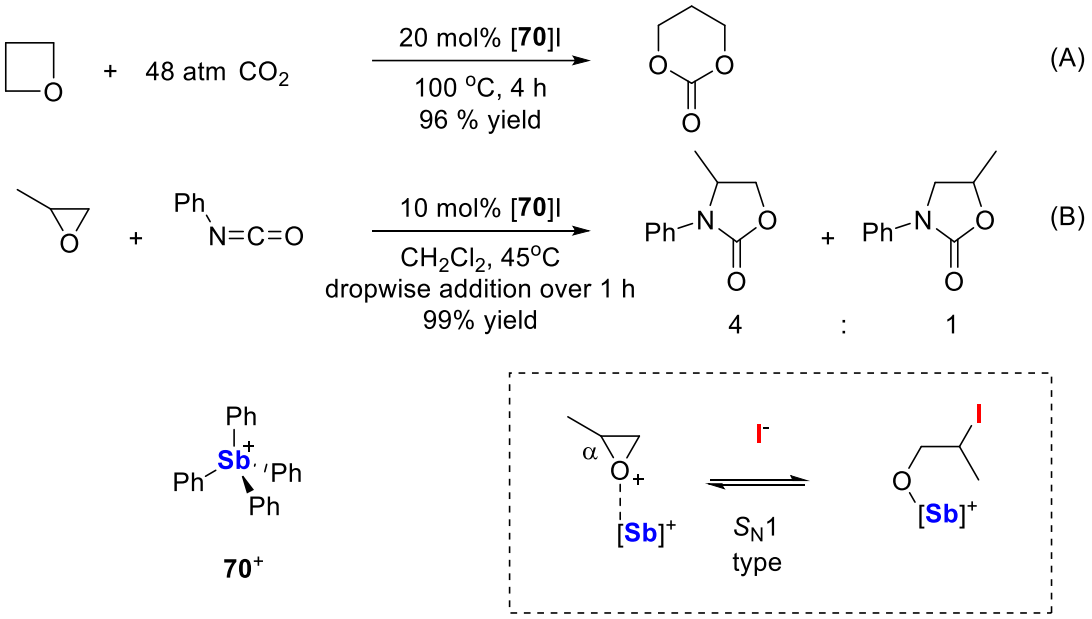

Figure 17. Cycloaddition reactions catalyzed by [**70**]I and the initiating step of the proposed mechanism of the α-cleavage of oxiranes.

In 2015, Qiu, Yin, and Xu *et al*. reported that the hydrolysis product of Ph_3SbCl_2, which is a μ_2-oxo-bis-stibonium dichloride complex, can be treated with the silver salt of a long-chain anion perfluorooctanesulfonates to form a "free" distibonium salt **48**. Compared with the triflate derivative **34**, which features triflate anions attached to the

cationic antimony center, the perfluorooctanesulfonates in **48** are free from these interactions due to the increased steric bulk and the enhanced electron withdrawing properties of the long perfluorinated chain.[107] The authors tested the water-stable distibonium salts **34** and **48** in the Michael addition of indoles to α,β-unsaturated ketones (Figure 18, A) whose background reaction in acetonitrile will result in a 9% yield in 12 h. Both stiboniums catalyzed the reaction and increased the yield at 1 hour to 71% and 91%, respectively. This difference in catalytic reactivity is consistent with the acidity of the antimony centers as observed by crystallography, as the cationic centers in **48** is stabilized by neutral water molecules, and can retain more acidity compared with **34** whose terminal donors are the triflate anions. Compound **48** also shows a higher catalytic efficiency in the allylation reaction of aldehydes (Figure 18, B). The reaction reaches a 94% yield in 1 hour compared to 82% when **34** is used as the catalyst, yet both catalysts have a higher reaction rate than the control experiment where only 23% conversion was observed without any catalysts.[107] Recently, noting that the carbonyl moiety can be activated by Lewis acids, Hudnall *et al*. applied stibonium cations in catalytic aldol condensations where the C-C bond is formed in between two equivalent of aldehydes resulting in α,β-unsaturated carbonyl species. To this end, a phosphine-supported stibonium on a naphthalene backbone ([**49**][OTf]) was synthesized as a triflate salt.[108] The ^{1}H NMR chemical shifts of [**49**][OTf] were observed to shift upfield upon heating a $CDCl_3$ solution of [**49**][OTf] with 3 equivalent of butyraldehyde to 70 °C, evident of the interaction of the carbonyl group with the cationic antimony center (Figure 18). Essentially, under the same conditions, [**49**][OTf] was found to catalyze the aldol condensation of butyraldehyde to form the

corresponding α,β-unsaturated aldehyde quantitively at 0.5 mol% catalyst loading in 24 h (Figure 18, C). No side products of the β-hydroxy aldehydes were formed, and the substrate scope studies revealed that the selective aldol condensation catalyzed by [**49**][OTf] can be applied to various aldehyde substrates containing two α-hydrogen atoms. Compound [**49**][OTf] was subsequently found to be highly reactive toward the catalytic acetalization of aldehydes using triethoxymethane in organic solvents (Figure 18, D), and was reported to be able to be recycled to up to 6 times without loss of efficiency.[109]

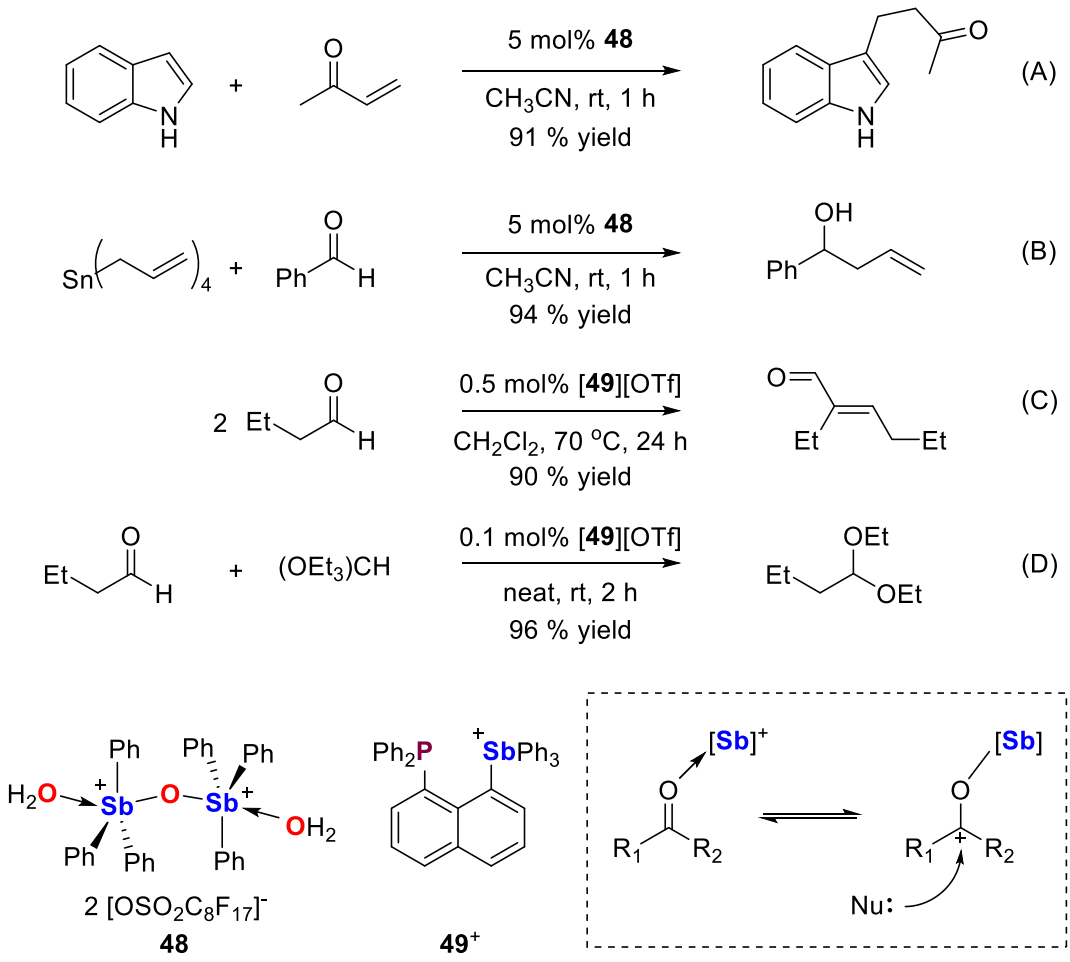

Figure 18. Selective transformations catalyzed by organoantimony(V) cations, and the activation of carbonyl group in the proposed mechanisms.

In 2014, our group reported a highly electron deficient tetraarylstibonium cation, tetrakis(pentafluorophenyl)stibonium, as a tetrakis(pentafluorophenyl)borate salt ($[Sb(C_6F_5)_4)][B(C_6F_5)_4]$, [**2**][$B(C_6F_5)_4$]). [13] Treatment of $SbCl_5$ with pentafluorophenyl lithium (LiC_6F_5) afforded **2**-Cl in moderate yields, and subsequent reaction of **2**-Cl with TMSOTf in CH_3CN or $[(Et_3Si)_2H][B(C_6F_5)_4]$ in toluene resulted in **2**(OTf) and

[**2**][$B(C_6F_5)_4$] as air-stable solids. The ^{19}F NMR resonances of $\mathbf{2}^+$ in [**2**][$B(C_6F_5)_4$] shifts distinctly downfield compared to that of **2**-Cl and **2**(OTf), supporting the ionic nature of the borate salt. In contrast to **2**-Cl and **2**(OTf) whose center atom adopts a trigonal bipyrimidal geometry, the cationic antimony center in [**2**][$B(C_6F_5)_4$] adopts a tetrahedral geometry and is free of interactions with the borate anion. DFT analysis reveals that the LUMO of $\mathbf{2}^+$ consists of the linear combination of the four Sb-C σ* orbitals. The strong acidity of $\mathbf{2}^+$ is evident by its ability to activate $[FB(C_6F_5)_3]^-$ and $[SbF_6]^-$ in THF to form **2**-F (Figure 19). This indicates that in THF, $\mathbf{2}^+$ is more acidic than $B(C_6F_5)_3$ and SbF_5 whose calculated FIAs are 489 and 444 kJ/mol,[110] respectively. The polymerization of THF was also observed in the presence of [**2**][$B(C_6F_5)_4$] upon standing, a phenomenon not observed with **2**-Cl nor **2**(OTf). Lastly, $\mathbf{2}^+$ is also shown to be an activator of Et_3SiH for the hydrodefluorination (HDF) reaction of 1-fluorooctane and trifluorotoluene (Figure 19). Unlike the HDF reaction catalyzed by fluorophosphonium $\mathbf{43}^+$,[7] NMR studies reveal that in the HDF system, $\mathbf{2}^+$ readily reacts with Et_3SiH to afford $Sb(C_6F_5)_3$, pentafluorobenzene, and the Et_3Si^+ cation. The latter functions as the active hydrodefluorination catalyst.

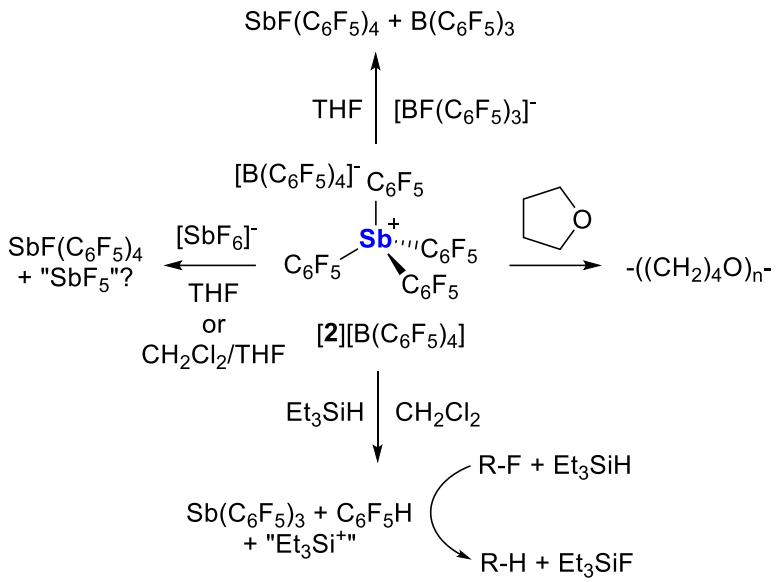

Figure 19. Reactivity of [**2**][B(C_6F_5)$_4$].

1.2.4 Bidentate Lewis acids in organic catalysis

Bidentate Lewis acids, as mentioned in section 1.1.3, display increased reactivity in small molecule recognition compared to the monodentate derivatives because of chelation effects. Heteroatomic bidentate systems such as the borane-phosphonium **39**$^+$ can be viewed as bifunctional systems as well. These bidentate Lewis acid can effect the double activation of small molecules. For example, a naphthalene based diborane, 1,8-naphthalenediylbis(dimethylborane) (**50**), was reported in 1985 to be an effective hydride sponge (Figure 20).[111] Compound **50** abstracts hydride from a variety of borohydrides, and the resulting bridging complex has been characterized by single-crystal crystallography.[112] Maruoka *et al*. reported the dialuminium Lewis acid **51** based on the 1,8-biphenylene backbone (Figure 20). When **51** is quantitatively mixed with ketones such

as acetophenone, it facilitates ketone reduction with Bu_3SnH, affording a 91% conversion in 5 h. In contrast, the conversion using the monodentate aluminum compounds only reaches 9% under the same conditions.[113] These two instances suggested that bidentate Lewis acids may be useful tools for the activation of organic substrates. In catalysis, it is reported that the pentafluorophenyl derivative of the naphthalene-based diborane, **52**, effectively catalyzed the hydrogenation of imines. It is proposed to activate dihydrogen via formation of a bridged hydride (Figure 20).[114] Matile *et al*. reported in 2017 that a series of dithienothiophene-based bidentate chalcogen bond donors such as **53** catalyzes the transfer hydrogenation of quinolines in the presence of Hantzsch-ester. The double electrophilic activation of the pyridine substrate was proposed as relevant in the catalytic cycle (Figure 20). [115]

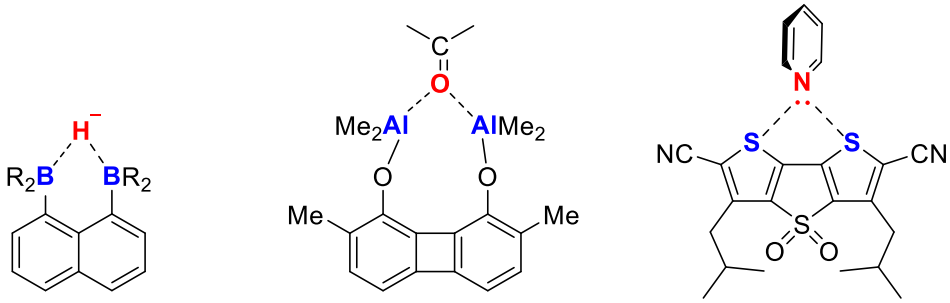

50: R = Me
52: R = C_6F_5

51

53

Figure 20. Selected activation modes of substrates by bifunctional Lewis acids.

As for Group 15 element containing bidentate Lewis acid as catalysts, Stephan *et al*. have prepared the bisphosphonium cation $\mathbf{54}^{2+}$ which is based on the naphthalene

backbone,[116] and **55** $^{2+}$ which is based on the ferrocene backbone,[117] both as tetrakis(pentafluorophenyl) borate salts. Both dications were tested as catalysts for the Friedel–Crafts dimerization of 1,1-diphenylethylene and the deoxygenation of ketones (Figure 21). The dicationic salt [**55**][$B(C_6F_5)_4]_2$ is more reactive than the corresponding monocation [$CpFe(\eta5\text{-}C_5H_4PFPh_2)$][$B(C_6F_5)_4$] (not shown), as evidenced by the fact that **55**$^{2+}$ was able to catalyze the Friedel–Crafts dimerization of 1,1-diphenylethylene at room temperature within 48 h. When catalyzed by the monocation, only a limited conversion of 10% was achieved after 96 hours at elevated temperature (50 °C). However, compared to the rigid naphthalene backbone in **54**$^{2+}$ that places the cationic centers in close proximity, the phosphoniums in **55**$^{2+}$ are separated from each other in the solid state due to the rotational flexibility of the ferrocene backbone. These structural differences explained why **54**$^{2+}$ is more reactive as a catalyst than **55**$^{2+}$. Thus, the reactions investigated took a shorter time to complete when [**54**][$B(C_6F_5)_4]_2$ is used as the catalyst.

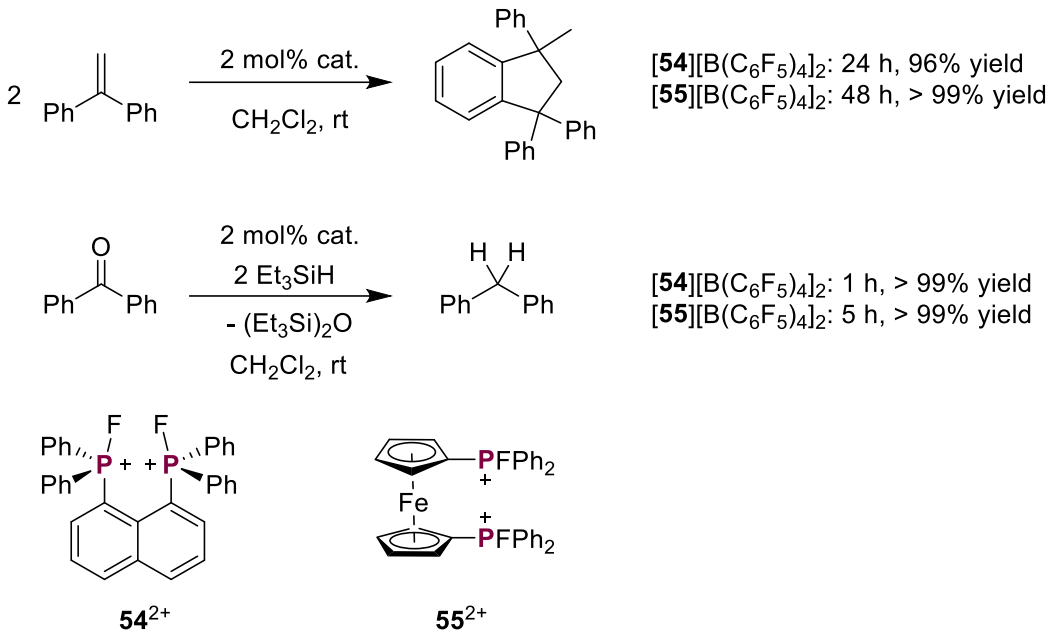

Figure 21. Bidentate phosphonium catalyzed Friedel–Crafts dimerization and deoxygenation of 1,1-diphenylethylene.

In 2016, our group reported a tetrafluoroborate salt of a bis-stibonium dication based on the *ortho*-phenylene backbone ([**83**][BF_4]$_2$). Compound [**83**][BF_4]$_2$ was reported to scavenge water during crystallization, and the cationic centers display interactions with both the BF_4^- anion and water molecules in the solid state, indicating the strong acidity possessed by this compound. In the catalytic hydrosilylation of benzaldehyde (Figure 22), a complete conversion in $CDCl_3$ was observed in 8 h using 1.5 mol% [**83**][BF_4]$_2$ as the catalyst, whereas 3 mol% of the monofunctional stibonium cation [Ph_3SbMe][BF_4] ([**56**][BF_4]) exhibited no reactivity. It is proposed that the higher activity of the distibonium arises from its ability to doubly activate the carbonyl group of the aldehyde. This view is supported by the adduct formed between **83**$^{2+}$ and dimethylformamide (DMF).

In this adduct, the carbonyl oxygen atom is chelated by two antimony(V) atoms. The adduct [**83**-μ_2-DMF]$^{2+}$ has a C-O stretching frequency of 1634 cm^{-1}, lower than that of 1675 cm^{-1} in free DMF, and this bond weakening event further supports the activation of the carbonyl group by the two cationic antimony centers.

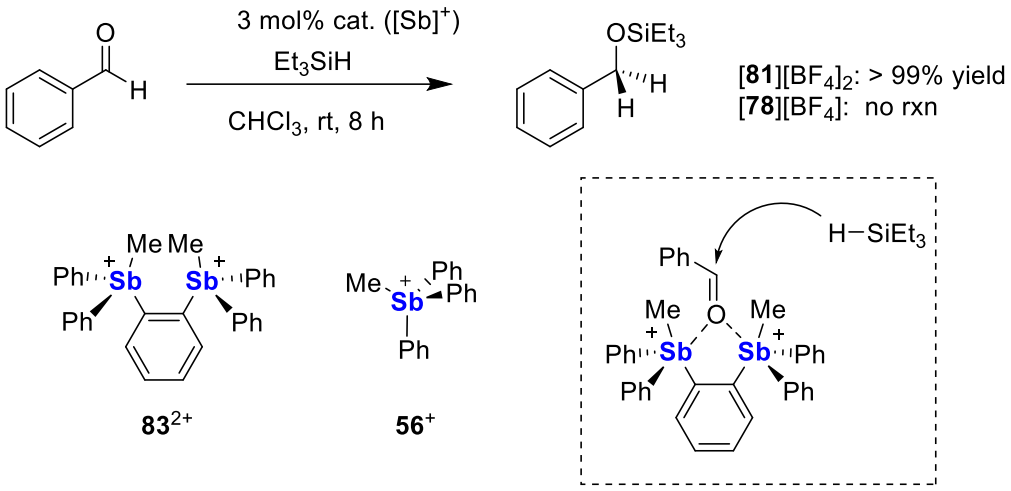

Figure 22. Hydrosilylation of benzaldehyde by organoantimony(V) cations and the double electrophilic activation of benzaldehyde by **83**$^{2+}$.

1.3 Electronic structures of fluorescent organoantimony(V) compounds

In section 1.1.4.3, we have discussed that stibonium cations with a chromophore substituent display a significant photophysical response upon binding with fluoride. For example, the anthryl-stibonium **72**$^+$ itself is non-emissive, but the emission is switched on by fluoride binding, making it an optical turn-on fluoride sensor. The fluorescence emission of **72**-F was assigned to the π-π* excited state of the anthracene moiety. The

reasons of why of **72**$^+$ has weak emissions despite having the same anthryl group remained unclear until Yokogawa and Irle *et al*. provided some insights in 2015.[118] Using DFT calculations, the structural optimization of **72**$^+$ in the ground state resulted in a tetrahedral geometry of the antimony center (Figure 23, **A**). However, in the first excited state of **72**$^+$, two local minima were found corresponding to either a tetrahedral (Figure 23, **B**) or a distorted seesaw (Figure 23, **C**) geometry. The frontier orbitals of geometry **B** resemble that of **A** where the HOMO and LUMO largely reside on the anthracene π and π* orbitals, respectively. On the other hand, in the seesaw geometry **C**, the energy of a Sb-C σ* orbital centered on the antimony atom drops below the π* orbital of the anthryl ligand (Figure 23, top). Based on the computed oscillator strengths, the authors assigned **B** (f = 0.16) as the diabatic "bright state" and **C** (f = 0.00) as the "dark state". With these local minima in hand, the potential energy surfaces (PES) of both the ground and excited states of **72**$^+$ were then constructed to study the accessibility of these geometries. It was found that the seesaw structure **C** is unfavorable in the ground state. In the excited state, however, geometry **C** is 8.8 kcal/mol more stable than **B**, and the relaxation from **A** to **C** occurs without barrier. Overall, the weak fluorescence of **72**$^+$ is attributed to its ability to access a diabatic dark state in the excited state via geometry relaxation. Interestingly, for analogs of **72**$^+$ with lighter pnictogens P and As, similar dark states with seesaw structures like **C** can be found in their excited states, but the energy barriers present on the PES prevent these dark states from being reached during the short lifetimes in the excited state.[118] Similarly, the crossing of antimony-based σ* and chromophore based π* orbitals in the excited state applies to the non-emissive property of the BODIPY-based stibonium fluoride sensor **33**$^+$.[119] Upon

formation of the Sb-F bond during the binding event, the low-lying σ* orbital of the stibonium was quenched by the electron lone pair of F^-, restoring the π-π* dominated excited state.

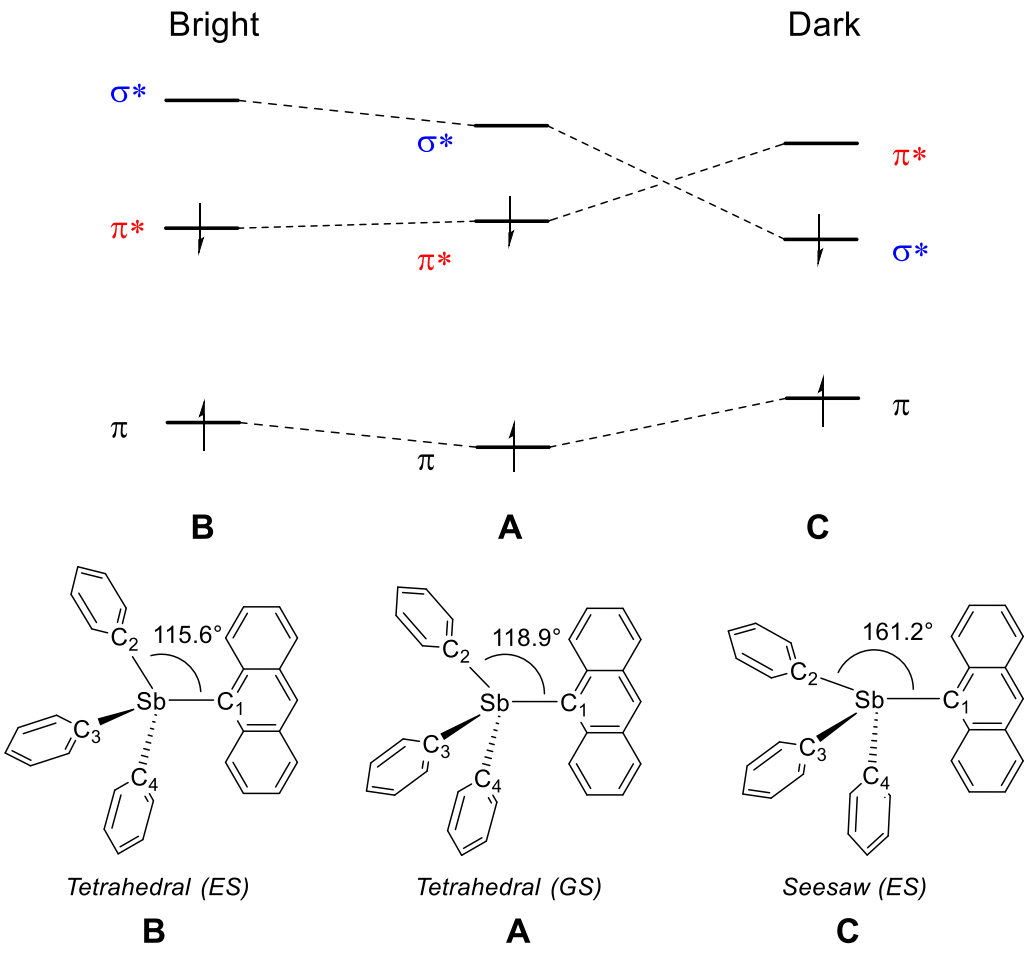

Figure 23. Top: The molecular orbital exchange after vertical excitation (**A**) toward the diabatic bright (**B**) and dark (**C**) states of **72**$^+$. Bottom: Optimized geometries in ground (GS) and the first excited (ES) states of **72**$^+$.

1.4 Objectives

It has been demonstrated by our group that organoantimony(V) compounds can be used as water-compatible, colorimetric and/or fluorescent fluoride sensors. In addition to sensing applications, such species have also been shown to act as catalysts for organic transformations such as hydrosilylation reactions or for the polymerization of epoxides. In this work, we will further exploit the potential of organoantimony compounds as Lewis acid catalysts. In particular, we will investigate the Lewis acidity of antimony-based compounds both in the +III and +V oxidation states. We plan to increase the Lewis acidity of the central atom by employing electron-withdrawing halogenated substituents or cationic charges, and enhance the stability of these electrophilic compounds by introducing coordinating anions, sterically bulky ligands, or ancillary donors. Once isolated, these compounds will be evaluated both computationally and experimentally for their ability to complex Lewis base donors, and will be tested as catalysts for transfer hydrogenation reactions, for Friedel-Craft type dimerization reactions as well as for the ring opening of cyclic ethers. We will also aim to exploit cooperative effects by targeting bifunctional Lewis acids. Lastly, efforts will be made to investigate the electronic structures of selected fluorescent organoantimony(V) compounds with the view to understand how coordination events at the antimony center affects the photophysical properties of these compounds, which will inspire the design of new chromophore-enhanced organoantimony compounds as fluoride sensors.

CHAPTER II

DIGGING THE SIGMA-HOLE OF ORGANOANTIMONY LEWIS ACIDS VIA OXIDATION*

2.1 Introduction

The chemistry of Group 15 Lewis acids is experiencing a surge of activity that has led to a series of stimulating developments in the area of phosphorus-mediated catalysis.[95, 120-130] Antimony, because of its intrinsically higher Lewis acidity,[63-64] is also drawing considerable attention both in the areas of small molecule activation and catalysis[13, 36, 107-109, 131-134] as well as in anion complexation.[4, 12, 29-30, 44-45, 57, 119, 135-136] Recent efforts in the chemistry of organoantimony(III)[137-138] have established that derivatives such as **3**[20] and **6**[139] **(**Figure 2**)** readily bind halide anions via donation into the σ* orbital (Figure 24).[139] Based on the same principle, we also found that antimony (III) halides could serve to promote activation of transition metals either via direct interaction with the metal as in the case of **4**-AuCl **(**Figure 2**)**[37] or via anion abstraction as in the case of **5**-AuCl **(**Figure 2**)**.[22]

It is interesting to note that the Lewis acidity at antimony can also be imparted through the use of perfluorinated ligands. While $SbPh_3$ (**57**) does not possess any notable Lewis acidity, Matile *et al.* have shown recently that $Sb(C_6F_5)_3$ (**58**) binds chloride anions and catalyzes anion pairing reactions involving organic chlorides (Figure 2).[9] This halide

* Reprinted with permission from: "Digging the sigma-hole of organoantimony Lewis acids by oxidation"; Yang, M.; Tofan, D.; Chen, C.-H.; Jack, K. M.; Gabbai, F. P., *Angew. Chem. Int. Ed.* **2018**, *57*, 13868-13872. Copyright 2018 by John Wiley & Sons, Inc.

binding event again illustrates the presence of low lying σ* orbitals which accept density from a donor orbital located on the incoming anion. This phenomenon can also be referred to as resulting from the presence of a so-called σ-hole,[8, 10-11, 140] a term that usually emphasizes the contribution of electrostatic forces to the interaction (Figure 24).[141] In this paper, we show that oxidation of antimony to the +V state can be used to carve the electrostatic potential profile about the antimony atom, leading to a deeper σ-hole. We also demonstrate that control over the depth of the σ-hole impacts the affinity of antimony for incoming electron-rich substrates and turns on catalysis.

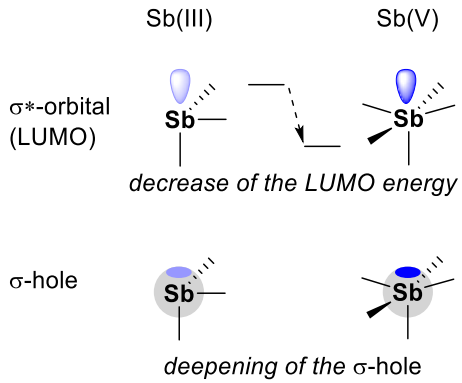

Figure 24. Orbital and electrostatic origin of the Lewis acidity in antimony derivatives.

2.2 Syntheses of compounds **57**-**62** and complexation reactions with Ph_3PO

To probe the effect of oxidation on antimony acceptors, we decided to compare the properties of $SbPh_3$ (**57**), $Sb(C_6F_5)_3$ (**58**), and $SbAr^F_3$ (**59**) with those of their tetrachlorocatecholate analogs $SbPh_3Cat$ (**60**), $Sb(C_6F_5)_3Cat$ (**61**), and $SbAr^F_3Cat$ (**62**) (Cat = *o*-$O_2C_6Cl_4$, Ar^F = 3,5-$(CF_3)_2C_6H_3$) (Figure 25). While most of these compounds have

been described previously,[4, 36, 142-144] **62** was prepared by reaction of **59** with *o*-chloranil and its structure was verified by X-ray crystallography (Figures 30-33, Table 3).

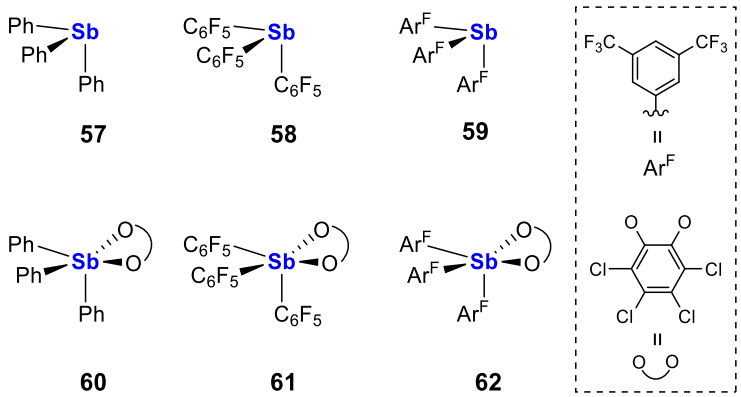

Figure 25. Antimony-based Lewis acids studied in this work.

With these compounds at our disposal, we decided to test their reactivity toward simple Lewis bases. For the purpose of this study, we chose to benchmark the Lewis acidity of these compounds against triphenylphosphine oxide, a base known to coordinate to antimony (V) compounds.[36] Using ^{1}H and ^{19}F NMR spectroscopy, we found that **57**, **58**, and **59** do not interact to any measurable extent with Ph_3PO in $CDCl_3$. By contrast, the ^{1}H, ^{31}P and ^{19}F NMR spectra of stiboranes **60**, **61** and **62** undergo drastic changes upon addition of Ph_3PO (Table 2). In the case of **60**, we observed that the 1:1 adduct $Ph_3PO \rightarrow SbPh_3Cat$ is in rapid equilibrium with **60** and Ph_3PO at NMR concentrations. Incremental addition of **60** to a solution of Ph_3PO induces a progressive downfield shift of the ^{31}P NMR resonance consistent with increasing concentrations of the 1:1 adduct. Treatment of this titration data affords a binding constant (K) of 120 ± 20 M^{-1}. (Figure 26)

Unlike **60**, the fluorinated stiboranes **61** and **62** form 1:1 adducts with the Ph_3PO ($Ph_3PO{\rightarrow}Sb(C_6F_5)_3Cat$ and $Ph_3PO{\rightarrow}SbAr^F{}_3Cat$, respectively) with no evidence of dissociation or exchange at NMR concentrations. Since the ^{31}P NMR chemical shift of Ph_3PO is equal to 29.6 ppm, that measured for the adducts (41.5 ppm for **61** and 40.0 ppm for **62**) suggests a substantial polarization of the P=O functionality upon coordination to antimony. UV-vis titration experiments carried out by adding incremental amounts of Ph_3PO to $CHCl_3$ solutions of **61** or **62** afford 1:1 binding isotherms that could be fitted with $K = 3\ (\pm\ 0.8) \times 10^4\ M^{-1}$ for **61** and $K = 3\ (\pm\ 1) \times 10^5\ M^{-1}$ for **62** (Figures 26, 36). These binding constants are one to two orders of magnitude higher than that measured for **60**. This enhancement in Lewis acidity can be attributed to the fluorination of the aryl rings and their resulting electron-withdrawing properties. The higher Lewis acidity measured for **62** corroborates fluoride ion affinity (FIA) trends computed by Krossing who found that $BAr^F{}_3$ (471 kJ/mol) has a higher fluoride anion affinity than $B(C_6F_5)_3$ (444 kJ/mol).[110] Given that the ^{31}P NMR shift of $Ph_3PO{\rightarrow}Sb(C_6F_5)_3Cat$ is more downfield than that of $Ph_3PO{\rightarrow}SbAr^F{}_3Cat$, these UV-vis titration results indicate that Lewis acidity measurements based on the simple measurement of the ^{31}P NMR chemical shift of a coordinated phosphine oxide can be inaccurate.[145] A more general conclusion of these experiments is that the Lewis acidity of stibines is readily enhanced by oxidization with *ortho*-chloranil.

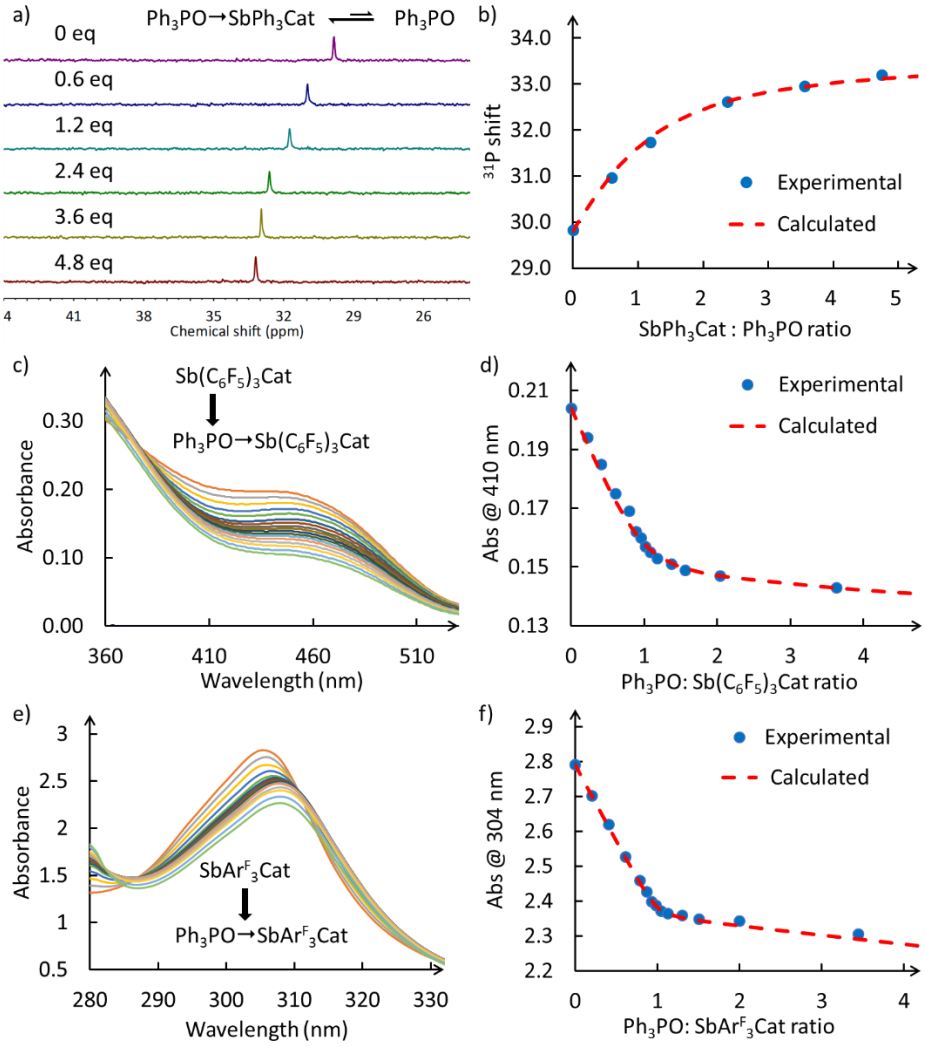

Figure 26. a) Spectral changes in the ^{31}P NMR spectra of Ph_3PO (1.47×10^{-2} M) in $CDCl_3$ observed upon incremental addition of $SbPh_3Cat$ (**60**). b) The experimental and the calculated 1:1 binding isotherm for **60** and Ph_3PO based on the ^{31}P NMR chemical shifts. The data were fitted with K = 120 ± 20 M^{-1}, δ(Ph_3PO) = 29.8 ppm, ε(Ph_3PO→$SbPh_3Cat$) = 33.6 ppm. c) Spectral changes observed in the UV-Vis absorption spectra of $Sb(C_6F_5)_3Cat$ (**61**) (5.34×10^{-4} M) upon addition of Ph_3PO (5.10×10^{-2} M) in $CHCl_3$. d) The experimental and the calculated 1:1 binding isotherm for **61** and Ph_3PO based on the UV-vis absorbance at 410 nm. The data were fitted with K = 3 (± 0.8) × 10^4 M^{-1}, ε(**61**) = 382 $M^{-1}cm^{-1}$, ε(Ph_3PO→$Sb(C_6F_5)_3Cat$) = 275 $M^{-1}cm^{-1}$. e) Spectral changes observed in the UV-Vis absorption spectra of $SbAr^F_3Cat$ (**62**) (5.88×10^{-4} M) upon addition of Ph_3PO (5.10×10^{-2} M) in $CHCl_3$. f) The experimental and the calculated 1:1 binding isotherm for **62** and Ph_3PO based on the UV-vis absorbance at 304 nm. The data were fitted with *K* = 3 (± 1) × 10^5 M^{-1}, ε(**62**) = 4.75×10^3 $M^{-1}cm^{-1}$, ε(Ph_3PO→$SbAr^F_3Cat$) = 4.05×10^3 $M^{-1}cm^{-1}$.

Although stibines **58** and **59** remain unchanged in the presence of Ph_3PO, formation of adducts appear to take place in hexanes, a solvent of lower polarity (Figure 34). Addition of stibine **58** and **59** to a solution of Ph_3PO in hexanes triggers a downfield shift of the ^{31}P NMR signal from 23.4 ppm to 28.5 ppm in the case of **58** and 28.4 ppm in the case of **59** (Figure 35). Crystals of $Ph_3PO{\rightarrow}Sb(C_6F_5)_3$ were obtained by cooling a pet ether (40-60) solution to −20°C, comfirming the molecular structure of the proposed adduct. The crystal structure of $Ph_3PO{\rightarrow}Sb(C_6F_5)_3$ confirms the presence of an interaction between the antimony center and the oxygen of the phosphine oxide in the solid state. The oxygen atom is positioned *trans* to the C1 carbon atom (∠O1-Sb-C1 = 164.8°) suggesting alignment of an oxygen lone pair with the σ-hole or σ* orbital of the Sb-C1 bond. The Sb1-O1 distance of 2.628(4) Å is well within the sum of the van der Walls radii of the two elements (ΣR_{vdW}(Sb,O) = 3.97 Å)[146], consistent with the presence of a secondary interaction. These structural results constitute the first crystallographic verification that $Sb(C_6F_5)_3$ is a pnictogen bond donor[11, 140] or an antimony(III) Lewis acid. These structural results are corroborated by a natural bond orbital (NBO) analysis[147] of the adduct. This analysis describes the Sb-O linkage as a lp(O)→σ*(Sb-C) donor-acceptor interaction of E_{del} = 15.6 kcal/mol (Figure 27). This adduct also appears to also be stabilized by an arene-perfluoroarene interaction involving the phenyl ring containing C31 and the pentafluorophenyl ring containing C13 and whose centroids are separated by 3.58 Å. The presence of this interaction indicates that **58** also possesses π-acidic properties.

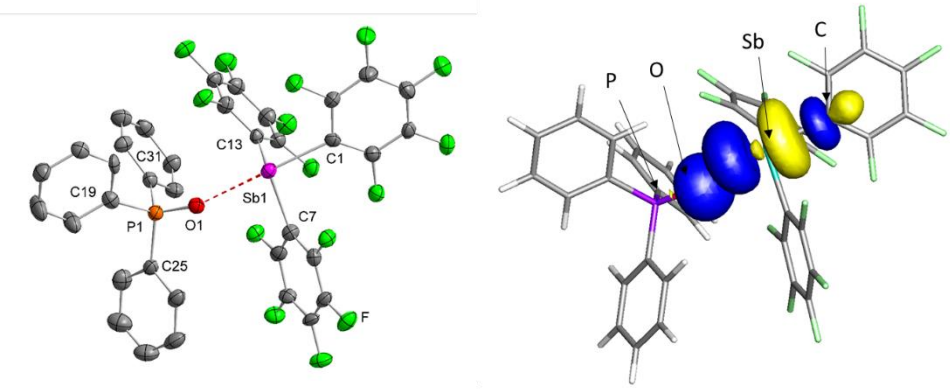

Figure 27. Left: The structure of $Ph_3PO{\rightarrow}Sb(C_6F_5)_3$ in the crystal. Thermal ellipsoids are drawn at the 50% probability level. Hydrogen atoms are omitted for clarity. Selected bond lengths (Å) and angles (deg): Sb1-O1 = 2.628(4), P1-O1-Sb1 = 161.2(2), O1-Sb1-C1 = 164.8(2). Right: Principal lp(O)→σ*(Sb-C) NBO donor-acceptor interactions found in the adduct. Isovalue = 0.05.

2.3 Computational studies on the Lewis acidity of compounds **57**-**62**

We propose that the higher Lewis acidity observed for the stiboranes results from a deepening of the σ-hole and a lowering of the antimony-centered σ* orbitals upon oxidation of the antimony atom (Figure 24). Such effects are illustrated in Figure 28 for **58** and **61**. Comparison of the electrostatic potential maps of these two compounds show a greater development of positive character at the antimony center of **61**. We also note that while both compounds feature directional σ* orbitals, that of **61** (-2.65 eV) is significantly lower in energy than that of **58** (-1.76 eV), in line with its higher Lewis acidity. As shown in Table 1, a lowering of the LUMO energy is also observed upon conversion of **57** into **60,** and **59** into **62**. Using fluoride ion affinity (FIA) as a computational probe of Lewis

acidity, our calculations reveal that oxidation of the stibines into their corresponding stiboranes raises their FIA by 110-150 kJ/mol (Tables 1, 4).

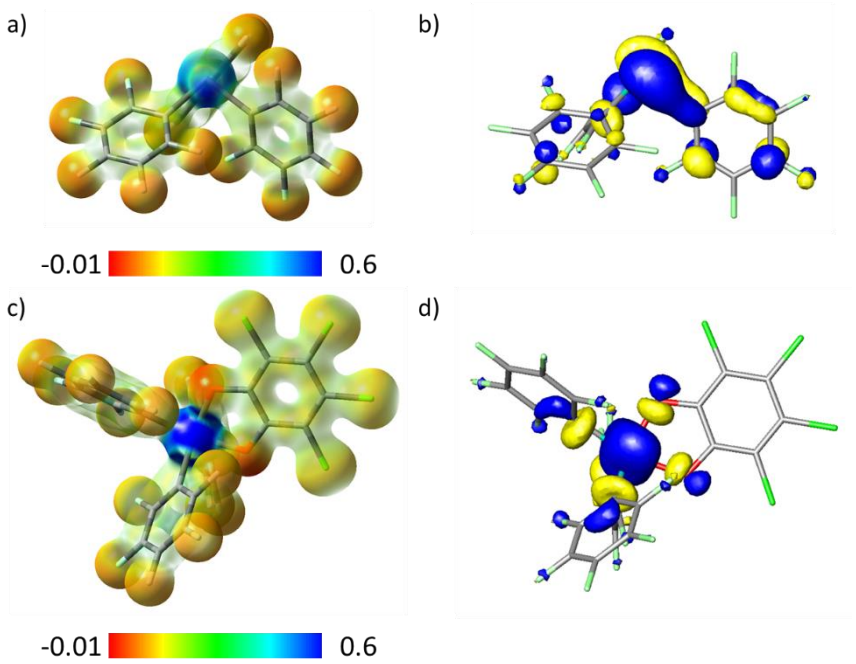

Figure 28. Electrostatic potential map (isovalue = 0.05) and LUMO contour plot (isovalue = 0.05) of **58** (a, b) and **61** (c, d).

Table 1. Calculated gas phase fluoride ion affinities and LUMO energies of the Lewis acids.

Compound	FIA (kJ/mol)	LUMO (eV)
57	248	-0.55
58	374	-1.76
59	365	-1.90
60	398*	-1.62
61	485*	-2.65
62	497*	-2.68

*Isomers are present of the fluoride adducts of **60**, **61**, **62**. The values reported here are based on the most thermally stable isomer. See experimental section 2.6.5 for further details.

2.4 Catalytic transfer hydrogenations and Ritter-like reactions

The next step of our study was to determine whether these derivatives can be used to catalyze organic transformations, and whether the Lewis acidity trend derived from the above titration experiments and calculations could also be reflected kinetically (Figure 29). We first tested these compounds as catalysts for the transfer hydrogenation reaction known to occur between Hantzsch ester and *N*-benzylideneaniline (Figures 37-38).[115, 148-149] This reaction was carried out in $CDCl_3$, with a 5 mol% catalyst loading. We found that the most Lewis acidic perfluorinated stiboranes **61** and **62** afforded an almost quantitative yield of the amine product after 10 min while **57** was essentially inactive. The non-fluorinated stiborane **60** proved to be significantly less active than **61** and **62**, leading to a 29% yield after 10 min. This yield is in fact comparable to that obtained with the perfluorinated stibines **58** and **59**. A comparable trend was found when these antinomy derivatives were used for the hydrogenation of quinoline using Hantzsch ester (Figures

39-40), with **61** and **62** displaying the highest performance (80% and 60%, respectively). We also probed the use of these compounds as catalysts for the formation of *N*-benzhydryl acetamide by reaction of diphenylbromomethane with acetonitrile and water (Figures 41-42).[150-151] Consistent with the trend established in the transfer hydrogenation reactions, the perfluorinated stiboranes showed the highest activity; however, the difference in reactivity observed with the fluorinated stibines, in particular **58**, was a lot less pronounced. Altogether, the catalytic activity of these antimony compounds correlates well with their experimentally-determined Lewis acidity as well as with the computed LUMO energy. A last important point of discussion concerns the unusually elevated activity of **58** in all three reactions, and especially in the Ritter-like reaction involving diphenylbromomethane. Given that the antimony-centered Lewis acidity in **58** is much lower than that in **61** and **62**, we believe that the commendable performance of this stibine results in part from the π-acidic properties of the C_6F_5 substituents, as seen in the structure of $Ph_3PO{\rightarrow}Sb(C_6F_5)_3$. We speculate that these π-acidic properties help acidify the electrophilic reagents involved in these reactions thus augmenting the catalytic properties of this simple fluorinated stibine.[152-153]

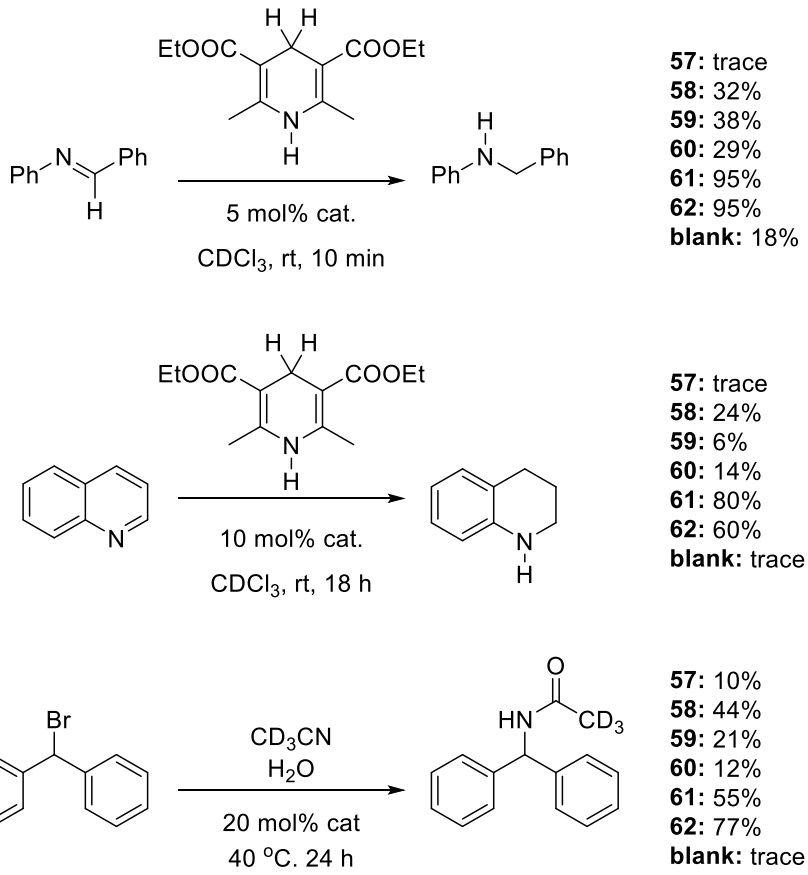

Figure 29. Transfer hydrogenation of *N*-benzylideneaniline and quinoline, and Ritter-like reactions showing yields when **57**-**62** are used as catalysts.

2.5 Conclusion

The results presented herein show that the Lewis acidity of pnictogen bond donor based on organoantimony is notably enhanced by oxidation to the +V state, a conclusion that parallels that drawn in the case of iodine(III) halogen bond donors.[154-155] Our analyses indicate that this Lewis acidity increase originates from a lowering of the antimony centered σ* orbital as well as a deepening of the σ-hole. These two effects, which

respectively capture the covalent and electrostatic nature of the interaction formed between the antimony Lewis acid and the incoming Lewis base, are manifested in the binding constants obtained when these organoantimony compounds complex with Ph_3PO. The same effects also readily enhance their catalytic properties in transfer hydrogenation and Ritter-like reactions when the antimony is in the +V state. Finally, the work described herein illustrates the duality that connects the orbital-based and σ-hole-based descriptors of Lewis acidity in a way that mirrors the continuum existing between covalent and ionic bonding extremes.

2.6 Experimental section

Antimony compounds are potentially toxic and should be handled accordingly. Isopropyl magnesium bromide (1 M in THF), 1,3-bis(trifluoromethyl)-5-bromobenzene and triphenyl phosphine were purchased from TCI America, antimony trichloride and *o*-chloranil from Acros Organics, hydrochloric acid from Macron Chemicals, magnesium powder, quinoline, and benzhydryl bromide from Alfa Aesar, bromopentafluorobenzene and diethyl 1,4-dihydro-2,6-dimethyl-3,5-pyridinedicarboxylate (Hantzsch Ester) from Matrix Scientific, magnesium sulfate from Oakwood Chemical, and triphenyl antimony from Milliporesigma. All chemicals were used without further purification. $Sb(C_6F_5)_3$ (**58**), [36, 142] $SbPh_3$(*o*-$O_2C_6Cl_4$) (**60**),[143] $Sb(C_6F_5)_3$(*o*-$O_2C_6Cl_4$) (**61**),[36] and *N*-benzylideneaniline[156] were synthesized according to reported procedures. Sb(3,5-$(CF_3)_2C_6H_3)_3$ (**59**)[144] was synthesized by a modification of a reported procedure. Solvents were dried by passing through an alumina column (pentane, CH_2Cl_2), heating to reflux

under N_2 over Na/K (Et_2O, hexanes, and THF), heating to reflux under N_2 over P_2O_5 ($CDCl_3$), or heating to reflux under N_2 over CaH_2 (CD_3CN). All other solvents were ACS reagent grade and used as received. NMR spectra were recorded on a Varian Unity Inova 400 FT NMR (399.52 MHz for ^1H, 375.92 MHz for ^{19}F, 161.74 MHz for ^{31}P, 100.46 MHz for ^{13}C) or a Varian Unity Inova 500 FT NMR (499.42 MHz for ^1H, 469.86 MHz for ^{19}F, 202.18MHz for ^{31}P, 125.60 MHz for ^{13}C) at ambient temperature. Chemical shifts (δ) are given in ppm and are referenced against solvent signals (^1H, ^{13}C) or external standards ($BF_3{\cdot}Et_2O$ for ^{19}F (-153 ppm), and 85% H_3PO_4 for ^{31}P (0 ppm). Elemental analyses were performed at Atlantic Microlab (Norcross, GA). Absorbance measurements were taken on a Shimadzu UV-2502PC UV-Vis spectrophotometer against a solvent reference. The synthesis of **59** was carried out using standard Schlenk techniques in the absence of oxygen and moisture.

2.6.1 Syntheses

2.6.1.1 Synthesis of $Sb(3,5\text{-}(CF_3)_2C_6H_3)_3(o\text{-}O_2C_6Cl_4)$ ($SbAr^F{}_3Cat$, **62**)

Solid *o*-chloranil (292 mg, 1.19 mmol) was added to a CH_2Cl_2 solution (2 mL) of **59** (903.2 mg, 1.19 mmol). The solution was stirred vigorously for 5 min. The resulting yellow precipitate was collected by filtration, washed with pentane, and dried under reduced pressure to afford $Sb(3,5\text{-}(CF_3)_2C_6H_3)_3(o\text{-}O_2C_6Cl_4)$ as a yellow powder (782 mg, 65% yield). X-ray quality crystals were grown by slow evaporation of a $CDCl_3$ solution of **62**. ^1H NMR ($CDCl_3$, 300 MHz) δ: 8.28 (s, 6H), 8.18 (s, 3H). ppm. ^{13}C NMR (126 MHz, $CDCl_3$) δ 142.69 (s), 136.71 (s), 135.19 (s), 133.94 (q, $J_{C\text{-}F}$ = 34.0 Hz), 127.22 (s),

123.06 (s), 122.60 (q, $J_{C\text{-}F}$ = 273.8 Hz), 117.91 (s). ^{19}F NMR ($CDCl_3$, 22 ℃, 282 MHz) δ: 63.17 (s, 6F). Anal. Calc. for $C_{30}H_9Cl_4F_{18}O_2Sb$: C, 35.78; H, 0.90. Found: C, 35.77; H, 0.97.

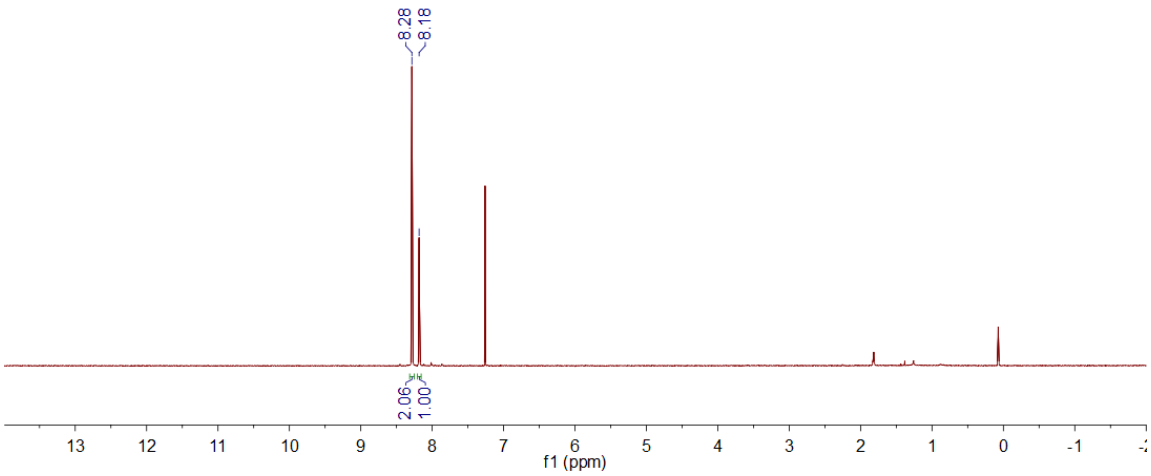

Figure 30. ^{1}H NMR of **62** in $CDCl_3$.

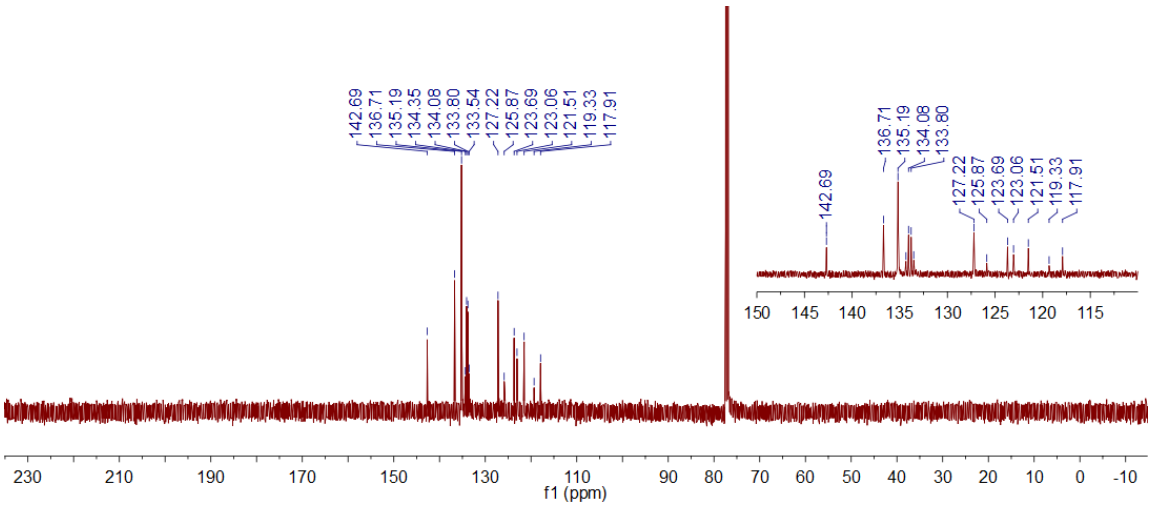

Figure 31. ^{13}C{^{1}H} NMR of **62** in $CDCl_3$.

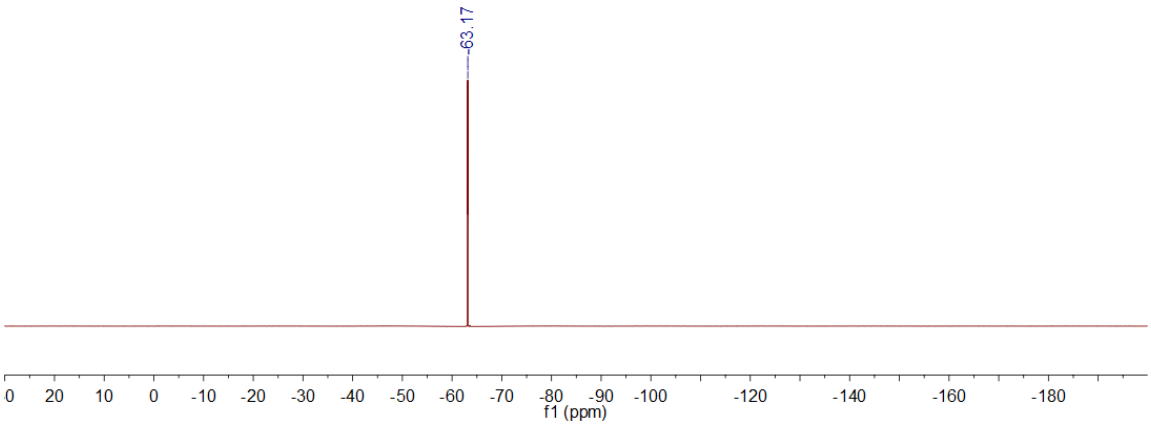

Figure 32. ^{19}F NMR of **62** in $CDCl_3$.

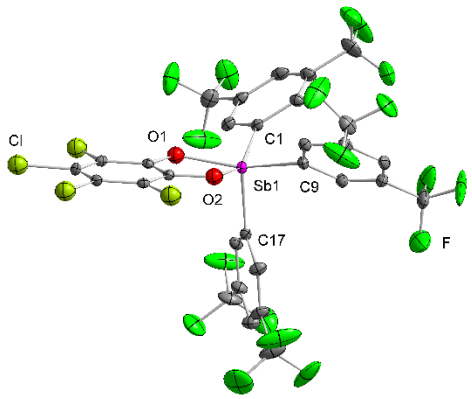

Figure 33. Crystal structure of **62**. Thermal ellipsoids are drawn at the 50% probability level. Hydrogen atoms and solvent molecules are omitted for clarity.

2.6.1.2 Isolation of the $Ph_3PO \rightarrow Sb(C_6F_5)_3$ adduct

Compound **58** (52.4 mg, 0.084 mmol) and triphenylphosphine oxide (24.1 mg, 0.086 mmol) were mixed in pet ether (40-60) solution (3 mL). Upon cooling to –25 °C for 24h, white crystals of $Ph_3PO \rightarrow Sb(C_6F_5)_3$ formed at the bottom of the vial (45.9 mg, 60%

yield). ^{31}P and ^{19}F NMR of this adduct in hexanes are identical to that obtained when mixing the two components in a 1:1 ratio. The identity of the adduct was verified by X-ray diffraction. Elemental analysis (%) calculated for $C_{36}H_{15}F_{15}OPSb$: C, 47.98; H, 1.68; found C, 48.37; H, 2.10.

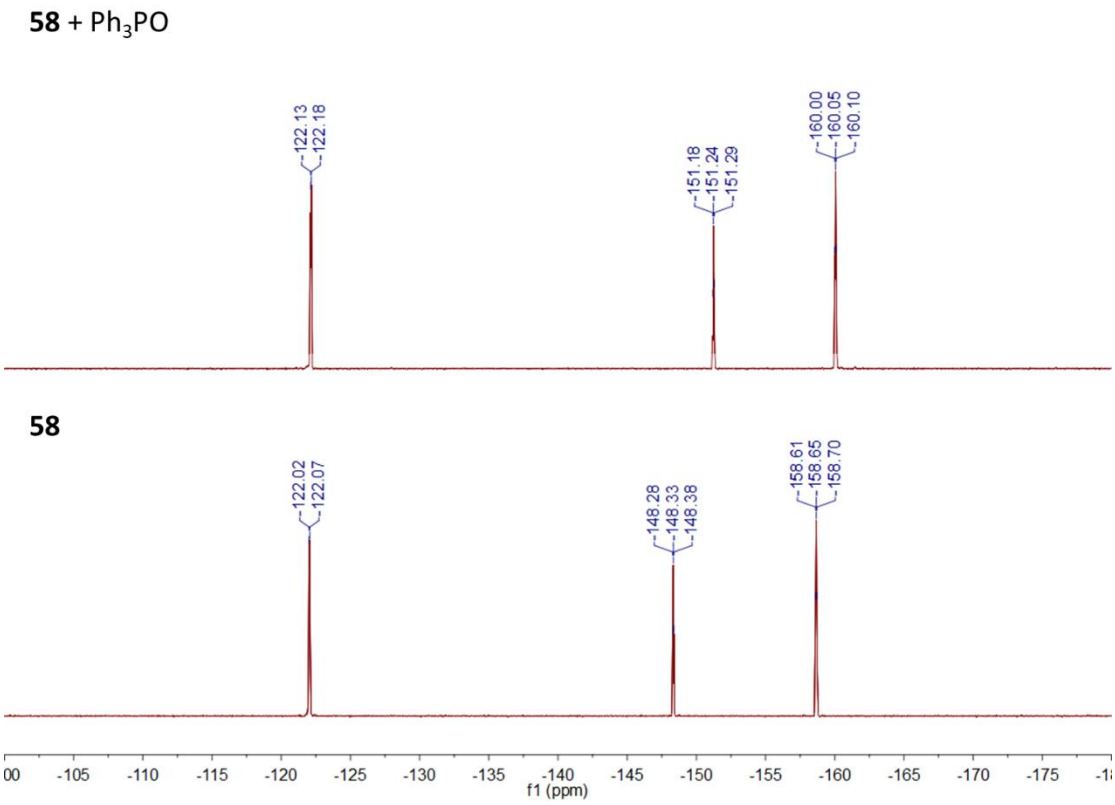

Figure 34. ^{19}F NMR spectra collected for **58** in hexanes in the absence (bottom) and in the presence of 1 equiv of Ph_3PO (top).

2.6.2 Complexation reactions

2.6.2.1 Ph_3PO complexation experiments in hexanes

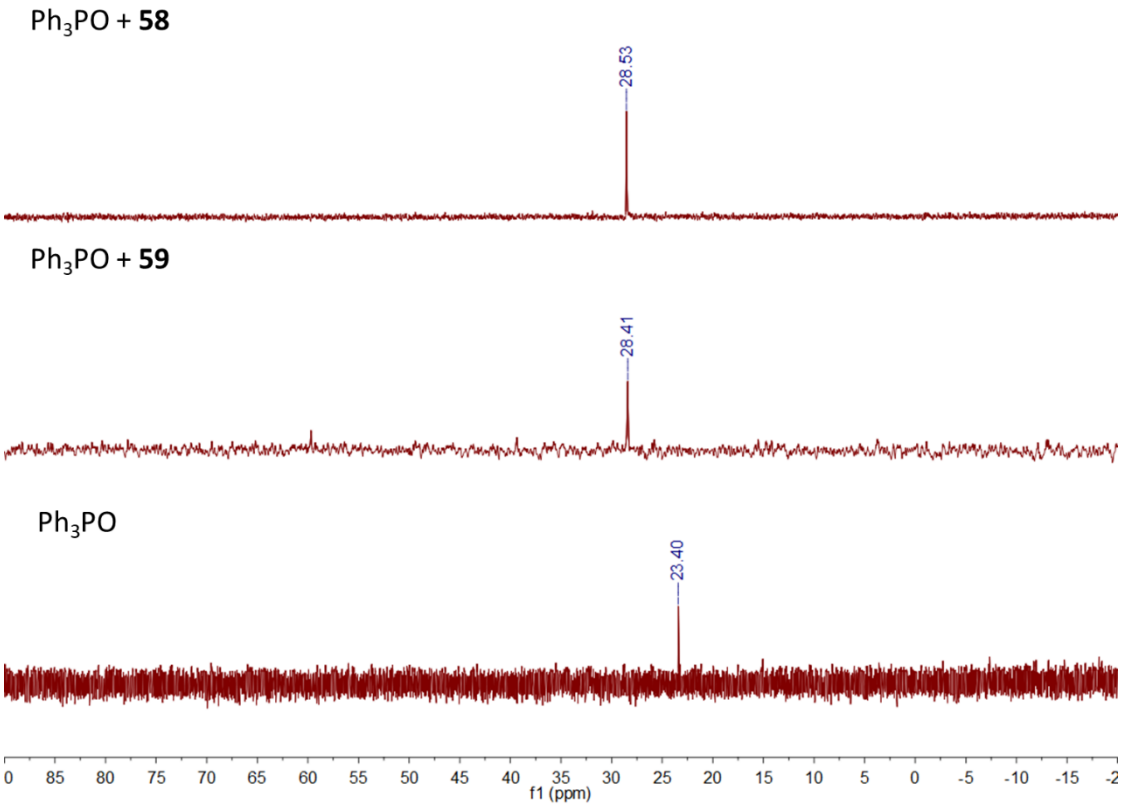

Figure 35. ^{31}P NMR spectra of Ph_3PO in hexanes in the absence of a Lewis acid (bottom), in the presence of 1 equiv. of **58** (top), and in the presence of 1 equiv. of **59** (middle).

2.6.2.2 Ph_3PO complexation experiments in $CHCl_3$

Table 2. ^{31}P NMR chemical shifts of the 1:1 mixture of Ph_3PO with organoantimony compounds in $CHCl_3$.

Compound	δ 31P (ppm)	Δδ 31P (ppm)*
57	29.7	0.1
58	29.7	0.1
59	29.7	0.1
60	33.0	3.4
61	41.5	11.9
62	40.0	10.4

* $\Delta\delta = \delta$ (adduct) - δ (Ph_3PO); δ (Ph_3PO) = 29.6 ppm

2.6.2.3 NMR study of the complexation of Ph_3PO by $SbPh_3(o\text{-}O_2C_6Cl_4)$ (**60**)

Stock solutions of stiborane **60** (52.3 mg/1200 L, 72.8 mM) and Ph_3PO (20.5 mg/1 mL, 73.7 mM) were prepared in $CDCl_3$. Six NMR tubes were charged with 100 L of the Ph_3PO stock solution. To these six tubes was respectively added 0, 50, 100, 200, 300 and 400 μL of the stock solution containing **60**. The volume of each tube was then adjusted to a total volume of 0.5 mL by addition of $CDCl_3$. The equilibrium constant *K* was obtained by fitting the ^{31}P NMR chemical shifts to a 1:1 binding isotherm.

2.6.2.4 UV titrations of $Sb(C_6F_5)_3(o\text{-}O_2C_6Cl_4)$ (**61**) or $Sb(3,5\text{-}(CF_3)_2C_6H_3)_3(o\text{-}O_2C_6Cl_4)$ (**62**) with Ph_3PO

Stock solutions of stiborane **61** (5.00×10^{-4} M) and Ph_3PO (5.00×10^{-2} M) were prepared in $CHCl_3$. A screw-cap cuvette was filled with 3.0 mL of the solution containing

61. Aliquots of the Ph_3PO stock solution were then added. The reaction mixture was stirred for ~ 3 s after each addition; the UV-vis spectrum was then recorded. Ph_3PO, was confirmed to not have any UV-vis absorbance in the spectrum window of 285 – 600 nm. The stability constant *K* of the $Ph_3PO\rightarrow Sb(C_6F_5)_3Cat$ adduct was obtained by fitting the absorbance at 410 nm to a 1:1 binding isotherm. The same protocol was used to determine the stability constant *K* of the $Ph_3PO\rightarrow SbAr^F{}_3Cat$. In this case the absorbance was monitored at 304 nm.

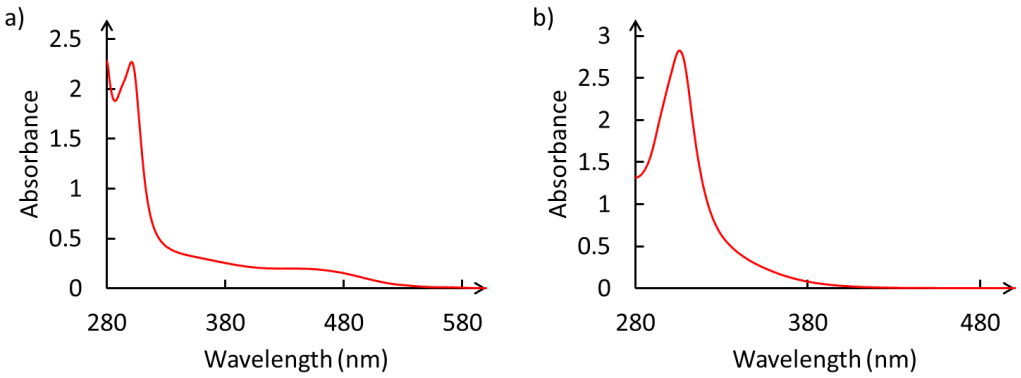

Figure 36. UV-vis spectrum of **61** (a) and **62** (b) in $CHCl_3$ at 5.00×10^{-4} M concentration.

2.6.3 Catalytic reactions

Each experiment was repeated 2-3 times. The yields provided in Figure 29 are averages.

2.6.3.1 The transfer hydrogenation reaction involving N-benzylideneaniline and Hantzsch ester

An NMR tube was charged with a dry $CDCl_3$ solution (0.6 mL) of the antimony catalyst (0.0045 mmol), Hantzsch-ester (30 mg, 0.12 mmol), and *N*-benzylideneaniline (17.2 mg, 0.09 mmol). The tube was then sealed and the formation of the products was monitored by ^{1}H NMR *in situ*. The yield of the product was calculated based on the integration of the resonance at 7.9 ppm (m, 2H). The amount of the unreacted substrate was calculated based on the integration of the resonance at 6.6 ppm (d, 2H).

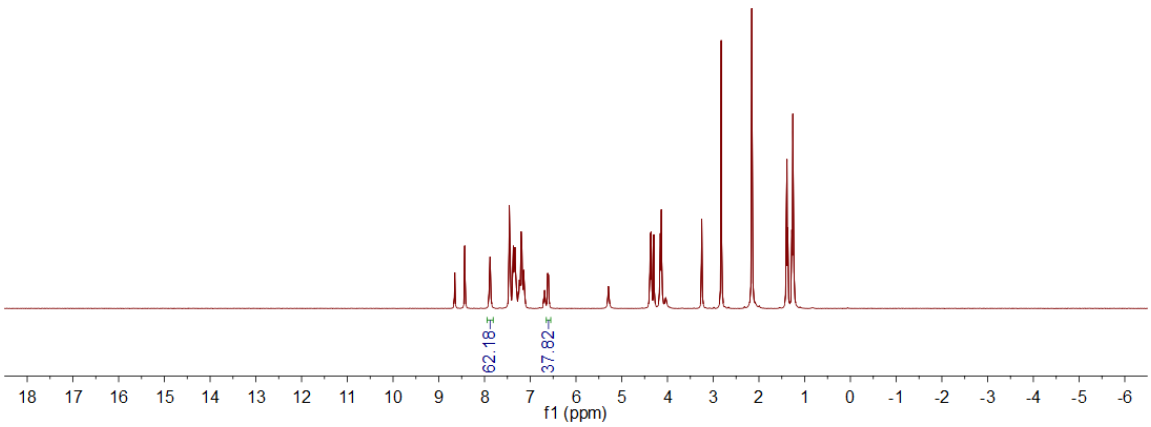

Figure 37. Representative ^{1}H NMR spectrum collected during the transfer hydrogenation reaction involving *N*-benzylideneaniline and Hantzsch ester with **58** as a catalyst.

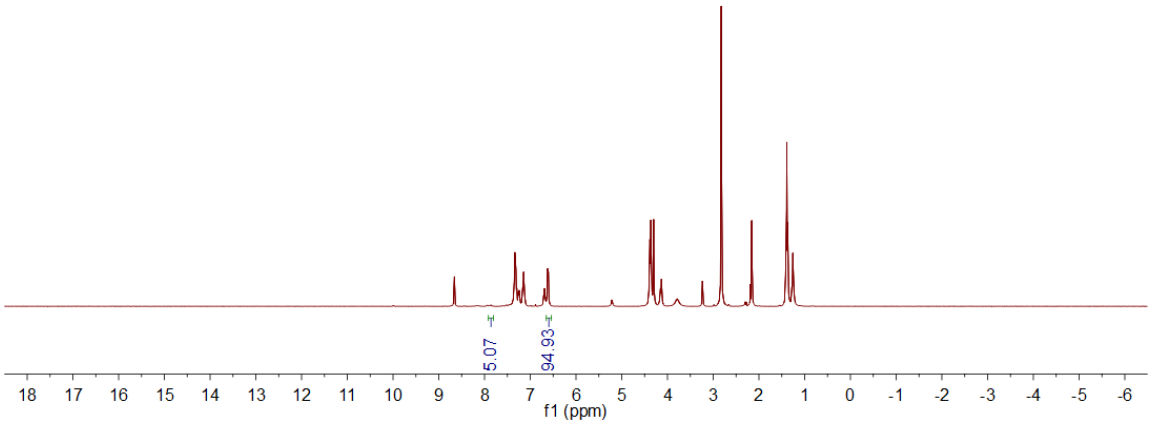

Figure 38. Representative ^{1}H NMR spectrum collected during the transfer hydrogenation reaction involving *N*-benzylideneaniline and Hantzsch ester with **62** as a catalyst.

2.6.3.2 The transfer hydrogenation reaction involving quinoline and Hantzsch ester.

An NMR tube was charged with a dry $CDCl_3$ solution (0.7 mL) of the antimony catalyst (0.008 mmol), Hantzsch-ester (50 mg, 0.20 mmol), and quinoline (9 μL, 0.08 mmol). The tube was then sealed and the formation of the products was monitored by ^{1}H NMR *in situ*. The yield of the product was calculated based on the integration of two resonances: 6.4 ppm (d, 1H) and 6.5 ppm (t, 1H). The amount of the unreacted substrate was calculated based on the integration of two resonances: 8.1 ppm (d, 1H) and 8.2 ppm (d, 1H).

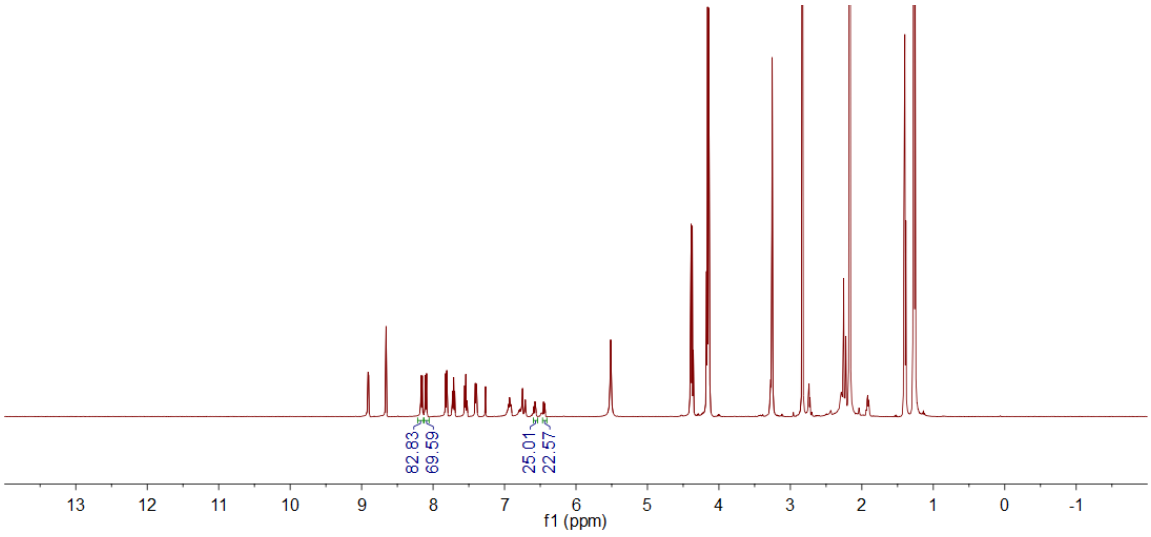

Figure 39. Representative ^{1}H NMR spectrum collected during the transfer hydrogenation reaction involving quinoline and Hantzsch ester with **58** as a catalyst.

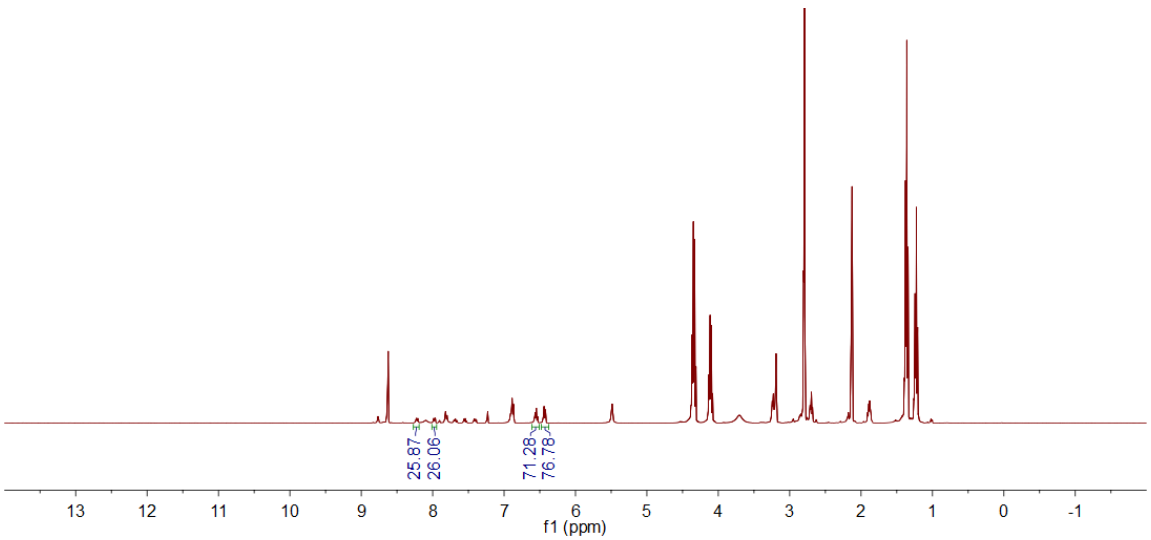

Figure 40. Representative ^{1}H NMR spectrum collected during the transfer hydrogenation reaction involving quinoline and Hantzsch ester with **62** as a catalyst.

2.6.3.3 The Ritter-like reaction involving benzhydryl bromide, CH_3CN and H_2O.

Preparation of the stock solutions. The stock solution of benzhydryl bromide (33.6 mM) in CD_3CN was prepared by dissolving benzhydryl bromide (83 mg) in dry CD_3CN (10 mL) under N_2 at room temperature. The stock solution of H_2O (128 mM) in CD_3CN was prepared by adding H_2O (23 μL) into dry CD_3CN (10 mL) under N_2 at room temperature.

General procedure for the Ritter-like reaction. The catalyst (2 μmol, 0.2 equiv)) was mixed with the stock solution of benzhydryl bromide (33.6 mM, 0.3 ml, 1 equiv) and the wet CD_3CN solution (0.3 ml, 3.8 equiv of H_2O) under N_2. The reaction mixture was then placed in and oil bath at 40 °C for 24 h. The reaction was analyzed by ^1H NMR spectroscopy. The yield of the reaction was determined from the ratio of the product peak (doublet at 6.16 ppm, ^3J = 8.3 Hz) to the peak of benzhydryl bromide (6.44 ppm). In the cases of using **57** and **60** as catalyst, formation of diphenylmethanol was observed as a side product in 27 % yield in the case of **57** and 42 % yield in the case of **60**.

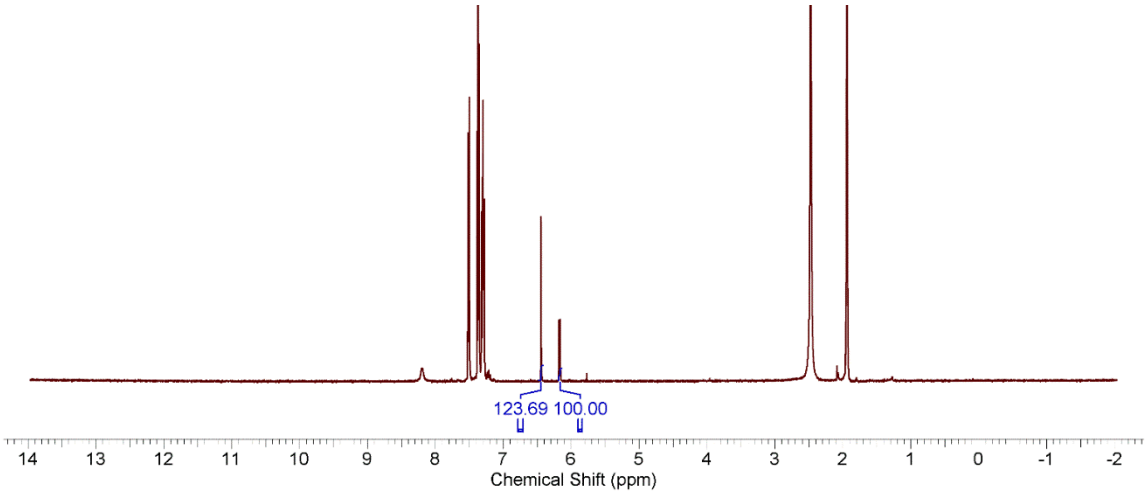

Figure 41. Representative ^{1}H NMR spectrum collected during the Ritter-like reaction involving benzhydryl bromide, CH_3CN and H_2O with **58** as a catalyst.

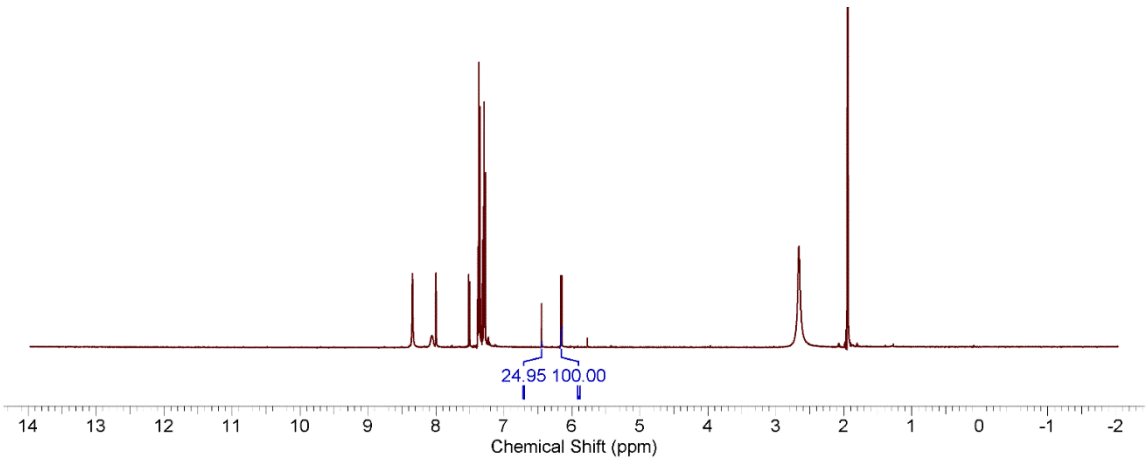

Figure 42. Representative ^{1}H NMR spectrum collected during the Ritter-like reaction involving benzhydryl bromide, CH_3CN and H_2O with **62** as a catalyst.

2.6.4 Crystallographic measurements

All crystallographic measurements were performed at 110(2) K using a Bruker SMART APEX II diffractometer or a Brucker D8 QUEST diffractometer (graphite monochromated Mo-Kα radiation, λ = 0.71073 Å). In each case, a specimen of suitable size and quality was selected and mounted onto a nylon loop. The semiempirical method SADABS was applied for absorption correction. The structures were solved by direct methods and refined by the full-matrix least-squares technique against F^2 with the anisotropic temperature parameters for all non-hydrogen atoms. All H-atoms were geometrically placed and refined in riding model approximation. Data reduction and further calculations were performed using the Bruker *SAINTplus* and *SHELXTL-NT* program packages.[157]

Table 3. Crystallographic and structure refinement details for $Sb(3,5\text{-}(CF_3)_2C_6H_3)_3$(*o*-$O_2C_6Cl_4$) (**62**) and $Ph_3PO{\rightarrow}Sb(C_6F_5)_3$.

Compound	**62**	**$Ph_3PO{\rightarrow}Sb(C_6F_5)_3$**
Empirical formula	C_{30} H_9 Cl_4 F_{18} O_2 Sb	C_{36} H_{15} F_{15} O P Sb
Formula weight	1006.92	901.20
Temperature	110 K	110 K
Wavelength	0.71073 Å	0.71073 Å
Crystal system	Monoclinic	Monoclinic
Space group	*P* 1 2_1/*n* 1	*P* 1 2_1/*n* 1
Unit cell dimensions	a = 10.6981(8) Å b = 24.0246(19) Å c = 13.3855(11) Å α = 90°. β = 91.547(2)°. γ = 90°.	a = 14.0986(19) Å b = 12.2263(18) Å c = 18.891(3) Å α = 90° β = 93.336(11)° γ = 90°
Volume	3439.1(5) $Å^3$	3250.8(8) $Å^3$
Z	4	4
Density (calculated)	1.945 Mg/m^3	1.841 Mg/m^3
Absorption coefficient	1.242 mm^{-1}	1.016 mm^{-1}
F(000)	1944	1760
Crystal size	0.33 x 0.32 x 0.28 mm^3	0.16 x 0.06 x 0.05 mm^3
Theta range for data collection	2.084 to 30.646°.	1.754 to 27.788°.
Index ranges	-15<=h<=15, -34<=k<=34, -19<=l<=19	-18<=h<=18, -15<=k<=15, -23<=l<=24
Reflections collected	132547	37850
Independent reflections	10618 [R(int) = 0.0547]	7563 [R(int) = 0.1732]
Completeness to theta = 25.242°	100.0 %	100.0 %
Absorption correction	Semi-empirical from equivalents	Semi-empirical from equivalents
Max. and min. transmission	0.7461 and 0.6669	0.7455 and 0.5532
Refinement method	Full-matrix least-squares on F^2	Full-matrix least-squares on F^2
Data / restraints / parameters	10618 / 53 / 513	7563 / 0 / 488
Goodness-of-fit on F^2	1.081	0.939
Final R indices [I>2sigma(I)]	$R1^a$ = 0.0360, $wR2^b$ = 0.0776	$R1^a$ = 0.0634, $wR2^b$ = 0.1337
R indices (all data)	R1 = 0.0439, wR2 = 0.0812	R1 = 0.1247, wR2 = 0.1633
Extinction coefficient	n/a	0.0067(5)
Largest diff. peak and hole	1.117 and -0.839 e.$Å^{-3}$	1.019 and -1.437 e.$Å^{-3}$

^{a}*R1* = $\Sigma||F_o| - |F_c||/\Sigma|F_o|$. ^{b}*wR2* $([w(F_o^2 - F_c^2)^2]/[\Sigma w(F_o^2)^2])^{1/2}$; $w = 1/[\sigma^2(F_o^2) + (ap)^2 + bp]$; $p = (F_o^2 + 2F_c^2)/3$ with a = 0.0244 and b = 9.1321 for **62**, and a = 0.0702 and b = 0.00 for $Ph_3PO{\rightarrow}Sb(C_6F_5)_3$.

2.6.5 Computational details

All computations were carried out using density functional theory (DFT) methods as implemented in the Gaussian 09 program.[158] All optimization and frequency calculations were carried out with the B3LYP[159-160] functional and mixed basis sets (cc-pVTZ-PP[161] with CRENBL ECP[162] for Sb, 6-31g(d') for H, C, O, F, Cl, P) starting from the crystal structure geometries if available. No imaginary frequencies were found for the optimized structures, confirming that a local minimum on the potential energy hypersurface had in all cases been reached. The optimized structures were also subjected to natural bond orbital (NBO)[147] analysis. The molecular orbitals and NBOs were visualized and plotted using the Jimp2 program.[163] The fluoride ion affinity of each antimony compound was derived from single point calculations in which the following basis sets were employed: aug-cc-pVTZ-PP[161] with CRENBL ECP[162] for Sb, 6-311+g(2d,p) for H, C, O, F, Cl, P. As shown in Table 4, all energies were corrected to enthalpy using the thermal correction term obtained in the aforementioned frequency calculations. The enthalpy for the fluoride anion was found to be –99.8579277 Hartree.

The structure of [**60**-F]$^-$ was optimized starting from the crystal structure known for this derivative. In the cases of [**61**-F]$^-$ and [**62**-F]$^-$, we considered two isomers that differ by the nature of the atom trans from the fluoride anion. Only the most stable structure was used to calculate the FIA.

Table 4. Computed FIA of compounds **57**-**62**.

Compound	Single point energy (Hartree)	Thermal correction to Enthalpy (Hartree)	Corrected energy (Hartree)	FIA (KJ/mol)
57	-935.4605714	0.288737	-935.1718344	247.66
[**57**-F]$^-$	-1035.414746	0.290655	-1035.1240911	
58	-2424.431979	0.180122	-2424.2518570	373.90
[**58**-F]$^-$	-2524.434162	0.181968	-2524.2521940	
59	-2957.48487	0.339179	-2957.1456914	364.94
[**59**-F]$^-$	-3057.484197	0.341581	-3057.1426158	
60	-3155.537029	0.35053	-3155.1864989	397.84
[**60**-F]$^-$	-3255.548698	0.352742	-3255.1959556	
61	-4644.482987	0.241403	-4644.2415835	471.27 (isomer 1) 485.44 (isomer 2)
[**61**-F]$^-$ (isomer 1)	-4744.522995	0.243987	-4744.2790081	
[**61**-F]$^-$ (isomer 2)	-4744.528251	0.243844	-4744.2844065	
62	-5178.461116	0.400427	-5178.0606891	497.12 (isomer 1) 497.03 (isomer 2)
[**62**-F]$^-$ (isomer 1)	-5278.511354	0.403394	-5278.1079598	
[**62**-F]$^-$ (isomer 2)	-5278.511116	0.403191	-5278.1079250	

CHAPTER III

ON THE SYNTHESIS AND PROPERTIES OF TRIARYLHALOSITBONIUM CATIONS*

3.1 Introduction

Electron deficient Group 15 compounds are attracting a growing interest in the field of Lewis acid catalysis. While it has been shown that simple phosphonium cations can promote a range of reactions including aldol additions,[164] the cyanosilylation of aldehydes[91] and hydroformylation reactions,[165] this field of research has attracted a renewed interest prompted by the introduction of highly electron deficient fluorophosphonium cations such as $[(C_6F_5)_3PF]^+$ (**43**$^+$, Figure 43)[7] and $[(SIMes)PFPh_2]^{2+}$ (**44**$^{2+}$, SIMes = 1,3-dimesitylimidazolidin-2-ylidene).[92] These electrophilic phosphorus cations[166] are highly reactive and catalyze hydrodefluorination,[7] hydrosilylation,[94] hydrodeoxygenation,[98] Friedel-Crafts-type dimerization,[92] and dehydrocoupling reactions.[95]

In parallel to these developments, several groups including ours have become interested in the Lewis acidic properties of antimony(V) compounds[55, 63-64, 167-168] and their use in the field of anion sensing[12, 14, 30, 45, 57, 169] as well as catalysis. With respect to the latter, it has long been known that simple stibonium cations such as $[Ph_4Sb]^+$ can catalyze the addition of isocyanates to oxiranes.[104-105] It has more recently been shown that stibonium cations can also be used to promote the hydrosilylation or allylstannation of

* Reprinted with permission from: "Synthesis and properties of triarylhalostibonium cations"; Yang, M.; Gabbaï, F. P., *Inorg. Chem.* **2017,** *56* (15), 8644-8650. Copyright 2017 American Chemical Society.

aldehydes[107, 131] among other reactions.[108] Based on the prediction that a higher Lewis acidity could be obtained through the use of electron withdrawing substituents, we synthesized the stibonium salt $[Sb(C_6F_5)_4]^+$ (**2**$^+$, Figure 43) and found that it is sufficiently acidic to polymerize THF or abstract a fluoride anion from $[SbF_6]^-$.[13] In a continuation of these studies and inspired by the work of Stephan on fluorophosphonium cations,[7, 92] we have now decided to investigate the synthesis and properties of stibonium cations whose Lewis acidity is enhanced by a halogen substituent (Figure 43).

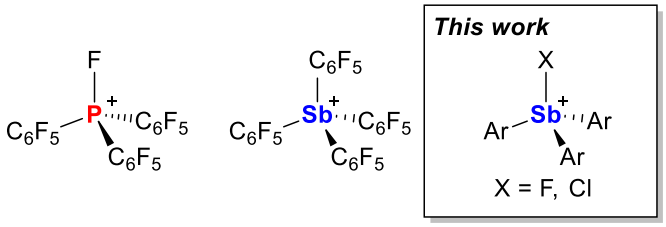

Figure 43. Existing group-15 element containing cations and the target of this work.

3.2 Syntheses and characterizations of the triarylfluorostibonium triflates

Realizing the stabilizing influence of the counter anion, we decided to first consider halostibonium salts with anions of intermediate coordinative ability. Based on the knowledge that stibonium triflates sometimes adopt molecular rather than ionic structures in the solid state, we investigated the reaction of Ar_3SbF_2 (Ar = Ph, Mes, Figure 51)[170-171] with a stoichiometric amount of trimethylsilyl triflate (TMSOTf). In situ ^{19}F NMR measurements confirmed the formation of the fluorostibonium triflates as indicated by the presence of a SbF resonance at -156 ppm for $Ph_3SbF(OTf)$ (**65**) and -145 ppm for

$Mes_3SbF(OTf)$ (**66**) in CH_2Cl_2. Efforts to isolate the pure salts from these mixtures were complicated by the oily nature of the residue which impeded purification. Faced with these difficulties, we considered an alternative approach based on ligand redistribution starting from the Ar_3SbF_2 and the corresponding $Ar_3Sb(OTf)_2$. This approach was inspired by the elegant work of Burford who recently described $Ph_3Sb(OTf)_2$ (**63**).[63-64] For the purpose of this study, we synthesized the mesityl analog, namely $Mes_3Sb(OTf)_2$ (**64**). This new compound, which could be conveniently obtained by the reaction of Mes_3SbBr_2 with AgOTf in CH_2Cl_2, has been spectroscopically characterized (Figures 52-53). Gratifyingly, we found that **63** and **64** react with their corresponding difluorides to afford $Ph_3SbF(OTf)$ (**65**) and $Mes_3SbF(OTf)$ (**66**), respectively (Figure 44). The ^{19}F NMR spectra of both **65** and **66** display two sets of resonances which correspond to the triflate-CF_3 and SbF moieties, respectively (Figures 56, 59). These two signals which appear at -78 ppm and -156 ppm for **65** and -78 ppm and -145 ppm for **66** show the expected 3:1 intensity ratio. It is interesting to note that the chemical shifts of the antimony-bound fluorine atoms are distinctly more upfield that those measured for Ph_3SbF_2 (-148 ppm) and Mes_3SbF_2 (-100 ppm). The origin of the larger change observed in the chemical shift of the antimony-bound fluorine atom upon conversion of Mes_3SbF_2 into **66** has not been elucidated. Compounds **65** and **66** have also been investigated by ^1H and ^{13}C NMR spectroscopy (Figures 54-55, 57-58). Clean spectra of compound **65** could not be obtained even when starting from thoroughly dried CD_2Cl_2 and recrystallized materials. We assign these difficulties to the reactive nature of this compound. By contrast, the ^1H and ^{13}C NMR of **66** show the expected resonances, with no sign of impurities or decomposition suggesting

that **66** is kinetically stabilized by the bulky mesityl ligands. Despite the asymmetry introduced by the presence of two different axial ligands in **66**, the *ortho*-methyl groups from the mesityl substituents are not differentiated, giving rise to a single ^{1}H NMR resonance at 2.50 ppm in CD_2Cl_2. The equivalence of these resonances is rationalized by invoking the rapid rotation of the mesityl substituents about the Sb-C_{ipso} bonds. In agreement with this view, we observed a single aromatic C*H* resonance at 7.10 ppm.

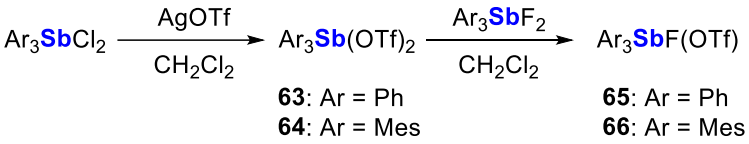

Figure 44. Synthesis of the ditriflate and fluorotriflate derivatives.

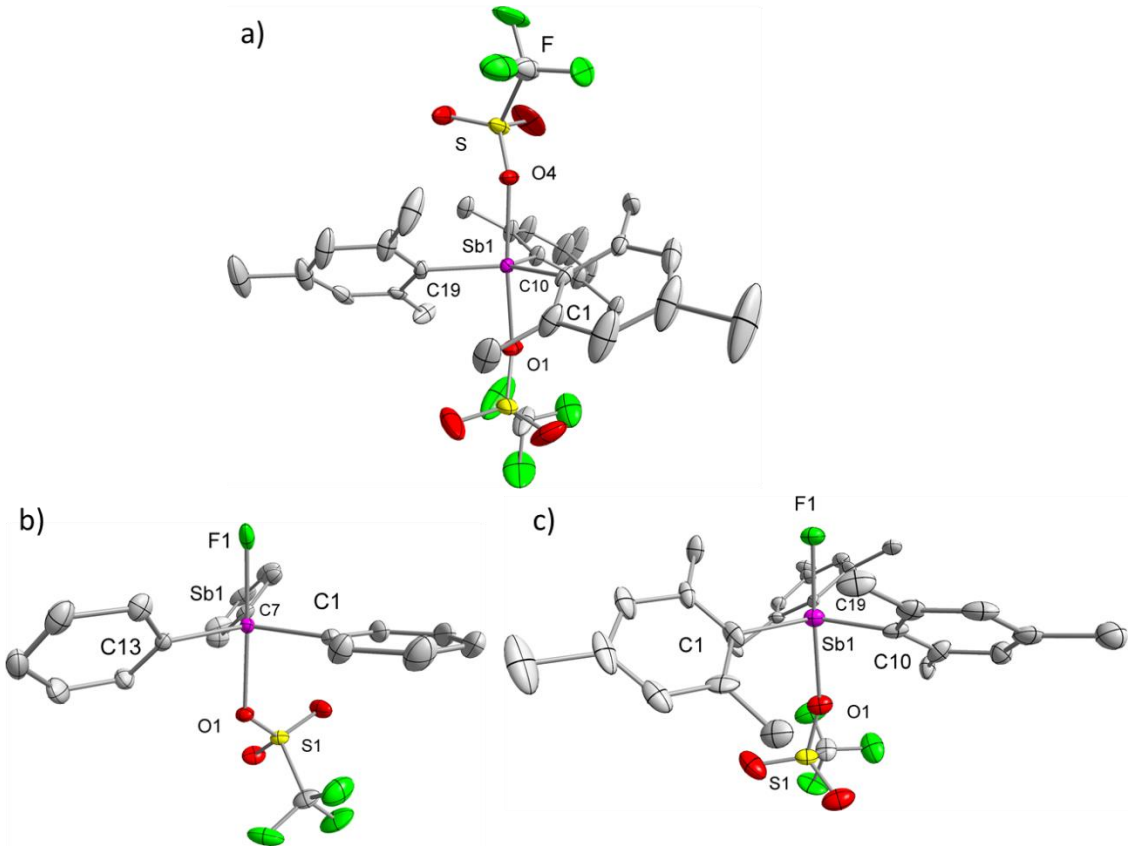

Figure 45. Structures of a) **64**, b) **65** and c) **66** in the crystal. Ellipsoids are drawn at the 50% probability level. Hydrogen atoms are omitted for clarity. The asymmetric unit of **66** contains two independent molecules, one of which resides about the C_3 axis. The molecule of **66** shown in the figure does not reside on a crystallographic special position.

Table 5. Selected structural parameters for compounds **64**-**66**.

Cpd.	Sb1-O1 (Å)	Sb1-F1/O4 (Å)	Avg. Sb-C (Å)	∠O1-Sb-F1/O4 (º)	Avg. ∠C-Sb-C (º)	Avg. ∠O1-Sb-C (º)	Avg. ∠F1/O4-Sb-C (º)
63[63]	2.1716(14)	2.1708(14)	2.084	173.21(5)	120.0	89.8	89.8
64	2.173(2)	2.178(2)	2.123	174.91(9)	120.0	89.3	90.7
65	2.2493(15)	2.0003(15)	2.085	177.75(6)	119.9	87.9	92.1
66*	2.325(9) [2.344(15)]	1.948(7) [1.958(12)]	2.096 [2.142]	176.5(3) [175.2(7)]	119.9 [120.0]	88.2 [88.9]	91.8 [91.8]

* The metrical parameters given in brackets correspond to the molecule that resides about the C_3 axis.

Colorless single crystals of compounds **64**-**66** could be obtained by layering a CH_2Cl_2 solution of the stibonium salt with hexanes at -20 °C. The structure of **64** resembles that reported for **63** (Figure 45, Tables 5, 8). The antimony center adopts a trigonal bipyramidal geometry with the triflate anions occupying the apical sites. It is interesting to note that the Sb-O distances in **64** (2.178(2) Å) are almost equal to those in **63** (2.1708(14) Å)[63] despite the larger steric demand of the mesityl substituents. The structures of **65** and **66** (Figure 45, Table 9) are again best described as trigonal pyramidal, with the fluoride and triflate anion spanning the apical sites. However, the Sb-O distances of 2.2493(15) Å in **65** and 2.325(9) Å in **66** are longer than those in **63** and **64**, thus indicating that the triflate anions are more loosely coordinated to the antimony atom. This lengthening is distinctly more acute in the case of **66**, a factor that we assign to the bulk of the mesityl substituents. The structures of **63**-**66** have been optimized using DFT methods as implemented in Gaussian 09.[158] These optimization were carried out using the M06 functional[172] and a mixed basis set: 6-31g(d) for C, H, O; 6-31g(d') for F; 6-311g*

for S, Cl; cc-pVTZ-PP[161] with Stuttgart relativistic small core ECP[162] for Sb, to produce structures that closely match those determined by X-ray diffraction. The optimized structures were also subjected to a Natural Bond Orbital (NBO) analysis to extract Natural Population Analysis (NPA) charges (Table 6). These charges, combined with the Wiberg Sb-F and Sb-O bond indices are in good agreement with the structural results and show that the antimony center of **65** and **66** have a greater cationic character while forming a weaker bond with the triflate anion.

Table 6. Calculated NBO partial charges (NPA) and Wiberg bond indices (WBI) of compounds **63**-**66** in the gas phase.

Compound	NPA on Sb	WBI Sb-O	WBI Sb-F
63	2.2926	0.2976	-
64	2.3226	0.2778	-
65	2.5806	0.2646	0.4601
66	2.3635	0.2297	0.4232

3.3 Syntheses and characterizations of the triarylchlorostibonium hexachloroantimonates

Following the observation that the triflate anions remain coordinated to the antimony center of **65** and **66**, we decided to investigate the use of a more weakly coordinating counteranion. A review of the literature shows that monohalostibonium cations such as $[Ph_3SbCl]^+$ have been previously isolated as hexachloroantimonate ($[SbCl_6]^-$) salts. Given the weakly coordinating nature of this anion, we decided to revisit

some aspects of this chemistry. While it has been shown previously that Ph_3SbCl_2 reacts with $SbCl_5$ in CCl_4 to afford $[Ph_3SbCl][SbCl_6]$ (**67**),[173] we found that this synthesis could be easily carried out in CH_2Cl_2 leading to a moderate yield (55%) of this salt. This approach also proved to be well adapted to the synthesis of $[Mes_3SbCl][SbCl_6]$ (**68**) which was obtained in 75% yield by reaction of Mes_3SbCl_2 with $SbCl_5$ in CH_2Cl_2 (Figures 46, 60-61). In the ^1H NMR spectrum, the methyl groups of **68** give rise to two resolved resonances at 2.45 ppm (6H) and 2.42 ppm (3H), respectively. Similar to compound **66**, we propose that the detection of only two methyl resonances originates from the rapid rotation of the mesityl substituents about the Sb-C_{ipso} bonds. In agreement with this view, we observe a single aromatic C*H* resonance at 7.22 ppm (2H). We also note that this resonance is more downfield than that measured for the ditriflate derivative **64** (7.11 ppm) and the fluorotriflate derivative **66** (7.09 ppm).

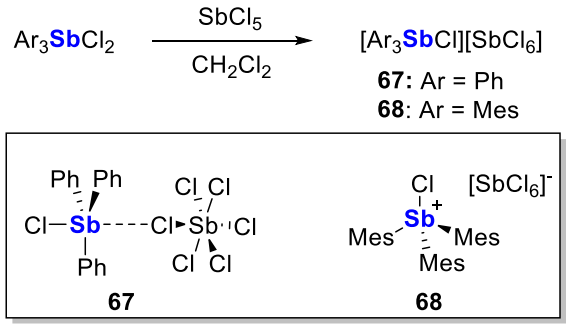

Figure 46. Synthesis of the triarylchlorostibonium hexachloroantimonates.

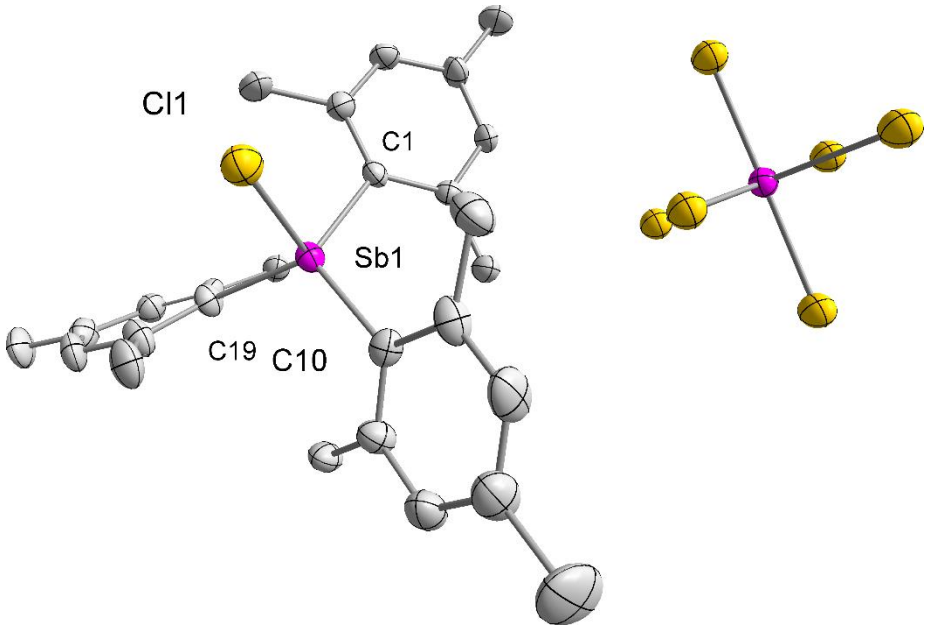

Figure 47. Structure of **68** in the crystal. Ellipsoids are drawn at the 50% probability level. Hydrogen atoms are omitted for clarity. Selected bond lengths (Å) and angles (º): Sb1-Cl1 = 2.322(2), Sb1-C1 = 2.112(9), Sb1-C10 = 2.092(10), Sb1-C19 = 2.105(9), average ∠C-Sb-C = 116.3, average ∠Cl-Sb-C = 101.2.

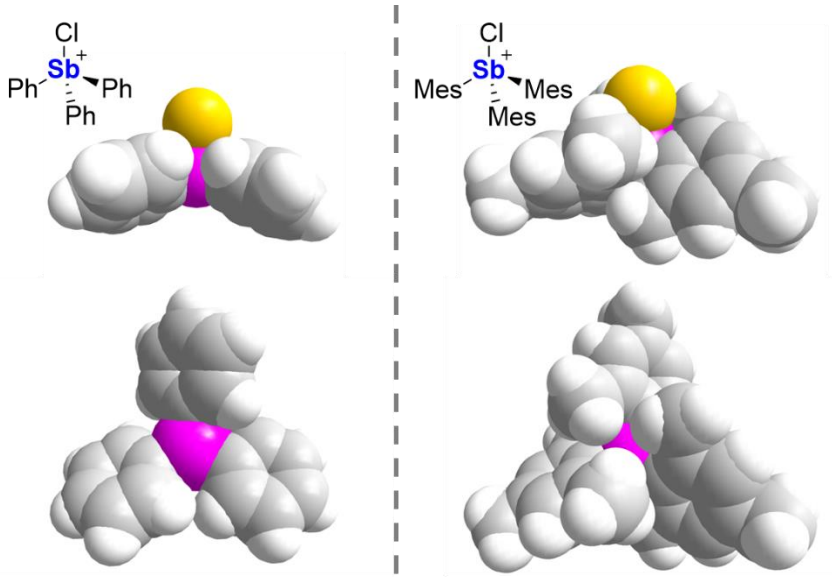

Figure 48. Space-filling model of cations $[Ph_3SbCl]^+$ (left) and $[Mes_3SbCl]^+$ (right).

In the crystal, we observe that **68** exists as a salt with no short contact between the $[SbCl_6]^-$ anion and the stibonium cation (Figure 47, Table 10). This is in contrast to the previously reported structure of **67** in which the $[SbCl_6]^-$ anion interacts with the stibonium center via a long Sb-Cl bond of 3.231(6) Å.[173] Congruent with the different degrees of cation-anion interactions observed in **67** and **68**, we find that the $[Mes_3SbCl]^+$ cation of **68** is closer to a tetrahedral geometry than the $[Ph_3SbCl]^+$ cation of **67**, with τ_4 values[174] of 0.84 for **67** and 0.89 for **68**, respectively. We attribute the absence of such short contacts between the $[SbCl_6]^-$ anion and the stibonium center of **68** to the protection offered by the *ortho* methyl groups of the mesityl substituents as illustrated in Figure 48. The antimony atom is 0.30 Å above the plane defined by the three *ipso*-carbon atoms in the structure of **67** and 0.41 Å in that of **68**. The distorted tetrahedral geometry of **68** is further

characterized by average ∠Cl-Sb-C and ∠C-Sb-C angles of 101.2º and 116.3º, respectively. The Sb-Cl bond distance in $[Mes_3SbCl]^+$ (2.322(2) Å) is as short as that in $[Ph_3SbCl]^+$ (2.325(7) Å)[173] pointing to a very electrophilic antimony center. This view is corroborated by the fact that this bond distance is shorter than that measured in $(C_6F_5)_4SbCl$ (2.45 Å),[13] Ph_3SbCl_2 (av. 2.49 Å)[175] and Ph_4SbCl (2.69 Å).[176-177]

Based on the knowledge that the Lewis acidity of Group 15 compounds originates from low-lying σ* orbitals centered on the pnictogen atom,[13] we examined the molecular orbitals of both $[Ph_3SbCl]^+$ and $[Mes_3SbCl]^+$. The geometries of the cations were optimized with the M06 functional and a mixed basis set (6-31+g(d') for C, H, Cl and cc-pVTZ-PP[161] with Stuttgart relativistic small core ECP[162] for Sb). The lowest unoccupied molecular orbital (LUMO) of both $[Ph_3SbCl]^+$ and $[Mes_3SbCl]^+$ is centered on the antimony atom and is dominated by σ*(Sb-Cl) character. Smaller components of the LUMO reside on the *ortho* and *para* positions of the arene substituents suggesting a small degree of σ*-π conjugation (Figure 49). The LUMO energy of $[Ph_3SbCl]^+$ is 42 kJ/mol lower that of $[Mes_3SbCl]^+$, consistent with the greater electron withdrawing ability of Ph *vs.* Mes as well as with the experimental observation that $[Ph_3SbCl]^+$ strongly interacts with the $[SbCl_6]^-$ anion in the solid state. Hence, electronic effects may also be partly responsible for the absence of a direct interaction between the mesityl stibonium $[Mes_3SbCl]^+$ cation and the $[SbCl_6]^-$ anion in the solid state of **68**.

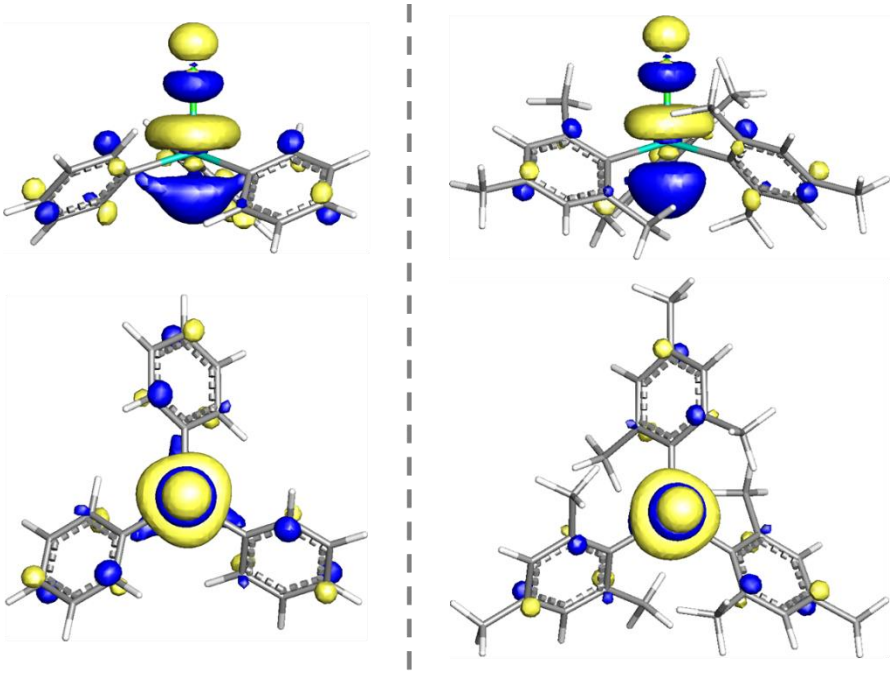

Figure 49. LUMO of $[Ph_3SbCl]^+$ (left) and $[Mes_3SbCl]^+$ (right). Isovalue = 0.02.

3.4 Catalytic polymerization of THF and Friedel-Crafts dimerization of 1,1-diphenlyethylene

We have investigated the reactivity of all compounds described above, with the exception of **65** whose ^1H and ^{13}C NMR spectra showed that it could not be reliably handled in solution (*vide supra*). We first decided to assess the relative reactivity of these derivatives by investigating their ability to polymerize THF (Figure 50, Table 7). With a catalyst loading of 0.1 mol% in neat THF, we observed that **63**, **64**, and **66** are almost inactive, with only 0.1% of the monomer polymerized after 2 hours as established by ^1H NMR spectroscopy. By contrast, **67** and **68** are significantly more active, leading to conversions of 17% (turnover frequency = TOF = 1.6 min^{-1}) for **67** and 15% (TOF = 1.3

min^{-1}) for **68** in 2 hours (Figures 62-63). Letting the reaction run for longer periods gave viscous polymer solutions thereby complicating NMR analysis. These results point to the inhibitory role played by the triflate anion which may coordinate too strongly to the Lewis acidic antimony center. Such limitations do not seem to affect **67** and **68**, in accordance with the more weakly coordinating nature of the $[SbCl_6]^-$ counter anion. The higher activity displayed by **5** most likely originates from steric effects, with the smaller phenyl substituents affording a more exposed and thus more reactive antimony center. This argument is supported by the observed catalytic activity of these compounds in the Friedel-Crafts dimerization of 1,1-diphenlyethylene (Figure 50). Compound **67** was the only one to show any activity, leading to a 99% yield of 1-methyl-1,3,3-triphenyl-2,3-dihydro-*1H*-indene after 20 min, with a catalyst loading of only 5%. Compounds **63**, **64**, **66**, and **68** show no activity even after 1 day (Figure 64). The fact that **68** is inactive also eliminates the possibility of the hexachloroantimonate anion being responsible for the catalytic properties of **67**. While a similar reactivity has been reported for electrophilic phosphoniums and fluorosulfoxonium cations,[92, 178] this is the first use of a stibonium catalyst for this reaction.

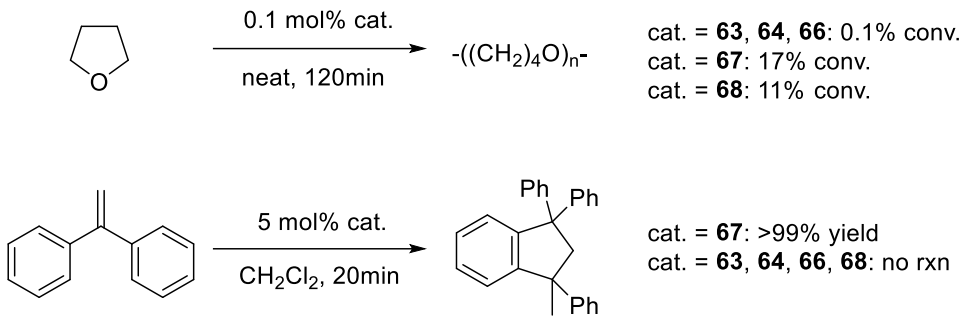

Figure 50. Catalytic reactions investigated.

3.5 Conclusion

Our results demonstrate that halostibonium cations of general formula $[Ar_3SbX]^+$ can be readily synthesized using either anion exchange or anion abstraction reactions. The high electrophilic character of the antimony center in these species is reflected by the tendency of these stibonium cations to interact with the counter anion as in the case of $Ph_3SbF(OTf)$ (**65**) and $Mes_3SbF(OTf)$ (**66**) which exist as molecular rather than ionic solids. The formation of halostibonium salts necessitates the use of the more weakly coordinating hexachloroantimonate anion as well as the steric protection of the antimony center as in the case of $[Mes_3SbCl][SbCl_6]$ (**68**). Computational studies show that the $[Ph_3SbCl]^+$ present in **67** is the most electron deficient cation investigated in this study. This view is supported by the highest reactivity that **67** displays in the polymerization of THF and the Friedel-Craft dimerization of 1,1-diphenlyethylene. These results show that the reactivity of such species is controlled by the coordinating nature of the counteranions, the steric accessibility of the reactive antimony center and possibly the greater electron withdrawing ability of the phenyl substituents present in **67**.

3.6 Experimental section

Antimony compounds are potentially toxic and should be handled accordingly. Air-sensitive experiments were carried out using standard glovebox or Schlenk techniques in the absence of oxygen and moisture. All glassware was dried in an oven and cooled under vacuum before use. Triphenyl antimony and potassium fluoride were purchased from EMD Millipore; 2-bromomestyliene, n-butyllithium (2.2 M in hexanes), and 1,1-diphenlyethylene were purchased from Alpha Aesar, methyl trifluoromethanesulfonate was purchased from Matrix Scientific, antimony pentachloride was purchased from Acros Organics. All commercially available chemicals were used without further purification. $SbMes_3$,[179] $PhICl_2$,[180] Ph_3SbCl_2,[181] Ph_3SbBr_2,[182] $Ph_3Sb(OTf)_2$ (**63**),[63] and Mes_3SbBr_2[179] were prepared according to reported procedures. Ph_3SbF_2[170] and Mes_3SbCl_2[179] were synthesized by modifications of reported procedures. The solvents were dried by passing through an alumina column (pentane and CH_2Cl_2), distillation under N_2 over Na/K (Et_2O, n-hexane, and THF) or distillation under N_2 over CaH_2 ($CDCl_3$, CD_2Cl_2, CD_3CN, CH_3CN). All other solvents were ACS reagent grade and used as received. NMR spectra were recorded on a Varian Unity Inova 400 FT NMR (399.52 MHz for ^1H, 375.92 MHz for ^{19}F, 161.74 MHz for ^{31}P, 100.46 MHz for ^{13}C) or a Varian Unity Inova 500 FT NMR (499.42 MHz for ^1H, 469.86 MHz for ^{19}F, 202.18MHz for ^{31}P, 125.60 MHz for ^{13}C) at ambient temperature. Chemical shifts (δ) are given in ppm and are referenced against residual solvent signals (^1H, ^{13}C) or external standards ($BF_3{\cdot}Et_2O$ for ^{19}F (-153 ppm), and 85% H_3PO_4 for ^{31}P (0 ppm)). Elemental analyses were performed at Atlantic Microlab (Norcross, GA).

3.6.1 Syntheses

3.6.1.1 Synthesis of Mes_3SbF_2

Mes_3SbF_2 was synthesized by a modification of reported procedure.[171] A methanol solution of KF (344 mg, 9 mmol) was added to a methanol suspension of Mes_3SbBr_2 (1.00 g, 1.5 mmol). After stirring for ~2 h, the solvent was removed under vacuum and dry CH_2Cl_2 was added to the residue. After passing through a short plug of celite, the solvent was removed under vacuum to afford Mes_3SbF_2 as a white powder (588 mg, 70% yield). The product appeared spectroscopically pure and was used as synthesized. ^{1}H NMR (400 MHz, $CDCl_3$) δ = 6.98 (s, 2H), 2.49 (s, 6H), 2.32 (s, 3H). ^{19}F NMR (376 MHz, $CDCl_3$) δ = -100.72 (s). ^{13}C{^{1}H}NMR (126 MHz, $CDCl_3$) δ = 143.33 (s, *o*-Mes), 140.88 (s, *p*-Mes), 137.56 (t, quaternary, $J_{C\text{-}F}$=13.6), 130.11 (s, *m*-Mes), 23.72 (t, *o*-*C*H3, $J_{C\text{-}F}$=3.7), 21.23 (s, *p*-*C*H_3). Single crystals were grown at room temperature in 3-5 days by vapor diffusion of Et_2O into a CH_2Cl_2 solution of Mes_3SbF_2.

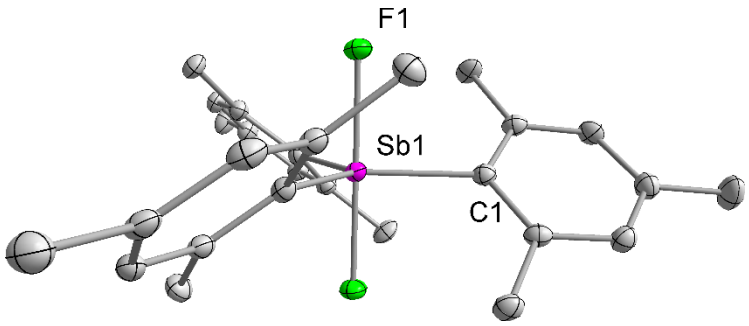

Figure 51. Structure of Mes_3SbF_2 in the crystal. Ellipsoids are drawn at the 50% probability level. Hydrogen atoms are omitted for clarity.

3.6.1.2 Synthesis of $Mes_3Sb(OTf)_2$ (**64**)

A suspension of AgOTf (720 mg, 2.80 mmol) in CH_2Cl_2 (5 mL) was added to a solution of Mes_3SbBr_2 (883 mg, 1.38 mmol) in CH_2Cl_2 (5 mL) in a 50 mL Schleck tube. After stirring in the dark for 1 h, the solution was filtered with a cannula and transferred to another Schlenk tube. Next, a large amount of hexanes (~ 40 mL) was added to the solution and the resulting suspension was left to stand at -40ºC overnight. The supernatant was discarded by cannula filtration affording a white precipitate which was dried *in vacuo*. This precipitate was identified as $Mes_3Sb(OTf)_2$ (800 mg, 75% yield). Single crystals were grown at -40ºC in 3-5 days after layering a CH_2Cl_2 solution of **64** with hexanes. $Mes_3Sb(OTf)_2$: ^{1}H NMR (399 MHz, CD_2Cl_2) δ = 7.11 (s, 2H, *m*-Mes), 2.38 (s, 6H, *o*-C*H*$_3$), 2.36 (s, 3H, *p*-C*H*$_3$). ^{19}F NMR (376 MHz, CD_2Cl_2) δ -79.50 (s). ^{13}C{^{1}H}NMR (100 MHz, CD_2Cl_2) δ = 145.43 (s), 143.41 (s, *o*-Mes), 131.90 (s), 130.83 (s, *m*-Mes), 119.84 (q, $J_{C\text{-}F}$=318.3, OTf), 24.07 (s, *o*-*C*H$_3$), 21.36 (s, *p*-*C*H$_3$). Elemental analysis calculated (%, $Mes_3Sb(OTf)_2 \cdot CH_2Cl_2$): C, 41.78; H, 4.09; found: C, 42.09; H, 4.67.

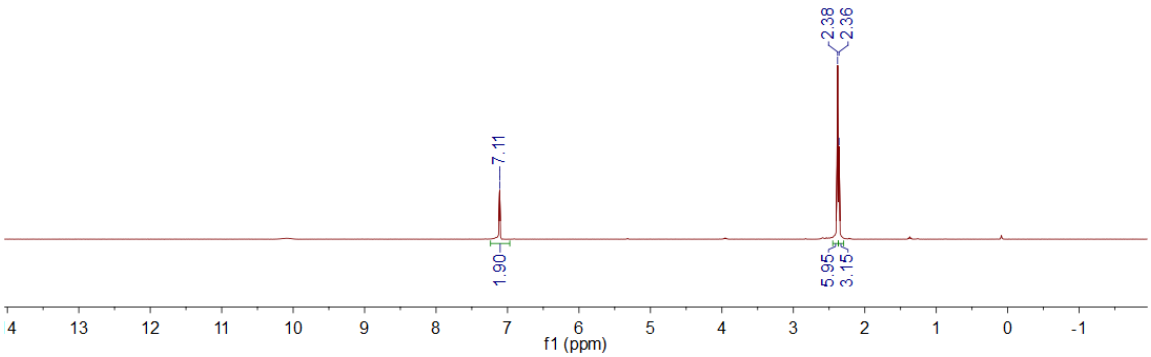

Figure 52. ^{1}H NMR spectrum of **64** in CD_2Cl_2.

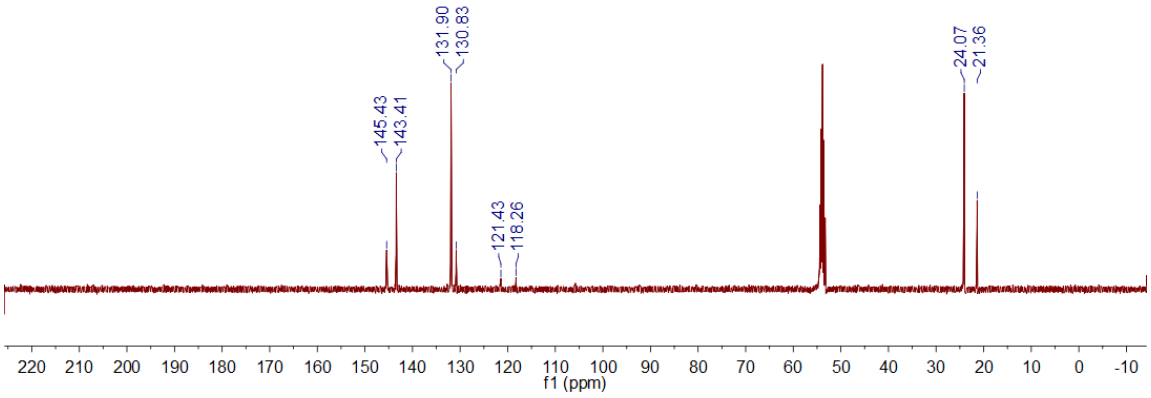

Figure 53. $^{13}C\{^{1}H\}$ NMR spectrum of **64** in CD_2Cl_2.

3.6.1.3 Synthesis of $Ph_3SbF(OTf)$ (**65**).

A solution of $Ph_3Sb(OTf)_2$ (187 mg, 0.28 mmol) in CH_2Cl_2 (5 mL) was added to a solution of Ph_3SbF_2 (141 mg, 0.36 mmol) in CH_2Cl_2 (5 mL) in a 50 mL Schleck tube. The reaction mixture was allowed to stir for 10 min at which point a large amount (~ 40 mL) of hexanes was added while the reaction was still stirring. The resulting suspension was left to stand at -40ºC overnight. The supernatant was discarded by cannula filtration

affording a white precipitate which was dried *in vacuo*. This precipitate was identified as impure $Ph_3SbF(OTf)$ (250 mg). Single crystals were grown at -40ºC in 4 days after layering a CH_2Cl_2 solution of **65** with hexanes. $Ph_3SbF(OTf)$: ^1H NMR (500 MHz, CD_2Cl_2) δ = 8.06 – 8.02 (m, 2H), 7.74 – 7.65 (m, 3H). ^{19}F NMR (470 MHz, CD_2Cl_2) δ = -78.57 (s, 3F, OTf), -156.27 (s, 1F, Sb-*F*). $^{13}C\{^1H\}$NMR (126 MHz, CD_2Cl_2) δ = 134.16 (d, *o*-Ph, *J*=2.9), 133.42 (s, *p*-Ph), 130.35 (s, *m*-Ph), 119.04 (q, J_{C-F}=318.3, OTf). Elemental analysis calculated (%): C, 43.79; H, 2.90; found: C, 44.06; H, 2.97. Note: Despite repeated recrystallizations under multiple conditions, the ^1H and ^{13}C NMR spectra showed the presence of other species leading to the conclusion that this compound could not be isolated or handled confidently in solution.

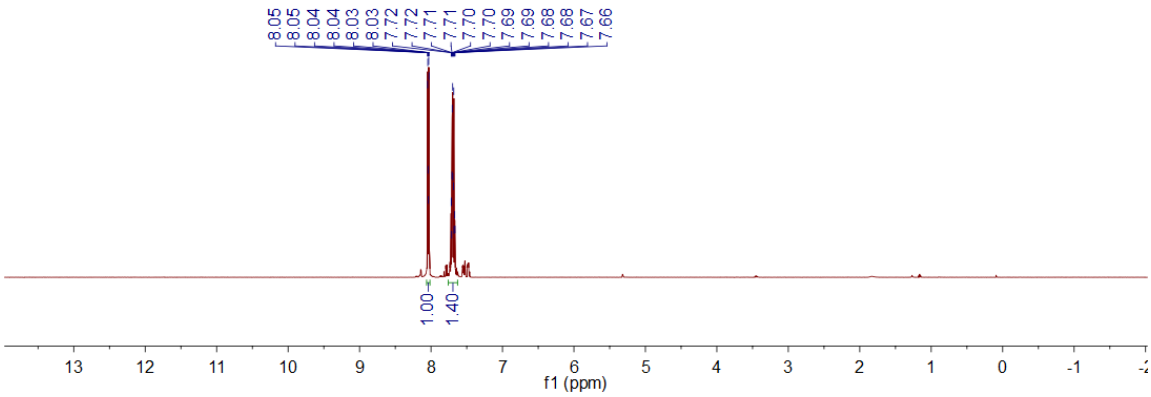

Figure 54. ^1H NMR spectrum of **65** in CD_2Cl_2.

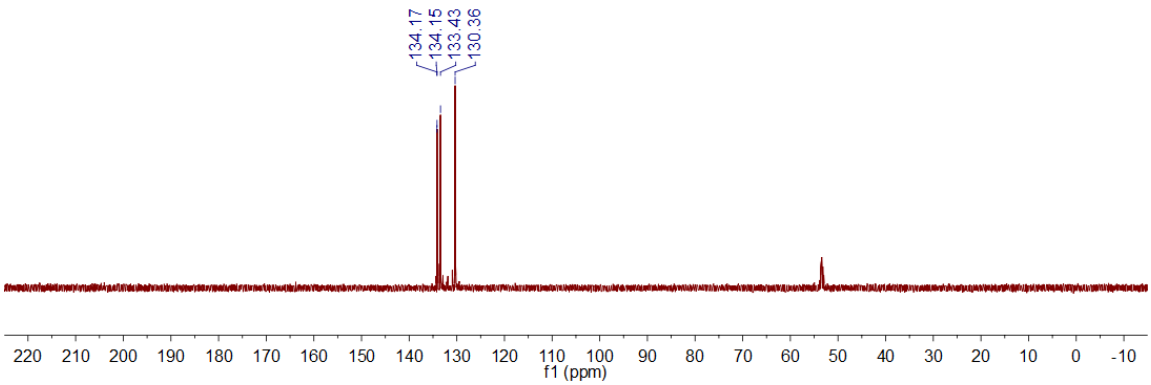

Figure 55. $^{13}C\{^{1}H\}$ NMR spectrum of **65** in CD_2Cl_2.

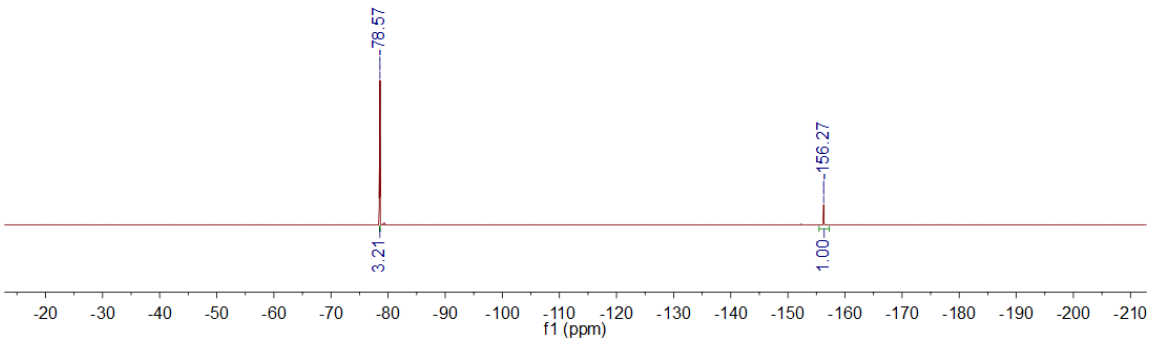

Figure 56. ^{19}F NMR spectrum of **65** in CD_2Cl_2.

3.6.1.4 Synthesis of $Mes_3SbF(OTf)$ (**66**)

A solution of $Mes_3Sb(OTf)_2$ (235 mg, 0.30 mmol) in CH_2Cl_2 (5 mL) was added to a solution of Mes_3SbF_2 (154 mg, 0.30 mmol) in CH_2Cl_2 (5 mL) in a 50 mL Schleck tube. The reaction mixture was allowed to stir for 10 min, at which point a large amount (~ 40 mL) of hexanes was added while the reaction was still stirring. The resulting suspension was left to stand at -40ºC overnight. The supernatant was discarded by cannula filtration

affording a white precipitate which was dried *in vacuo*. This precipitate was identified as $Mes_3SbF(OTf)$ (285 mg, 74% yield). Single crystals were grown at -40ºC in 3-5 days after layering a CH_2Cl_2 solution of **66** with hexanes. $Mes_3SbF(OTf)$: ^1H NMR (500 MHz, CD_2Cl_2) δ = 7.10 (s, 2H, *m*-Mes), 2.50 (s, 6H, *o*-C*H*$_3$), 2.35 (3H, *p*-C*H*$_3$). ^{19}F NMR (470 MHz, CD_2Cl_2) δ = -78.52 (s, 3F, OTf), -144.66 (s, br, 1F, Sb-*F*).$^{13}C\{^1H\}$NMR (126 MHz, CD_2Cl_2) δ = 143.69 (s), 143.56 (s), 137.70 (s), 131.38 (s, *m*-Mes), 119.93 (q, $J_{C\text{-}F}$=319.6 OTf), 23.60 (s, *o*-*C*H$_3$), 21.30 (s, *p*-*C*H$_3$). Elemental analysis calculated (%): C, 51.95; H, 5.14; found: C, 51.67; H, 5.09.

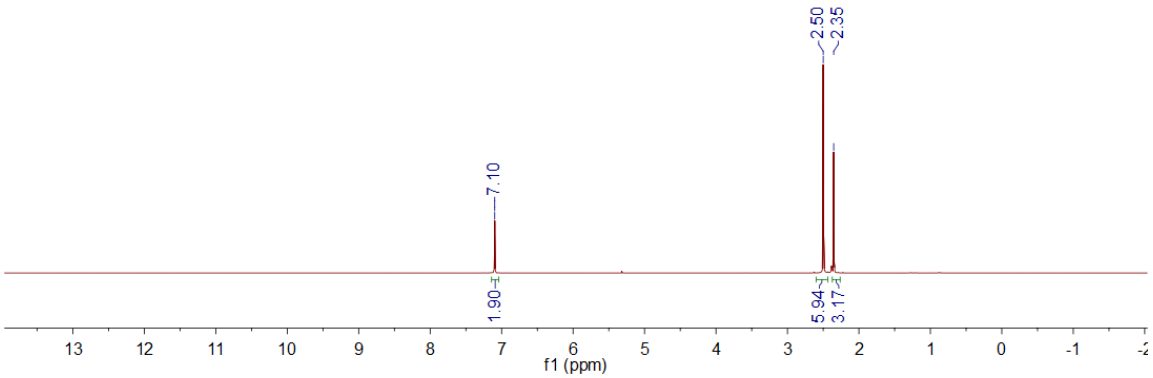

Figure 57. ^1H NMR spectrum of **66** in CD_2Cl_2.

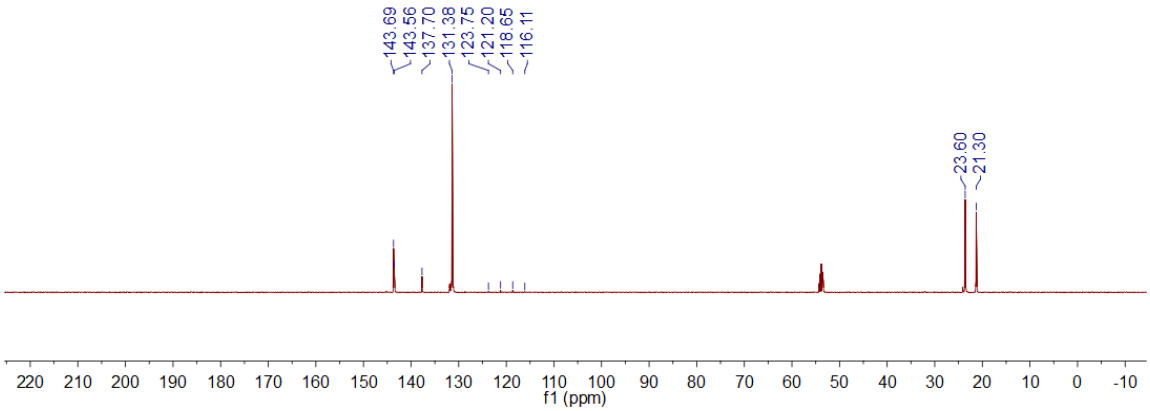

Figure 58. $^{13}C\{^{1}H\}$ NMR spectrum of **66** in CD_2Cl_2.

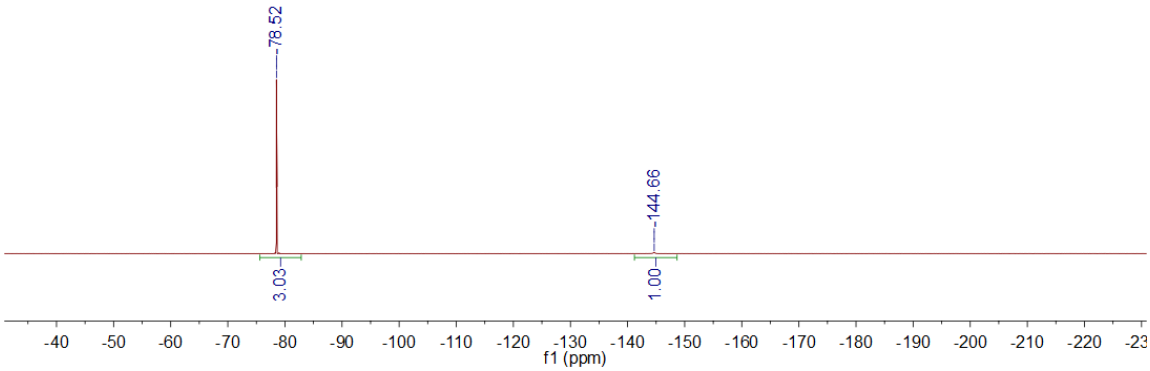

Figure 59. ^{19}F NMR spectrum of **66** in CD_2Cl_2.

3.6.1.5 Synthesis of $[Ph_3SbCl][SbCl_6]$ (**67**)

This procedure is a variant of that available in the literature.[173] A solution of $SbCl_5$ (396 mg, 1.33 mmol) was slowly added to a solution of Ph_3SbCl_2 (563 mg, 1.33 mmol) in CH_2Cl_2 (5 mL) in a 50 mL Schleck tube. The resulting yellow solution was allowed to stir for 10 min, at which point a large amount (~ 40 mL) of hexanes was added while the reaction was still stirring. The resulting suspension was left to stand at -40ºC overnight.

The supernatant was discarded by cannula filtration affording a yellow precipitate which was dried *in vacuo*. This precipitate was identified as $[Ph_3SbCl][SbCl_6]$ (558 mg, 55% yield). The product was stored in the -40ºC freezer in the glovebox. Single crystals were grown at -40ºC in 3-5 days after layering a CH_2Cl_2 solution of **67** with pentanes. The unit cell matches the reported data. $[Ph_3SbCl][SbCl_6]$: ^{1}H NMR (500 MHz, CD_2Cl_2) δ 7.97-7.94 (m, 2H), 7.93-7.89 (m, 1H), 7.88-7.83 (m, 2H). $^{13}C\{^1H\}$NMR (126 MHz, CD_2Cl_2) δ 135.80 (s, *p*-Ph), 134.96 (s, *o*-Ph), 132.37 (s, *m*-Ph), 127.31 (quaternary). Elemental analysis calculated (%): C, 29.90; H, 2.09; found: C, 29.52; H, 2.40.

3.6.1.6 Synthesis of $[Mes_3SbCl][SbCl_6]$ (**68**)

A solution of $SbCl_5$ (179 mg, 0.59 mmol) in CH_2Cl_2 (5 mL) was slowly added to a solution of Mes_3SbCl_2 (304 mg, 0.59 mmol) in CH_2Cl_2 (5 mL) in a 50 mL Schleck tube. The reaction mixture was allowed to stir for 10 min, at which point a large amount (~ 40 mL) of hexanes was added while the reaction was still stirring. The resulting suspension was left to stand at -40ºC overnight. The supernatant was discarded by cannula filtration affording a white precipitate which was dried *in vacuo*. This precipitate was identified as $[Mes_3SbCl][SbCl_6]$ (380 mg, 75% yield). Single crystals were grown at -40ºC in 3-5 days after layering a CH_2Cl_2 solution of **68** with hexanes. $[Mes_3SbCl][SbCl_6]$: ^{1}H NMR (500 MHz, CD_2Cl_2) δ 7.22 (s, 2H, *m*-Mes), 2.45 (s, 6H, *o*-C*H*$_3$), 2.42 (s, 3H, *p*-C*H*$_3$). $^{13}C\{^1H\}$NMR (126 MHz, CD_2Cl_2) δ 146.30 (s, *p*-Mes), 142.84 (s, *o*-Mes), 132.41 (s, *m*-Mes), 131.27 (s, quaternary), 24.60 (s, *o*-*C*H$_3$), 21.05 (s, *p*-*C*H$_3$). Elemental analysis calculated (%): C, 38.19; H, 3.92; found: C, 37.90; H, 3.80.

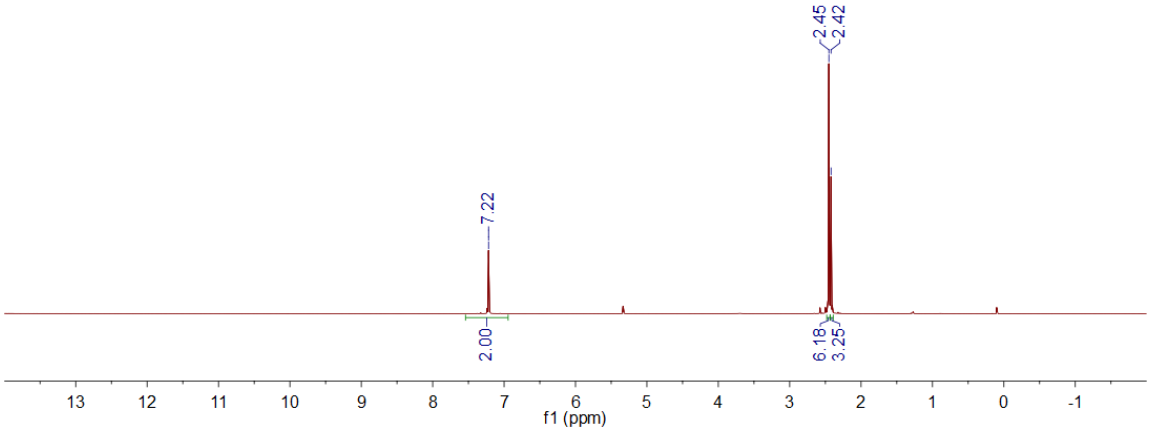

Figure 60. ^{1}H NMR spectrum of **68** in CD_2Cl_2.

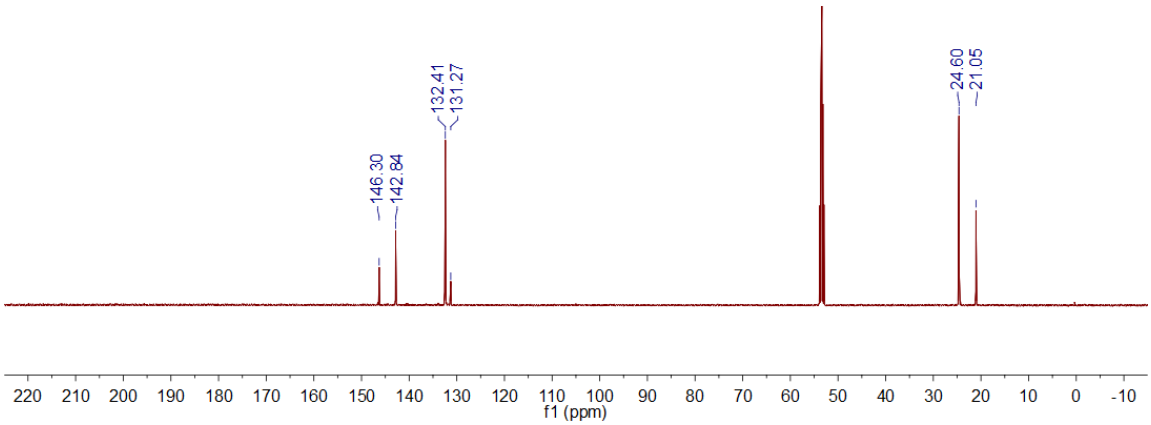

Figure 61. $^{13}C\{^{1}H\}$ NMR spectrum of **68** in CD_2Cl_2.

3.6.2 Catalytic reactions

3.6.2.1 Catalytic polymerization of THF

In the glove box, the antimony catalyst (0.01 mmol) was dissolved in THF (1 mL) in a vial. Aliquots from the reaction mixture were transferred into NMR tubes, mixed with $CDCl_3$ and analyzed by ^{1}H NMR. The progress of the reaction was derived from the integrated signals of the monomer and the polymer.

Table 7. Polymerization of THF promoted by the antimony catalysts.

Catalyst	Time (min)	Conversion (%)	TON	TOF (min^{-1})
63	120	0.1	-	-
63	1440 (1d)	1.0	-	-
64	120	0.1	-	-
64	1440 (1d)	2.2	-	-
66	120	0.1	-	-
66	1440 (1d)	0.1	-	-
67	60	12	125	2.1
67	120	17	190	1.6
68	60	6.1	80	1.4
68	120	11	150	1.3

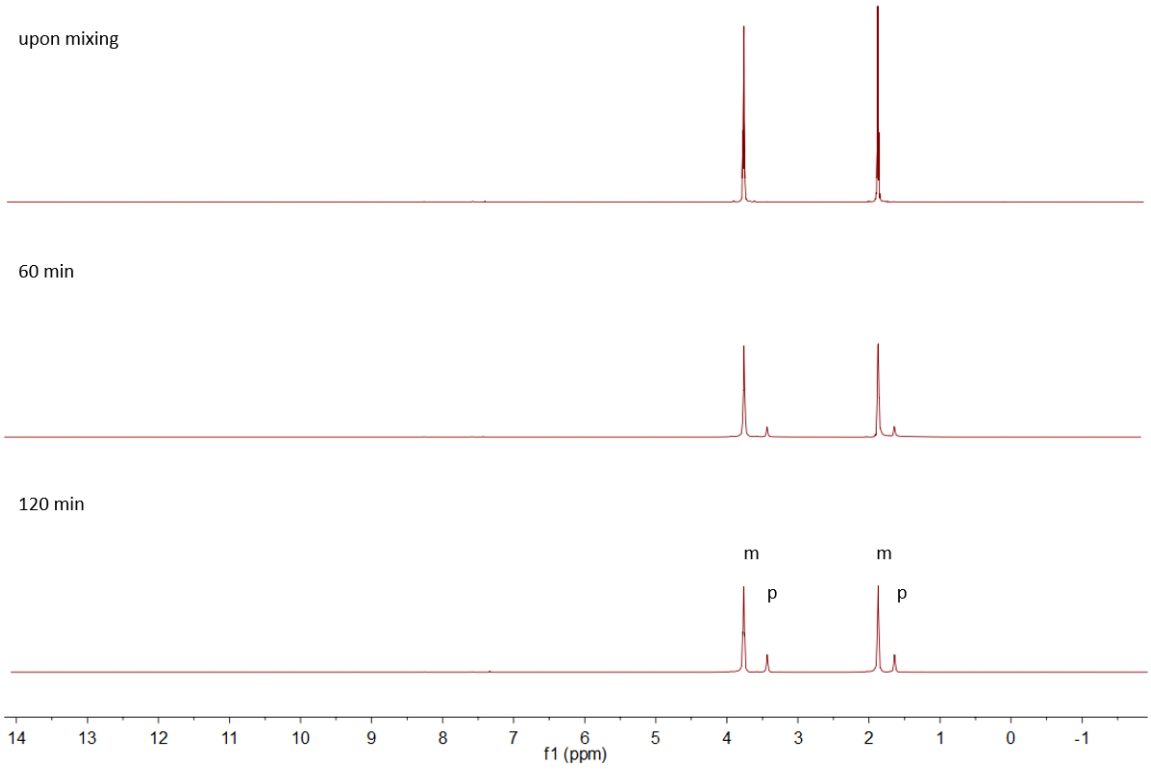

Figure 62. ^{1}H NMR spectra for the polymerization of THF (1 mL) promoted by compound **67** (8.2 mg, 0.011 mmol). The monomer THF resonances are marked by "m", those of the polymer by "p".

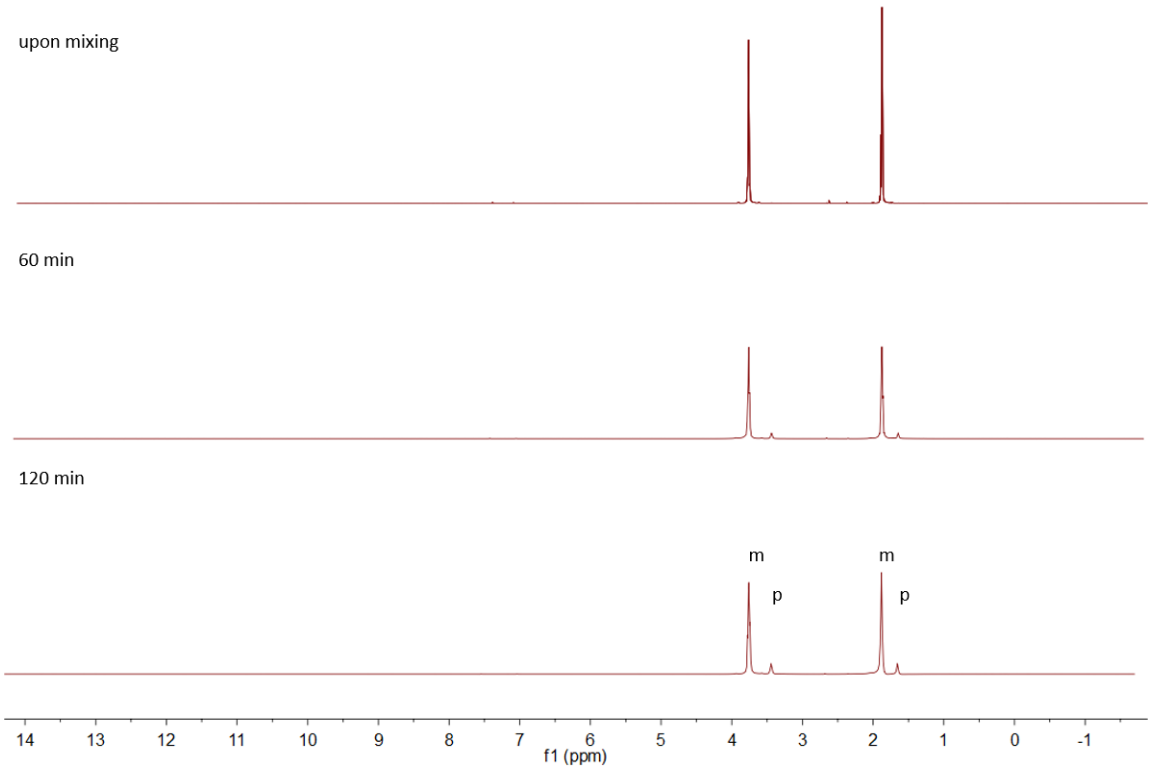

Figure 63. ^{1}H NMR spectra for the polymerization of THF (1 mL) promoted by compound **68** (7.9 mg, 0.009 mmol). The monomer THF resonances are marked by "m", those of the polymer by "p".

3.6.2.2 Catalytic Friedel-Crafts dimerization of 1,1-diphenylethylene.

In the glove box, a NMR tube was charged with a CH_2Cl_2 solution (0.6 mL) of the antimony catalyst (0.025 mmol). Next, 1,1-diphenlyethylene (64 μL(0.49 mmol) was added to the NMR tube via a microsyringe. The reaction was monitored by *in situ* ^{1}H NMR.

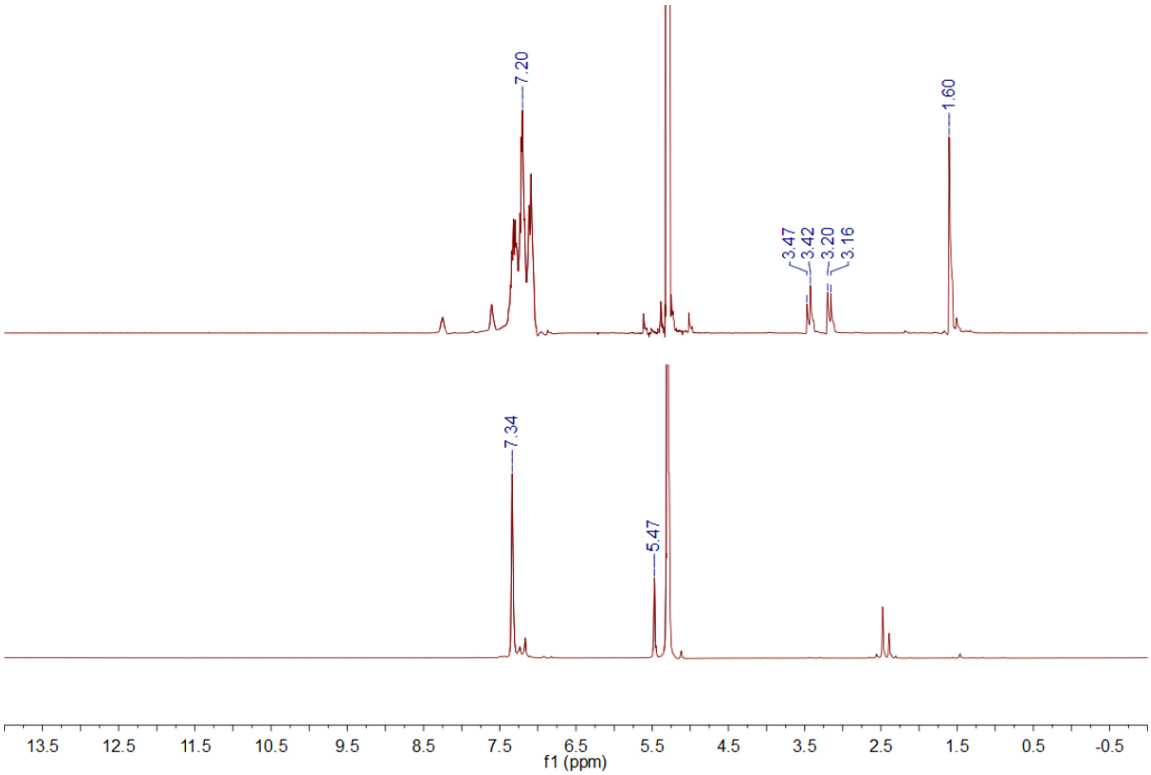

Figure 64. ^{1}H NMR spectra for the dimerization of 1,1-diphenylethylene. Top: Formation of the dimer is observed with compound **67** as a catalyst. Bottom: No dimerization happened with compound **68** as a catalyst.

3.6.3 Crystallographic measurements

All crystallographic measurements were performed at 110(2) K using a Bruker SMART APEX II diffractometer with a CCD area detector (graphite monochromated Mo-Kα radiation, λ = 0.71073 Å) at 110 K. In each case, a specimen of suitable size and quality was selected, coated with paratone oil, and mounted onto a nylon loop. Crystals of **65** and **66** and were mounted on a nylon loop over dry ice to avert decomposition. The

semiempirical method SADABS was applied for absorption correction. The structures were solved by direct methods and refined by the full-matrix least-squares technique against F^2 with the anisotropic temperature parameters for all non-hydrogen atoms. All H-atoms were geometrically placed and refined using the riding model approximation. Data reduction and further calculations were performed using the Bruker SAINT and SHELXTL NT program packages.[157]

Table 8. Crystallographic and structure refinement details for Mes_3SbF_2 and **64**.

Compound	**Mes_3SbF_2**	**64**
Empirical formula	C_{27} H_{33} F_2 Sb	C_{29} H_{33} F_6 O_6 S_2 Sb
Formula weight	517.28	777.42
Temperature	110(2) K	110(2) K
Wavelength	0.71073 Å	0.71073 Å
Crystal system	Monoclinic	Triclinic
Space group	*C* 2/c	*P* -1
Unit cell dimensions	a = 10.2678(8) Å b = 12.7918(10) Å c = 18.0561(17) Å α = 90°. β = 104.478(3)°. γ = 90°.	a = 10.8717(4) Å b = 11.1644(4) Å c = 17.4203(7) Å α = 74.358(2)°. β = 78.509(2)°. γ = 62.115(2)°.
Volume	2296.2(3) $Å^3$	1793.03(12) $Å^3$
Z	4	2
Density (calculated)	1.496 Mg/m^3	1.440 Mg/m^3
Absorption coefficient	1.229 mm^{-1}	0.953 mm^{-1}
F(000)	1056	784
Crystal size	0.240 x 0.150 x 0.100 mm^3	0.26 x 0.14 x 0.09 mm^3
Theta range for data collection	2.330 to 27.526°.	1.218 to 27.618°.
Index ranges	-13<=h<=12, -16<=k<=16, -23<=l<=23	-14<=h<=14, -14<=k<=12, -22<=l<=22
Reflections collected	21340	20695
Independent reflections	2639 [R(int) = 0.0370]	8243 [R(int) = 0.0476]
Completeness to theta = 25.242°	100.0 %	99.9 %
Absorption correction	Semi-empirical from equivalents	Semi-empirical from equivalents
Max. and min. transmission	0.7456 and 0.6569	0.7456 and 0.6686
Refinement method	Full-matrix least-squares on F^2	Full-matrix least-squares on F^2
Data / restraints / parameters	2639 / 0 / 143	8243 / 22 / 470
Goodness-of-fit on F2	1.098	1.034
Final R indices [I>2sigma(I)]	R1 [a] = 0.0183, wR2 [b] = 0.0485	R1 [a] = 0.0436, wR2 [b] = 0.0894
R indices (all data)	R1 = 0.0190, wR2 = 0.0489	R1 = 0.0559, wR2 = 0.0957
Extinction coefficient	n/a	n/a
Largest diff. peak and hole	0.423 and -0.516 e.$Å^{-3}$	0.822 and -0.880 e.$Å^{-3}$

[a] $R1 = \Sigma||F_o| - |F_c||/ \Sigma|F_o|$. [b] $wR2$ $([w(F_o^2 - F_c^2)^2]/[\Sigma w(F_o^2)^2])^{1/2}$; $w = 1/[\sigma^2(F_o^2) + (ap)^2 + bp]$; $p = (F_o^2 + 2F_c^2)/3$ with $a = 0.0188$ and $b = 3.9774$ for Mes_3SbF_2, and $a = 0.0298$ and $b = 2.7299$ for **64**.

Table 9. Crystallographic and structure refinement details for **65** and **66**.

Compound	**65**	**66**
Empirical formula	C_{19} H_{15} F_4 O_3 S Sb	C_{28} H_{33} F_4 O_3 S Sb
Formula weight	521.12	647.35
Temperature	110(2) K	110.15 K
Wavelength	0.71073 Å	0.71073 Å
Crystal system	Monoclinic	Trigonal
Space group	*P* 2_1/c	*R* 3
Unit cell dimensions	a = 8.5391(3) Å b = 27.6302(11) Å c = 8.3426(3) Å α = 90°. β = 95.240(2)°. γ = 90°.	a = 27.1408(10) Å b = 27.1408(10) Å c = 12.7751(6) Å α = 90°. β = 90°. γ = 120°.
Volume	1960.10(13) $Å^3$	8149.7(7) $Å^3$
Z	4	12
Density (calculated)	1.766 Mg/m^3	1.583 Mg/m^3
Absorption coefficient	1.568 mm^{-1}	1.148 mm^{-1}
F(000)	1024	3936
Crystal size	0.29 x 0.25 x 0.08 mm^3	0.1 x 0.06 x 0.05 mm^3
Theta range for data collection	2.506 to 25.997°.	1.501 to 24.997°.
Index ranges	-10<=h<=10, -34<=k<=34, -10<=l<=10	-32<=h<=31, -32<=k<=32, -14<=l<=15
Reflections collected	30390	39533
Independent reflections	3854 [R(int) = 0.0336]	6372 [R(int) = 0.1853]
Completeness to theta = 25.242°	99.9 %	97.7 %
Absorption correction	Semi-empirical from equivalents	Semi-empirical from equivalents
Max. and min. transmission	0.7456 and 0.6290	0.7456 and 0.6276
Refinement method	Full-matrix least-squares on F^2	Full-matrix least-squares on F^2
Data / restraints / parameters	3854 / 4 / 253	6372 / 95 / 493
Goodness-of-fit on F^2	1.094	1.078
Final R indices [I>2sigma(I)]	$R1^a$ = 0.0214, $wR2^b$ = 0.0470	$R1^a$ = 0.0601, $wR2^b$ = 0.0963
R indices (all data)	R1 = 0.0235, wR2 = 0.0479	R1 = 0.0691, wR2 = 0.1015
Extinction coefficient	n/a	n/a
Largest diff. peak and hole	0.928 and -0.586 e.$Å^{-3}$	1.241 and -1.501 e.$Å^{-3}$

^{a}*R1* = $\Sigma||F_o| - |F_c||/ \Sigma|F_o|$. ^{b}*wR2* $([w(F_o^2 - F_c^2)^2]/[\Sigma w(F_o^2)^2])^{1/2}$; $w = 1/[\sigma^2(F_o^2) + (ap)^2 + bp]$; $p = (F_o^2 + 2F_c^2)/3$ with a = 0.0133 and b = 2.5442 for **65** and a = 0.0000 and b = 78.035 for **66**.

Table 10. Crystallographic and structure refinement details for **68**.

Compound	**68**
Empirical formula	C_{29} H_{33} Cl_{11} Sb_2
Formula weight	1015.00
Temperature	110(2) K
Wavelength	0.71073 Å
Crystal system	Orthorhombic
Space group	$P\ 2_12_12_1$
Unit cell dimensions	a = 13.1353(6) Å
	b = 14.9499(6) Å
	c = 21.8393(10) Å
	α= 90°.
	β= 90°.
	γ = 90°.
Volume	4288.6(3) $Å^3$
Z	4
Density (calculated)	1.572 Mg/m^3
Absorption coefficient	1.964 mm^{-1}
F(000)	1984
Crystal size	0.210 x 0.130 x 0.090 mm^3
Theta range for data collection	1.651 to 28.368°.
Index ranges	-17<=h<=17, -19<=k<=19, -29<=l<=29
Reflections collected	73310
Independent reflections	10681 [R(int) = 0.1231]
Completeness to theta = 25.242°	99.8 %
Absorption correction	Semi-empirical from equivalents
Max. and min. transmission	0.7457 and 0.6150
Refinement method	Full-matrix least-squares on F^2
Data / restraints / parameters	10681 / 6 / 377
Goodness-of-fit on F^2	1.032
Final R indices [I>2sigma(I)]	$R1^a$ = 0.0520, $wR2^b$ = 0.1239
R indices (all data)	R1 = 0.0812, wR2 = 0.1421
Extinction coefficient	n/a
Largest diff. peak and hole	1.389 and -1.831 e.$Å^{-3}$

$^aR1 = \Sigma||F_o| - |F_c||/ \Sigma|F_o|$. $^bwR2$ $([w(F_o^2 - F_c^2)^2]/[\Sigma w(F_o^2)^2])^{1/2}$; $w = 1/[\sigma^2(F_o^2) + (ap)^2 + bp]$; $p = (F_o^2 + 2F_c^2)/3$ with a = 0.0649 and b = 7.0161 for **68**.

3.6.4 Computational details

All structures were optimized starting from the crystal structure geometries, using the program and level of theory specified in the result and discussion section. For

compounds **64** and **66**, weakly negative frequencies associated to methyl group rotation were observed. Since these rotations affect peripheral groups, efforts to carry out additional optimization cycles were not considered. None of the other structures displayed imaginary frequencies indicated that a local minimum on its potential energy hypersurface had been reached. The optimized structures were also subjected to natural bond orbital (NBO)[147] analysis. The molecular orbitals were visualized and plotted in Jimp2 program.[163]

CHAPTER IV

INFLUENCE OF THE CATALYST STRUCTURE IN THE CYCLOADDITION OF ISOCYANATES TO OXIRANES PROMOTED BY TETRAARYLSTIBONIUM CATIONS[*]

4.1 Introduction

Antimony(V) halides have long been recognized for their unusual Lewis acidity which has been exploited for the generation of superacids. However, these main group halides are highly corrosive, which greatly complicates their use in organic chemistry. This limitation has served as an incentive for the development of Lewis acidic antimony derivatives whose hydrolytic reactivity is passivated by the introduction of organic ligands.[63-64, 183-185] This approach has led to the development of both neutral and cationic organoantimony derivatives which can be used as water-compatible anion receptors.[12, 14, 30, 36, 57, 119, 186-192] In parallel to these efforts, organoantimony compounds have also found applications in organic reaction catalysis. Example of such reactions include Michael additions,[107] aldol condensations,[108] and hydrosilylations[131] and acetalization[109] of aldehydes which have all been catalyzed by stibonium cations. The most acidic examples of such antimony Lewis acids have proven capable of promoting the polymerization of THF or the Friedel-Craft dimerization of 1,1-diphenlyethylene.[13, 133]

[*] Reproduced with permission from: "Influence of the catalyst structure in the cycloaddition of isocyanates to oxiranes promoted by tetraarylstibonium cations"; M. Yang, N. Pati, G. Bélanger-Chabot, M. Hirai and F. P. Gabbaï, *Dalton Trans.*, 2018, *47*, 11843-11850. Copyright 2018 The Royal Society of Chemistry.

Stibonium cations have also been used to promote cycloaddition reactions between oxiranes and simple heterocumulenes such as CO_2 and isocyanate.[103-106, 193] In the latter case, the reactions afford oxazolidinones, a class of five membered heterocycles that hold broad pharmaceutical potential.[194-197] Such reactions are promoted by various catalysts[198-201] including $[Ph_4Sb]^+$ which typically favors formation the 3,4-isomer **69A** over the 3,5-isomer **69B** (Figure 65).[104-106] Given our interest in the chemistry of stibonium cations, we have decided to revisit this reaction with the view of understanding how the nature of the aromatic substituents bound to antimony influences the catalytic properties of the stibonium cations.

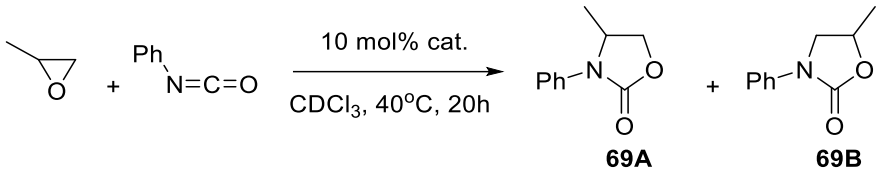

Figure 65. Cycloaddition reaction of propylene oxide with phenyl isocyanate.

4.2 Syntheses and structures of the stibonium salts [**70**][OTf]-[**75**][OTf]

To address the question articulated at the end of the introduction, we decided to prepare a the tetraarylstibonium cations $\mathbf{70}^+$-$\mathbf{75}^+$ which only differ by the nature of a single aromatic substituent. In addition to [**70**][OTf]**,** [**71**][OTf] and [**72**][OTf], which have been previously described, we also synthesized the triflate salts of $[MesSbPh_3]^+$ ($\mathbf{73}^+$), [(*o*-$(Me_2N)C_6H_4)SbPh_3]^+$ ($\mathbf{74}^+$) and [(*o*-$(Me_2NCH_2)C_6H_4)SbPh_3]^+$ ($\mathbf{75}^+$) (Figures 66-67). These compounds were obtained by treatment of Ph_3SbBr_2 with one equiv. of the aryl

lithium reagent followed by the reaction of the resulting heteroleptic tetraarylstibonium bromide with silver triflate. The resulting salts [**73**][OTf], [**74**][OTf] and [**75**][OTf] have been isolated in 25 – 50% overall yield based on Ph_3SbBr_2 after silica gel chromatography. These salts, which are air- and moisture- stable, have been fully characterized (Figures 73-78). Salt [**73**][OTf] has distinctive ^{1}H NMR resonances at 7.08(2H), 2.38(3H) and 2.27(6H) ppm in $CDCl_3$ corresponding to the mesityl group. The *N*-dimethyl groups of [**74**][OTf] and [**75**][OTf] give rise to a ^{1}H NMR resonance at 2.43 ppm and 1.66 ppm, respectively. These triflate salts are soluble in most polar organic solvents such as ethyl acetate, chloroform, dichloromethane, methanol, as well as propylene oxide. Finally, we also synthesized $[Sb(C_6F_5)_4][SbCl_6]$ ([**2**] $[SbCl_6]$) by treating the corresponding tetrakis(pentafluorophenyl) antimony chloride[13] with $SbCl_5$ (Figures 79-80). The ^{19}F NMR of [**2**][$SbCl_6$] is identical to that of **2**$^+$ in [**2**][$B(C_6F_5)_4$][13] which has been previously described.

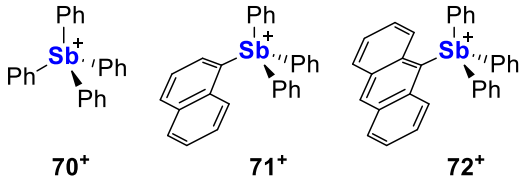

Figure 66. Reported tetraarylstibonium ions.

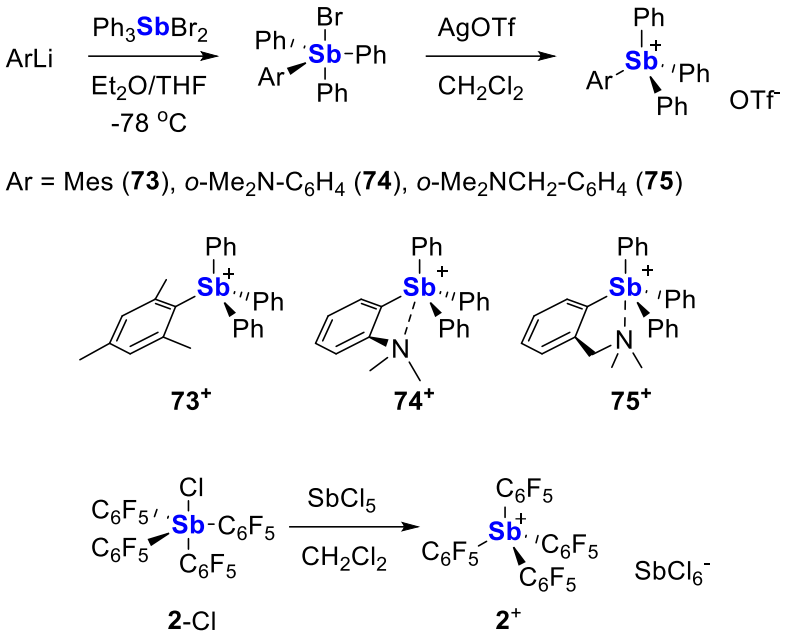

Figure 67. Syntheses of the stibonium salts [**73**][OTf], [**74**][OTf], [**75**][OTf] and [**2**][$SbCl_6$].

Single crystals of the four new stibonium salts could be easily obtained, allowing for an elucidation of their structure in the crystalline state (Figures 69-70, Tables 13-15). No short contacts between the counter-anion and the antimony center are observed in these structures, thus pointing to the relevance of the stibonium formulation. While the antimony center of **73**$^+$ adopts a regular tetrahedral geometry, that of **74**$^+$ and **75**$^+$ is best described as distorted trigonal bipyrimidal as a result of the intramolecular coordination of the dimethylamino group to the antimony center. The resulting N→Sb bond distances of 2.760(3)Å in **74**$^+$ and 2.693(11)Å in **75**$^+$, respectively, are well within the sum of van der Waals radii of the two elements (Σ_{vdWR}(Sb,N) = 4.13 Å).[146] The N→Sb distances in **74**$^+$ and **75**$^+$ are slightly longer than those measured in the related derivatives such as

dichloro[2-(N,N-dimethylaminomethyl)phenyl]bis(4-methylphenyl)-λ^5-stibane (**76** , 2.658(4) Å) and dichloro-1-[8-(*N*,*N*-dimethylamino)naphthyl]bis(4-methylphenyl)-λ^5-stibane (**77**, 2.584(5) Å) shown in Figure 68.[202] We assign these differences to the steric bulk of the phenyl substituents in $\mathbf{74}^+$ and $\mathbf{75}^+$ which prevents a closer approach of the Lewis basic functionality. The structure of $\mathbf{2}^+$ in the [**2**][$SbCl_6$] is tetrahedral and virtually identical to that observed for the $[B(C_6F_5)_4]^-$ salt.[13]

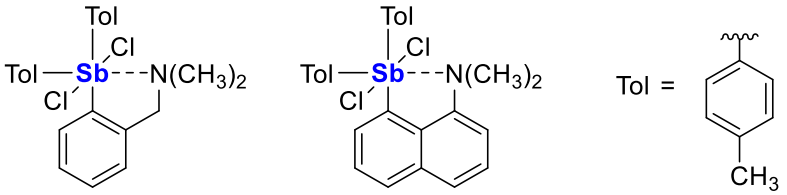

76 **77**

Figure 68. Reported stiboranes with hypervalent Sb···N interactions.

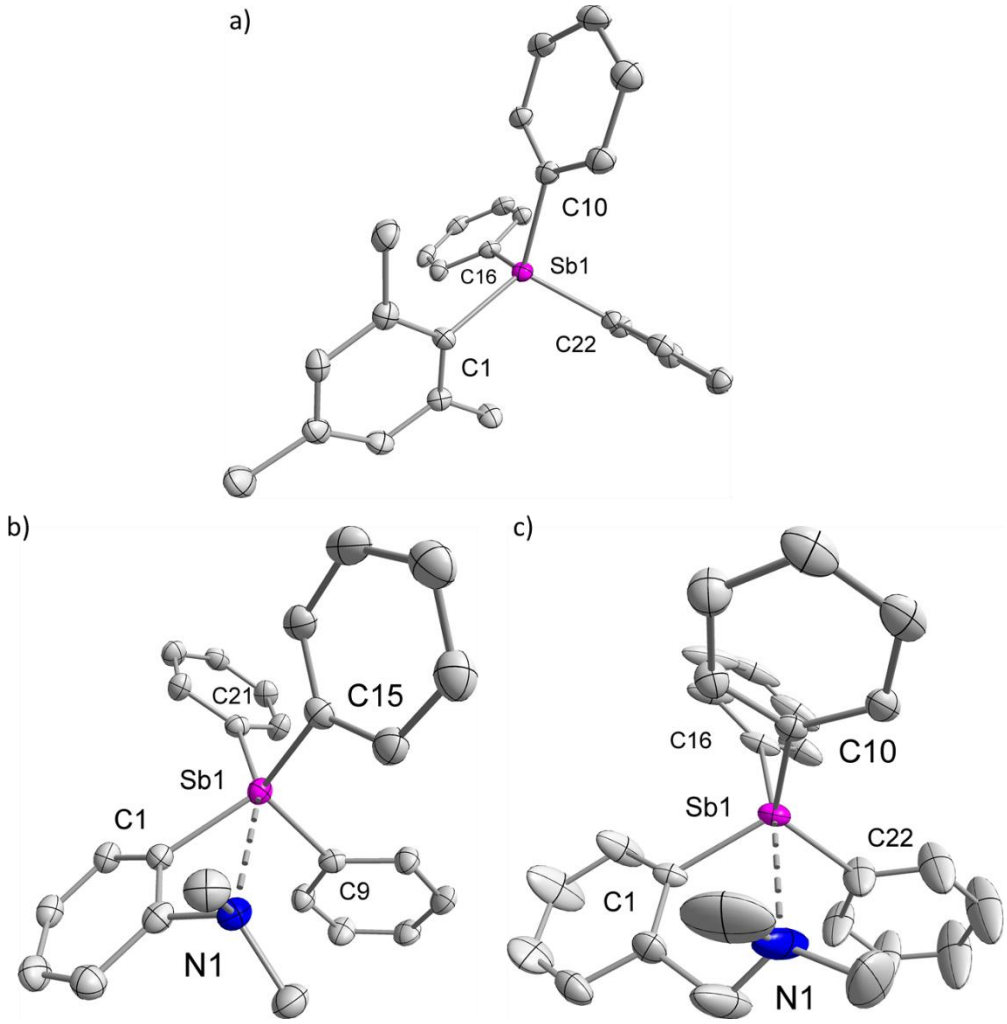

Figure 69. Structures of a) **73**$^+$, b) **74**$^+$ and c) **75**$^+$ in the crystal of the triflate salts. Ellipsoids are drawn at the 50% probability level for **73**$^+$ and **74**$^+$, and 25% for **75**$^+$. The counteranions and the hydrogen atoms are omitted for clarity. Selected bond lengths (Å) and angles (deg) for **73**$^+$: Sb1 – C1 = 2.113(3), Sb1 – C10 = 2.102(3), Sb1 – C16 = 2.094(3), Sb1 – C22 = 2.103(3), C10 – Sb1 – C1 = 119.80(12), ∠C10 – Sb1 – C22 = 106.48(13), ∠C16 – Sb1 – C1 = 104.60(13), ∠C16 – Sb1 – C10 = 105.29(13), ∠C22 – Sb1 – C1 = 112.97(12); for **74**$^+$: Sb1 – C21 = 2.102(4), Sb1 – C15 = 2.103(4), Sb1 – C1 = 2.086(4), Sb1 – C9 = 2.094(4), Sb1 – N1 = 2.760(3), ∠C1 – Sb1 – C21 = 104.47(15), ∠C1 – Sb1 – C15 = 125.81(16), ∠C1 – Sb1 – C9 = 104.53(15), ∠C9 – Sb1 – C21 = 103.22(15), ∠C9 – Sb1 – C15 = 110.78(16), ∠C1 – Sb1 – N1 = 56.65(13), ∠C9 – Sb1 – N1 = 89.64 (13); for **75**$^+$: Sb1 – C1 = 2.092(10), Sb1 – C10 = 2.097(8), Sb1 – C16 = 2.143(10), Sb1 – C22 = 2.067(7), Sb1 – N1 = 2.693(11), ∠C1 – Sb1 – C10 = 113.4(3), ∠C1 – Sb1 – C16 = 103.1(4), ∠C10 – Sb1 – C16 = 101.4(3), ∠C22 – Sb1 – C1 = 113.0(4), ∠C22 – Sb1 – C10 = 120.5(4), ∠C1 – Sb1 – N1 = 71.28(34), ∠C22 – Sb1 – N1 = 80.83(45).

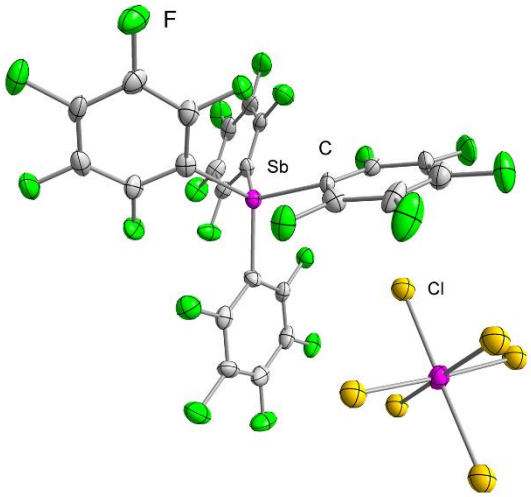

Figure 70. Structure of [**2**][$SbCl_6$] in the crystal. Ellipsoids are drawn at the 50% probability level. The asymmetric unit contains four independent cation-anion pairs, only one is shown. The metrical parameters of the cation are analogous to those previously reported for [**2**][$B(C_6F_5)_4$].[13]

The N→Sb bonds present in **74**$^+$ and **75**$^+$ have been analyzed using the natural bond orbital (NBO) method which was implemented on the computationally optimized geometries of the cations. Both **74**$^+$ and **75**$^+$ show donor-acceptor interactions of lp(N) → σ*(Sb-C) (Figure 71). This interaction is associated with a deletion energy E_{del} of 11.9 kcal/mol in **74**$^+$ and 18.8 kcal/mol in **75**$^+$. The higher stabilizing energy of N-Sb interaction in **75**$^+$ is consistent with the greater flexibility of the CH_2NMe_2 arm whose N atom forms a closer and less constrained contact with the antimony center.

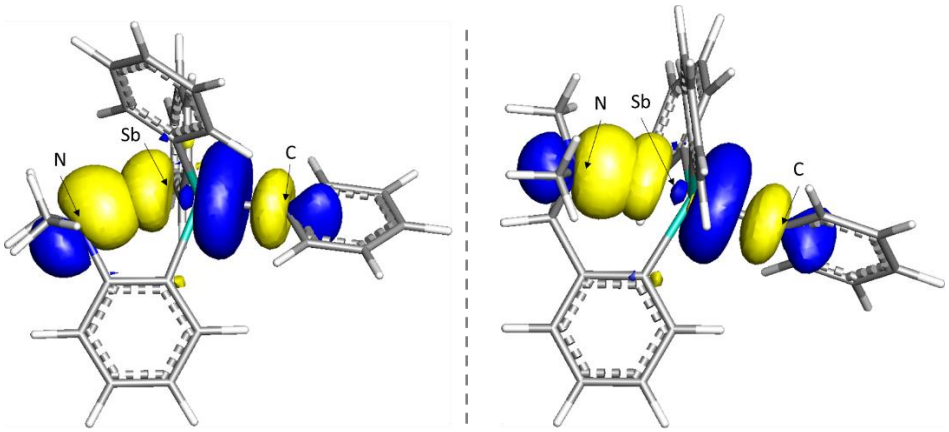

Figure 71. Principal N→Sb NBO donor-acceptor interactions found in **74**$^+$ (left) and **75**$^+$ (right). Isovalue = 0.05.

4.3 Catalytic cycloaddition of oxiranes with isocyanates

Next, we decided to investigate the catalytic properties of these stibonium cations in the reaction of propylene oxide with phenyl isocyanate. In all cases, propylene oxide was used in a 15-fold excess in order to counter the trimerization of phenyl isocyanide which always competes with product formation. These reactions were carried out at 40°C, with N(^{n}Bu)$_4$Br (TBABr) as a co-catalyst. Because coordinating solvents could potentially dampen the Lewis acidity of the stibonium catalysts, we tested the use of toluene and $CHCl_3$ using **70**$^+$ as a catalyst. We observed a cleaner reaction in $CHCl_3$ and chose this solvent for the rest of our studies. We also considered N(^{n}Bu)$_4$I as a co-catalyst and observed product yields analogous to those with TBABr while N(^{n}Bu)$_4$Cl led to significantly lower yields. All reactions were allowed to proceed for 18h at which point the yield and product distribution were analyzed by ^{1}H NMR spectroscopy. The results are summarized in Table 11. As anticipated, the presence of an intramolecular

dimethylamino group in catalysts $\mathbf{74}^+$ and $\mathbf{75}^+$ (Table 11, Entries 5-6) leads to lower catalytic activity, especially in the case of $\mathbf{75}^+$ which features a more stable N→Sb dative interaction. The correlation existing between the presence of an intramolecular base-stabilization of the stibonium center and the yield of the reaction verifies that the Lewis acidity at antimony is indeed at the origin of the catalytic activity of these compounds. In the case of $\mathbf{74}^+$ and $\mathbf{75}^+$, no reaction took place when these cations were mixed with a stoichiometric amount of propylene oxide in $CDCl_3$ over the course of 12 hours at 40°C. (SI) This observation reinforces our interpretation that the low catalytic activity of $\mathbf{74}^+$ and $\mathbf{75}^+$ originates from the presence of an intramolecular N→Sb dative interaction. Another interesting result is observed with the highly Lewis acidic $[Sb(C_6F_5)_4]^+$ cation $\mathbf{2}^+$ for which no oxazolidinone product is observed. (Table 11, Entry 7) Instead, $\mathbf{2}^+$ triggers triggers polymerization of the oxirane as evidenced by ^{1}H NMR analysis.

The best catalysts are the simple tetraarylstibonium derivatives $\mathbf{70}^+$-$\mathbf{73}^+$ which all afford the products in reasonable yields in the 40-55% range (Table 11, Entries 1-4). The most interesting aspect is the increased selectivity observed in the cases of [**71**][OTf] - [**73**][OTf] which all feature a bulky aryl group. The best selectivity is observed in the case of catalysts [**73**][OTf] which possesses a bulky mesityl substituents (Figure 81). The increase in the selectivity ratio of 4.0 in the case $\mathbf{1}^+$ to 7.3 in the case of $\mathbf{73}^+$ is significant. This catalyst was selected for additional scrutiny. In particular, it was used in a scaled-up version of the reaction which was carried out in CH_2Cl_2. This reaction was subjected to a classical workup, leading to product isolation in 44% yield. More significantly, we also observed an increase in the selectivity of the reaction with an 4-methyl-3-phenyl-2-

oxalidinone/5-methyl-3-phenyl-2-oxalidinone ratio (**69A**/**B**) of 11.5 (Table 11, Entry 4). Finally, when TBABr is used alone, the reaction proceeds very slowly with **B** as the only product (Table 11, Entry 8). This last result underscores the crucial role played by the stibonium catalysts in promoting these reactions and altering their selectivity.

Table 11. Cycloaddition of propylene oxide and phenyl isocyanate catalyzed by stibonium ions.[a]

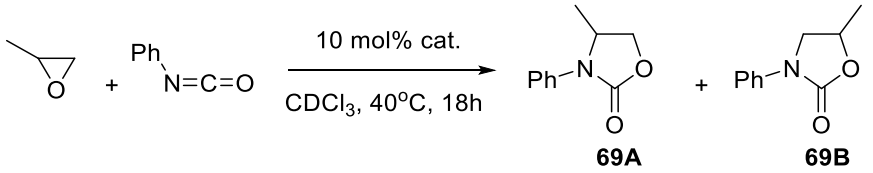

Entry	Cat.	Yield[b] (A+B)%	A/B ratio[b]
1	**70**$^+$	53	4.0:1
2	**71**$^+$	41	6.7:1
3	**72**$^+$	52	5.3:1
4	**73**$^+$	46 [44][c]	7.3:1 [11.5:1][c]
5	**74**$^+$	32	6.1:1
6	**75**$^+$	8	1.1:1
7	**2**$^+$	0[d]	-
8	-	4	0:1

[a]Reaction conditions:10 mol% catalyst and 10 mol% TBABr, $CDCl_3$, 40ºC, 18h, propylene oxide: phenyl isocyanate = 15:1. [b]Yield and **A**/**B** ratio determined by ^{1}H NMR spectroscopy of the unpurified reaction mixture. [c]Isolated yield in CH_2Cl_2. [d]Polymerization of propylene oxide was observed.

The cycloaddition of propylene oxide and phenyl isocyanate may be decomposed in three distinct steps: i) ring opening of the oxirane, ii) insertion of the isocyanate C = O bond into the Lewis acid-alkoxide bond, and iii) cyclization by nucleophilic displacement of the halide by the imine moiety (Figure 72).[106, 198] The regioselectivity of the reaction is

determined by the initial ring opening of the oxirane. If the opening proceeds via an S_N2-type mechanism, the 3,5-isomer **B** is expected as often observed with transition metal-based catalysts.[198-201] On the other hand, harder Lewis acids including those based on antimony and tin tend to favor a S_N1-type mechanism, leading to the 3,4-isomer **A**.[106, 203] The fact that both isomers are often observed indicates that intermediates **I**, **I'**, **II** and **II'** are in equilibrium with each other. The results obtained in this work also suggest that the S_N1-type mechanism dominates. We propose that the higher regioselectivity observed with **73**$^+$ originates from the greater steric encumbrance of the stibonium cation and the more congested nature of the oxirane binding pocket. This increased congestion is proposed to rotate the oxirane such that the more encumbered C2 carbon is directed away from the antimony atom and thus more exposed to the incoming nucleophile.

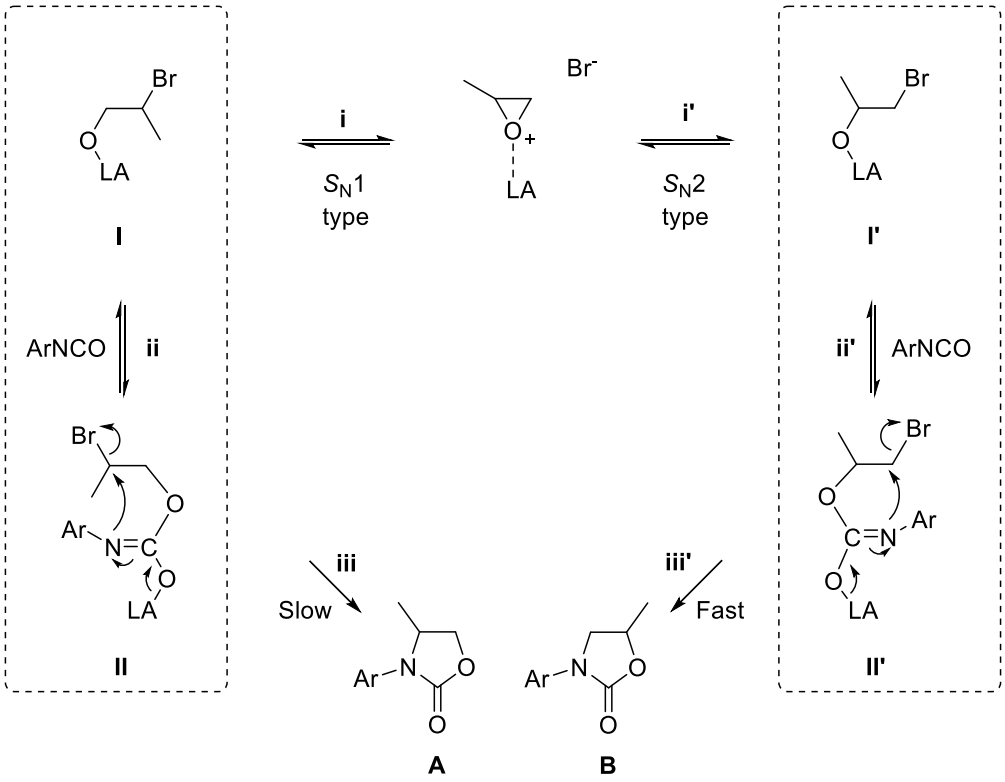

Figure 72. Proposed mechanism for the formation of oxazolidinones.

Table 12. Cycloaddition of oxiranes and isocyanates catalyzed by stibonium ions.[a]

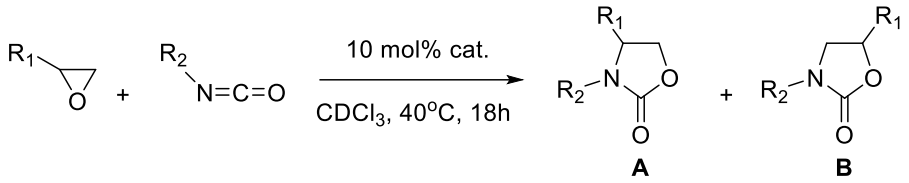

Entry	Oxirane R_1	Isocyanate R_2	cat.	Yield[b] (A+B)%	Ratio[b] A:B
1	Ph	Ph	**70**$^+$	62	3.9:1
2	Ph	Ph	**73**$^+$	57 [47][c]	3.9:1 [13.3:1][c]
3	Me	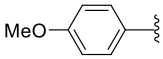	**70**$^+$	25	4.5:1
4	Me	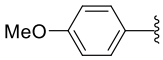	**73**$^+$	49	14.6:1
5	Me	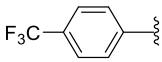	**70**$^+$	23	0.8:1
6	Me	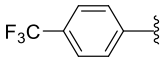	**73**$^+$	15	1.1:1

[a]Reaction conditions:10 mol% catalyst and 10 mol% TBABr, $CDCl_3$, 40ºC, 18h, propylene oxide: phenyl isocyanate = 15:1. [b]Yield and **A**/**B** ratio determined by ^{1}H NMR spectroscopy of the unpurified reaction mixture. [c]Isolated yield in CH_2Cl_2.

Lastly, a variation of substrates was tested with catalysts **70**$^+$ and **73**$^+$ (Table 12). Consistent with the data shown in Table 11, the bulkier catalyst **73**$^+$ is more selective and favors the 3,4 isomer **A** (Figures 82-84). When styrene oxide was used instead of propylene oxide, the reaction displayed a slightly decreased regioselectivity which we assigned to the greater steric of the phenyl ring when compared to the methyl group of the propylene oxide (Table 12, Entries 1-2). The electronic properties of the isocyanate were also varied. When 4-(methoxy)-phenyl isocyanate was used, the reaction becomes more regioselective in favor of isomer **A** (Table 12, Entries 3-4). We propose that the increased

nucleophilicity of the nitrogen in the imine intermediate makes the nucleophilic attack of the secondary carbon atom in step **iii** a more likely process. When the nucleophilicity of this nitrogen atom is decreased, as in the reaction involving 4-(trifluoromethyl)-phenyl isocyanate (Table 12, Entries 5-6), this last step (**iii**) becomes prohibitively slow, especially when compared to step **iii'** which entails nucleophilic attack of a primary carbon. It follows that while intermediates **III** and **IV** may be favored in the overall equilibrium, their conversion in the final isomer **A** becomes affected by the rate of the last step. By contrast, the small proportion of intermediate **IV'** formed in the S_N2-type mechanism is quickly converted into product **B**, leading to an increase in the yield of the latter. Furthermore, in agreement with the importance of steps **ii** and **ii'** in the ultimate fate of these reactions, we note that the overall yield of the reactions involving 4-(trifluoromethyl)-phenyl isocyanate is lower due to the decreased nucleophilicity of the nitrogen atom as well as the decreased electrophilicity of the carbon atom.

4.4 Conclusion

In conclusion, we have synthesized a number of stibonium cations and compared their catalytic activity in the cycloaddition of isocyanates and oxiranes. In agreement with earlier studies, these antimony Lewis acids favor the opening of the oxirane via an S_N1-type mechanism that produces preferentially the 3,4-isomer of the oxazolidinone product. Stibonium cations with intramolecular dimethylamino groups, as in the case of $\mathbf{74}^+$ and $\mathbf{75}^+$, have a lower catalytic activity because donation from the nitrogen atom to the antimony atom attenuates the Lewis acidity of the latter. We also observed that bulkier

stibonium cation as well as electron-rich isocyanates increased the regioselectivity of the reactions, again in favor of the 3,4-isomer. The catalyst that emerges as the most selective in these studies is $[MesSbPh_3]^+$ (**73**$^+$), a stibonium that can be obtained in two straightforward steps starting from Ph_3SbBr_2 and LiMes.

4.5 Experimental section

Antimony compounds are potentially toxic and should be handled accordingly. Air-sensitive syntheses were carried out using standard glovebox or Schlenk techniques in the absence of oxygen and moisture. All glassware was dried in an oven and cooled under vacuum before use. 1-Bromonaphthalene, 2-bromomestilyene, *n*-butyllithium (2.2 M in hexanes), 4-(methoxy)-phenyl isocyanate, and bromine were purchased from Alfa Aesar, N,N-dimethylaniline from Oakwood Chemicals, 9-bromoanthracene from TCI America, propylene oxide and tetrabutylammonium bromide (TBABr) from Acros Organics, $N(^nBu)_4I$ and styrene oxide from Aldrich, phenyl isocyanate and 4-(trifluoromethyl)phenyl isocyanate from BeanTown Chemical, triphenyl antimony from EMD Millipore, and silver trifluoromethanesulfonate (AgOTf) from Matrix Scientific. $N(^nBu)_4Cl$ is recrystallized before use. Ph_3SbBr_2,[182] tetraphenyl stibonium triflate ([**70**][OTf]),[64] 1-naphthyltriphenylstibonium triflate ([**71**][OTf]),[108] 9-anthryltriphenylstibonium triflate ([**72**][OTf]),[14] mesityllithium (LiMes),[204] o-lithiodimethylaniline,[205] and 2-lithio-N,N-dimethylbenzylamine[205] were prepared according to reported procedures. Solvents used in synthesis were dried by passing through an alumina column (CH_2Cl_2) or heating to reflux under N_2 over Na/K (Et_2O,

hexanes, and THF). All other solvents were ACS reagent grade and used as received. NMR spectra were recorded on a Varian Unity Inova 400 FT NMR (399.52 MHz for ^{1}H, 375.92 MHz for ^{19}F, 161.74 MHz for ^{31}P, 100.46 MHz for ^{13}C) or Varian Unity Inova 500 FT NMR (499.42 MHz for ^{1}H, 469.86 MHz for ^{19}F, 202.18MHz for ^{31}P, 125.60 MHz for ^{13}C) at ambient temperature. Chemical shifts (δ) are given in ppm and are referenced against residual solvent signals (^{1}H, ^{13}C) or external standards ($BF_3{\cdot}Et_2O$ for ^{19}F (-153 ppm), and 85% H_3PO_4 for ^{31}P (0 ppm)). Flash chromatography was performed using a CombiFlash Rf + UV model with RediSep sample cartridges, 230-400 mesh silica gel, and commercial ACS reagent grade solvents. Elemental analyses were performed at Atlantic Microlab (Norcross, GA).

4.5.1 Syntheses

4.5.1.1 Synthesis of [MesSbPh$_3$][OTf] ([**73**][OTf])

A solution of mesityllithium (490 mg, 3.85 mmol) in THF (20 mL) was added dropwise to a solution of Ph_3SbBr_2 (1.46 g, 2.86 mmol) in THF/Et_2O (6 mL/30 mL) at -78 ºC. The resulting pale-yellow solution was allowed to warm to room temperature overnight. The solvent was then removed *in vacuo* to afford a pale yellow solid. The solid was extracted with CH_2Cl_2 and passed through a short plug of Celite. The filtrate was evaporated to dryness affording a solid which was taken up in MeOH prior to another filtration through Celite. The solvent was removed to afford crude **73**-Br as an off-white solid. Crude **73**-Br was dissolved in CH_2Cl_2 (20 mL) and treated with AgOTf (504 mg, 1.96 mmol) under an N_2 atmosphere. The resulting yellow suspension was allowed to stir

at room temperature in the dark for 2 h. The suspension was then filtered through Celite, and the filtrate was reduced and purified by flash chromatography over silica gel (100% ethyl acetate). The second major fraction was collected and washed with hexanes to yield [**73**][OTf] as an air-stable white crystalline powder (875 mg, 49% yield based on Ph_3SbBr_2). [**73**][OTf]: ^{1}H NMR (500 MHz, $CDCl_3$) δ = 7.79 – 7.72 (m, 6H), 7.68 – 7.56 (m, 9H), 7.08 (s, 2H, *m*-Mes), 2.38 (s, 3H, *p*-Mes), 2.27 (s, 6H, *o*-Mes). ^{13}C NMR (100 MHz, $CDCl_3$) δ = 144.06 (s, *p*-Mes), 143.95 (s, *o*-Mes), 135.38 (s, *o*-Ph), 133.11 (s, *p*-Ph), 131.23 (s, *m*-Mes), 131.02 (s, *m*-Ph), 127.60 (s, quaternary-Ph), 120.61 (q, $J_{C\text{-}F}$ = 320.7, OTf), 25.87 (s, *o*-CH_3-Mes), 21.38 (s, *p*-CH_3-Mes). ^{19}F NMR (470 MHz, $CDCl_3$) δ = -78.87 (s). Elemental analysis calculated (%): C, 54.13; H, 4.22; found: C, 53.83; H, 4.21. Single crystals suitable for X-ray diffraction were obtained by slow evaporation of hexanes into a CH_2Cl_2 solution in air.

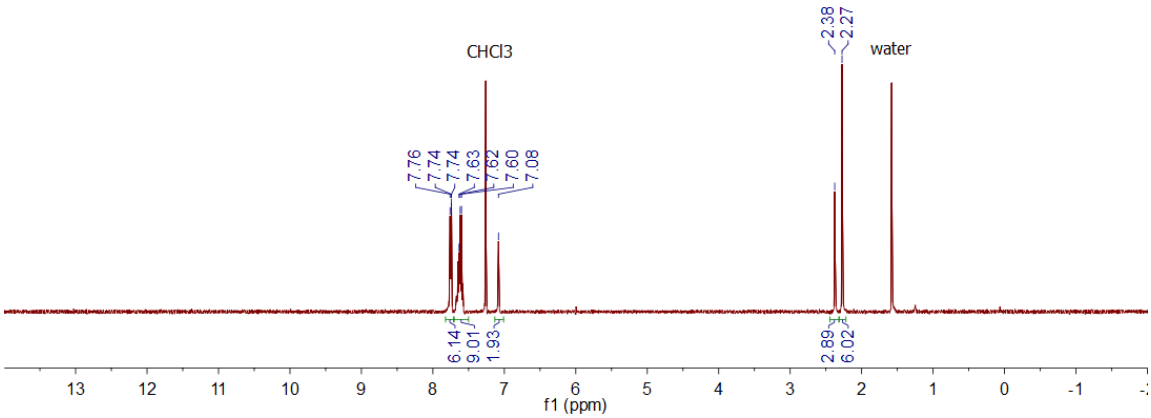

Figure 73. ^{1}H NMR spectrum of [**73**][OTf] in $CDCl_3$.

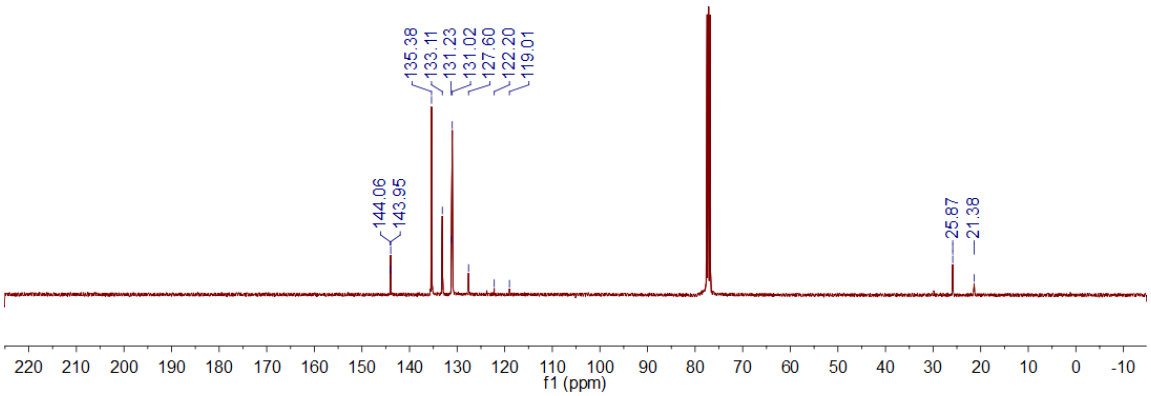

Figure 74. $^{13}C\{^{1}H\}$ NMR spectrum of [**73**][OTf] in $CDCl_3$.

4.5.1.2 Synthesis of [(*o*-$(Me_2N)C_6H_4$)$SbPh_3$][OTf] ([**74**][OTf])

A solution of *o*-lithiodimethylaniline (220 mg, 1.7 mmol) in THF (20 mL) was added dropwise to a solution of Ph_3SbBr_2 (710 mg, 1.4 mmol) in THF/Et_2O (5 mL/25 mL) at -78 ºC. The resulting pale-yellow solution was allowed to warm to room temperature overnight. The solvent was then removed *in vacuo* to afford a pale yellow solid. The solid was extracted with CH_2Cl_2 and passed through a short plug of Celite. The solvent was removed to afford crude **74**-Br as an off-white solid. Crude **74**-Br was dissolved in CH_2Cl_2 (20 mL) and treated with AgOTf (260 mg, 1.0 mmol) under an N_2 atmosphere. The resulting yellow suspension was allowed to stir at room temperature in the dark for 2 h. The suspension was then filtered through Celite, and the filtrate was reduced and purified by flash chromatography over silica gel (100% ethyl acetate). The second major fraction was collected and washed with hexanes to yield [**74**][OTf] as an air-stable white powder (324 mg, 35% yield based on Ph_3SbBr_2). [**74**][OTf]: ^{1}H NMR (500 MHz, $CDCl_3$) $\delta = 7.77$

(t, J = 7.6, 1H), 7.72 – 7.59 (m, 16H), 7.59 – 7.52 (m, 2H), 2.43 (s, 6H, NMe_2). ^{13}C NMR (126 MHz, $CDCl_3$) δ = 156.47 (s, quaternary Me_2N-phenylene), 135.47 (s, phenylene), 135.38 (s, *o*-Ph), 135.03 (s, phenylene), 133.07 (s, *p*-Ph), 130.86 (s, *m*-Ph), 130.22 (s, phenylene), 125.48 (s, quaternary Sb-phenylene), 124.24 (s, quaternary, Sb-Ph), 120.76 (q, $J_{C\text{-}F}$ = 319.9, OTf), 47.49 (s, NMe_2). ^{19}F NMR (470 MHz, $CDCl_3$) δ = -78.56 (s). Elemental analysis calculated (%): C, 52.11; H, 4.05; found: C, 52.36; H, 4.15. Single crystals suitable for X-ray diffraction were obtained by slow evaporation of pentane into a CH_2Cl_2 solution in air.

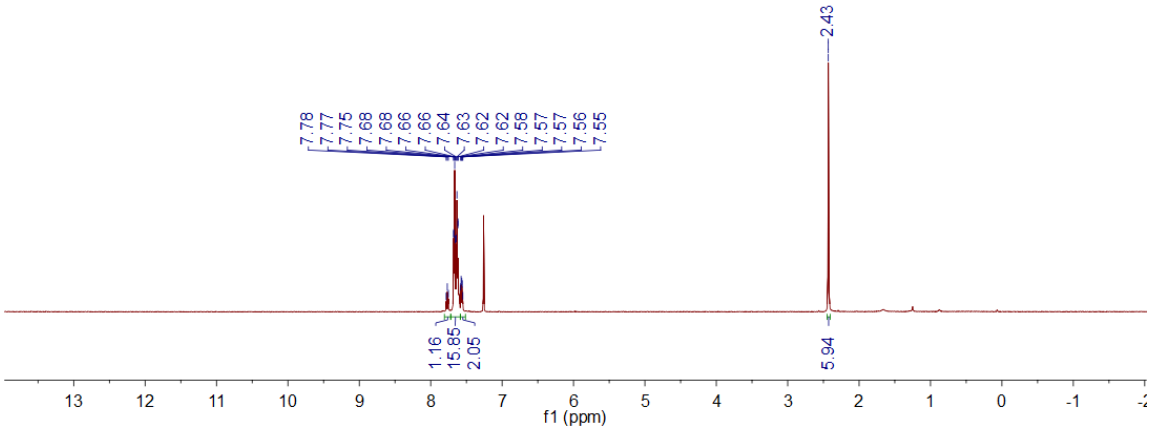

Figure 75. ^{1}H NMR spectrum of [**74**][OTf] in $CDCl_3$.

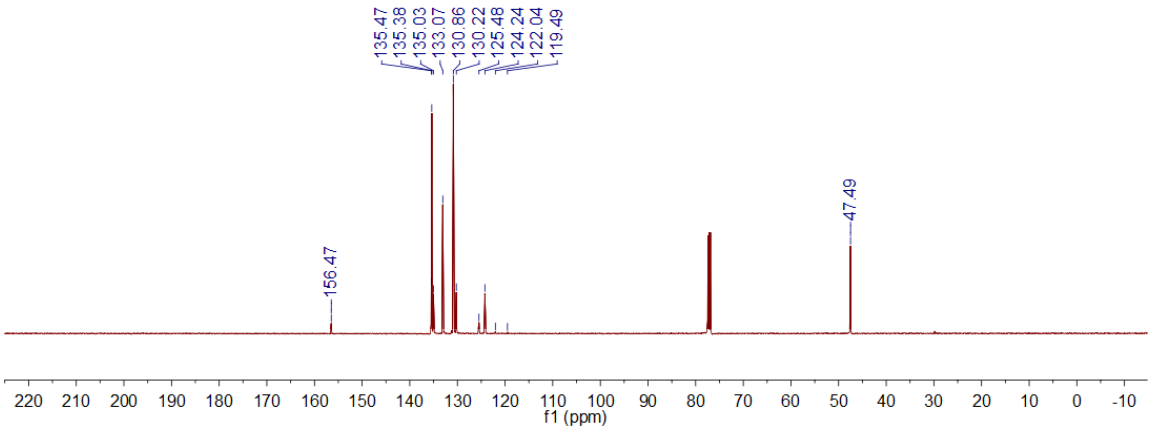

Figure 76. $^{13}C\{^{1}H\}$ NMR spectrum of [**74**][OTf] in $CDCl_3$.

4.5.1.3 Synthesis of [(*o*-(Me_2NCH_2)C_6H_4)$SbPh_3$][OTf] ([**75**][OTf])

A solution of 2-lithio-*N*,*N*-dimethylbenzylamine (312 mg, 2.21 mmol) in THF (20 mL) was added dropwise to a solution of Ph_3SbBr_2 (950 mg, 1.85 mmol) in THF/Et_2O (5 mL/25 mL) at -78 ºC. The resulting pale-yellow solution was allowed to warm to room temperature overnight. The solvent was then removed *in vacuo* to afford a pale yellow solid. The solid was extracted with CH_2Cl_2 and passed through a short plug of Celite. The filtrate was reduced and purified by flash chromatography on silica gel (ethyl acetate: methanol = 1: 1). The first major fraction was collected and washed with Et_2O to afford **75**-Br (270 mg, 26% yield based on Ph_3SbBr_2) as white powder. The product appeared spectroscopically pure and was used as synthesized. **75**-Br: ^{1}H NMR (500 MHz, $CDCl_3$) δ = 7.75 – 7.58 (m, 17H), 7.54 – 7.47 (m, 2H), 3.81 (s, 2H, C*H*$_2$), 1.79 (s, 6H, N*Me*$_2$). ^{13}C NMR (126 MHz, $CDCl_3$) δ = 142.53 (s, quaternary CH_2-phenylene), 136.65 (s, phenylene), 134.41 (s, *o*-SbPh), 133.88 (s, phenylene), 132.42 (s, *p*-SbPh), 131.26 (s, phenylene),

130.81 (s, *m*-SbPh), 130.03 (s, phenylene), 129.38 (s, quaternary Sb-Ph), 129.25 (s, quaternary Sb-phenylene), 62.53 (s, *C*H_2), 45.79 (s, N*Me*$_2$).

Next, **75**-Br (380 mg, 0.66 mmol) was dissolved in CH_2Cl_2 (20 mL) and treated with AgOTf (170 mg, 0.66 mmol) under an N_2 atmosphere. The resulting yellow suspension was allowed to stir at room temperature in the dark for 2 h. The suspension was then filtered through Celite, and the filtrate was reduced and purified by flash chromatography over silica gel (gradient 0 - 50% methanol in ethyl acetate). The first major fraction was collected and washed with diethyl ether to afford [**75**][OTf] as air-stable white powder (320 mg, 75% yield). [**75**][OTf]: ^{1}H NMR (500 MHz, $CDCl_3$) δ = 7.83 – 7.56 (m, 17H), 7.56 – 7.43 (m, 2H), 3.75 (s, 2H, C*H*$_2$), 1.66 (s, 6H, N*Me*$_2$). ^{13}C NMR (126 MHz, $CDCl_3$) δ = 143.46 (s, quaternary CH_2-phenylene), 137.43 (s, phenylene), 134.58 (s, phenylene), 133.99 (s, *o*-SbPh), 132.91 (s, *p*-SbPh), 131.46 (s, phenylene), 131.23 (s, *m*-SbPh), 130.32 (s, phenylene), 127.37(s, quaternary Sb-Ph), 121.10 (q, J_{C-F} = 321.0, OTf), 120.31 (s, quaternary Sb-phenylene), 62.30 (s, *C*H_2), 45.38 (s, N*Me*$_2$). ^{19}F NMR (470 MHz, $CDCl_3$) δ = -78.41 (s, OTf). Elemental analysis calculated (%): C, 52.85; H, 4.28; found: C, 53.13; H, 4.32. Single crystals suitable for X-ray diffraction were obtained by slow evaporation of pentane into a CH_2Cl_2 solution in air.

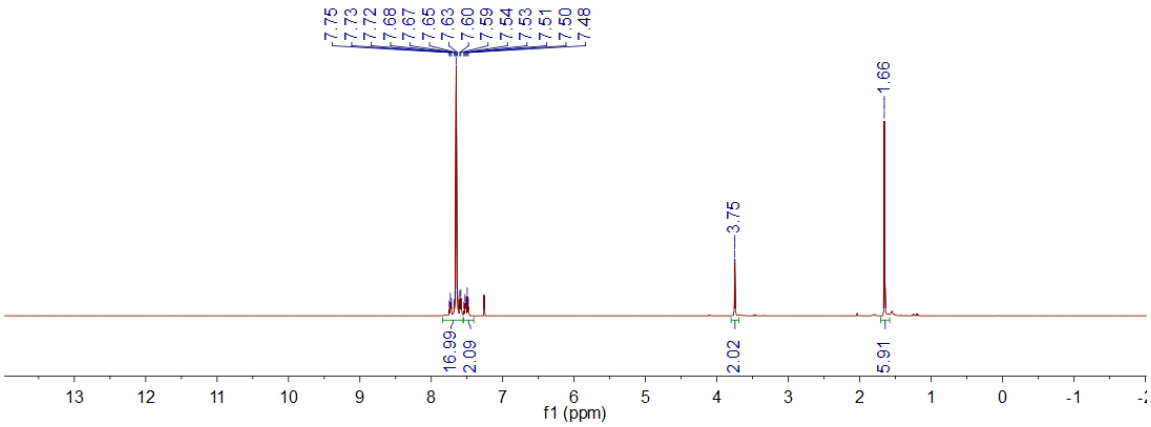

Figure 77. ^{1}H NMR spectrum of [**75**][OTf] in $CDCl_3$.

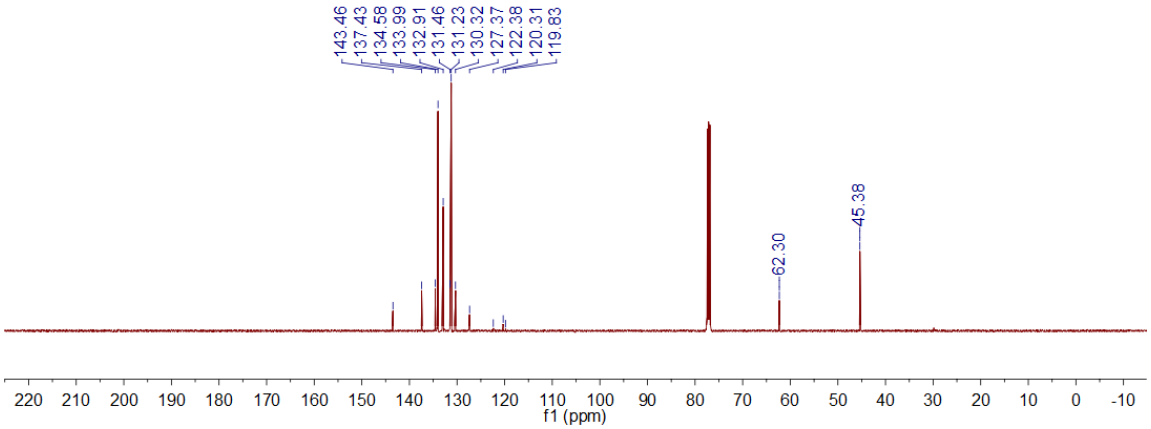

Figure 78. $^{13}C\{^{1}H\}$ NMR spectrum of [**75**][OTf] in $CDCl_3$.

4.5.1.4 Synthesis of $[Sb(C_6F_5)_4][SbCl_6]$ ([**2**][$SbCl_6$])

A $SbCl_5$ (41 mg; 0.14 mmol) solution in CH_2Cl_2 (*ca* 1 mL) prepared in a glovebox was cannulated into a Schlenk vessel containing a solution of $Sb(C_6F_5)_4Cl$ (102 mg; 0.12 mmol) in CH_2Cl_2 (*ca* 3 mL), resulting in copious amounts of white precipitate, which was stirred for 30 minutes, filtered by cannulation and washed with CH_2Cl_2 (*ca* 3 mL). The

solid was dried under a dynamic vacuum overnight, yielding 101 mg (73 % recovered yield based on $Sb(C_6F_5)_4Cl$) of the stibonium salt as a very light fibrous white solid. The compound is virtually insoluble in chloroform, very sparingly soluble in CH_2Cl_2 and soluble in acetonitrile. [**2**][$SbCl_6$]: ^{19}F NMR(470 Hz, CD_3CN): δ = -123.3 (*o*-F), -141.4 (*p*-F), -157.2 (*m*-F). ^{13}C NMR(100 Hz, CD_3CN): δ = 148.9 (dm J_{C-F} = 252 Hz), 147.3 (dtm J_{C-F} = 269 Hz), 139.6 (dm, J_{C-F} = 257 Hz), 104.2 (bs, *C*-Sb). Elemental analysis calculated (%): C, 25.64; found: C, 25.46.

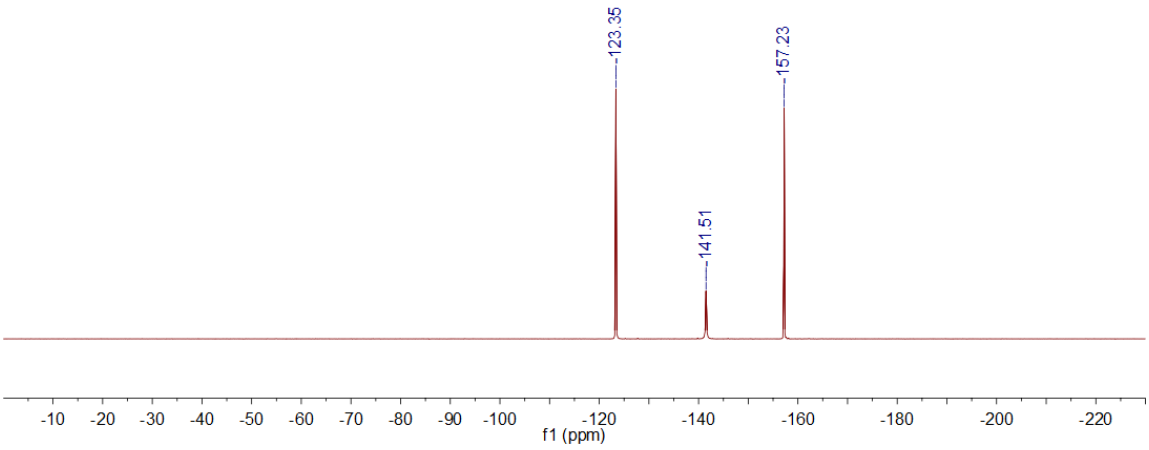

Figure 79. ^{19}F NMR spectrum of [**2**][$SbCl_6$] in CD_3CN.

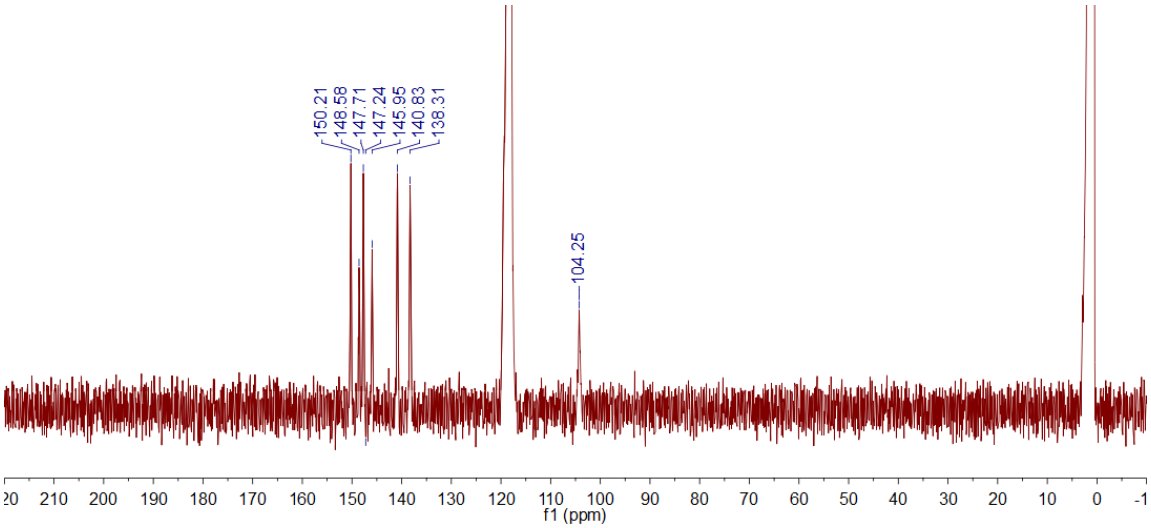

Figure 80. $^{13}C\{^{1}H\}$ NMR spectrum of [**2**][$SbCl_6$] in CD_3CN.

4.5.2 Catalytic cycloaddition of oxiranes and isocyanates

Stock solutions of catalyst (0.09 mmol/mL) and co-catalyst TBABr (0.09 mmol/mL) were prepared in $CDCl_3$. In a typical experiment, an NMR tube was loaded with neat $CDCl_3$ (0.4 mL) and combined with 0.1 mL (9 μmol) of the catalyst and co-catalyst stock solutions and neat propylene oxide (95 μL, 1.35 mmol). Phenyl isocyanate (10 μL, 0.09 mmol) was added to the NMR tube which was sealed and kept at 40°C for 18 h. The reaction yield was determined by ^{1}H NMR spectroscopy using resonances from the tetrabutylammonium cation as the internal standard. Each experiment was reproduced 2-4 times and the results were averaged over the multiple trials. The same general protocol was used for all other NMR scale reactions summarized in Table 11 and Table 12.

4.5.2.1 *In situ* NMR spectra collected during the experiments presented in Table 11.

The formation of the products was monitored by ^{1}H NMR *in situ*. The integration of the resonance at 3.0 ppm (m, 12H) of the tetrabutylammonium cation was used as a standard. The yield of the major isomer A was calculated based on the integration of two resonances: 4.4 ppm (m, 2H) and 3.8 ppm (m, 1H). The yield of the minor isomer B was calculated based on the integration of three resonances: 4.6 ppm (m, 1H), 4.0 ppm (t, 1H), and 3.5 ppm (dd, 1H). An impurity in the reaction mixture gives three resonances in the 2.5 – 5.0 ppm region, two of which overlap with isomer A: 4.7 ppm (1H), 4.4 ppm (1H) and 3.8 ppm (1H). Additionally, no reaction took place when catalysts [**74**][OTf] and [**75**][OTf] were mixed with a stoichiometric amount of propylene oxide in $CDCl_3$ over the course of 12 hours at 40°C.

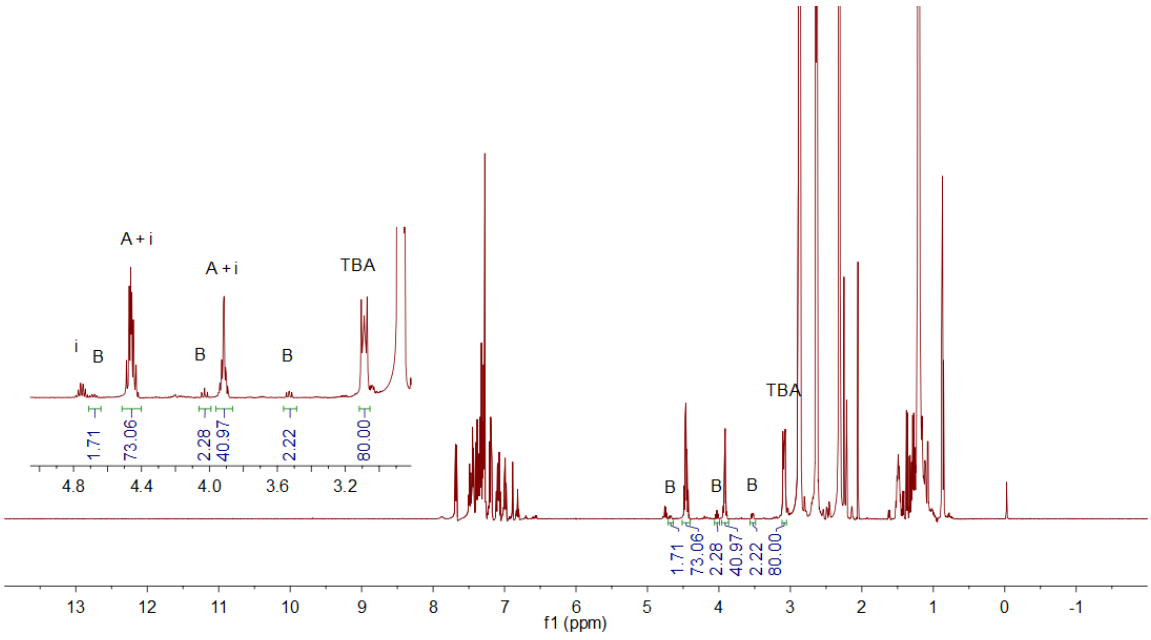

Figure 81. Representative ^{1}H NMR spectrum collected during the experiment presented in Table 11, Entry 4.

4.5.2.2 *In situ* NMR spectra collected during the experiments presented in Table 12.

***In situ* NMR spectrum of Table 12, Entries 1-2.** The formation of the products was monitored by ^{1}H NMR *in situ*. The integration of the resonance at 1.5 ppm (m, 12H) of the tetrabutylammonium cation was used as a standard. The yield of the major isomer A was calculated based on the integration of three resonances: 5.4 ppm (dd, 1H), 4.7 ppm (t, 1H), and 4.2 ppm (dd, 1H). The yield of the minor isomer B was calculated based on the integration of three resonances: 5.6 ppm (dd, 1H), 4.7 ppm (t, 1H), and 4.3 ppm (dd, 1H).

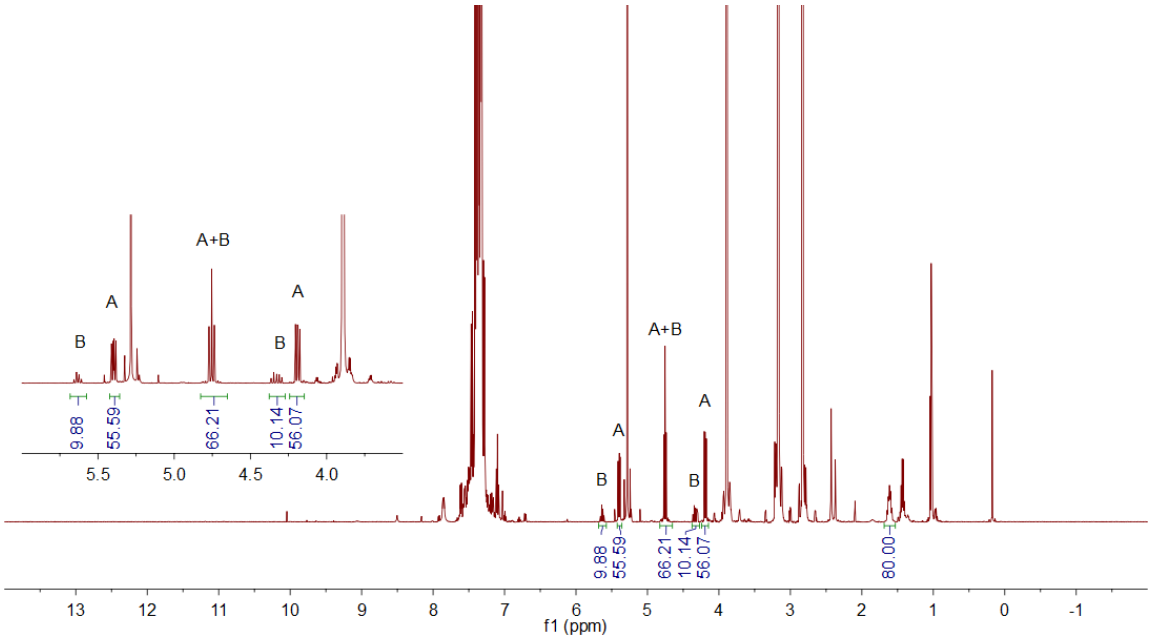

Figure 82. Representative ^{1}H NMR spectrum collected during the experiment presented in Table 12, Entry 2.

***In situ* NMR spectrum of Table 12, Entries 3-4.** The formation of the products was monitored by ^{1}H NMR *in situ*. The integration of the resonance at 3.0 ppm (m, 12H) of the tetrabutylammonium cation was used as a standard. The yield of the major isomer A was calculated based on the integration of three resonances: 4.5 ppm (t, 1H), 4.4 ppm (m, 1H), and 3.9 ppm (dd, 1H). The yield of the minor isomer B was calculated based on the integration of three resonances: 4.7 ppm (m, 1H), 4.0 ppm (t, 1H), and 3.5 ppm (dd, 1H). An impurity in the reaction mixture gives three resonances in the 2.5 – 5.0 ppm region, one of which overlaps with isomer A: 4.8 ppm (m, 1H), 4.5 ppm (t, 1H) and 3.9 ppm (dd, 1H).

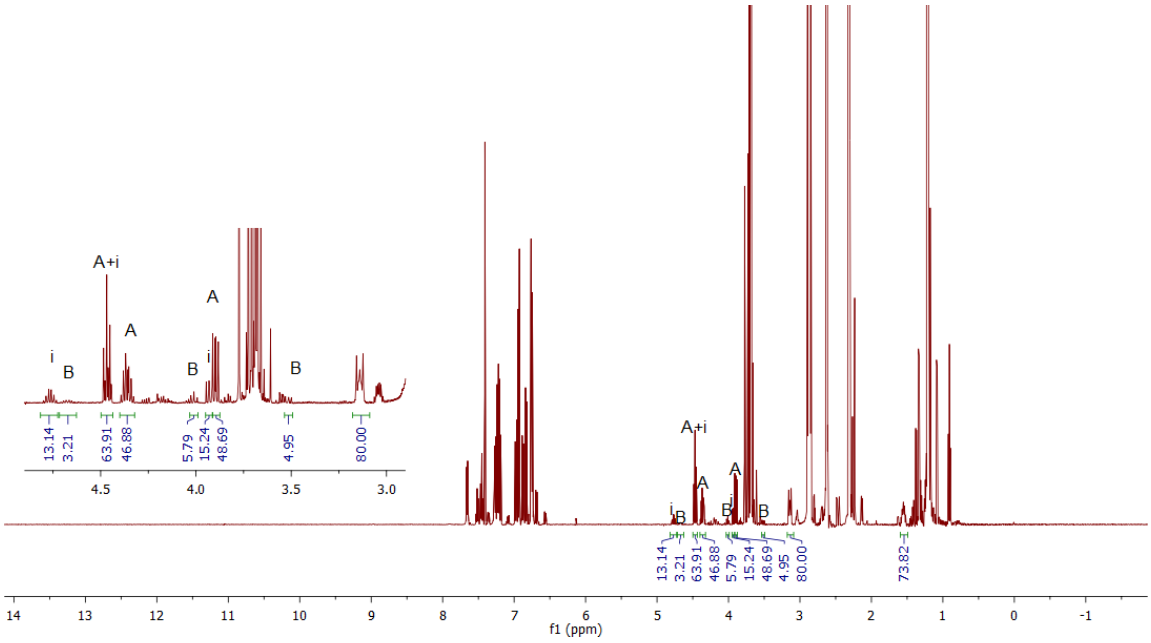

Figure 83. Representative ^{1}H NMR spectrum collected during the experiment presented in Table 12, Entry 4.

***In situ* NMR spectrum of Table 12, Entries 5-6.** The formation of the products was monitored by ^{1}H NMR *in situ*. The integration of the resonance at 3.0 ppm (m, 12H) of the tetrabutylammonium cation was used as a standard. The yield of the major isomer A was calculated based on the integration of three resonances: 4.4 ppm (m, 1H), 4.3 ppm (t, 1H), and 3.8 ppm (dd, 1H). The yield of the minor isomer B was calculated based on the integration of three resonances: 4.6 ppm (m, 1H), 4.0 ppm (t, 1H), and 3.4 ppm (dd, 1H).

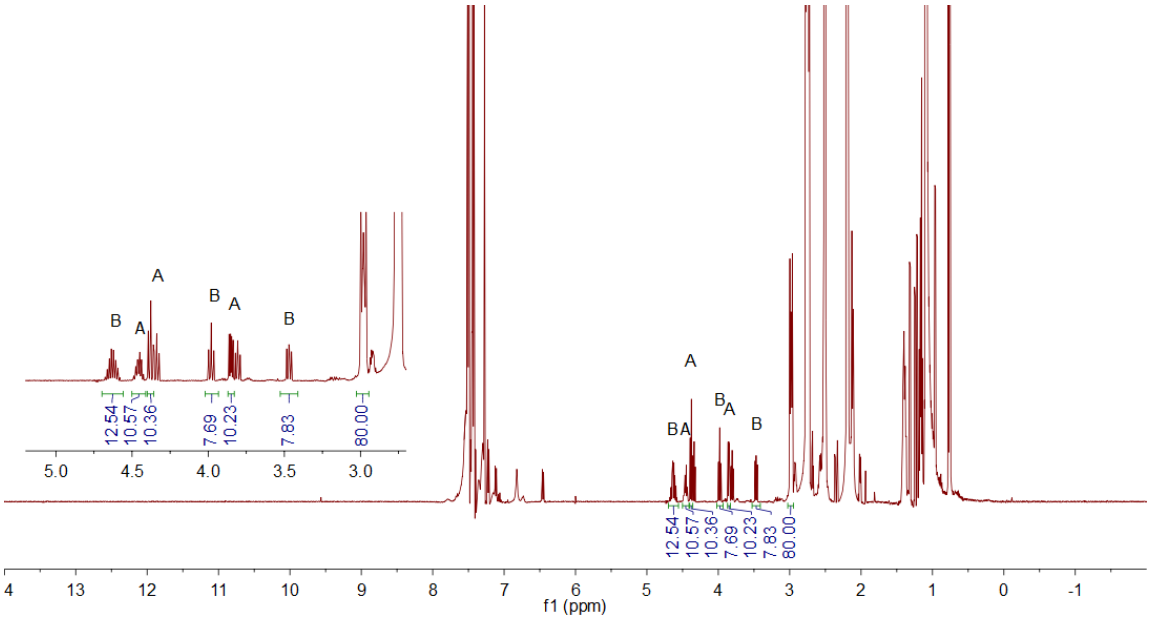

Figure 84. Representative ^{1}H NMR spectrum collected during the experiment presented in Table 12, Entry 6.

4.5.2.3 Catalytic cycloaddition of propylene oxide and phenyl isocyanate

To a stirred solution containing [**73**][OTf] (150 mg, 0.24 mmol, 0.1 eq) and TBABrr (77 mg, 0.24 mmol, 0.1 eq) in CH_2Cl_2 (5 mL), was added propylene oxide (2.5 mL, 36 mmol, 15 eq) and phenyl isocyanate (286 mg, 2.4 mmol, 1 eq). The reaction was stirred in a 40 °C bath for 18 h under N_2. An aliquot was taken from the reaction mixture and the yield of the two regioisomeric oxazolidinones was determined by ^{1}H NMR spectroscopy. The crude reaction mixture was subjected to flash chromatography over silica gel (3% ethyl acetate in hexanes). The third major fraction (very close to the second one) was collected washed with diethyl ether to afford product 5-methyl-3-phenyl-2-oxazolidinone (**69B**) as white powder (16 mg, 4%), and the fourth major fraction was collected to afford product 4-methyl-3-phenyl-2-oxazolidinone (**69A**) as colorless oil (170 mg, 40%). Spectral data of **69A** and **69B** are in accord with the previous report.[105]

4.5.2.4 Catalytic cycloaddition of styrene oxide and phenyl isocyanate

To a stirred solution of catalyst [**73**][OTf] (125 mg, 0.20 mmol, 0.1 eq), co-catalyst TBABr (65 mg, 0.20 mmol, 0.1 eq) in CH_2Cl_2 (5 mL) was added styrene oxide (3.5 mL, 30 mmol, 15 eq) and phenyl isocyanate (243 mg, 2.0 mmol, 1 eq). The reaction was stirred in a 40 °C bath for 18 h under N_2. An aliquot was taken from the reaction mixture and the yield of two regioisomeric oxazolidinones was determined by ^{1}H NMR spectroscopy. The reaction mixture was treated to flash chromatography over silica gel (gradient 0-50% ethyl acetate in hexanes) and the third major fraction was collected and treated again to flash chromatography over silica gel (gradient 5-20% ethyl acetate in hexanes). The third major

fraction was collected and recrystallized with diethyl ether to afford product 3,5-diphenyl-2-oxazolidinone (**78B**) as white powder (16 mg, 3%), and the fourth major fraction was collected and washed with hexanes to afford product 3,4-diphenyl-2-oxazolidinone (**78A**) as white powder (210 mg, 43%). Spectral data are in accord with the previous report.[105]

4.5.3 Crystallographic measurements

All crystallographic measurements were performed at 110(2) K using a Bruker SMART APEX II diffractometer with a CCD area detector (graphite monochromated Mo-Kα radiation, λ = 0.71073 Å) at 110 K. In each case, a specimen of suitable size and quality was selected and mounted onto a nylon loop. The semiempirical method *SADABS* was applied for absorption correction. The structures were solved by direct methods and refined by the full-matrix least-squares technique against F^2 with the anisotropic temperature parameters for all non-hydrogen atoms. All H-atoms were geometrically placed and refined in riding model approximation. Data reduction and further calculations were performed using the Bruker *SAINT* and *SHELXTL-NT* program packages. [157] Single crystals of [**71**][OTf] suitable for X-ray diffraction were obtained by slow evaporation of hexanes into a $CDCl_3$ solution in air.

Table 13. Crystallographic and structure refinement details for [**71**][OTf] and [**73**][OTf].

Compound	**[71][OTf]**	**[73][OTf]**
Empirical formula	C_{29} H_{22} F_3 O_3 S Sb	C_{28} H_{26} F_3 O_3 S Sb
Formula weight	629.27	621.30
Temperature	110 K	110 K
Wavelength	0.71073 Å	0.71073 Å
Crystal system	Monoclinic	Monoclinic
Space group	*C* 1 2/*c* 1	*P* 1 2_1/*n* 1
Unit cell dimensions	a = 14.848(7) Å b = 14.208(7) Å c = 24.673(17) Å α = 90°. β = 102.698(9)°. γ = 90°.	a = 11.4672(4) Å b = 19.4493(8) Å c = 11.7980(5) Å α = 90°. β = 95.029(2)°. γ = 90°.
Volume	5078(5) $Å^3$	2621.17(18) $Å^3$
Z	8	4
Density (calculated)	1.646 Mg/m^3	1.574 Mg/m^3
Absorption coefficient	1.221 mm^{-1}	1.181 mm^{-1}
F(000)	2512	1248
Crystal size	0.42 x 0.3 x 0.1 mm^3	0.36 x 0.29 x 0.1 mm^3
Theta range for data collection	2.296 to 27.447°.	2.025 to 27.900°.
Index ranges	-18< = h< = 18, -18< = k< = 18, -31< = l< = 31	-15< = h< = 15, -25< = k< = 25, -15< = l< = 15
Reflections collected	78867	96586
Independent reflections	5413 [R(int) = 0.0800]	6238 [R(int) = 0.0997]
Completeness to theta = 25.242°	99.9 %	100.0 %
Absorption correction	Semi-empirical from equivalents	Semi-empirical from equivalents
Max. and min. transmission	0.7455 and 0.5966	0.7456 and 0.6324
Refinement method	Full-matrix least-squares on F^2	Full-matrix least-squares on F^2
Data / restraints / parameters	5413 / 121 / 437	6238 / 0 / 328
Goodness-of-fit on F2	1.025	1.009
Final R indices [I>2sigma(I)]	R1[a] = 0.0400, wR2[b] = 0.0761	R1[a] = 0.0352, wR2[b] = 0.0756
R indices (all data)	R1 = 0.0769, wR2 = 0.0904	R1 = 0.0648, wR2 = 0.0885
Extinction coefficient	n/a	n/a
Largest diff. peak and hole	0.575 and -0.538 e.$Å^{-3}$	0.742 and -1.319 e.$Å^{-3}$

[a] $R1 = \Sigma||F_o| - |F_c||/ \Sigma|F_o|$. [b] $wR2$ $([w(F_o^2 - F_c^2)^2]/[\Sigma w(F_o^2)^2])^{1/2}$; $w = 1/[\sigma^2(F_o^2) + (ap)^2 + bp]$; $p = (F_o^2 + 2F_c^2)/3$ with a = 0.02430 and b = 20.4903 for [**71**][OTf], and a = 0.0370 and b = 4.2008 for[**73**][OTf].

Table 14. Crystallographic and structure refinement details for [**74**][OTf] and [**75**][OTf].

Compound	**[74][OTf]**	**[75][OTf]**
Empirical formula	C_{27} H_{25} F_3 N O_3 S Sb	C_{28} H_{27} F_3 N O_3 S Sb
Formula weight	622.29	636.31
Temperature	110.0 K	110.0 K
Wavelength	0.71073 Å	0.71073 Å
Crystal system	Orthorhombic	Monoclinic
Space group	Pbca	*P* 1 2_1/c 1
Unit cell dimensions	a = 18.642(2) Å b = 14.0067(18) Å c = 19.752(2) Å α = 90°. β = 90°. γ = 90°.	a = 9.9453(7) Å b = 11.0052(8) Å c = 25.4792(17) Å α = 90°. β = 101.217(4)°. γ = 90°.
Volume	5157.5(10) $Å^3$	2735.4(3) $Å^3$
Z	8	4
Density (calculated)	1.603 Mg/m^3	1.545 Mg/m^3
Absorption coefficient	1.202 mm^{-1}	1.135 mm^{-1}
F(000)	2496	1280
Crystal size	0.45 x 0.05 x 0.04 mm^3	0.55 x 0.1 x 0.1 mm^3
Theta range for data collection	2.062 to 27.974°.	1.630 to 27.696°.
Index ranges	-24< = h< = 24, -18< = k< = 18, -25< = l< = 25	-12< = h< = 12, -14< = k< = 14, -33< = l< = 33
Reflections collected	114700	87657
Independent reflections	6139 [R(int) = 0.1617]	6349 [R(int) = 0.1112]
Completeness to theta = 25.242°	100.0 %	100.0 %
Absorption correction	Semi-empirical from equivalents	Semi-empirical from equivalents
Max. and min. transmission	0.7456 and 0.5849	0.7455 and 0.5519
Refinement method	Full-matrix least-squares on F^2	Full-matrix least-squares on F^2
Data / restraints / parameters	6139 / 0 / 328	6349 / 205 / 392
Goodness-of-fit on F^2	1.049	1.171
Final R indices [I>2sigma(I)]	$R1^a$ = 0.0448, $wR2^b$ = 0.1024	$R1^a$ = 0.0991, $wR2^b$ = 0.1890
R indices (all data)	R1 = 0.0722, wR2 = 0.1220	R1 = 0.1296, wR2 = 0.2027
Extinction coefficient	0.00058(14)	0.0014(3)
Largest diff. peak and hole	1.445 and -1.334 e.$Å^{-3}$	1.332 and -1.787 e.$Å^{-3}$

^{a}*R1* = $\Sigma||F_o| - |F_c||/ \Sigma|F_o|$. ^{b}*wR2* $([w(F_o^2 - F_c^2)^2]/[\Sigma w(F_o^2)^2])^{1/2}$; $w = 1/[\sigma^2(F_o^2) + (ap)^2 + bp]$; $p = (F_o^2 + 2F_c^2)/3$ with a = 0.00313 and b = 14.5167 for[**74**][OTf] and a = 0.0001 and b = 35.9234 for[**75**][OTf].

Table 15. Crystallographic and structure refinement details for [**2**][$SbCl_6$].

Compound	**[2][$SbCl_6$]**
Empirical formula	C_{24} Cl_6 F_{20} Sb_2
Formula weight	1124.44
Temperature	150(2) K
Wavelength	0.71073 Å
Crystal system	Monoclinic
Space group	P 1 2_1 1
Unit cell dimensions	a = 17.482(4) Å b = 21.716(5) Å c = 19.115(4) Å a = 90°. b = 116.456(6)°. g = 90°.
Volume	6497(3) $Å^3$
Z	8
Density (calculated)	2.299 Mg/m^3
Absorption coefficient	2.292 mm^{-1}
F(000)	4224
Crystal size	0.426 x 0.186 x 0.092 mm^3
Theta range for data collection	1.19 to 30.66°.
Index ranges	-25< = h< = 24, -30< = k< = 31, -27< = l< = 27
Reflections collected	159165
Independent reflections	39702 [R(int) = 0.1041]
Completeness to theta = 25.242°	99.1 %
Absorption correction	Semi-empirical from equivalents
Max. and min. transmission	0.82 and 0.66
Refinement method	Full-matrix least-squares on F^2
Data / restraints / parameters	39702 / 1 / 1874
Goodness-of-fit on F^2	1.005
Final R indices [I>2sigma(I)]	$R1^a$ = 0.0472, $wR2^b$ = 0.0922
R indices (all data)	R1 = 0.0823, wR2 = 0.1167
Extinction coefficient	0.143(16)
Largest diff. peak and hole	1.079 and -1.346 e.$Å^{-3}$

$^a R1 = \Sigma||F_o| - |F_c||/ \Sigma|F_o|$. $^b wR2$ $([w(F_o^2 - F_c^2)^2]/[\Sigma w(F_o^2)^2])^{1/2}$; $w = 1/[\sigma^2(F_o^2) + (ap)^2 + bp]$; $p = (F_o^2 + 2F_c^2)/3$ with a = 0.0407 and b = 0.00 for[**2**][$SbCl_6$].

4.5.4 Computational details

Structures are optimized by Gaussian 09 program[158] using density functional theory (DFT) methods with the M06-2X functional[172] and mixed basis sets (cc-pVTZ-

pp[161] with CRENBL ECP[162] for Sb, 6-31+g(d') for H, C, N), starting from the crystal structure geometries if available. No imaginary frequencies were found for the optimized structures, confirming that a local minimum on its potential energy hypersurface had been reached. The optimized structures were also subjected to natural bond orbital (NBO)[147] analysis, and the resulting NBOs were plotted using the Jimp2[163] program.

CHAPTER V

CATALYTIC TRANSFER HYDROGENATION BY BIFUNCTIONAL PNICTOGEN-BASED LEWIS ACIDIC DICATIONS

5.1 Introduction

Group 15 Lewis acids are attracting a growing interest in the field of small molecule activation and catalysis. The unique acidity displayed by these compounds arise from low-lying σ* orbitals located on the central atom. From an electrostatic perspectives, the Lewis acidity can also be seen as arising from σ-holes, an area of positive potential whose location typically corresponds to the area where the σ* orbital features its largest lobe. [7, 9, 11, 206] Bifunctional Lewis acids display increased reactivity when compared to their monofunctional analogs because of cooperative effects. These cooperative effects are illustrated by the properties of 1,8-naphthalenediylbis(dimethylborane) (**50**),[112] a diborane that abstracts hydride from a variety of borohydrides to form a stable bridging hydride complex (Figure 85). Our group has reported a series of bifunctional Lewis acids such as the borane-phosphonium (**39**$^+$) which behaves as a fluoride complexing agent (Figure 85).[5] Similar properties have also been found for a series of diboranes as well as bis-antimony(V) compounds based on dimethylxanthene,[4] triptycene[30] or biphenylene[207] backbones. Besides their high affinity for small anions, bifunctional Lewis acids have also been shown to activate carbonyl substrates. Maruoka *et al*. reported in 2004 that a dialuminum Lewis acid on the 1,8-biphenylene backbone (**51**) facilitates the reduction of ketones due to chelation effects (Figure 85).[113] These results inspired additional

applications in Lewis acid catalysis with bifunctional systems. For example, Stephan *et al*. reported that bis-fluorophosphonium compounds[117] supported by 1,8-naphthalenediyl (**54**$^{2+}$)[116] are potent catalysts for a variety of organic transformations including the Friedel–Crafts dimerization of 1,1-diphenylethylene, hydrodefluorination of fluoroalkanes and the deoxygenation of ketones (Figure 85). Our group reported an *ortho*-phenylene based bis-stibonium (**83**$^{2+}$) which catalyzes the hydrosilylation of benzaldehyde. A previous group member was able to isolate, [**83**-η_2-DMF]$^{2+}$, a complex that was crystallographically characterized and which showed that the carbonyl oxygen atom simultaneously interacting with the two antimony centers (Figure 85).[131] Recently, Matile *et al*. reported that dithienothiophenes such as **53** behave as chalcogen-bond donors and catalyze the transfer hydrogenation of quinolines in the presence of Hantzsch-ester. Computational studies analysis suggest that the nitrogen lone pair on the pyridine substrate can bridge the two group 16 center and as a result, experience a greater electrophilic activation (Figure 85).[115] In this chapter, we explore the possibility of similar phenomena in the chemistry of *ortho*-phenylene-based bis-pnictogen cations.

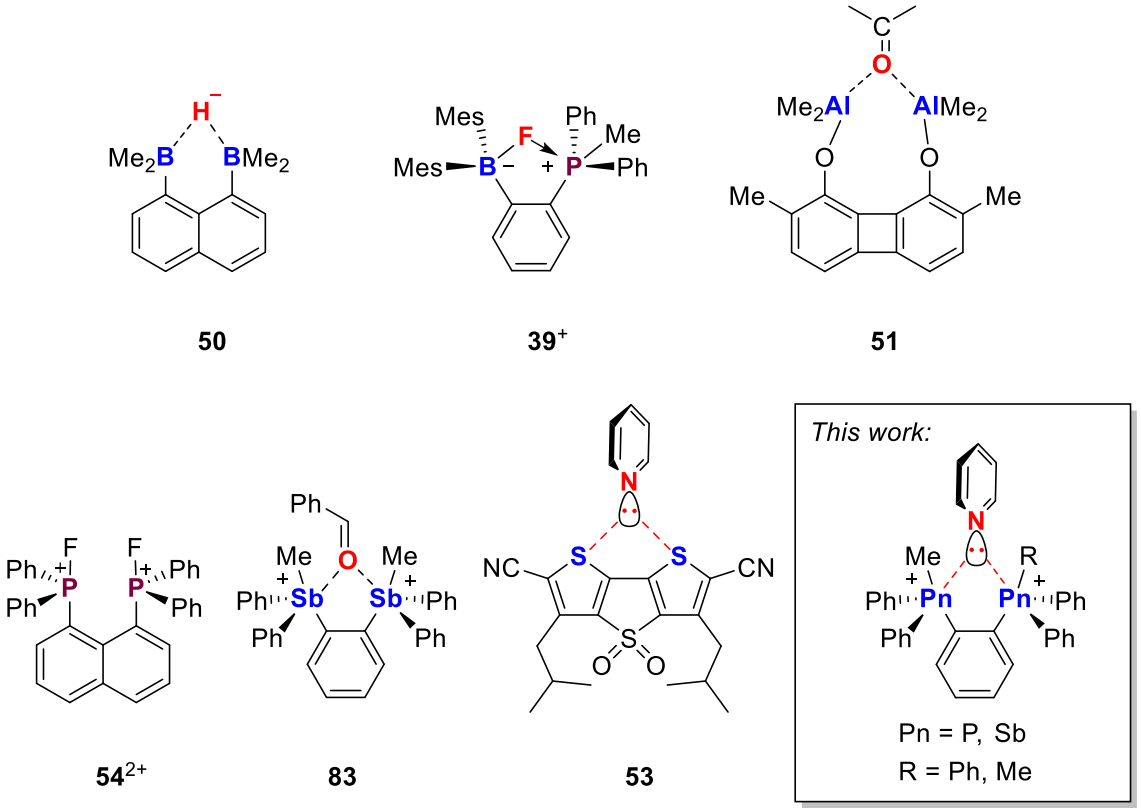

Figure 85. Bifunctional Lewis acids in small molecule complexation or in catalysis.

5.2 Background

A former group graduate, Dr. Masato Hirai, reported in his dissertation the syntheses of cations **81**$^{+}$ and **82**$^{2+}$ partially with the intention to explore the potential of pnictogen-containing ambiphilic compounds and their use in frustrated Lewis pair (FLP) chemistry.[208] He synthesized the phosphino-stibonium bromide **81**-Br by the reaction of 2-lithio(diphenylphosphino)benzene with Ph_3SbBr_2 in a mixture of Et_2O/THF at -78 °C (Figure 86). Treatment of [**81**]Br with AgOTf afforded the triflate salt [**81**][OTf], and single-crystal X-ray established that the cationic antimony center is well separated from

the counteranion. Reaction of [**81**][OTf] with excess MeOTf afforded the oxidized dication [**82**][OTf]$_2$ (Figure 86). In the crystal structure of [**82**][OTf]$_2$, while one triflate anion is free from short contacts, the other weakly interacts with the antimony center resulting in a Sb-O separation of 2.871(7) Å, indicating the enhanced acidity of the antimony center of **82**$^{2+}$ compared to that in **81**$^{+}$. The coordination chemistry of [**81**]Br and [**81**][OTf] with gold chloride was subsequently discussed in this previous study.[208]

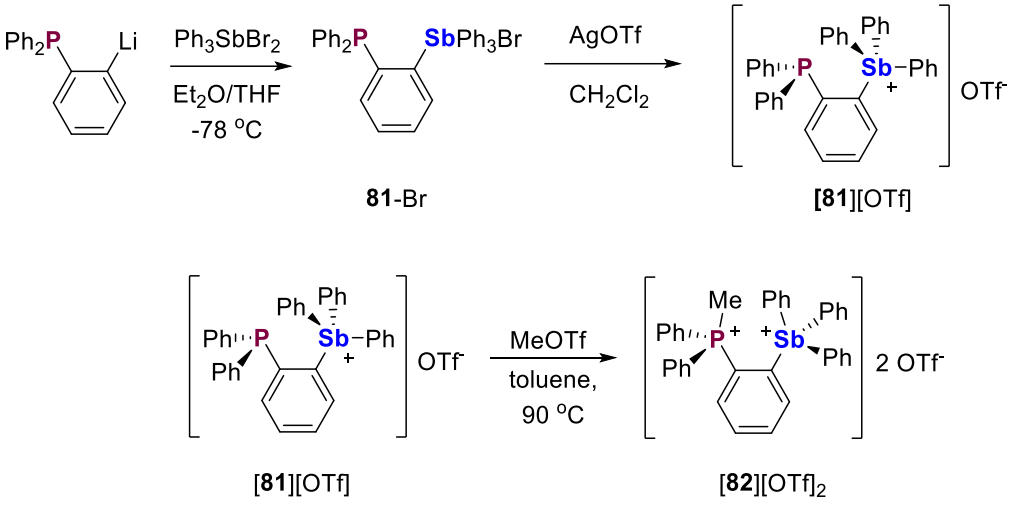

Figure 86. Reported synthesis of the stibonium [**81**]$^{+}$ and the phosphonium-stibonium dication [**82**]$^{2+}$ as triflate salts.

5.3 Synthesis of the cations containing Group 15 elements

With this existing series of *ortho*-phenylene based cations in hand, aiming to systematically study the catalytic activity of these cations, we prepared the monofunctional compounds [Ph$_4$Sb][BF$_4$] ([**70**][BF$_4$])[209] and [Ph$_3$MeP][BF$_4$]

([**79**][BF_4])[210] which have both been previously described. We also synthesized the tetrafluoroborate salts of the cations **80**$^+$, **81**$^+$ and **82**$^{2+}$ which are all based on the *ortho*-phenylene backbone. Treatment of the known compound *o*-(Ph_2P)$C_6H_4SbPh_2$[211] with methyl iodide results in the iodine salt of the phosphonium monocation [*o*-($MePPh_2$)$C_6H_4SbPh_2$]I (**80**-I) (Figures 91-93), which is subsequently subjected to an anion exchange process with $NaBF_4$ to afford the tetrafluoroborate salt [**80**][BF_4] (Figures 87, 94-96). The tetrafluoroborate salt of the stibonium monocation [*o*-(PPh_2)$C_6H_4SbPh_3$]$^+$ (**81**$^+$) was synthesized by treatment of the corresponding bromide **81**-Br with the halide abstractor $AgBF_4$ (Figures 87, 97-99). Similar to the methylation of [**81**][OTf], [**81**][BF_4] can be readily methylated by trimethyloxonium tetrafluoroborate to generate the corresponding dication [*o*-($MePPh_2$)$C_6H_4SbPh_3$][BF_4]$_2$ ([**82**][BF_4]$_2$) in 80% yield (Figures 87, 100-102). Compared with the ^{31}P chemical shift in triphenylphosphine (-6.0 ppm), the ^{31}P NMR signal shifts downfield to 19.0 ppm in **81**-Br, then further downfield to 11.3 ppm in [**81**][BF_4], suggesting an enhanced donor-acceptor interaction between the lone pair of the phosphine moiety to the empty Sb-C_{Ph} σ* orbital. Consistent with the presence of this interaction, the ^{13}C NMR spectrum of **81**$^+$ features the $^2J_{C\text{-}P}$ coupling of 11.6 Hz of the quaternary carbon of antimony-bound phenyl rings, larger than that of 6.6 Hz in **81**-Br. This donor-acceptor interaction ceased to exist once the phosphonium center is oxidized into [**82**]$^{2+}$. The ^{31}P NMR signal of **82**$^{2+}$ is a singlet at 26.5 ppm in [**82**][BF_4]$_2$, more downfield compared to that of **80**$^+$ (11.3 ppm) and **81**$^+$ (25.2 ppm). The characteristic ^{1}H NMR resonance of the methyl protons appear at 2.50 ppm for [**82**][BF_4]$_2$ in $CDCl_3$. The

methyl resonance in both salts features a $^{2}J_{P\text{-}H}$ coupling constant of 13.3 Hz with the proximate phosphorus atom.

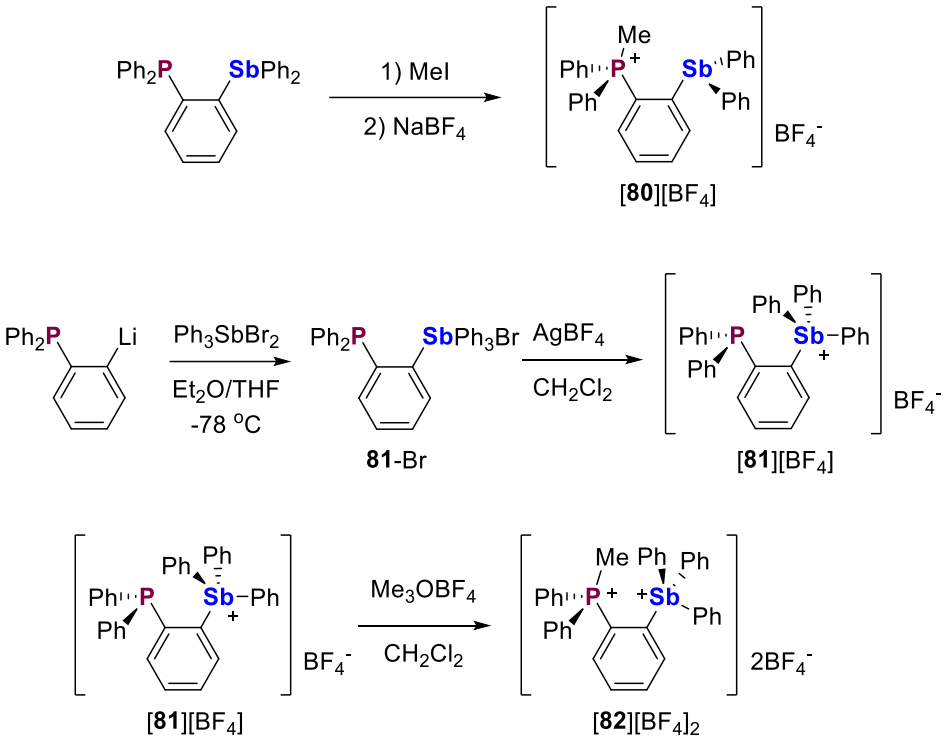

Figure 87. Synthesis of the phosphonium **80**$^{+}$, the stibonium **81**$^{+}$, and the phosphonium-stibonium dication **82**$^{2+}$ as tetrafluoroborate salts.

Single crystals of [**80**][BF_4] - [**82**][BF_4]$_2$ could be obtained by diffusing hexanes into $CDCl_3$ or CH_2Cl_2 solutions of these salts (Figure 88, Tables 17-18). The P-Sb distances in the crystal structure of [**80**][BF_4] and [**81**][BF_4] are 3.540 Å and 3.321(1) Å, respectively. Both distances are well within the sum of the covalent radii of the two elements (Σ_{vdWR}(P,Sb) = 4.37 Å),[146] suggesting donor-acceptor interactions between these

pnictogen centers. The stronger interaction in **81**$^{+}$ is corroborated by the P1-C2-C1 angle of 118.3(3)°, as the phosphine moiety is tilted towards the antimony center. Because oxidation eliminates such donor-acceptor interactions, the inter-pnictogen distance becomes much larger in the structure of [**82**][BF_4]$_2$ (3.922(1) Å). The lengthening is also driven by steric and electronic repulsions between the adjacent cationic centers. While both **80**$^{+}$ and **81**$^{+}$ are free from short contacts with the triflate or tetrafluoroborate anions in the solid state, one of the two anions in [**82**][BF4]$_2$ interacts with the stibonium center with a Sb-F distance of 3.038(2) Å, pointing to the enhanced electrophilicity in this dication (Figure 88).

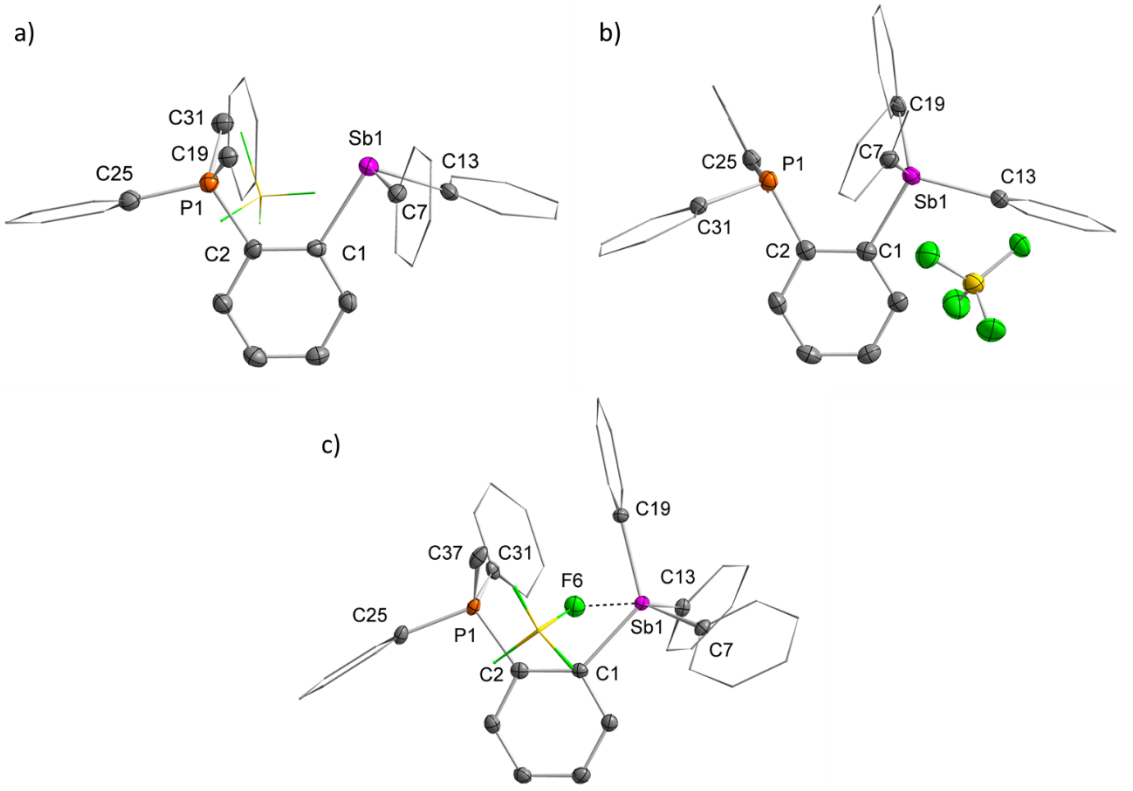

Figure 88. Crystal structure of a) [**80**][BF_4], b) [**81**][BF_4], and c) [**82**][BF_4]$_2$. Thermal ellipsoids ae drawn at the 50 % probability level. The hydrogen atoms and the free anions are omitted for clarity. Selected bond lengths (Å) and angles (deg) for [**80**][BF_4]: Sb1-P1 = 3.540(2), C1-Sb1-C7 = 96.1(2), C1-Sb1-C13 = 96.7(2), C7-Sb1-C13 = 98.5(2), C2-P1-C31 = 112.3(3), C2-P1-C19 = 107.6(3), C2-P1-C25 = 109.8(3), Sb1-C1-C2 = 122.7(4), P1-C2-C1 = 121.6(4); For [**81**][BF_4]: P1-Sb1 = 3.321(1), P1-Sb1-C13 = 161.3(1), C1-Sb1-C7 = 106.2(1), C1-Sb1-C19 = 113.3(1), C7-Sb1-C19 = 115.4(1), P1-C2-C1 = 118.3(3) Sb1-C1-C2 = 119.8(3); For [**82**][BF_4]$_2$: Sb1-P1 = 3.922(1), Sb1-F6 = 3.038(2), C1-Sb1-C7 = 106.4(1), C1-Sb1-C19 = 123.7(1), C7-Sb1-C13 = 108.3(1), C2-P1-C25 = 104.8(2), C2-P1-C31 = 107.6(2), C25-P1-C31 = 111.6(2), C2-C1-Sb1 = 132.7(3), C1-C2-P1 = 126.0(3).

The Pn(III)→Pn(V) bond present in **80**$^+$ and **81**$^+$ have been analyzed using the natural bond orbital (NBO) method which was implemented on the computationally optimized geometries of the cations. Both **80**$^+$ and **81**$^+$ show lp(Pn(III)) → σ*(Pn(V)-C) donor-acceptor interactions (Figure 89). This interaction is associated with a deletion energy E_{del} of 8.27 kcal/mol in **81**$^+$ and 1.01 kcal/mol in **80**$^+$. The higher stabilization energy in **81**$^+$ is consistent with the shorter P-Sb distance observed in the crystal structure of **81**$^+$. This feature can be explained by the higher basicity of the electron lone pair on phosphorus and the higher acidity of the cationic antimony center.

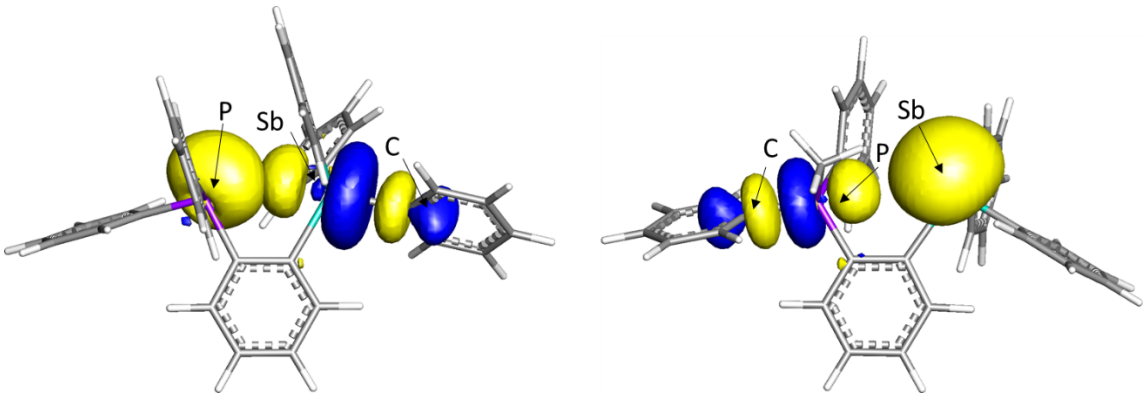

Figure 89. Principle donor-acceptor interactions present in **80**$^+$ (left) and **81**$^+$ (right). Isovalue = 0.05.

5.4 Catalytic transfer hydrogenation reactions

With compounds [**70**][BF_4] and [**79**][BF_4] - [**82**][BF_4]$_2$ in hand, we investigated their use as Lewis acid catalysts. Specifically, we tested these compounds, together with the reported bis-stibonium salt [**83**][BF_4]$_2$, as catalysts for the transfer hydrogenation

reaction known to occur between Hantzsch ester and 2-phenylquinoline (Figure 103).[148] This reaction was carried out in $CDCl_3$ with a 5 mol% catalyst loading. It is found that the bis-stibonium dication [**83**][BF_4]$_2$ afforded an almost quantitative yield of the amine product after 1 hour, followed by the phosphonium-stibonium dications [**82**][BF_4]$_2$ with a yield of 60% (Table 16, Entries 6-7). The monostibonium cations [**70**][BF_4] and [**81**][BF_4] display a moderate level of reactivity, resulting in a 26% and 24% conversion, respectively (Table 16, Entries 1, 4). The slight decrease of yield when **81**$^+$ was used as catalyst can be attributed to the donation from the *ortho*-phosphine that quenches the reactivity of the stibonium center. The monophosphonium cations [**80**][BF_4] and [**79**][BF_4] were essentially inactive (< 1%) (Table 16, Entries 2, 3). The fact that **83**$^{2+}$ is a better catalyst than **82**$^{2+}$, and that **81**$^+$ is a better catalyst than **80**$^+$, shows that cationic antimony centers are more potent than their phosphorous counterparts. This conclusion is well aligned with the intrinsic higher Lewis acidity for the heavier Group 15 elements. When these pnictogen cations were used for the transfer hydrogenation of 3-bromoquinoline using Hantzsch ester, reactivity trends consistent with that established for the 2-phenylquinoline substrate were observed (Figure 104, Table 16). In general, the dications are better catalysts than the monocations, the stibonium centers are better than the phosphonium centers, and the simple monocations are better than their corresponding *ortho*-phenylene-based pnictogen monocations featuring ancillary donors. The best catalysis result in the reaction was obtained with [**83**][BF_4]$_2$ which gave an 86% yield of the hydrogenation product after 10 minutes. It is also worth noting that the phosphonium-stibonium [**82**][BF_4] surpasses the monostibonium [**70**][BF_4] in both catalytic reactions.

Table 16. Transfer hydrogenation of 2-phenylquinoline and 3-bromoquinoline when the cations **70**$^{+}$ and **79**$^{+}$-**83**$^{2+}$ are used as catalysts.[a]

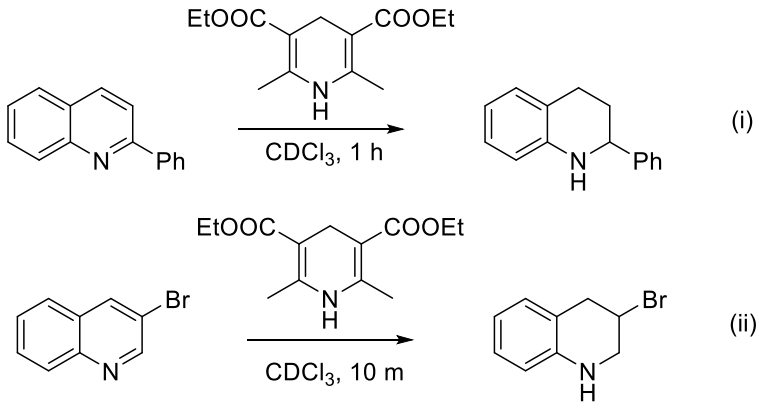

Entry	Cat.	Yield of rxn i	Yield of rxn ii
1	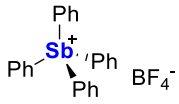	26%	60%
2	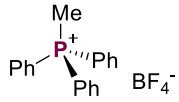	<1%	23%
3	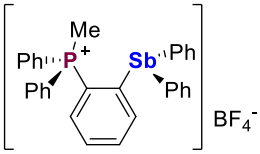	< 1%	< 1%
4	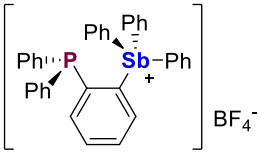	24%	51%
6	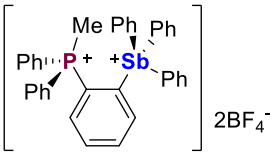	61%	76%
7	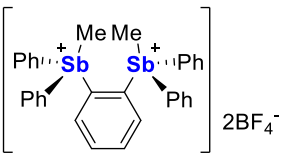	90%	86%
8	N/A	3%	< 1%

[a]Reaction conditions: catalyst loading with 10 mol% pnictogen centers. rt.

Lastly, DFT calculations were used to simulate the double electrophilic activation of the substrate. Optimizations were carried out in Gaussian 09 program [158] with the M062X[172] functional and mixed basis sets (cc-pVTZ-PP[161] with CRENBL ECP[162] for Sb, cc-pVTZ for P, 6-31g(d') for H, C, N, F, 6-311g* for S, Cl). Using **83**$^{2+}$ and pyridine as model molecules, a local minimum was found featuring a pyridine molecule chelated between the two cationic antimony centers (Figure 90). The calculated Sb-N distances are 3.146 Å and 3.063 Å, respectively. These distances are within the sum of van der Waals radii of the two elements (Σ_{vdWR}(Sb,N) = 4.13 Å).[146] NBO analysis[147] reveals a deletion energy of 8.6 kcal/mol involving two σ* orbitals of the antimony centers and the lone pair on the nitrogen atom of pyridine. This energy value is smaller than that of 12 kcal/mol calculated for the sum of the two lp(O) → σ*(Sb-C) interactions in [**83**-η_2-DMF]$^{2+}$, which is consistent with the lower nucleophilicity of pyridine compared to the carbonyl group of the DMF molecule.

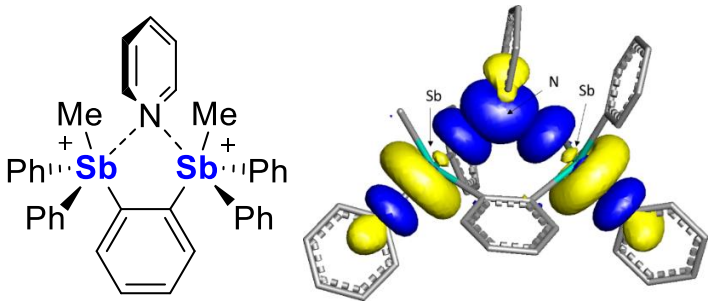

Figure 90. Double electrophilic activation of a pyridine substrate by **83**$^{2+}$.

5.5 Conclusion

In conclusion, we have synthesized a series of *ortho*-phenylene based mono- and bis-pnictogen compounds, and tested their catalytic activity in the transfer hydrogenation of quinoline derivatives using Hantzsch ester. Consistent with the Lewis acidity of these pnictogen cations, their catalytic activity follows the trend that dications are better than monocations, and stiboniums are better than phosphoniums. The best catalyst is found to be [**83**][BF_4]$_2$ that catalyzes the transfer hydrogenation of 2-phenylquinoline with a 90% conversion in 1 hour, and 3-bromoquinoline with a 86% conversion in 10 minutes. Computational analysis provided mechanistic insights and suggested that the bifunctional Lewis acids have the ability to doubly activate the pyridine substrate via the nitrogen atom.

5.6 Experimental section

Antimony compounds are potentially toxic and should be handled accordingly. Air-sensitive compounds were carried out using standard glovebox or Schlenk techniques in the absence of oxygen and moisture. All glassware was dried in oven and cooled under vacuum before use. 1,2-dibromo benzene and iodomethane were bought from Oakwood Chemical, 1-Bromo-2-Iodobenzene from ArkPharm, Tetrakis(triphenylphosphine)palladium from Strem Chemicals, trimethylamine from TCI America, *n*-n-Butyllithium (2.2 M in hexanes) from Alfa Aesar, triphenyl antimony from Milliporesigma, antimony trichloride from Acros, trimethyloxonium tetrafluoroborate from BeanTown Chemical, and all were used as received. Ph_2SbCl,[212] Ph_3SbBr_2,[182] (2-bromophenyl)diphenylphosphine,[213] [1,2-(Ph_2MeSb)$_2C_6H_4$][BF_4]$_2$[131], *o*-

(PPh_2)$C_6H_4SbPh_3Br$[208] and *o*-(Ph_2P)$C_6H_4SbPh_2$[211] were synthesized according to reported procedures. [Ph3SbMe][BF_4], [214] [Ph3PMe][BF_4],[210] *o*-Br-C_6H_4-$SbPh_2$,[215] and *o*-phenylene-bis(diphenylstibine)[215] were synthesized by a modifications of reported procedures. Solvents were dried by passing through an alumina column (*n*-pentane and CH_2Cl_2), heating to reflux under N_2 over Na/K (Et_2O, hexanes, and THF), or distilling from CaH_2 (1,2-dichloroethane). All other solvents were used as received. Deuterated solvents were bought from Cambridge Isotope. NMR spectra were recorded on a Varian Unity Inova 400 FT NMR (399.52 MHz for ^1H, 375.92 MHz for ^{19}F, 161.74 MHz for ^{31}P, 100.46 MHz for ^{13}C) or Varian Unity Inova 500 FT NMR (499.42 MHz for ^1H, 469.86 MHz for ^{19}F, 202.18MHz for ^{31}P, 125.60 MHz for ^{13}C) at ambient temperature. Chemical shifts (δ) are given in ppm and are referenced against residual solvent signals (^1H, ^{13}C) or external standards ($BF_3{\cdot}Et_2O$ for ^{19}F (-153 ppm), and 85% H_3PO_4 for ^{31}P (0 ppm)). Flash chromatography was performed using CombiFlash Rf + UV model with RediSep sample cartridges, 230-400 mesh silica gel, and commercial ACS reagent grade solvents. Elemental analyses were performed at Atlantic Microlab (Norcross, GA).

5.6.1 Syntheses

5.6.1.1 Synthesis of [*o*-($MePPh_2$)$C_6H_4SbPh_2$]I (**80**-I)

Methyl iodide (0.05 mL, 0.80 mmol) was added to a solution of *o*-(Ph_2P)$C_6H_4SbPh_2$ (210 mg, 0.4 mmol) in CH_2Cl_2 (10 mL). After stirring under N_2 at room temperature overnight, the solution was concentrated to a volume of 3 mL and added Et_2O (20 mL) to result a white precipitate, which was collected by filtration and washed with

Et_2O (2 × 5 mL) to afford [o-($MePPh_2$)$C_6H_4SbPh_2$]I as off-white solid (220 mg, 83% yield). The product appeared spectroscopically pure and was used as synthesized. [o-($MePPh_2$)$C_6H_4SbPh_2$]I: ^{1}H NMR (499 MHz, $CDCl_3$) δ 7.85 – 7.75 (m, 4H), 7.73 – 7.59 (m, 6H), 7.58 – 7.43 (m, 4H), 7.39 – 7.23 (m, 6H), 7.12 (d, J = 6.7 Hz, 4H), 3.41 (d, $J_{P\text{-}H}$ = 12.7 Hz, 3H). ^{13}C NMR (126 MHz, $CDCl_3$) δ 145.64 (d, $J_{C\text{-}P}$ = 17.7 Hz, Sb-bound *o*-phenylene quaternary), 141.13 (d, $J_{C\text{-}P}$ = 15.1 Hz, *o*-phenylene), 136.80 (d, $J_{C\text{-}P}$ = 15.2 Hz, , *o*-phenylene, overlapping with Sb*Ph* quaternary), 136.74 (s, Sb*Ph* quaternary, overlapping with *o*-phenylene), 135.96 (s, *o*-Sb*Ph*), 135.17 (d, $J_{C\text{-}P}$ = 3.0 Hz, *p*-P*Ph*), 134.92 (d, $J_{C\text{-}P}$ = 3.3 Hz, *o*-phenylene), 133.80 (d, $J_{C\text{-}P}$ = 10.5 Hz, *m*-P*Ph*), 130.62 (d, $J_{C\text{-}P}$ = 12.8 Hz, *o*-P*Ph*), 130.45 (d, $J_{C\text{-}P}$ = 12.9 Hz, *o*-phenylene), 129.58 (s, *p*-Sb*Ph*), 129.47 (s, *m*-Sb*Ph*), 126.92 (d, $J_{C\text{-}P}$ = 91.0 Hz, P-bound *o*-phenylene quaternary), 119.71 (d, $J_{C\text{-}P}$ = 87.1 Hz, P*Ph* quaternary), 14.11 (d, $J_{C\text{-}P}$ = 56.5 Hz P*C*H_3). ^{31}P NMR (162 MHz, $CDCl_3$) δ 23.9 (s).

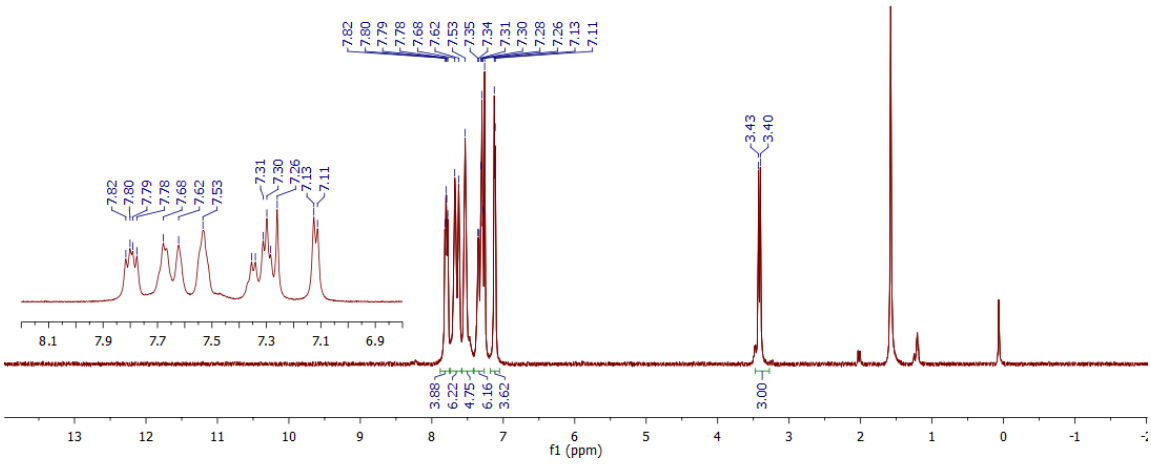

Figure 91. ^{1}H NMR spectrum of **80**-I in $CDCl_3$.

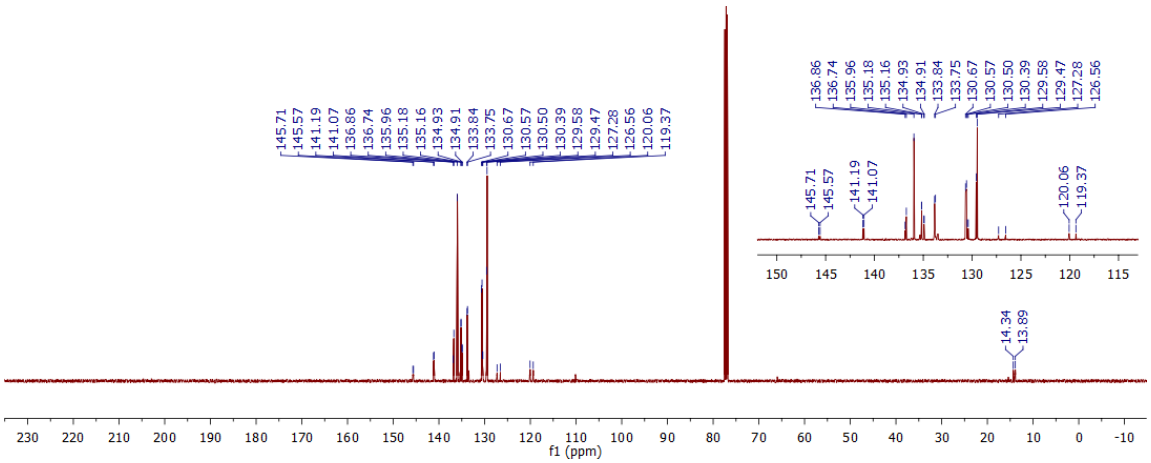

Figure 92. $^{13}C\{^{1}H\}$ NMR spectrum of **80**-I in $CDCl_3$.

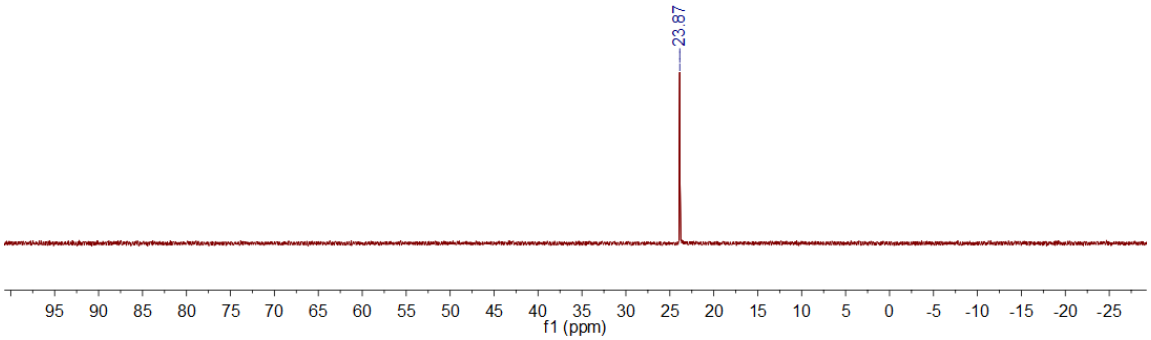

Figure 93. $^{31}P\{^{1}H\}$ NMR spectrum of **80**-I in $CDCl_3$.

5.6.1.2 Synthesis of [*o*-(MePPh$_2$)C$_6$H$_4$SbPh$_2$][BF$_4$] ([**80**][BF$_4$])

To the MeOH (20 mL) solution of [o-(MePPh$_2$)C$_6$H$_4$SbPh$_2$]I (500 mg, 0.74 mmol) was added a solution of excess NaBF$_4$ (650 mg, 5.93 mmol) in mixed solvents (15 mL, water: MeOH = 1: 1). The mixture was stirred for 4h, after which a white precipitate

formed and was collected by filtration. The precipitate was then dissolved into 20 mL of CH_2Cl_2 and passed through a celite plug. The final product was crashed out with Et_2O and dried *in vacuo* to afford [*o*-($MePPh_2$)$C_6H_4SbPh_2$][BF_4] as white powder (400 mg, 85% yield). Single crystals of [*o*-($MePPh_2$)$C_6H_4SbPh_2$][BF_4] were obtained as colorless blocks by diffusing hexanes into a $CDCl_3$ solution. [*o*-($MePPh_2$)$C_6H_4SbPh_2$][BF_4]: ^{1}H NMR (499 MHz, $CDCl_3$) δ 7.71 – 7.64 (m, 7H), 7.64 – 7.55 (m, 3H), 7.55 – 7.49 (m, 4H), 7.38 – 7.32 (m, 2H), 7.32 – 7.27 (m, 4H), 7.11 (dd, J = 8.0, 1.3 Hz, 1H), 3.14 (d, $J_{P\text{-}H}$ = 13.0 Hz, 3H). ^{13}C NMR (126 MHz, $CDCl_3$) δ = 145.64 (d, $J_{C\text{-}P}$ =18.0, Sb-bound *o*-phenylene quaternary), 141.13 (d, $J_{C\text{-}P}$ =15.1, *o*-phenylene), 136.78 (s, Sb*Ph* quaternary), 136.55 (d, $J_{C\text{-}P}$ =14.9, *o*-phenylene), 135.95 (s, *o*-Sb*Ph*), 135.17 (d, $J_{C\text{-}P}$ =3.0, *p*-P*Ph*), 134.91 (d, $J_{C\text{-}P}$ =3.4, *o*-phenylene), 133.53 (d, $J_{C\text{-}P}$ =10.3, *m*-P*Ph*), 130.62 (d, $J_{C\text{-}P}$ =12.8, *o*-P*Ph*), 130.41 (d, $J_{C\text{-}P}$ =12.9, *o*-phenylene), 129.59 (s, *p*-Sb*Ph*), 129.48 (s, *m*-Sb*Ph*), 126.99 (d, $J_{C\text{-}P}$ =91.1, P-bound *o*-phenylene quaternary), 119.81 (d, $J_{C\text{-}P}$ =86.9, P*Ph* quaternary), 12.05 (d, $J_{C\text{-}P}$ =57.3, P*C*H_3). ^{19}F NMR (470 MHz, $CDCl_3$) δ = -152.41 (s, 1F) -152.46 (s, 4F). ^{31}P NMR (202 MHz, $CDCl_3$) δ = 23.6 (s). Elemental analysis calculated (%) for $C_{31}H_{27}BF_4PSb$: C, 58.26; H, 4.26; found C, 58.14; H, 4.40.

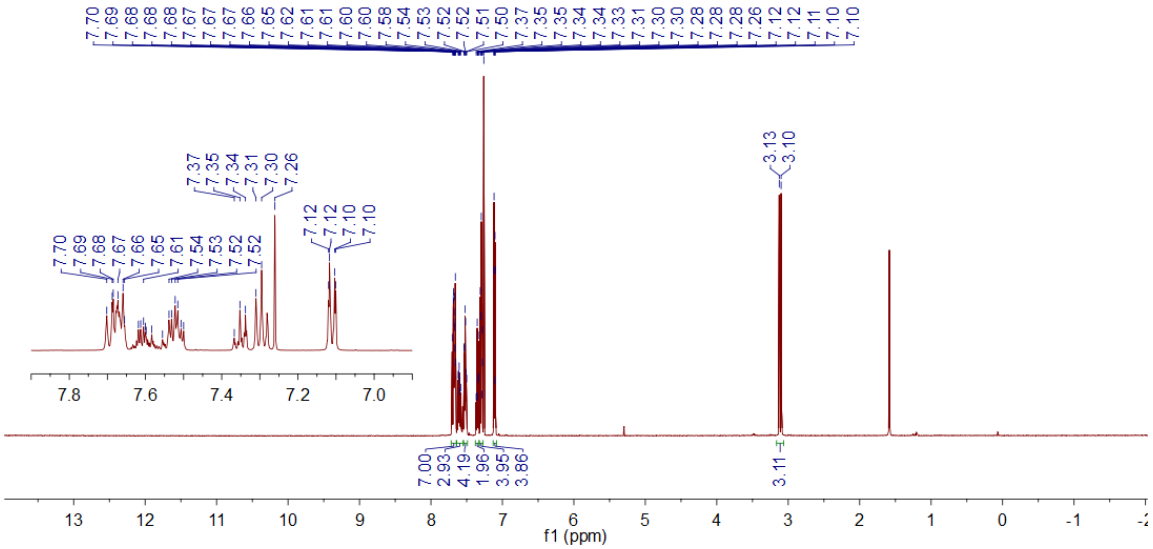

Figure 94. $^{13}C\{^{1}H\}$ NMR spectrum of [**80**][BF_4] in $CDCl_3$.

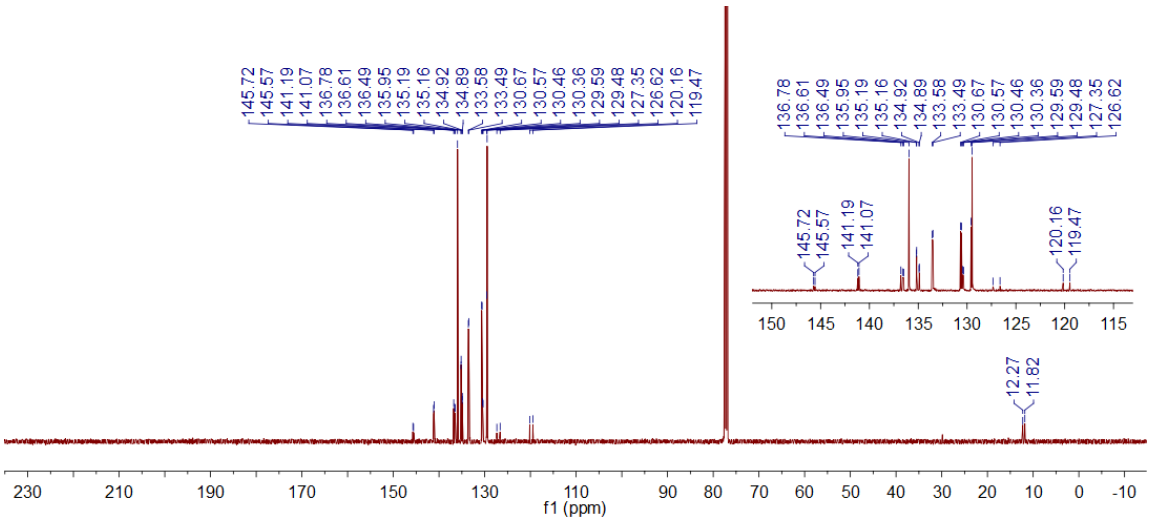

Figure 95. $^{13}C\{^{1}H\}$ NMR spectrum of [**80**][BF_4] in $CDCl_3$.

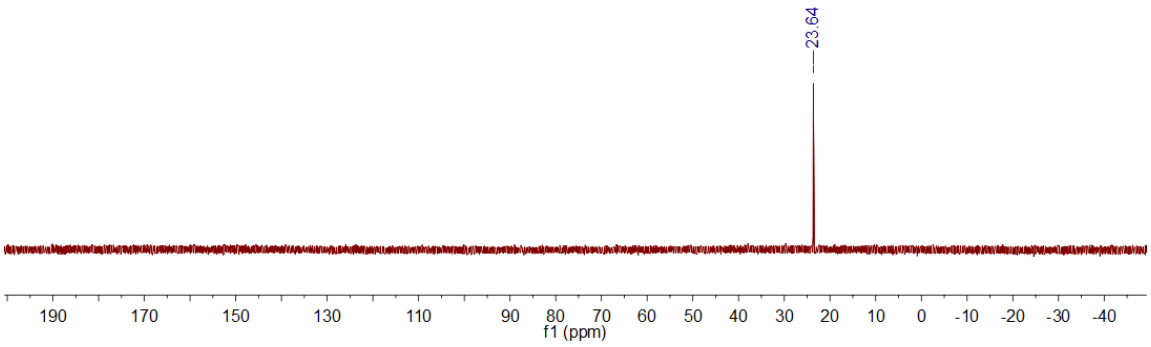

Figure 96. $^{13}C\{^{1}H\}$ NMR spectrum of [**80**][BF_4] in $CDCl_3$.

5.6.1.3 Synthesis of [*o*-(PPh_2)$C_6H_4SbPh_3$][BF_4] ([**81**][BF_4])

In the glove box, $AgBF_4$ (100 mg, 0.51 mmol) was added to a stirred CH_2Cl_2 solution of *o*-(PPh_2)$C_6H_4SbPh_3Br$ (340 mg, 0.49 mol). The reaction was stirred in the absence of light for 3 h, at which time it was filtered over a Celite plug. All volatiles were removed from the filtrate to give a sticky, colorless oil, which was triturated with two portions of Et_2O (3 mL each) to afford [*o*-(PPh_2)$C_6H_4SbPh_3$][BF_4] as white powder (252 mg, 65% yield). Single crystals of [*o*-(PPh_2)$C_6H_4SbPh_3$][BF_4] were obtained as colorless blocks by diffusing hexanes into a $CDCl_3$ solution. [*o*-(PPh_2)$C_6H_4SbPh_3$][BF_4]: ^{1}H NMR (499 MHz, $CDCl_3$) δ 7.82 – 7.76 (m, 2H), 7.75 – 7.70 (m, 1H), 7.71 – 7.66 (m, 6H), 7.67 – 7.59 (m, 4H), 7.59 – 7.53 (m, 6H), 7.36 – 7.30 (m, 2H), 7.27 – 7.22 (m, 3H), 6.98 – 6.90 (m, 4H). ^{13}C NMR (100 MHz, $CDCl_3$) δ 142.59 (d, $J_{C\text{-}P}$ = 2.8 Hz, Sb-bound *o*-phenylene quaternary), 137.22 (d, $J_{C\text{-}P}$ = 1.1 Hz, *o*-phenylene), 137.09 (d, $J_{C\text{-}P}$ = 19.5 Hz, P-bound *o*-phenylene quaternary), 135.29 (d, $J_{C\text{-}P}$ = 2.3 Hz, *o*-Sb*Ph*), 134.72 (d, $J_{C\text{-}P}$ = 1.1 Hz, *o*-phenylene), 133.63 (s, *o*-phenylene), 133.48 (s, *p*-Sb*Ph*), 132.83 (d, $J_{C\text{-}P}$ = 16.7 Hz, *o*-

P*Ph*), 132.81 (s, *o*-phenylene), 131.25 (s, *m*-Sb*Ph*), 129.98 (s, *p*-P*Ph*), 129.18 (d, $J_{C\text{-}P}$ = 7.7 Hz, *m*-Sb*Ph*), 124.67 (d, $J_{C\text{-}P}$ = 11.8 Hz, Sb*Ph* quaternary). ^{19}F NMR (470 MHz, $CDCl_3$) δ -152.95 (s, 1F), -153.00 (s, 4F). ^{31}P NMR (202 MHz, $CDCl_3$) δ 11.4 (s). Elemental analysis calculated (%) for $C_{36}H_{29}BF_4PSb$: C, 61.67; H, 4.17; found C, 61.55; H, 4.20.

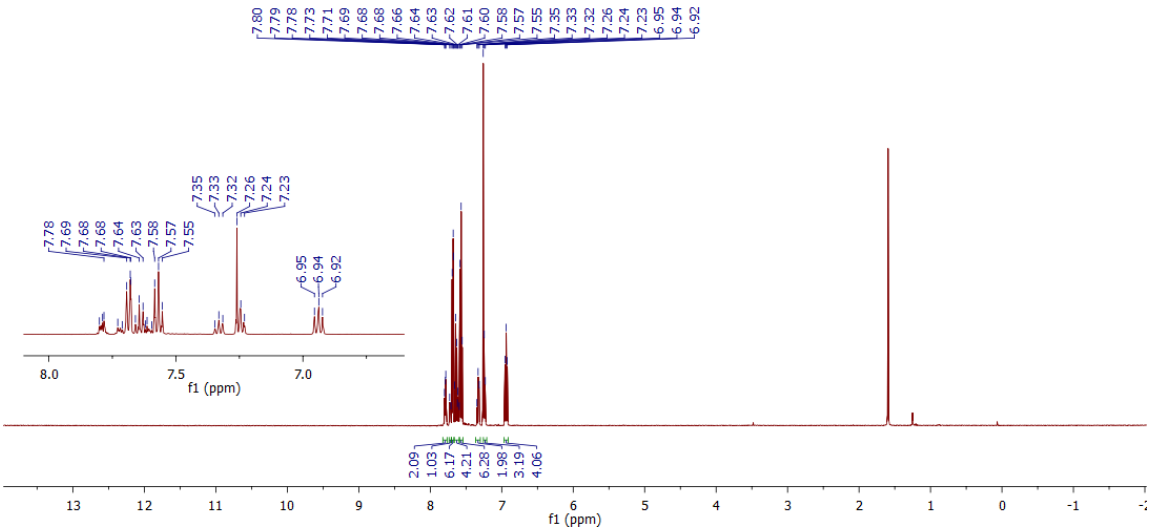

Figure 97. ^1H NMR spectrum of [**81**][BF_4] in $CDCl_3$.

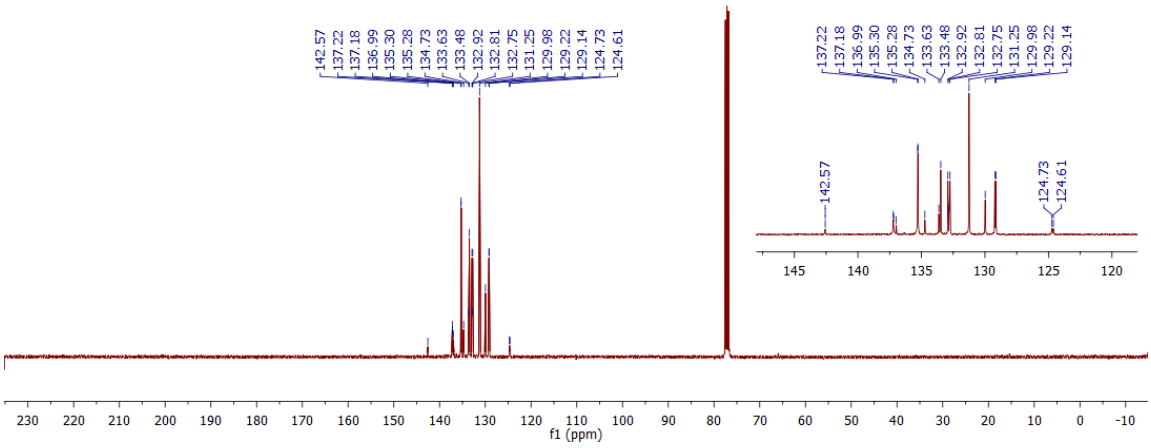

Figure 98. $^{13}C\{^{1}H\}$ NMR spectrum of [**81**][BF_4] in $CDCl_3$.

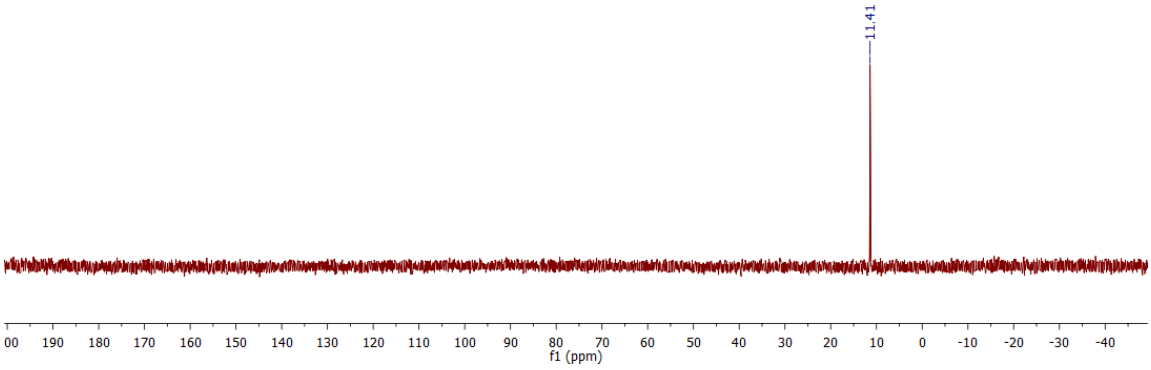

Figure 99. $^{31}P\{^{1}H\}$ NMR spectrum of [**81**][BF_4] in $CDCl_3$.

5.6.1.4 Synthesis of [*o*-($MePPh_2$)$C_6H_4SbPh_3$][BF_4]$_2$ ([**82**][BF_4]$_2$)

In a 25 mL Schlenk tube, Me_3OBF_4 (105 mg, 0.71 mol) was added to a solution of [*o*-(PPh_2)$C_6H_4SbPh_3$][BF_4] (470 mg, 0.67 mmol) in mixed solvents of toluene (2 mL) and 1,2-dichloroethane (1 mL). The Schlenk tube was sealed under N_2 atmosphere and the

mixture was left to stir in a 90 ºC bath for 12 h, after which a white precipitate formed. The solid was filtered, washed with three portions of Et_2O (5 mL each), and dried *in vacuo* to afford [*o*-($MePPh_2$)$C_6H_4SbPh_3$][BF_4]$_2$ as white powder (460 mg, 85 % yield). Single crystals of [*o*-($MePPh_2$)$C_6H_4SbPh_3$][BF_4]$_2$ were obtained as colorless blocks by diffusing pentane into a CH_2Cl_2 solution. [*o*-($MePPh_2$)$C_6H_4SbPh_3$][BF_4]$_2$: ^{1}H NMR (399 MHz, CD_2Cl_2) δ 8.05 – 7.96 (m, 2H), 7.94 – 7.87 (m, 1H), 7.81 – 7.73 (m, 5H), 7.65 (t, J = 7.8 Hz, 6H), 7.58 – 7.40 (m, 15H), 2.50 (d, $J_{P\text{-}H}$ = 13.3 Hz, 3H). ^{13}C NMR (100 MHz, CD_2Cl_2) δ 142.10 (d, $J_{C\text{-}P}$ = 12.9 Hz, *o*-phenylene), 140.36 (d, $J_{C\text{-}P}$ = 11.0 Hz, *o*-phenylene), 136.56 (d, $J_{C\text{-}P}$ = 2.9 Hz, *p*-P*Ph*), 136.22 (s, *o*-Sb*Ph*), 135.41 (s, *o*-phenylene), 134.81 (s, br, *p*-Sb*Ph*), 134.28 (d, $J_{C\text{-}P}$ = 12.2 Hz, *o*-phenylene), 133.97 (d, $J_{C\text{-}P}$ = 10.7 Hz, *m*-P*Ph*), 131.98 (s, br, *m*-Sb*Ph*), 131.42 (d, $J_{C\text{-}P}$ = 12.9 Hz, *o*-P*Ph*), 129.83 (s, br, Sb-bound *o*-phenylene quaternary), 125.42 (d, $J_{C\text{-}P}$ = 91.0 Hz, P-bound *o*-phenylene quaternary), 123.21 (s, br, Sb*Ph* quaternary), 118.33 (d, $J_{C\text{-}P}$ = 88.3 Hz, P*Ph* quaternary), 10.11 (d, $J_{C\text{-}P}$ = 56.1 Hz, P*C*H_3). ^{19}F NMR (470 MHz, CD_2Cl_2) δ -149.96 (s, 1F), -150.02 (s, 4F). ^{31}P NMR (202 MHz, CD_2Cl_2) δ 26.5 (s). Elemental analysis calculated (%) for $C_{37}H_{32}B_2F_8PSb$: C, 55.34; H, 4.02; found C, 54.85; H, 4.04.

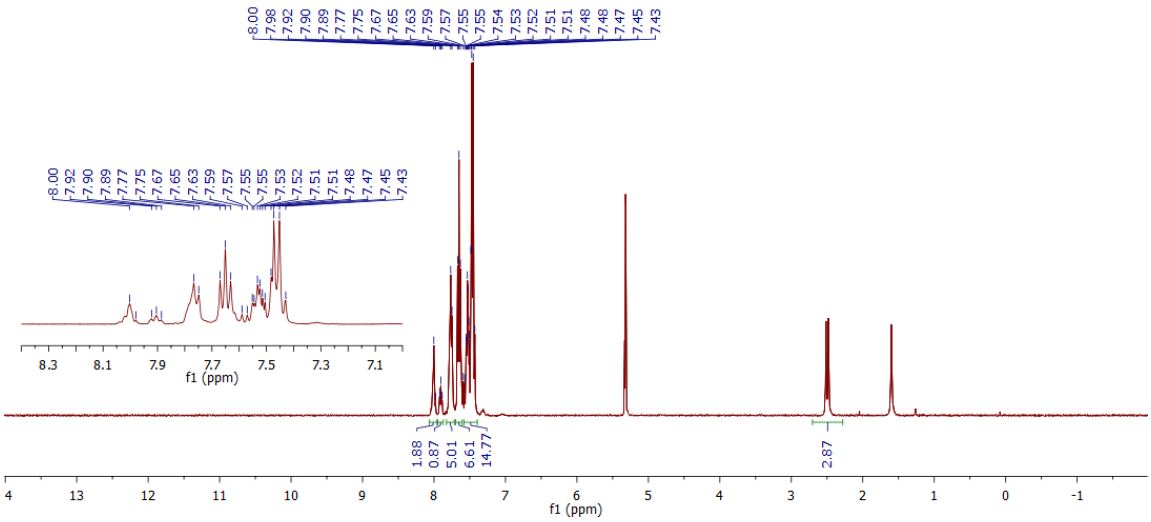

Figure 100. ^{1}H NMR spectrum of [**82**][BF_4]$_2$ in $CDCl_3$.

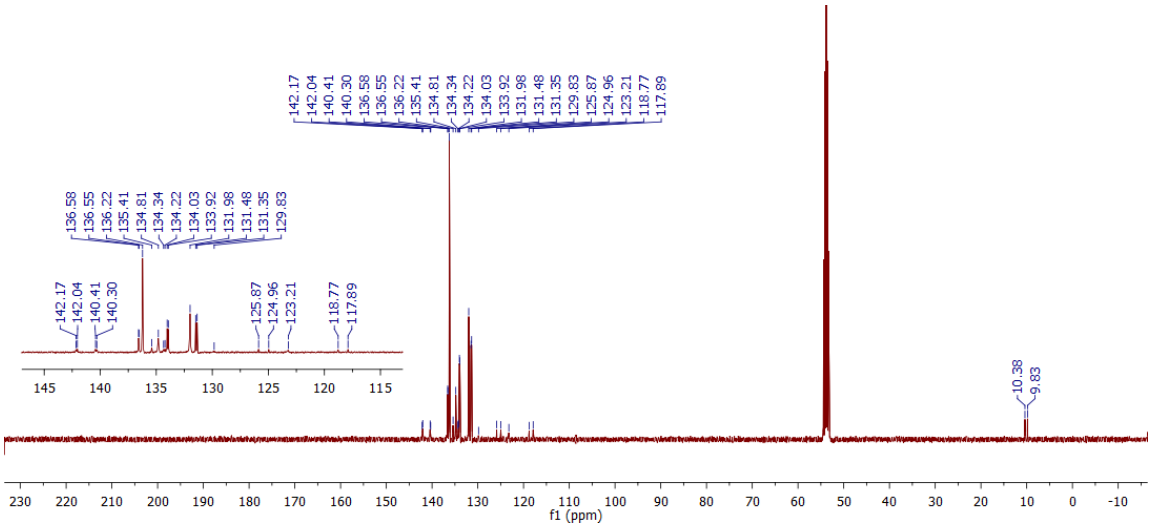

Figure 101. $^{13}C\{^{1}H\}$ NMR spectrum of [**82**][BF_4]$_2$ in $CDCl_3$.

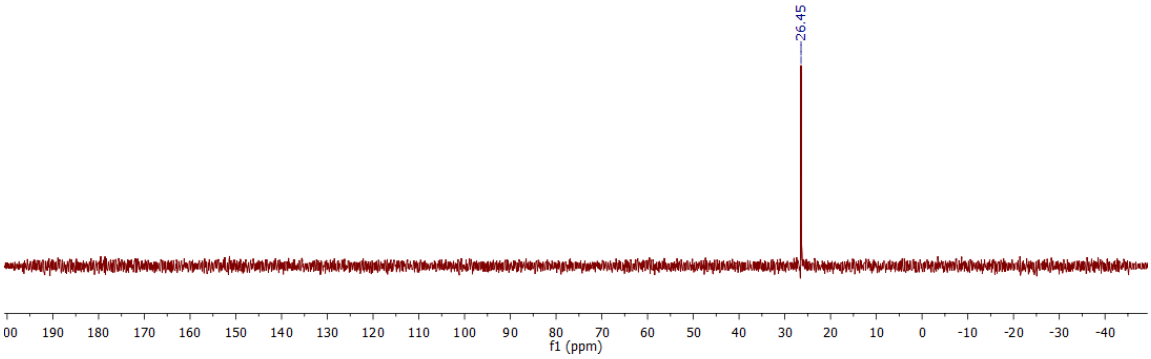

Figure 102. $^{31}P\{^{1}H\}$ NMR spectrum of [**82**][BF_4]$_2$ in $CDCl_3$.

5.6.2 Catalytic transfer hydrogenation reactions

Each experiment was repeated 2-3 times. The yields provided in Table 16 are averages.

5.6.2.1 The transfer hydrogenation reaction involving 2-phenylquinoline and Hantzsch ester

An NMR tube was charged with a dry $CDCl_3$ solution (0.7 mL) of the antimony catalyst (0.004 mmol), Hantzsch-ester (50 mg, 0.20 mmol), and 2-phenylquinoline (16 mg, 0.08 mmol). The tube was then sealed and the formation of the products was monitored by ^{1}H NMR *in situ*. The yield of the product was calculated based on the integration of two resonances: 6.6 ppm (d, 1H) and 6.7 ppm (t, 1H). The amount of the unreacted substrate was calculated based on the integration of two resonances: 7.8 ppm (d, 1H) and 7.9 ppm (d, 1H).

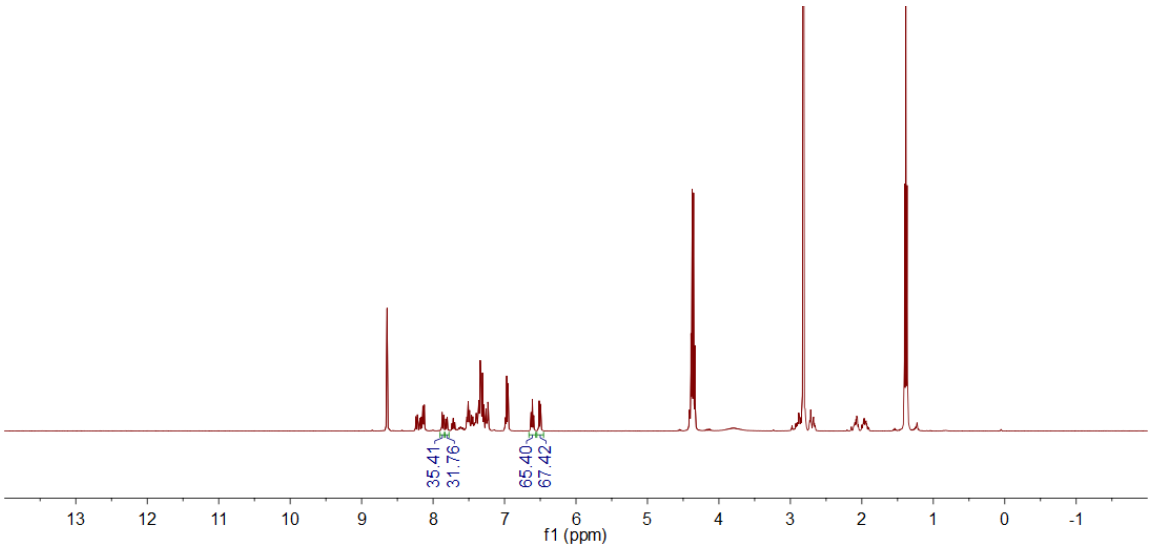

Figure 103. Representative ^{1}H NMR spectrum collected during the transfer hydrogenation reaction involving 2-phenylquinoline and Hantzsch ester with [**82**][BF_4]$_2$ as a catalyst.

5.6.2.2 The transfer hydrogenation reaction involving 3-bromoquinoline and Hantzsch ester

An NMR tube was charged with a dry $CDCl_3$ solution (0.7 mL) of the antimony catalyst (0.004 mmol), Hantzsch-ester (50 mg, 0.20 mmol), and 3-bromoquinoline (11 μL, 0.08 mmol). The tube was then sealed and the formation of the products was monitored by ^{1}H NMR *in situ*. The yield of the product was calculated based on the integration of two resonances: 6.5 ppm (d, 1H) and 6.7 ppm (t, 1H). The amount of the unreacted substrate was calculated based on the integration of two resonances: 8.1 ppm (d, 1H) and 8.3 ppm (d, 1H).

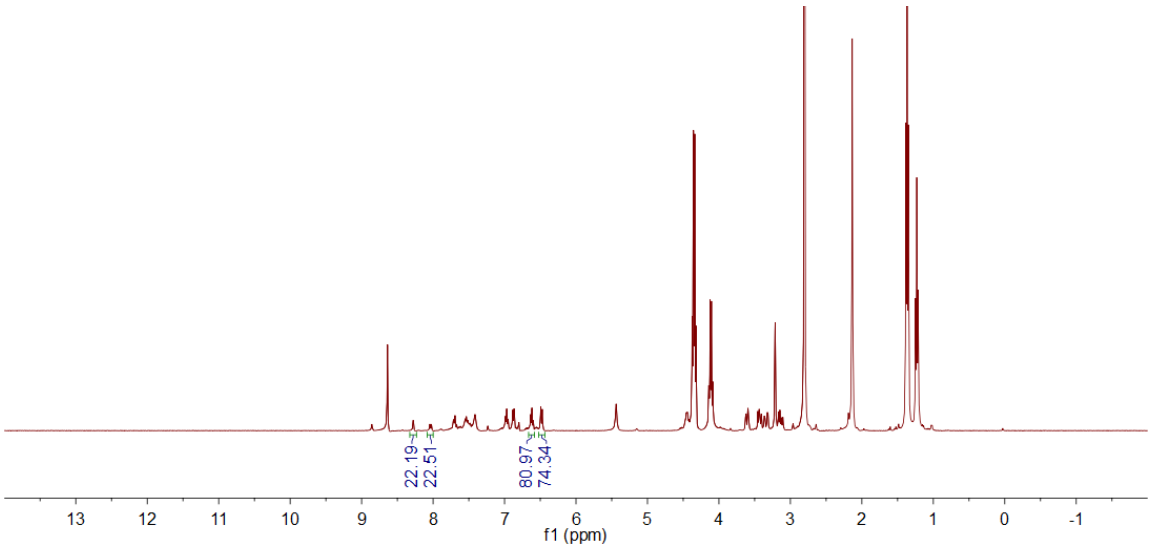

Figure 104. Representative ^{1}H NMR spectrum collected during the transfer hydrogenation reaction involving 3-bromoquinoline and Hantzsch ester with [**82**][BF_4]$_2$ as a catalyst.

5.6.3 Crystallographic measurements

All crystallographic measurements were performed at 110(2) K using a Bruker SMART APEX II diffractometer or a Brucker D8 QUEST diffractometer (graphite monochromated Mo-Kα radiation, λ = 0.71073 Å). In each case, a specimen of suitable size and quality was selected and mounted onto a nylon loop. The semiempirical method SADABS was applied for absorption correction. The structures were solved by direct methods and refined by the full-matrix least-squares technique against F^2 with the anisotropic temperature parameters for all non-hydrogen atoms. All H-atoms were geometrically placed and refined in riding model approximation. Data reduction and further calculations were performed using the Bruker *SAINTplus* and *SHELXTL-NT* program packages.[157]

Table 17. Crystallographic and structure refinement details for [**80**][BF_4] and [**81**][BF_4].

Compound	**[80][BF_4]**	**[81][BF_4]**
Empirical formula	C_{31} H_{27} B F_4 P Sb	C_{36} H_{29} B F_4 P Sb
Formula weight	639.05	701.12
Temperature	110.0 K	110 K
Wavelength	0.71073 Å	0.71073 Å
Crystal system	Orthorhombic	Monoclinic
Space group	$P2_12_12_1$	$P\ 1\ 2_1/n\ 1$
Unit cell dimensions	a = 10.7939(5) Å	a = 10.9669(5) Å
	b = 12.0638(5) Å	b = 22.7967(10) Å
	c = 21.0206(10) Å	c = 13.2630(6) Å
	α= 90°.	α= 90°.
	β= 90°.	β= 111.988(2)°.
	γ = 90°.	γ = 90°.
Volume	2737.2(2) $Å^3$	3074.7(2) $Å^3$
Z	4	4
Density (calculated)	1.551 Mg/m^3	1.515 Mg/m^3
Absorption coefficient	1.113 mm^{-1}	0.998 mm^{-1}
F(000)	1280	1408
Crystal size	0.24 x 0.24 x 0.07 mm^3	0.38 x 0.2 x 0.16 mm^3
Theta range for data collection	1.938 to 27.499°	1.787 to 27.823°.
Index ranges	-14<=h<=13, -15<=k<=15, -27<=l<=27	-14<=h<=14, -29<=k<=29, -17<=l<=17
Reflections collected	47592	66668
Independent reflections	6282 [R(int) = 0.1074]	7289 [R(int) = 0.1201]
Completeness to theta = 25.242°	100.0 %	100.0 %
Absorption correction	Semi-empirical from equivalents	Semi-empirical from equivalents
Max. and min. transmission	0.7456 and 0.6073	0.7456 and 0.5786
Refinement method	Full-matrix least-squares on F^2	Full-matrix least-squares on F^2
Data / restraints / parameters	6282 / 2 / 372	7289 / 0 / 388
Goodness-of-fit on F2	1.064	1.032
Final R indices [I>2sigma(I)]	R1[a] = 0.0404, wR2[b] = 0.0850	R1[a] = 0.0436, wR2[b] = 0.0983
R indices (all data)	R1 = 0.0491, wR2 = 0.0892	R1 = 0.0726, wR2 = 0.1108
Extinction coefficient	n/a	n/a
Largest diff. peak and hole	0.649 and -0.968 e.$Å^{-3}$	1.271 and -0.972 e.$Å^{-3}$

[a] $R1 = \Sigma||F_o| - |F_c||/\Sigma|F_o|$. [b] $wR2\ ([w(F_o^2 - F_c^2)^2]/[\Sigma w(F_o^2)^2])^{1/2}$; $w = 1/[\sigma^2(F_o^2) + (ap)^2 + bp]$; $p = (F_o^2 + 2F_c^2)/3$ with a = 0.0351 and b = 2.0977 for [**80**][BF_4] and a = 0.0488 and b = 1.4156 for [**81**][BF_4].

Table 18. Crystallographic and structure refinement details for [**82**][BF_4]$_2$.

Compound	**[82][BF_4]$_2$**
Empirical formula	C_{37} H_{32} B_2 F_8 P Sb
Formula weight	802.96
Temperature	99.98 K
Wavelength	0.71073 Å
Crystal system	Monoclinic
Space group	*P* 1 2_1/*c* 1
Unit cell dimensions	a = 18.8422(17) Å b = 10.1309(9) Å c = 17.5792(17) Å α= 90°. β= 93.042(3)°. γ = 90°.
Volume	3350.9(5) Å^3
Z	4
Density (calculated)	1.592 Mg/m^3
Absorption coefficient	0.943 mm^{-1}
F(000)	1608
Crystal size	0.4 x 0.26 x 0.11 mm^3
Theta range for data collection	2.283 to 27.870°.
Index ranges	-24<=h<=24, -13<=k<=13, -23<=l<=23
Reflections collected	150424
Independent reflections	7944 [R(int) = 0.0897]
Completeness to theta = 25.242°	99.9 %
Absorption correction	Semi-empirical from equivalents
Max. and min. transmission	0.7456 and 0.5882
Refinement method	Full-matrix least-squares on F^2
Data / restraints / parameters	7944 / 0 / 443
Goodness-of-fit on F2	1.205
Final R indices [I>2sigma(I)]	R1[a] = 0.0433, wR2[b] = 0.0917
R indices (all data)	R1 = 0.0526, wR2 = 0.0945
Extinction coefficient	n/a
Largest diff. peak and hole	1.994 and -1.875 e.Å^{-3}

[a]*R1* = $\Sigma||F_o| - |F_c||/\Sigma|F_o|$. [b]*wR2* $([w(F_o^2 - F_c^2)^2]/[\Sigma w(F_o^2)^2])^{1/2}$; $w = 1/[\sigma^2(F_o^2) + (ap)^2 + bp]$; $p = (F_o^2 + 2F_c^2)/3$ with $a = 0.0000$ and $b = 15.4158$ for [**82**][BF_4]$_2$.

5.6.4 Computational details

All computations were carried out using density functional theory (DFT) methods as implemented in the Gaussian 09 program.[158] All optimization and frequency

calculations were carried out with the M062X[172] functional and mixed basis sets (cc-pVTZ-PP[161] with CRENBL ECP[162] for Sb, cc-pVTZ for P, 6-31g(d') for H, C, N, F, 6-311g* for S, Cl) starting from the crystal structure geometries if available. No imaginary frequencies were found for the optimized structures, confirming that a local minimum on the potential energy hypersurface had in all cases been reached. The optimized structures were also subjected to natural bond orbital (NBO)[147] analysis. The molecular orbitals and NBOs were visualized and plotted using the Jimp2 program.[163]

CHAPTER VI

COMPUTATIONAL STUDIES OF THE OFF-ON FLUORESCENCE SENSING OF FLUORIDE BY DONOR–ANTIMONY(V) LEWIS ACIDS[*]

6.1 Introduction

Fluoride anion sensing is a topic of ongoing interest because of the possible adverse effects caused by excessive intake of this anion.[216-219] Lewis acidic compounds based on boron[190, 220-225] and antimony(V)[4, 12, 14, 29-30, 39, 48, 57, 119, 133, 139, 169, 189, 192] have recently been exploited as fluoride sensors for their high affinity. In particular, organoantimony(V) compounds are attracting a growing interest due to their stability and high sensitivity toward fluoride in both organic and aqueous media.[4, 12, 14, 29-30, 39, 48, 57, 119, 133, 139, 169, 189, 192] Additionally, when substituted with a fluorescent reporter, these antimony-containing compounds sometime produce a turn-on fluorescence response upon fluoride anion complexation.[12, 14, 57, 119] In previous studies,[14, 57] it has been demonstrated that while stibonium cations of general formula $[FLUO\text{-}SbPh_2R]^+$ (R = Ph, FLUO = 9-anthryl **72**$^+$, 9-phenanthryl **84** $^+$, 1-pyrenyl **31**$^+$) are almost non-emissive, their fluorostiboranes (**72**-F, **84**-F, **31**-F) show intense fluorescence from the fluorophore (Figure 105). This OFF-ON mechanism rests on a structural distortion that takes place in the excited state of the stibonium cation. In this process, the antimony atom coordination geometry distorts from a tetrahedral geometry (**A**) to a seesaw geometry (**B**) resulting in

[*] Reproduced with permission from: "OFF–ON Fluorescence Sensing of Fluoride by Donor–Antimony(V) Lewis Acids"; Kumar, A.; Yang, M.; Kim, M.; Gabbaï, F. P.; Lee, M. H., *Organometallics* **2017,** *36* (24), 4901-4907. Copyright 2018 American Chemical Society.

an inversion of the π* and σ*(Sb–C) orbital energies. It follows that **B** is no longer emissive because of the π-σ*(Sb–C) rather than π–π* nature of the excited state (Figure 106, Left). Since fluoride anion binding occurs by donation of a fluoride lone pair into a σ*(Sb–C) orbital, this dark excited state is no longer accessible after anion binding, leading to the observed turn-on response.[118-119] The same mechanism has been invoked to explain the fluorescence quantum yield increase observed upon anion coordination to the BODIPY-stibonium platform **33**$^+$.[119] With the view of adding credence to this model, we have now become interested in platforms for which the σ*(Sb–C) orbital falls between the π and π* orbitals of the fluorophore, even at the ground state geometry (Figure 106, Right). It occurred to us that such an electronic structure could be generated using a fluorophore whose π and π* levels are higher than those of the aromatic hydrocarbons used in systems of type **72**$^+$. These considerations have led us to focus on electron rich moieties such as the 10*H*-phenoxazine, diphenylamine, and 9*H*-carbazole units and their incorporation as peripheral fluorophores (FLUO) in stibonium cations of general formula [Ph_2MeSb-(*p*-(C_6H_4))-FLUO]$^+$ (**85**$^+$-**87**$^+$, Figure 105).

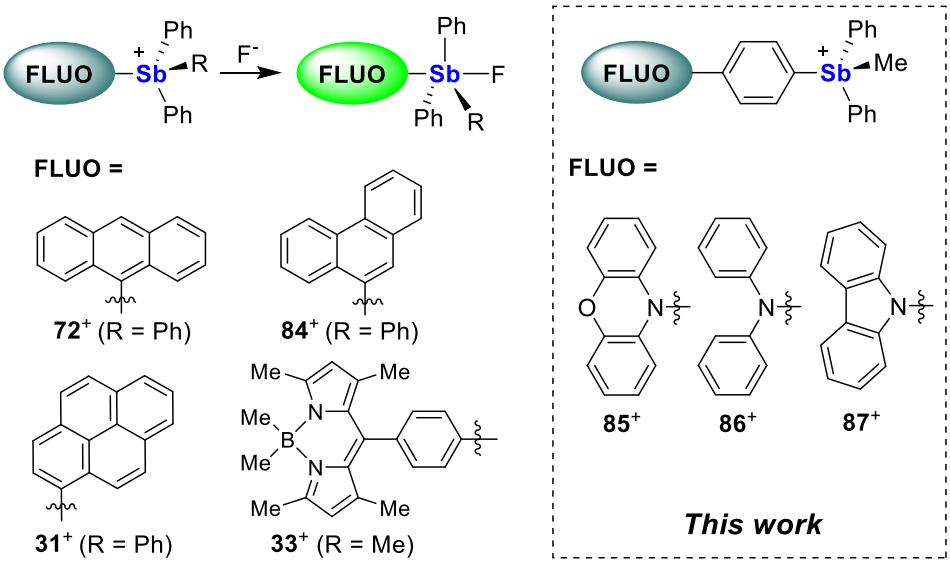

Figure 105. Fluorophore–[Sb(V)] Lewis Acids and Turn-on Fluorescence Response toward Fluoride Binding.

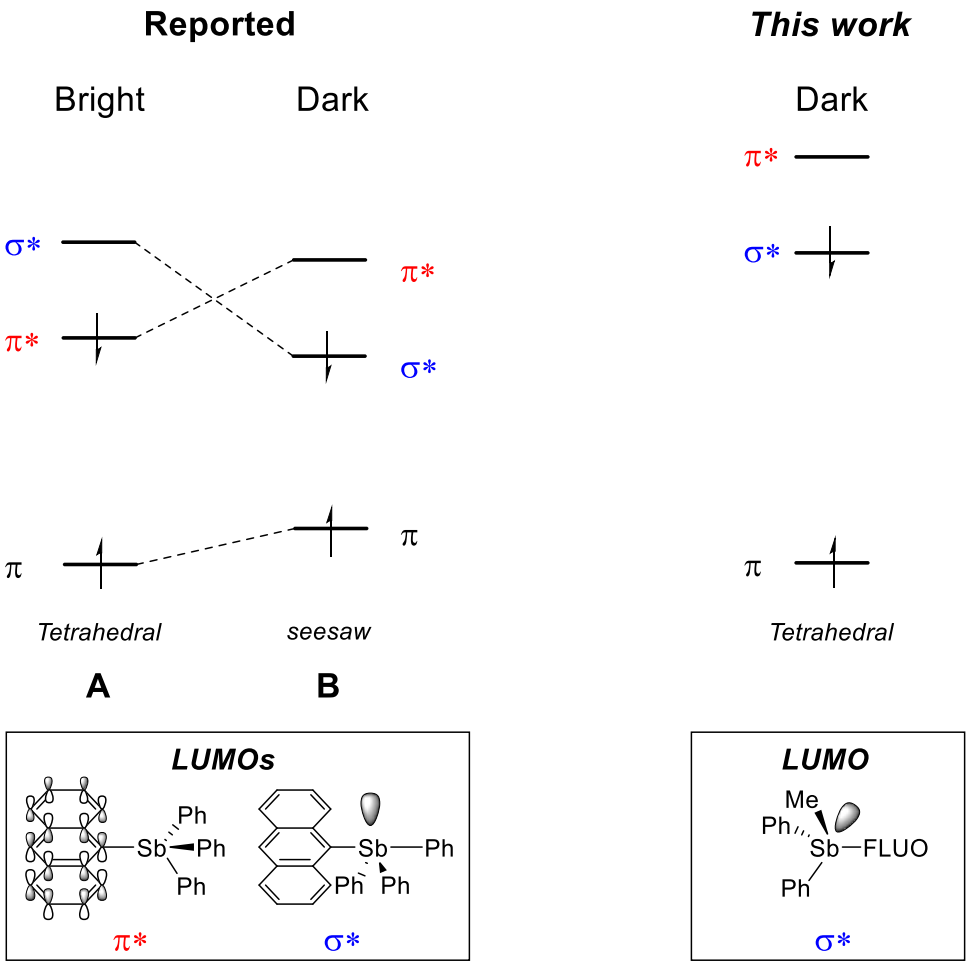

Figure 106. Left: Energy diagram showing the frontier molecular orbitals of **72**$^{+}$ in the excited state, before and after distortion. Right: Frontier orbital energy diagram of the compounds targeted in this study, with a σ*(Sb–C) orbital acting as the LUMO, even without distortion from the ground state geometry.

6.2 Background

Our collaborator, Ajay Kumar and Minji Kim of Dr. Min Hyung Lee's group at University of Ulsan, performed the synthesis of the triflate salts of the methylstibonium

cations $[Ph_2MeSb\text{-}(p\text{-}(C_6H_4))\text{-}FLUO]^+$ (FLUO = 10*H*-phenoxazine (**85**$^+$), diphenylamine (**86**$^+$), and 9*H*-carbazole (**87**$^+$)), and studied the formation of the corresponding fluorostiboranes (**85**-F - **87**-F) upon treatment of these stibonium cations with fluoride anions (Figure 107). They observed that while the stibonium cations are almost non-emissive, the fluorostiboranes display fluorophore-centered emissions. Among the stiboniums tested, the carbazole containing derivative **87**$^+$ exhibits the most intense fluorescence turn-on response whose fluorescence quantum yield (Φ_{PL}) increases from 0.7% in **87**$^+$ to 6% in **87**-F. Complex [**87**][OTf] also displays a high binding constant ($K > 10^7$ M^{-1}) in CH_3CN (Figure 108) and shows compatibility with protic media such as MeOH (K = 950(±50) M^{-1}).

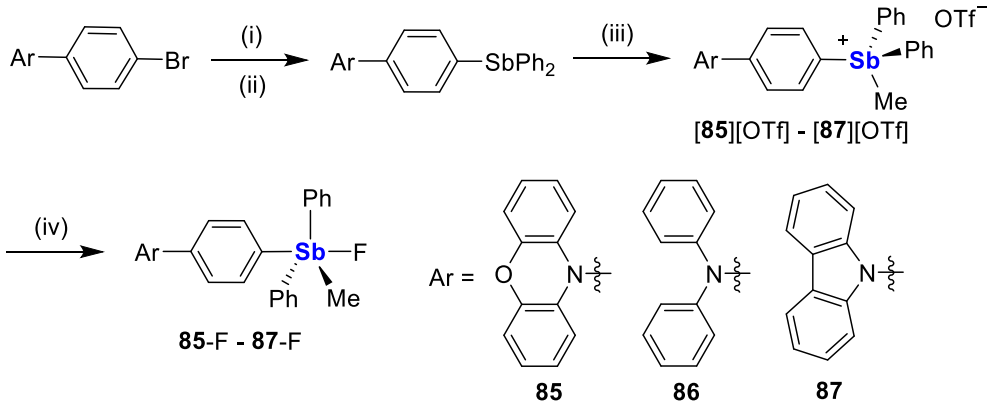

Figure 107. Synthesis of methylstiboniums [**85**][OTf] - [**87**][OTf] and their corresponding fluorostiboranes **85**-F - **87**-F.

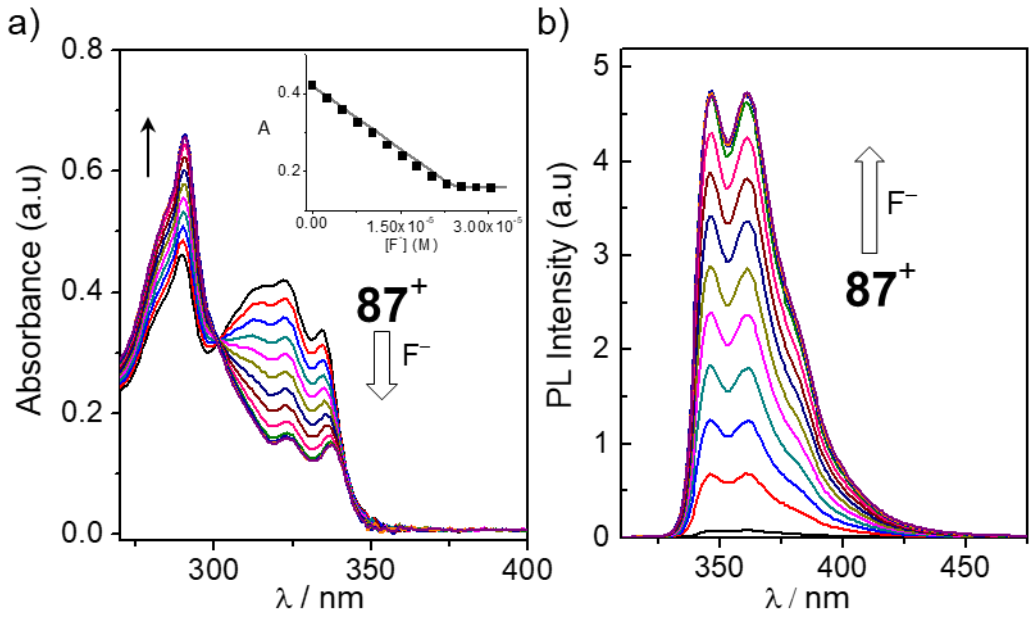

Figure 108. Changes in the a) UV-Vis absorption and b) PL spectra of [**87**][OTf] (2.5×10^{-5} M) in CH_3CN upon addition of Bu_4NF (0–1.4 equiv). λ_{ex} = 301 nm. The left inset shows the absorbance at 322 nm as a function of [F^-]. The line corresponds to the binding isotherm calculated with $K = 1.0 \times 10^7$ M^{-1}.

6.3 Computational studies on the electronic structures of **87**$^+$ and **87**-F

TD-DFT calculations were performed on both the ground state (S_0) and the first singlet excited state (S_1) optimized structures of **87**$^+$ and the ground state of **87**-F to gain insight into their photophysical properties. Among different isomers of **87**-F, we chose to only consider the geometry in which the fluorine atom is *trans* to the donor group because it is energetically most favorable (see chapter 6.5 below). The HOMO and LUMO of **87**-F are localized in the carbazole-based π and π* orbitals, as expected from its fluorescence

spectrum (Figure 109). In the case of **87**$^{+}$, however, the LUMO is instead localized at the [Ph_2MeSb-(*p*-(C_6H_4))] fragment. A more careful inspection of this orbital shows that it has π*/σ*[Ph_2MeSb-(*p*-(C_6H_4))] character, with the σ* component arising from the combination of the σ*(Sb–Ph) and σ*(Sb–Me) orbitals and the π* component from the π* orbital of the *p*-phenylene linker as well as the antimony-bound phenyls (Figure 109). Applying the polarizable continuum model with CH_3CN as a solvent does not alter the results much, with the HOMO of **87**$^{+}$ retaining its carbazole-based π character and the LUMO its π*/σ*[Ph_2MeSb-(*p*-(C_6H_4))] character (Figure 110, left and Figure 111). TD-DFT calculations identify low energy excitations with significant oscillator strength at 333 nm for **87**$^{+}$ and at 294 nm for **87**-F which matches the low energy band observed experimentally in the UV-Vis spectra of these derivatives. These computational results can be reconciled with experimental ones by assigning the π(carbazole)–π*/σ*[Ph_2MeSb-(*p*-(C_6H_4))] excited state of **87**$^{+}$ as non-emissive and the carbazole-based π–π* excited state of **87**-F as emissive (Figure 110).

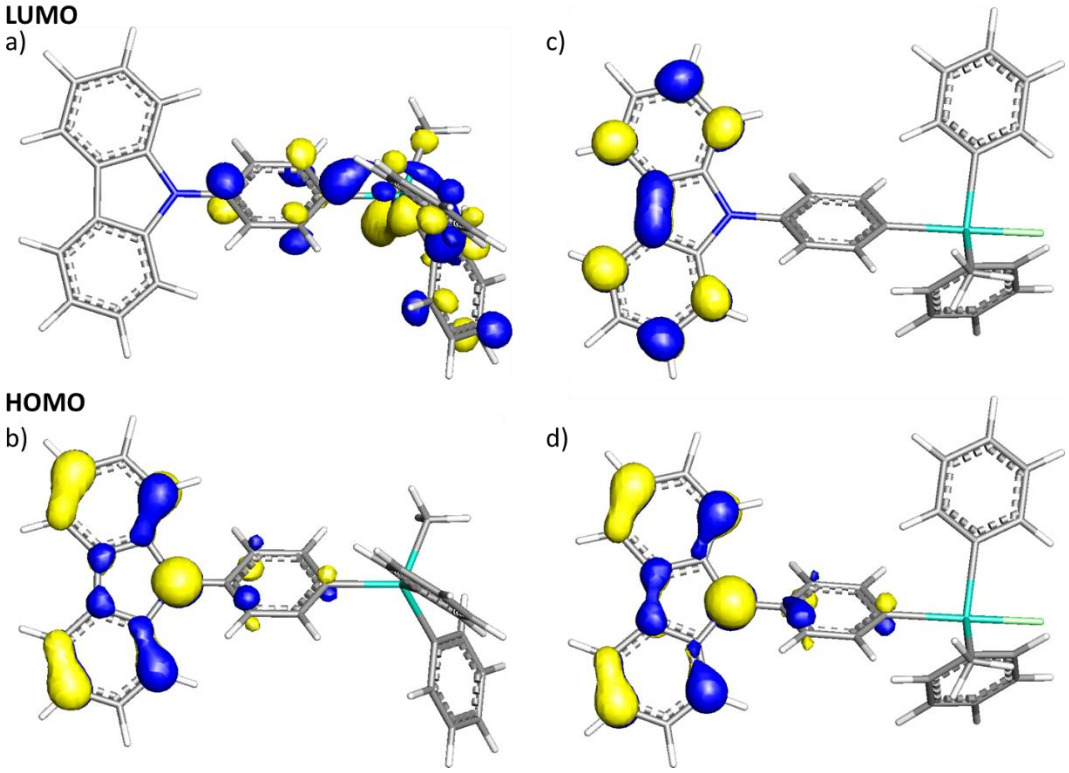

Figure 109. Frontier orbitals of **87**$^{+}$ (a, b) and **87**-F (c,d) in the gas phase. Isovalue = 0.05.

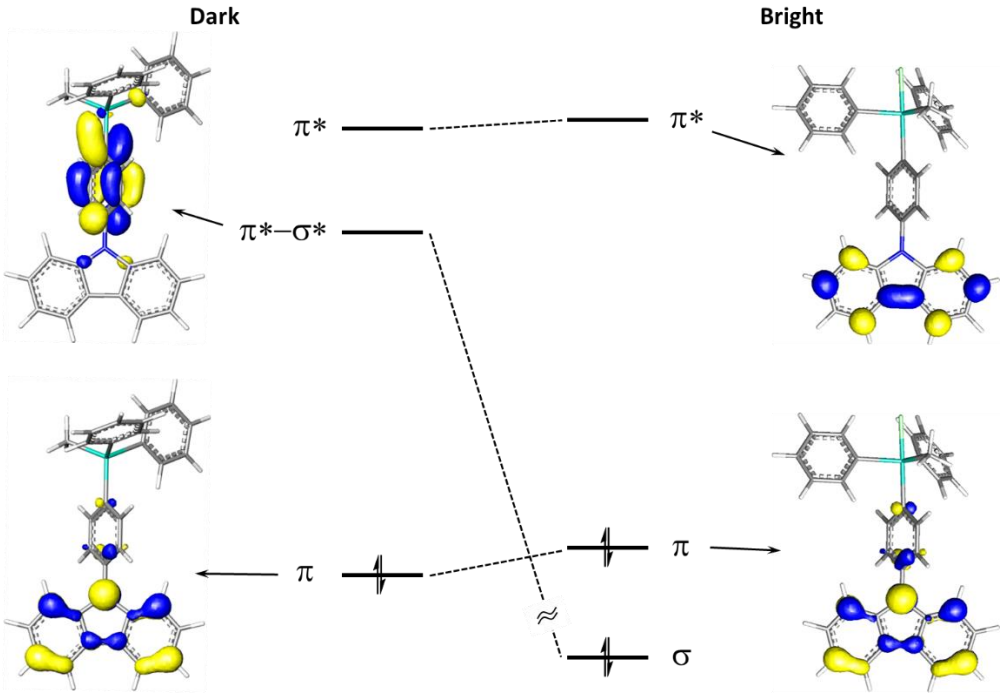

Figure 110. Energy diagram with contour plots of computed frontier molecular orbitals of the ground state of **87**$^+$ (left) and of **87**-F (right) in CH_3CN solution phase. Isovalue = 0.05.

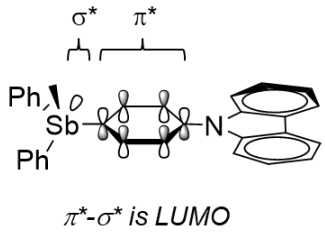

Figure 111. The LUMO of **87**$^+$.

6.4 Conclusion

We have demonstrated that stibonium Lewis acids connected to electron rich fluorophores such as 10*H*-phenoxazine, diphenylamine, or 9*H*-carbazole, function as an

OFF-ON fluorescent sensor for fluoride anions. Experimental and computational results show that the OFF-ON response results from the neutralization of the stibonium cation by coordination of a fluoride anion. This coordination affects the frontier orbitals of the platform leading to a change in the nature of the excited state. Before anion binding, the excited state has π(fluorophore)-π*/σ*[Ph_2MeSb-(*p*-(C_6H_4))] character and is non-emissive. After fluoride binding, the fluorophore-centered π–π* excited state is restored, leading to a revival of the fluorescence. The carbazole derivative **87**$^+$ shows the most appealing sensing properties, including a drastic increase in fluorescence quantum yield upon fluoride anion binding. It is also sufficiently Lewis acidic to be used in protic media such as methanol. Altogether, these results validate the notion that electron rich fluorophores with elevated π and π* levels can be effectively quenched by stibonium-based acceptors, leading to a new approach for the design of fluorescence anion sensors.

6.5 Computational details

Computational studies were performed to investigate the electronic structures and transition of **87**$^+$ and **87**-F. Structures are optimized by Gaussian 09 program[158] using density functional theory (DFT) methods. For ground state optimizations in the gas phase, the M06-2X[172] functional and mixed basis sets (cc-pVTZ-pp[161] with CRENBL ECP[162] for Sb, 6-31+g(d') for H, C, N, F) were used, starting from the variation of the crystal structure geometry of **85**$^+$. No imaginary frequencies were found for the ground state optimized structures, thus each structure was confirmed to be located at a local minimum on its potential energy hypersurface. For time-dependent DFT (TD-DFT) calculations, the

mPW1PW91[226] functional and mixed basis sets (aug-cc-pVTZ-pp[161] with CRENBL ECP[162] for Sb, 6-31+g(d') for H, C, N, F) were used, and the polarizable continuum model (PCM) of acetonitrile was applied. Excited state calculations were performed in the same condition except with CAM-B3LYP[227] functional. The molecular orbitals were visualized and plotted in Jimp2 program.[163]

6.5.1 Gas phase ground state optimization

Structures for the free **87**$^+$ and the fluoride-bound form **87**-F were first optimized in the gas phase. For **87**-F, there are three possible geometries: **A**) F trans to 9*H*-carbazole (Cz), **B**) F trans to Ph, and **C**) F trans to Me. The crystal structure of Ph_3SbMeF[1] has shown that Ph has a stronger trans-effect than Me, so geometry **C** (F trans to Me) was first ruled out. Optimizations were performed on geometries **A** and **B**, and geometry **A** is 1.3 kcal/mol more stable than geometry **B**, thus geometry **A** (F trans to Cz) was determined to be the geometry of compound **87**-F.

6.5.2 Solution phase excited state optimization

The following approach was taken to calculate the solution phase excited state geometry: First, the ground state (S_0) geometry of **87**$^+$ was optimized with the acetonitrile solvation (PCM) and resulted in a S_0-optimized geometry (R^{GS}) without imaginary frequencies. Then a single-point TD-DFT calculation was performed with the default non-equilibrium solvation to examine the vertical excitation energy of the first few excited states. The first excited state was confirmed to be a singlet (S_1) with significant oscillation

strength (f = 0.4625), and has primarily HOMO→LUMO transition. Then a TD-DFT geometry optimization was done with equilibrium, linear response solvation to find the minimum energy point of the excited state potential energy surface, resulting in the S_1-optimized geometry (R^{ES}). Unfortunately, we were not able to carry the vibrational frequencies of the optimized excited structure due to the limitations of our computing resources. Both the vertical excitation (3.98 eV) from the ground state to the excited state, and the vertical emission (3.67 eV) from the relaxed excited state geometry to the ground state, were computed with state-specific equilibrium solvation, as the energy diagram shown in Figure 112. The energy difference from the relaxation of the geometry in the first excited state is 0.06 eV.

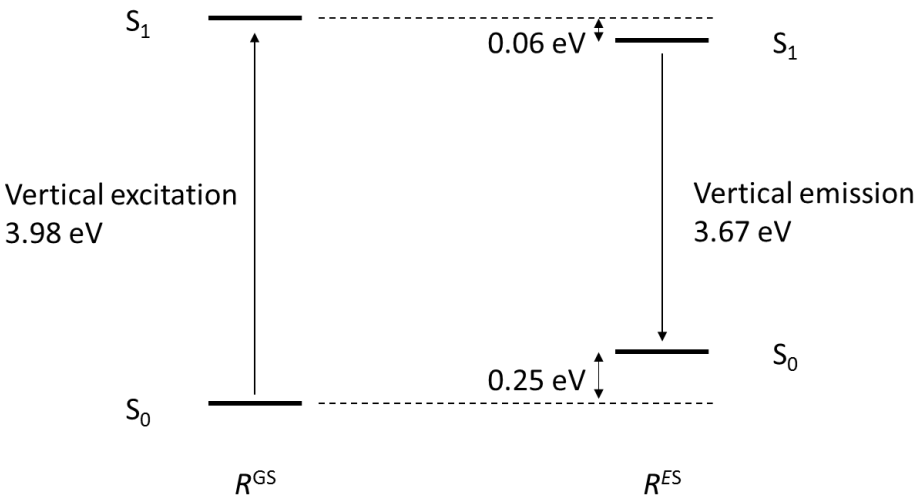

Figure 112. Energies calculated for the ground and excited states of **87**$^+$ in the S_0-optimized (R^{GS}) and S_1-optimized (R^{ES}) geometries.

The frontier orbitals of the S_0-optimized (R^{GS}) and the S_1-optimized (R^{ES}) geometries of **87**$^+$ in solution phase are shown in Figure 113. Both geometries feature a tetrahedral antimony center. Similar to the molecular orbitals in the gas phase, the HOMO of the S_0-optimized geometry is localized at the carbazole p orbital. However, the LUMO mostly resides on the π* orbital of the phenylene linker between the carbazole and the stibonium moieties with a small contribution of Sb-Ph σ* orbitals in the solution phase. Note that LUMO+1 bears a large contribution from Sb-Ph σ* orbitals. The frontier orbitals of the S_1-optimized geometry are almost identical to those of the S_0-optimized geometry, with a shrink of the HOMO-LUMO gap as the HOMO is 0.06 eV higher and the LUMO is 0.39 eV lower in energies (Table 19). The HOMO→LUMO transition being the carbazole π to [Ph_2MeSb-(*p*-(C_6H_4))] π*–σ* charge transfer suggests that **87**$^+$ is nonemissive in the solution phase as well.

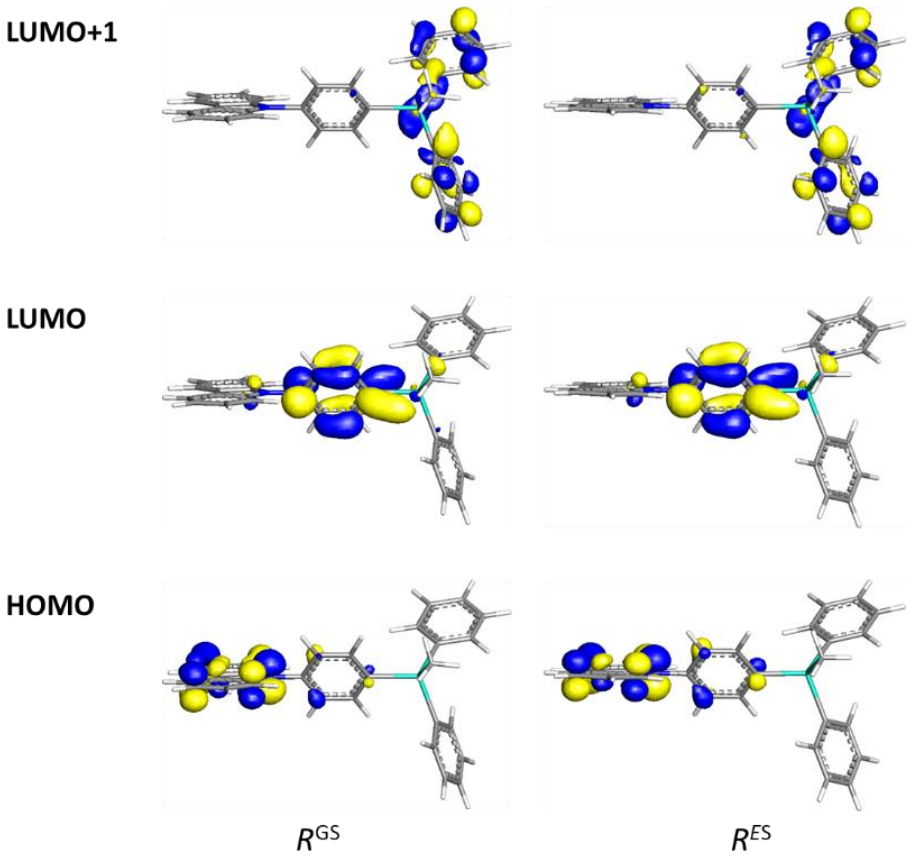

Figure 113. Frontier orbitals of S_0-optimized (R^{GS}) and S_1-optimized (R^{ES}) geometries of **87**$^+$. Isovalue = 0.05.

Table 19. Energy (eV) of the frontier orbitals of S_0-optimized (R^{GS}) and S_1-optimized geometries (R^{ES}) of **87**$^+$.

	87$^+$(R^{GS})	**87$^+$(R^{ES})**	**Energy difference due to excited-state relaxation**
LUMO+1	-0.36	-0.33	+0.03
LUMO	-0.49	-0.88	-0.39
HOMO	-7.21	-7.15	+0.06

CHAPTER VII

SUMMARY

7.1 Digging the sigma-hole of organoantimony Lewis acids *via* oxidation

The development of Group 15 Lewis acids is an area of active investigation that has led to numerous advances in anion sensing and catalysis. While phosphorus has drawn considerable attention, emerging research shows that organoantimony(III) reagents may also act as potent Lewis acids. By comparing the properties of $SbPh_3$ (**57**), $Sb(C_6F_5)_3$ (**58**), and $SbAr^F_3$ (**59**) with those of their tetrachlorocatecholate analogs $SbPh_3Cat$ (**60**), $Sb(C_6F_5)_3Cat$ (**61**), and $SbAr^F_3Cat$ (**62**, Cat = *o*-$O_2C_6Cl_4$, Ar^F = 3,5-$(CF_3)_2C_6H_3$), we have demonstrated that the Lewis acidity of the electron deficient organoantimony(III) reagents can be readily enhanced by oxidation to the +V state as verified by binding studies with triphenyl phosphine oxide. Computational studies have shown an increase in FIA of 110-150 kJ/mol from the +III to the +V states. These Lewis acidity trend is also corroborated by the catalytic activity of these compounds in the transfer hydrogenation reaction that occurs between Hantzsch ester and N-benzylideneaniline or quinoline, as well as in the Ritter-like reaction involving benzhydryl bromide, acetonitrile and water. The results are rationalized by explaining that oxidation of the antimony center leads to a lowering of the accepting σ* orbital and a deeper carving of the associated σ-hole.

7.2 On the synthesis and properties of triarylhalostibonium cations

As part of our fundamental interest in the chemistry of main group Lewis acids, we decided to target stibonium cations whose Lewis acidity is enhanced by the presence of a halogen substituent directly bound to antimony. Starting from $Ph_3Sb(OTf)_2$ (**63**) and $Mes_3Sb(OTf)_2$ (**64**), we successfully prepared the triflate derivatives $Ph_3SbF(OTf)$ (**65**) and $Mes_3SbF(OTf)$ (**66**). We also synthesized the hexachloroantimonate salt of $[Mes_3SbCl]^+$ (**68**), an analog of the known $[Ph_3SbCl][SbCl_6]$ (**67**). While a direct interaction is observed between the anion and the stibonium center in compounds **65-67**, compound **68** exists as an ionic solid with the four coordinate $[Mes_3SbCl]^+$ stibonium cation separated from the $[SbCl_6]^-$ anion. The structural difference observed between the two hexachloroantimonate derivatives **67** and **68** is ascribed to the increased steric protection provided by the larger mesityl substituents. To understand how these structural differences affect the properties of these antimony species, we have compared their catalytic activity in two simple reactions, namely the polymerization of THF and the Friedel-Craft dimerization of 1,1-diphenlyethylene. These studies show that **67** is the most active catalyst for both reactions thus suggesting that the reactivity of these species is controlled both by the coordinating nature of the counteranions and the steric accessibility of the reactive antimony center.

7.3 Influence of the catalyst structure in the cycloaddition of isocyanates to oxiranes promoted by tetraarylstibonium cations

In the context of our work on electron deficient Group 15 cations as Lewis acid catalysts, we have also synthesized the triflate salts of a series of tetraarylstibonium cations of general formula $[ArSbPh_3]^+$ with Ar = Mes (**73**$^+$), *o*-(dimethylamino)phenyl (**74**$^+$), and *o*-(dimethylaminomethyl)phenyl (**75**$^+$). These new cationic antimony derivatives, along with the known $[Ph_4Sb]^+$ (**70**$^+$), 1-naphthyltriphenylstibonium (**71**$^+$), and $[(Ant)SbPh_3][OTf]$ (**72**$^+$) have been evaluated as catalysts for the cycloaddition of oxiranes and isocyanates under mild conditions. While all stibonium cations favor the 3,4-oxazolidinone products, the reactivity of **74**$^+$ and **75**$^+$ are hindered by the ancillary amino donor which quenches the Lewis acidity of the antimony center. Overall, **73**$^+$ is found to be the most selective catalyst that results in a yield of 46% and a regioselective ratio of 7.3: 1 in the cycloaddition of propylene oxide and phenyl isocyanide at 10 mol% catalyst loading under mild conditions. The efficiency of **73**$^+$ is assigned to the steric hindrance of the mesityl ligand.

7.4 Catalytic transfer hydrogenation by bifunctional pnictogen-based Lewis acidic dications

Bifunctional Lewis acidic Group 15 compounds have attracted growing interest in catalysis due to the observation of chelation effects in their interactions with small molecules. In this chapter, we investigated a series of *ortho*-phenylene based mono- and bis- cationic pnictogen-containing compounds, namely $[o\text{-}(MePPh_2)C_6H_4SbPh_2]^+$ (**80**$^+$),

[*o*-(PPh_2)$C_6H_4SbPh_3$]$^+$ (**81**$^+$), and [*o*-($MePPh_2$)$C_6H_4SbPh_3$]$^{2+}$ (**82**$^{2+}$). The activity of these compounds as catalysts in the hydrogenation of quinolines by Hantzsch ester was compared to that of the previously reported bis-stibonium dication [*o*-($MeSbPh_2$)$C_6H_4SbPh_2Me$]$^{2+}$ (**83**$^{2+}$). Simple monodentate pnictogen cations [Ph_4Sb]$^+$ (**70**$^+$) and [Ph_3MeP]$^+$ (**79**$^+$) were also included in this comparative study. Consistent with the Lewis acidity of these pnictogen cations, the catalytic activity of these compounds increase in the order Sb dication > Sb monocation > P monocation, with compound **83**$^{2+}$ being the best catalyst. Computational analysis suggests that the bifunctional Lewis acid catalyst doubly activate the substrate via a three-center two-electron interaction involving the nitrogen lone pair and the two Lewis acidic antimony centers.

7.5 Computational studies of the OFF-ON fluorescence sensing of fluoride by donor-antimony(V) Lewis acids

A series of triarylmethylstibonium Lewis acids of general formula [Ph_2MeSb-(*p*-(C_6H_4))-FLUO]$^+$ bearing a peripheral electron rich fluorophore (FLUO = 10*H*-phenoxazine (**85**$^+$), diphenylamine (**86**$^+$), and 9*H*-carbazole (**87**$^+$)) have been synthesized and investigated for the fluorescence turn-on sensing of fluoride anions. Treatment of the stibonium cations with fluoride anions leads to the corresponding fluorostiboranes (**85**-F–**87**-F). While the stibonium cations are almost non-emissive, the fluorostiboranes display fluorophore-centered emissions arising from the corresponding π–π* excited state. The carbazole containing derivative **87**$^+$ exhibits the most intense fluorescence turn-on response. It also displays a high binding constant ($K > 10^7$ M^{-1}) in CH_3CN and shows

compatibility with protic media such as MeOH (K = 950(±50) M^{-1}). Computational studies aimed at identifying the origin of the turn-on response show that the excited state of the stibonium cations is best described as charge transfer in nature with the π-system of the fluorophore acting as the donor and the π*–σ* system of the stibonium unit acting as the acceptor. This π(FLUO)–π*/σ*[Ph_2MeSb-(*p*-(C_6H_4))] excited state is non-emissive making these cations dark in the absence of fluoride anions. Conversion to the fluorostiboranes occurs via donation of a fluoride lone pair into the antimony-centered σ*. Formation of this Sb–F bond modifies the electronic structure of the platform and restores the emissive π–π* excited state of the fluorophore thus accounting for the observed OFF-ON fluorescence response.

7.6 Outlook

Despite the versatile redox chemistry of heavy main-group metals such as antimony, cyclic voltammetry data has rarely been collected for organoantimony compounds. This is partially due to the fact that the one-electron oxidation products of stibines, as well as the one-electron reduction products of stiboranes, are highly reactive radical species and easily undergo side reactions, resulting in irreversible events in their voltammograms. However, the isolation of organoantimony radicals **29**$^{\bullet+}$ and **30**$^{\bullet+}$ demonstrated the possibility to stabilize such radical species. It is also known that quinone-oxidized stiboranes such as the catecholates **14** and **15** have the ability to activate and reversibly bind molecular oxygen. Coupling these ideas together, there might be the possibility of using sterically protected organoantimony(V) catecholates as

electrocatalysts for oxygen or CO_2 reduction. Alternatively, taking advantage of the oxophilic property of antimony, catecholates of organoantimony(III) could have potential as electrocatalysts for oxygen evolution reactions.

In terms of catalysis design, we note that there are only a few instances where chiral Lewis acidic antimony-containing compounds act as organic catalysts, whereas the library of chiral phosphorus-containing catalysts keeps growing and is no longer limited to chiral phosphates. For example, the binaphthyl-modified phosphonium cation (**88**$^+$) is reported to catalyze the asymmetric amination of β-keto esters for up to 99% yield and 90% *ee* (Figure 114).[228] The synthesis of the BINOL stiborane **89** or stibonium cation **90** emerges as a stimulating possibility with a broad range of applications in organic synthesis.

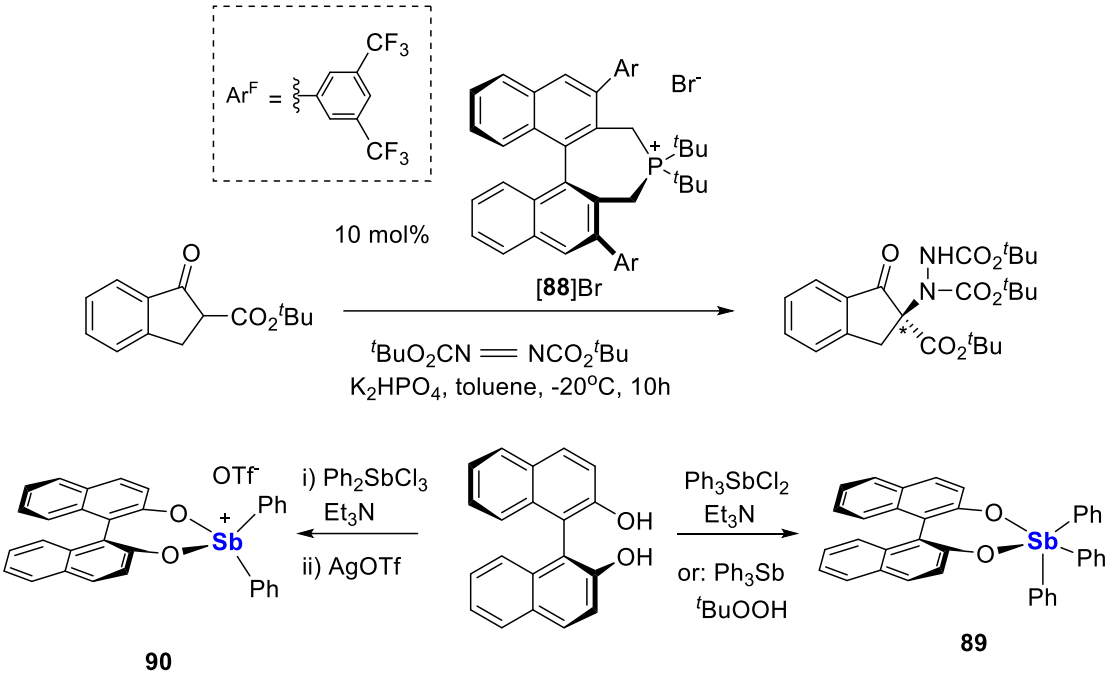

Figure 114. Chiral phosphonium **88**$^+$ catalyzed asymmetric amination of β-keto esters, and proposed chiral organoantimony compounds such as **89** and **90**.

Meanwhile, the potential remains to expand the applications of antimony Lewis acids in a variety of catalytic reactions. Since it has been demonstrated that the ambiphilic antimony-phosphorus compound **17** selectively binds formaldehyde,[36] we could explore reactions that involve formaldehyde as substrates such as allylations[107] or acetalizations.[109] Moreover, it has been known that in the reaction of oxiranes with carbon dioxide, the nature of the catalyst acid-base pair determines the product to be either the cycloaddition product or a co-polymer. Typically, using a mild Lewis acid and a weak Lewis base as co-catalyst would favor chain growth and eventually result in polymeric products. For example, the reaction between oxetane and CO_2 in Figure 17 is reported to result in

polymerization products if catalyzed by Ph_3SbI_2, however it was not determined whether the product is a polyether or a copolymer of oxetane and carbon dioxide.[103] Recently, Zhang and Darensbourg *et al.* reported the copolymerization of carbonyl sulfide and oxiranes catalyzed by triethyl borane paired with a Lewis base such as 1,8-diazabicyclo[5.4.0]undec-7-ene (DBU).[229] Their results show an almost quantitative selectivity for the perfectly alternating co-polymer over the cycloaddition products (Figure 115). It would be interesting to test the selectivity of stibonium cations as catalysts for this reaction under similar polymerization conditions.

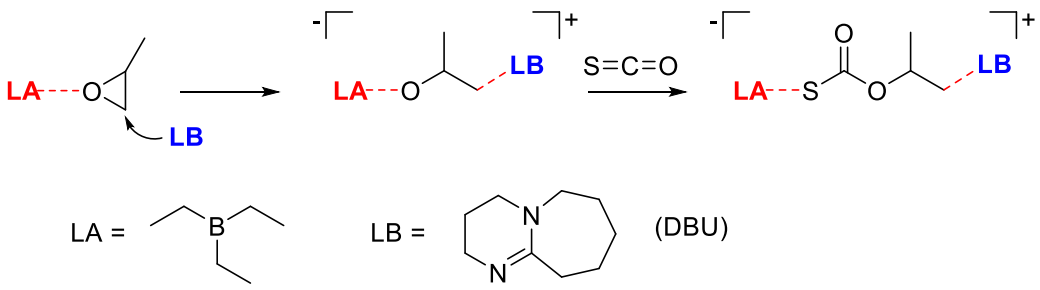

Figure 115. Conceptual copolymerization catalyzed by Lewis pairs.

7.7 Conclusion

In conclusion, we have synthesized a variety of neutral and cationic antimony containing compounds, evaluated their Lewis acidity and found that the oxidation states of antimony and the bulk/electronic properties of the ligands affect their reactivity. We have tested these electrophilic organoantimony compounds in a range of catalytic systems such as the transfer hydrogenation of imine and quinoline derivatives using Hantzsch ester,

the dimerization of 1,1-diphenylethylene, the polymerization of THF, and the cycloaddition of the oxiranes with isocyanates. Meanwhile, we have also studied the mechanism of the fluorescence turn-on response displayed by stibonium cations upon fluoride binding. We are positive that the development of these neutral or cationic antimony-based compounds will keep growing in the future with potential applications in small molecule activations, electrochemistry, enantioselective catalysis, and polymer chemistry.

REFERENCES

(1) Power, P. P., *Nature* **2010,** *463*, 171-177.

(2) Krossing, I.; Raabe, I., *Chem. Eur. J.* **2004,** *10*, 5017-5030.

(3) Piers, W. E.; Chivers, T., *Chem. Soc. Rev.* **1997,** *26*, 345-354.

(4) Hirai, M.; Gabbaï, F. P., *Angew. Chem. Int. Ed.* **2015,** *54*, 1205-1209.

(5) Hudnall, T. W.; Kim, Y.-M.; Bebbington, M. W. P.; Bourissou, D.; Gabbaï, F. P., *J. Am. Chem. Soc.* **2008,** *130*, 10890-+.

(6) Zhao, H. Y.; Gabbaï, F. P., *Nature Chem.* **2010,** *2*, 984-990.

(7) Caputo, C. B.; Hounjet, L. J.; Dobrovetsky, R.; Stephan, D. W., *Science* **2013,** *341*, 1374-7.

(8) Lim, J. Y. C.; Beer, P. D., *Chem* **2018,** *4*, 731-783.

(9) Benz, S.; Poblador-Bahamonde, A. I.; Low-Ders, N.; Matile, S., *Angew. Chem. Int. Ed.* **2018,** *57*, 5408-5412.

(10) Clark, T.; Hennemann, M.; Murray, J. S.; Politzer, P., *J. Mol. Model.* **2007,** *13*, 291-296.

(11) S., M. J.; Pat, L.; Peter, P., *Int. J. Quantum Chem* **2007,** *107*, 2286-2292.

(12) Hirai, M.; Gabbaï, F. P., *Chem. Sci.* **2014,** *5*, 1886-1893.

(13) Pan, B.; Gabbaï, F. P., *J. Am. Chem. Soc.* **2014,** *136*, 9564-9567.

(14) Ke, I.-S.; Myahkostupov, M.; Castellano, F. N.; Gabbaï, F. P., *J. Am. Chem. Soc.* **2012,** *134*, 15309-11.

(15) Doherty, N. M.; Hoffmann, N. W., *Chem. Rev.* **1991,** *91*, 553-573.

(16) Levason, W.; Reid, G., *Coord. Chem. Rev.* **2006,** *250*, 2565-2594.

(17) Aroney, M. J.; Buys, I. E.; Davies, M. S.; Hambley, T. W., *J. Chem. Soc., Dalton Trans.* **1994**, 2827-2834.

(18) Gutmann, V., *Coord. Chem. Rev.* **1976,** *18*, 225-255.

(19) Milićev, S.; Hadĉi, D., *Inorg. Chim. Acta* **1977,** *21*, 201-207.

(20) Qiu, J.; Song, B.; Li, X.; Cozzolino, A. F., *Phys. Chem. Chem. Phys.* **2018,** *20*, 46-50.

(21) Yang, H.; Gabbaï, F. P., *J. Am. Chem. Soc.* **2014,** *136*, 10866-10869.

(22) Jones, J. S.; Gabbaï, F. P., *Chem. Eur. J* **2017,** *23*, 1136-1144.

(23) Olah, G. A.; Schlosberg, R. H., *J. Am. Chem. Soc.* **1968,** *90*, 2726-2727.

(24) Olah, G. A.; Comisarow, M. B.; Cupas, C. A.; Pittman, C. U., *J. Am. Chem. Soc.* **1965,** *87*, 2997-2998.

(25) Wheatley, P. J., *J. Chem. Soc.* **1964**, 3718-23.

(26) Beauchamp, A. L.; Bennett, M. J.; Cotton, F. A., *J. Am. Chem. Soc.* **1968,** *90*, 6675-6680.

(27) García-Monforte, M. A.; Alonso, P. J.; Ara, I.; Menjón, B.; Romero, P., *Angew. Chem. Int. Ed.* **2012,** *51*, 2754-2757.

(28) Holmes, R. R.; Day, R. O.; Chandrasekhar, V.; Holmes, J. M., *Inorg. Chem.* **1987,** *26*, 157-163.

(29) Christianson, A. M.; Rivard, E.; Gabbaï, F. P., *Organometallics* **2017**.

(30) Chen, C.-H.; Gabbaï, F. P., *Angew. Chem. Int. Ed.* **2017,** *56*, 1799-1804.

(31) Abakumov, G. A.; Poddel'sky, A. I.; Grunova, E. V.; Cherkasov, V. K.; Fukin, G. K.; Kurskii, Y. A.; Abakumova, L. G., *Angew. Chem. Int. Ed.* **2005,** *44*, 2767-2771.

(32) Bordner, J.; Doak, G. O.; Everett, T. S., *J. Am. Chem. Soc.* **1986,** *108*, 4206-4213.

(33) Cherkasov, V. K.; Abakumov, G. A.; Grunova, E. V.; Poddel'sky, A. I.; Fukin, G. K.; Baranov, E. V.; Kurskii, Y. V.; Abakumova, L. G., *Chem. Eur. J* **2006,** *12*, 3916-3927.

(34) Poddel'sky, A. I.; Smolyaninov, I. V.; Kurskii, Y. A.; Berberova, N. T.; Cherkasov, V. K.; Abakumov, G. A., *Russ. Chem. Bull.* **2009,** *58*, 532-537.

(35) Cherkasov, V. K.; Grunova, E. V.; Poddel'sky, A. I.; Fukin, G. K.; Kurskii, Y. A.; Abakumova, L. G.; Abakumov, G. A., *J. Organomet. Chem.* **2005,** *690*, 1273-1281.

(36) Tofan, D.; Gabbaï, F. P., *Chem. Sci.* **2016,** *7*, 6768-6778.

(37) Yang, H.; Gabbaï, F. P., *J. Am. Chem. Soc.* **2015,** *137*, 13425-13432.

(38) Wade, C. R.; Gabbaï, F. P., *Angewandte Chemie-International Edition* **2011,** *50*, 7369-7372.

(39) Jones, J. S.; Wade, C. R.; Gabbaï, F. P., *Organometallics* **2015**.

(40) Sen, S.; Ke, I.-S.; Gabbaï, F. P., *Inorg. Chem.* **2016,** *55*, 9162-9172.

(41) Jones, J. S.; Wade, C. R.; Gabbaï, F. P., *Angew. Chem. Int. Ed.* **2014**, n/a-n/a.

(42) Sen, S.; Ke, I.-S.; Gabbaï, F. P., *Organometallics* **2017,** *36*, 4224-4230.

(43) Ke, I. S.; Gabbaï, F. P., *Inorg. Chem.* **2013,** *52*, 7145-7151.

(44) Ke, I.-S.; Jones, J. S.; Gabbaï, F. P., *Angew. Chem. Int. Ed.* **2014,** *53*, 2633-2637.

(45) Jones, J. S.; Gabbaï, F. P., *Acc. Chem. Res.* **2016,** *49*, 857-867.

(46) Dostál, L.; Novák, P.; Jambor, R.; Růžička, A.; Císařová, I.; Jirásko, R.; Holeček, J., *Organometallics* **2007,** *26*, 2911-2917.

(47) Dostál, L.; Jambor, R.; Jirásko, R.; Padělková, Z.; Růžička, A.; Holeček, J., *J. Organomet. Chem.* **2010,** *695*, 392-397.

(48) Chitnis, S. S.; Burford, N.; Ferguson, M. J., *Angew. Chem. Int. Ed.* **2013,** *52*, 2042-2045.

(49) Power, P. P., *Chem. Rev.* **2003,** *103*, 789-810.

(50) Soleilhavoup, M.; Bertrand, G., *Acc. Chem. Res.* **2015,** *48*, 256-266.

(51) Martin, C. D.; Soleilhavoup, M.; Bertrand, G., *Chem. Sci.* **2013,** *4*, 3020-3030.

(52) Li, T.; Wei, H.; Fang, Y.; Wang, L.; Chen, S.; Zhang, Z.; Zhao, Y.; Tan, G.; Wang, X., *Angew. Chem. Int. Ed.* **2016,** *56*, 632-636.

(53) Pan, X.; Chen, X.; Li, T.; Li, Y.; Wang, X., *J. Am. Chem. Soc.* **2013,** *135*, 3414-3417.

(54) Goel, R. G., *Can. J. Chem.* **1969,** *47*, 4607-4612.

(55) Bowen, L. H.; Rood, R. T., *J. Inorg. Nucl. Chem.* **1966,** *28*, 1985-1990.

(56) Jean, M., *Anal. Chim. Acta* **1971,** *57*, 438-439.

(57) Hirai, M.; Myahkostupov, M.; Castellano, F. N.; Gabbaï, F. P., *Organometallics* **2016,** *35*, 1854-1860.

(58) Sharutin, V. V.; Sharutina, O. K.; Pakusina, A. P.; Platonova, T. P.; Gerasimenko, A. V.; Bukvetskii, B. V.; Pushilin, M. A., *Russ. J. Coord. Chem.* **2004,** *30*, 13-22.

(59) Sharutin, V. V.; Sharutina, O. K.; Gabitova, D. M.; Shaikhvaleeva, S. Y., *Russ. J. Inorg. Chem.* **2017,** *62*, 55-62.

(60) Sharutin, V. V.; Molokova, O. V.; Sharutina, O. K.; Gerasimenko, A. V.; Pushilin, M. A., *Russ. J. Gen. Chem.* **2004,** *74*, 1485-1491.

(61) Preut, H.; Ruther, R.; Huber, F., *Acta Crystallographica Section C* **1986,** *42*, 1154-1157.

(62) Verma, S.; Shlichta, P. J., *Prog. Cryst. Growth Charact. Mater.* **2008,** *54*, 1-120.

(63) Robertson, A. P. M.; Burford, N.; McDonald, R.; Ferguson, M. J., *Angew. Chem. Int. Ed.* **2014,** *53*, 3480-3483.

(64) Robertson, A. P. M.; Chitnis, S. S.; Jenkins, H. A.; McDonald, R.; Ferguson, M. J.; Burford, N., *Chem. Eur. J.* **2015,** *21*, 7902-7913.

(65) Sharutin, V. V.; Sharutina, O. K.; Senchurin, V. S., *Russ. J. Inorg. Chem.* **2015,** *60*, 166-169.

(66) Sharutin, V. V.; Sharutina, O. K.; Senchurin, V. S., *Russ. J. Inorg. Chem.* **2016,** *61*, 708-711.

(67) Yang, X.; Stern, C. L.; Marks, T. J., *J. Am. Chem. Soc.* **1994,** *116*, 10015-31.

(68) Scollard, J. D.; McConville, D. H., *J. Am. Chem. Soc.* **1996,** *118*, 10008-10009.

(69) Ishihara, K.; Funahashi, M.; Hanaki, N.; Miyata, M.; Yamamoto, H., *Synlett* **1994,** *1994*, 963-964.

(70) Parks, D. J.; Piers, W. E., *J. Am. Chem. Soc.* **1996,** *118*, 9440-9441.

(71) Li, P.; Yamamoto, H., *J. Am. Chem. Soc.* **2009,** *131*, 16628-16629.

(72) Wang, X.; Chakrapani, H.; Madine, J. W.; Keyerleber, M. A.; Widenhoefer, R. A., *J. Org. Chem.* **2002,** *67*, 2778-2788.

(73) Chen, E. Y.-X.; Marks, T. J., *Chem. Rev.* **2000,** *100*, 1391-1434.

(74) Marciniec, B., **2009,** *1*.

(75) North, M.; Usanov, D. L.; Young, C., *Chem. Rev.* **2008,** *108*, 5146-5226.

(76) Rao, B.; Kinjo, R., *Chemistry – An Asian Journal* **2018,** *13*, 1279-1292.

(77) Rohde, V. H. G.; Müller, M. F.; Oestreich, M., *Organometallics* **2015,** *34*, 3358-3373.

(78) Rohde, V. H. G.; Pommerening, P.; Klare, H. F. T.; Oestreich, M., *Organometallics* **2014,** *33*, 3618-3628.

(79) Simonneau, A.; Biberger, T.; Oestreich, M., *Organometallics* **2015,** *34*, 3927-3929.

(80) Lipke, M. C.; Tilley, T. D., *J. Am. Chem. Soc.* **2014,** *136*, 16387-16398.

(81) Liberman-Martin, A. L.; Bergman, R. G.; Tilley, T. D., *J. Am. Chem. Soc.* **2015,** *137*, 5328-5331.

(82) Chase, P. A.; Welch, G. C.; Jurca, T.; Stephan, D. W., *Angew. Chem. Int. Ed.* **2007,** *46*, 8050-8053.

(83) Courtemanche, M.-A.; Légaré, M.-A.; Maron, L.; Fontaine, F.-G., *J. Am. Chem. Soc.* **2013,** *135*, 9326-9329.

(84) Stephan, D. W.; Erker, G., *Angew. Chem. Int. Ed.* **2015,** *54*, 6400-6441.

(85) Lam, J.; Szkop, K. M.; Mosaferi, E.; Stephan, D. W., *Chem. Soc. Rev.* **2018**.

(86) Hounjet, L. J.; Caputo, C. B.; Stephan, D. W., *Angew. Chem. Int. Ed.* **2012,** *51*, 4714-4717.

(87) Teruaki, M.; Shigekazu, M.; Kouichi, K., *Chem. Lett.* **1989,** *18*, 993-996.

(88) Teruaki, M.; Kouichi, K.; Shigekazu, M., *Chem. Lett.* **1989,** *18*, 1397-1400.

(89) Barrado, A. G.; Bayne, J. M.; Johnstone, T. C.; Lehmann, C. W.; Stephan, D. W.; Alcarazo, M., *Dalton Trans.* **2017,** *46*, 16216-16227.

(90) Terada, M.; Kouchi, M., *Tetrahedron* **2006,** *62*, 401-409.

(91) Córdoba, R.; Plumet, J. n., *Tetrahedron Lett.* **2003,** *44*, 6157-6159.

(92) Holthausen, M. H.; Mehta, M.; Stephan, D. W., *Angew. Chem. Int. Ed.* **2014,** *53*, 6538-6541.

(93) Zhu, J.; Pérez, M.; Stephan, D. W., *Angew. Chem. Int. Ed.* **2016,** *55*, 8448-8451.

(94) Pérez, M.; Hounjet, L. J.; Caputo, C. B.; Dobrovetsky, R.; Stephan, D. W., *J. Am. Chem. Soc.* **2013,** *135*, 18308-18310.

(95) Perez, M.; Caputo, C. B.; Dobrovetsky, R.; Stephan, D. W., *Proc. Natl. Acad. Sci. U. S. A.* **2014,** *111*, 10917-10921.

(96) vom Stein, T.; Peréz, M.; Dobrovetsky, R.; Winkelhaus, D.; Caputo, C. B.; Stephan, D. W., *Angew. Chem. Int. Ed.* **2015,** *54*, 10178-10182.

(97) LaFortune, J. H. W.; Szkop, K. M.; Farinha, F. E.; Johnstone, T. C.; Postle, S.; Stephan, D. W., *Dalton Trans.* **2018,** *47*, 11411-11419.

(98) Mehta, M.; Holthausen, M. H.; Mallov, I.; Pérez, M.; Qu, Z.-W.; Grimme, S.; Stephan, D. W., *Angew. Chem.* **2015,** *127*, 8368-8372.

(99) Fasano, V.; LaFortune, J. H. W.; Bayne, J. M.; Ingleson, M. J.; Stephan, D. W., *Chem. Commun.* **2018,** *54*, 662-665.

(100) Nomura, R.; Hasegawa, Y.; Ishimoto, M.; Toyosaki, T.; Matsuda, H., *J. Org. Chem.* **1992,** *57*, 7339-7342.

(101) Xia, J.; Qiu, R.; Yin, S.; Zhang, X.; Luo, S.; Au, C.-T.; Xia, K.; Wong, W.-Y., *J. Organomet. Chem.* **2010,** *695*, 1487-1492.

(102) Zhang, X.; Yin, S.; Qiu, R.; Xia, J.; Dai, W.; Yu, Z.; Au, C.-T.; Wong, W.-Y., *J. Organomet. Chem.* **2009,** *694*, 3559-3564.

(103) Baba, A.; Kashiwagi, H.; Matsuda, H., *Tetrahedron Lett.* **1985,** *26*, 1323-1324.

(104) Baba, A.; Fujiwara, M.; Matsuda, H., *Tetrahedron Lett.* **1986,** *27*, 77-80.

(105) Fujiwara, M.; Baba, A.; Matsuda, H., *J. Heterocycl. Chem.* **1988,** *25*, 1351-1357.

(106) Fujiwara, M.; Baba, A.; Matsuda, H., *Bull. Chem. Soc. Jpn.* **1990,** *63*, 1069-1073.

(107) Li, N.; Qiu, R.; Zhang, X.; Chen, Y.; Yin, S.-F.; Xu, X., *Tetrahedron* **2015,** *71*, 4275-4281.

(108) Arias Ugarte, R.; Devarajan, D.; Mushinski, R. M.; Hudnall, T. W., *Dalton Trans.* **2016,** *45*, 11150-61.

(109) Arias Ugarte, R.; Hudnall, T. W., *Green Chem.* **2017,** *19*, 1990-1998.

(110) Krossing, I.; Raabe, I., *Angew. Chem. Int. Ed.* **2004,** *43*, 2066-2090.

(111) Katz, H. E., *J. Am. Chem. Soc.* **1985,** *107*, 1420-1421.

(112) Katz, H. E., *J. Org. Chem.* **1985,** *50*, 5027-5032.

(113) Ooi, T.; Takahashi, M.; Yamada, M.; Tayama, E.; Omoto, K.; Maruoka, K., *J. Am. Chem. Soc.* **2004,** *126*, 1150-1160.

(114) Jiang, C.; Blacque, O.; Berke, H., *Chem. Commun.* **2009**, 5518-5520.

(115) Benz, S.; López-Andarias, J.; Mareda, J.; Sakai, N.; Matile, S., *Angew. Chem. Int. Ed.* **2017,** *56*, 812-815.

(116) Holthausen, M. H.; Hiranandani, R. R.; Stephan, D. W., *Chem. Sci.* **2015,** *6*, 2016-2021.

(117) Mallov, I.; Stephan, D. W., *Dalton Trans.* **2016,** *45*, 5568-5574.

(118) Usui, K.; Ando, M.; Yokogawa, D.; Irle, S., *J. Phys. Chem. A* **2015,** *119*, 12693-12698.

(119) Christianson, A. M.; Gabbaï, F. P., *Chem. Commun.* **2017,** *53*, 2471-2474.

(120) Dunn, N. L.; Ha, M.; Radosevich, A. T., *J. Am. Chem. Soc.* **2012,** *134*, 11330-11333.

(121) Cui, J.; Li, Y.; Ganguly, R.; Inthirarajah, A.; Hirao, H.; Kinjo, R., *J. Am. Chem. Soc.* **2014,** *136*, 16764-16767.

(122) Holthausen, M. H.; Bayne, J. M.; Mallov, I.; Dobrovetsky, R.; Stephan, D. W., *J. Am. Chem. Soc.* **2015,** *137*, 7298-7301.

(123) Perez, M.; Qu, Z.-W.; Caputo, C. B.; Podgorny, V.; Hounjet, L. J.; Hansen, A.; Dobrovetsky, R.; Grimme, S.; Stephan, D. W., *Chem. Eur. J* **2015,** *21*, 6491-6500.

(124) Reichl, K. D.; Dunn, N. L.; Fastuca, N. J.; Radosevich, A. T., *J. Am. Chem. Soc.* **2015,** *137*, 5292-5295.

(125) Zhao, W.; Yan, P. K.; Radosevich, A. T., *J. Am. Chem. Soc.* **2015,** *137*, 616-619.

(126) Adams, M. R.; Tien, C. H.; McDonald, R.; Speed, A. W. H., *Angew. Chem. Int. Ed.* **2017,** *56*, 16660-16663.

(127) Micheal, G.; M., F. C.; H., S. S.; Johannes, B.; Martin, N.; Dietrich, G., *Chem. Eur. J* **2017,** *23*, 11560-11569.

(128) Stephan, D. W., *Angew. Chem. Int. Ed.* **2017,** *56*, 5984-5992.

(129) Hynes, T.; Welsh, E. N.; McDonald, R.; Ferguson, M. J.; Speed, A. W. H., *Organometallics* **2018,** *37*, 841-844.

(130) Rao, B.; Chong, C. C.; Kinjo, R., *J. Am. Chem. Soc.* **2018,** *140*, 652-656.

(131) Hirai, M.; Cho, J.; Gabbaï, F. P., *Chem. Eur. J* **2016,** *22*, 6537-6541.

(132) Chitnis, S. S.; Sparkes, H. A.; Annibale, V. T.; Pridmore, N. E.; Oliver, A. M.; Manners, I., *Angew. Chem. Int. Ed.* **2017,** *56*, 9536-9540.

(133) Yang, M.; Gabbaï, F. P., *Inorg. Chem.* **2017,** *56*, 8644-8650.

(134) Yang, M.; Pati, N.; Belanger-Chabot, G.; Hirai, M.; Gabbaï, F. P., *Dalton Trans.* **2018,** *47*, 11843-11850.

(135) Kumar, A.; Yang, M.; Kim, M.; Gabbaï, F. P.; Lee, M. H., *Organometallics* **2017,** *36*, 4901-4907.

(136) Jones, J. S.; Wade, C. R.; Yang, M.; Gabbaï, F. P., *Dalton Trans.* **2017,** *46*, 5598-5604.

(137) Ohkata, K.; Takemoto, S.; Ohnishi, M.; Akiba, K.-y., *Tetrahedron Lett.* **1989,** *30*, 4841-4844.

(138) Carmalt, C. J.; Cowley, A. H.; Culp, R. D.; Jones, R. A.; Kamepalli, S.; Norman, N. C., *Inorg. Chem.* **1997,** *36*, 2770-2776.

(139) Christianson, A. M.; Gabbaï, F. P., *Organometallics* **2017,** *36*, 3013-3015.

(140) Schmauck, J.; Breugst, M., *Org. Biomol. Chem.* **2017,** *15*, 8037-8045.

(141) Pascoe, D. J.; Ling, K. B.; Cockroft, S. L., *J. Am. Chem. Soc.* **2017,** *139*, 15160-15167.

(142) Fild, M.; Glemser, O.; Christoph, G., *Angew. Chem.* **1964,** *76*, 953-953.

(143) Sidky, M. M.; Maharan, M. R.; Abdu, W. M., *Phosphorus and Sulfur and the Related Elements* **1983,** *15*, 129-135.

(144) Yasuike, S.; Nakata, K.; Qin, W.; Matsumura, M.; Kakusawa, N.; Kurita, J., *J. Organomet. Chem.* **2015,** *788*, 9-16.

(145) Beckett, M. A.; Brassington, D. S.; Coles, S. J.; Hursthouse, M. B., *Inorg. Chem. Commun.* **2000,** *3*, 530-533.

(146) Alvarez, S., *Dalton Trans.* **2013,** *42*, 8617-8636.

(147) Glendening, E. D.; Badenhoop, J. K.; Reed, A. E.; Carpenter, J. E.; Bohmann, J. A.; Morales, C. M.; Weinhold, F., *NBO 5.9*, Theoretical Chemistry Institute, University of Wisconsin, Madison, WI, 2011.

(148) Benz, S.; Mareda, J.; Besnard, C.; Sakai, N.; Matile, S., *Chem. Sci.* **2017,** *8*, 8164-8169.

(149) Itoh, T.; Nagata, K.; Miyazaki, M.; Ishikawa, H.; Kurihara, A.; Ohsawa, A., *Tetrahedron* **2004,** *60*, 6649-6655.

(150) Walter, S. M.; Kniep, F.; Herdtweck, E.; Huber, S. M., *Angew. Chem. Int. Ed.* **2011,** *50*, 7187-7191.

(151) Wonner, P.; Vogel, L.; Düser, M.; Gomes, L.; Kniep, F.; Mallick, B.; Werz Daniel, B.; Huber Stefan, M., *Angew. Chem. Int. Ed.* **2017,** *56*, 12009-12012.

(152) Zhao, Y.; Beuchat, C.; Domoto, Y.; Gajewy, J.; Wilson, A.; Mareda, J.; Sakai, N.; Matile, S., *J. Am. Chem. Soc.* **2014,** *136*, 2101-2111.

(153) Lu, T.; Wheeler, S. E., *Org. Lett.* **2014,** *16*, 3268-3271.

(154) Heinen, F.; Engelage, E.; Dreger, A.; Weiss, R.; Huber Stefan, M., *Angew. Chem. Int. Ed.* **2018,** *57*, 3830-3833.

(155) Seidl, T. L.; Stuart, D. R., *J. Org. Chem.* **2017,** *82*, 11765-11771.

(156) Blanco-Ania, D.; Hermkens, P. H. H.; Sliedregt, L. A. J. M.; Scheeren, H. W.; Rutjes, F. P. J. T., *Tetrahedron* **2009,** *65*, 5393-5401.

(157) Bruker, SAINTPlus. *Data Reduction and Correction Program v. 6.2*, Bruker AXS, Madison, Wisconsin, USA, 2001.

(158) Frisch, M. J.; Trucks, G. W.; Schlegel, H. B.; Scuseria, G. E.; Robb, M. A.; Cheeseman, J. R.; Scalmani, G.; Barone, V.; Mennucci, B.; Petersson, G. A.; Nakatsuji, H.; Caricato, M.; Li, X.; Hratchian, H. P.; Izmaylov, A. F.; Bloino, J.; Zheng, G.; Sonnenberg, J. L.; Hada, M.; Ehara, M.; Toyota, K.; Fukuda, R.; Hasegawa, J.; Ishida, M.; Nakajima, T.; Honda, Y.; Kitao, O.; Nakai, H.; Vreven, T.; Montgomery, J., J. A.; ; Peralta, J. E.; Ogliaro, F.; Bearpark, M.; Heyd, J. J.; Brothers, E.; Kudin, K. N.; Staroverov, V. N.; Kobayashi, R.; Normand, J.; Raghavachari, K.; Rendell, A.; Burant, J. C.; Iyengar, S. S.; Tomasi, J.; Cossi, M.; Rega, N.; Millam, J. M.; Klene, M.; Knox, J. E.; Cross, J. B.; Bakken, V.; Adamo, C.; Jaramillo, J.; Gomperts, R.; Stratmann, R. E.; Yazyev, O.; Austin, A. J.; Cammi, R.; Pomelli, C.; Ochterski, J. W.; Martin, R. L.; Morokuma, K.; Zakrzewski, V. G.; Voth, G. A.; Salvador, P.; Dannenberg, J. J.; Dapprich, S.; Daniels, A. D.; Farkas, Ö.; Foresman, J. B.; Ortiz, J. V.; Cioslowski, J.; Fox, D. J., *Gaussian 09*, Revision D.01, Gaussian, Inc., Wallingford, CT: 2013.

(159) Becke, A. D., *J. Chem. Phys.* **1993,** *98*, 5648-5652.

(160) Stephens, P. J.; Devlin, F. J.; Chabalowski, C. F.; Frisch, M. J., *J. Phys. Chem.* **1994,** *98*, 11623-11627.

(161) Peterson, K. A., *J. Chem. Phys.* **2003,** *119*, 11099-11112.

(162) Metz, B.; Stoll, H.; Dolg, M., *J. Chem. Phys.* **2000,** *113*, 2563-2569.

(163) Manson, J.; Webster, C. E.; Pérez, L. M.; Hall, M. B., http://www.chem.tamu.edu/jimp2/index.html.

(164) Mukaiyama, T.; Matsui, S.; Kashiwagi, K., *Chem. Lett.* **1989,** *18*, 993-996.

(165) Li, Y.-Q.; Wang, P.; Liu, H.; Lu, Y.; Zhao, X.-L.; Liu, Y., *Green Chem.* **2016,** *18*, 1798-1806.

(166) Bayne, J. M.; Stephan, D. W., *Chem. Soc. Rev.* **2016,** *45*, 765-74.

(167) Olah, G. A.; Baker, E. B.; Evans, J. C.; Tolgyesi, W. S.; McIntyre, J. S.; Bastien, I. J., *J. Am. Chem. Soc.* **1964,** *86*, 1360-73.

(168) Jean, M., *Anal. Chim. Acta* **1971,** *57*, 438-439.

(169) Wade, C. R.; Gabbaï, F. P., *Organometallics* **2011,** *30*, 4479-4481.

(170) Frohn, H. J.; Maurer, H., *J. Fluorine Chem.* **1986,** *34*, 129-145.

(171) Nikitin, E. V. K., A. A.; Parakin, O. V.; Kargin, Yu. M., *Zh. Obshch. Khim.* **1982,** *52*, 2027-2029.

(172) Zhao, Y.; Truhlar, D., *Theor. Chem. Acc.* **2008,** *120*, 215-241.

(173) Hall, M.; Sowerby, D. B., *J. Chem. Soc., Dalton Trans.* **1983**, 1095-1099.

(174) Yang, L.; Powell, D. R.; Houser, R. P., *Dalton Trans.* **2007**, 955-964.

(175) Begley, M. J.; Sowerby, D. B., *Acta Crystallogr. Sect. C: Cryst. Struct. Commun.* **1993,** *49*, 1044-1046.

(176) Sharutin, V. V.; Sharutina, O. K.; Pakusina, A. P.; Smirnova, S. A.; Pushilin, M. A., *Russ. J. Coord. Chem.* **2005,** *31*, 108-114.

(177) Sharutin, V. V.; Sharutina, O. K.; Pakusina, A. P.; Platonova, T. P.; Zadachina, O. P.; Gerasimenko, A. V., *Russ. J. Coord. Chem.* **2003,** *29*, 89-92.

(178) Tsao, F. A.; Waked, A. E.; Cao, L.; Hofmann, J.; Liu, L.; Grimme, S.; Stephan, D. W., *Chem. Commun.* **2016,** *52*, 12418-12421.

(179) M. Ates, H. J. B., A. Soltani-Neshan, M. Tegeler, *Z. Naturforsch* **1986,** *41b*, 321-326.

(180) Zhao, X.-F.; Zhang, C., *Synthesis* **2007,** *2007*, 551-557.

(181) Rahman, A. F. M. M.; Murafuji, T.; Ishibashi, M.; Miyoshi, Y.; Sugihara, Y., *J. Organomet. Chem.* **2005,** *690*, 4280-4284.

(182) Bricklebank, N.; Godfrey, S. M.; Lane, H. P.; McAuliffe, C. A.; Pritchard, R. G., *J. Chem. Soc., Dalton Trans.* **1994**, 1759-1763.

(183) Chitnis, S. S.; Robertson, A. P. M.; Burford, N.; Patrick, B. O.; McDonald, R.; Ferguson, M. J., *Chem. Sci.* **2015**.

(184) Suter, R.; Sinclair, H.; Burford, N.; McDonald, R.; Ferguson, M. J.; Schrader, E., *Dalton Trans.* **2017,** *46*, 7681-7685.

(185) Burford, N.; Frazee, C.; McDonald, R.; Ferguson, M.; Patrick, B.; Decken, A., *Chem. Eur. J* **2018,** *24*, 4011-4013.

(186) Hudnall, T. W.; Gabbaï, F. P., *Chem. Commun.* **2008**, 4596-4597.

(187) Wade, C. R.; Gabbaï, F. P., *Dalton Trans.* **2009**, 9169-9175.

(188) Kim, Y.; Huh, H.-S.; Lee, M. H.; Lenov, I. L.; Zhao, H.; Gabbaï, F. P., *Chem. Eur. J.* **2011,** *17*, 2057-2062.

(189) Wade, C. R.; Ke, I.-S.; Gabbaï, F. P., *Angew. Chem. Int. Ed.* **2012,** *51*, 478-481.

(190) Zhao, H.; Leamer, L. A.; Gabbaï, F. P., *Dalton Trans.* **2013,** *42*, 8164-8178.

(191) Christianson, A. M.; Gabbaï, F. P., *Inorg. Chem.* **2016,** *55*, 5828-5835.

(192) Christianson, A. M.; Gabbaï, F. P., *J. Organomet. Chem.* **2017,** *847*, 154-161.

(193) Fujiwara, M.; Imada, M.; Baba, A.; Matsuda, H., *Tetrahedron Lett.* **1989,** *30*, 739-742.

(194) Zhou, Y.; Wang, J.; Gu, Z.; Wang, S.; Zhu, W.; Aceña, J. L.; Soloshonok, V. A.; Izawa, K.; Liu, H., *Chem. Rev.* **2016,** *116*, 422-518.

(195) Barbachyn, M. R.; Ford, C. W., *Angew. Chem. Int. Ed. Engl.* **2003,** *42*, 2010-23.

(196) Mahy, W.; Plucinski, P. K.; Frost, C. G., *Org. Lett.* **2014,** *16*, 5020-3.

(197) Nicolaou, K. C.; Baran, P. S.; Zhong, Y. L.; Barluenga, S.; Hunt, K. W.; Kranich, R.; Vega, J. A., *J. Am. Chem. Soc.* **2002,** *124*, 2233-44.

(198) Paddock, R. L.; Adhikari, D.; Lord, R. L.; Baik, M.-H.; Nguyen, S. T., *Chem. Commun.* **2014,** *50*, 15187-15190.

(199) Wang, P.; Qin, J.; Yuan, D.; Wang, Y.; Yao, Y., *ChemCatChem* **2015,** *7*, 1145-1151.

(200) Baronsky, T.; Beattie, C.; Harrington, R. W.; Irfan, R.; North, M.; Osende, J. G.; Young, C., *ACS Catalysis* **2013,** *3*, 790-797.

(201) Beattie, C.; North, M., *Chem. Eur. J* **2014,** *20*, 8182-8188.

(202) Tokunaga, T.; Seki, H.; Yasuike, S.; Ikoma, M.; Kurita, J.; Yamaguchi, K., *Tetrahedron* **2000,** *56*, 8833-8839.

(203) Shibata, I.; Baba, A.; Iwasaki, H.; Matsuda, H., *J. Org. Chem.* **1986,** *51*, 2177-2184.

(204) Lindley, B. M.; Jacobs, B. P.; MacMillan, S. N.; Wolczanski, P. T., *Chem. Commun.* **2016,** *52*, 3891-3894.

(205) Slocum, D. W.; Reinscheld, T. K.; White, C. B.; Timmons, M. D.; Shelton, P. A.; Slocum, M. G.; Sandlin, R. D.; Holland, E. G.; Kusmic, D.; Jennings, J. A.; Tekin, K. C.; Nguyen, Q.; Bush, S. J.; Keller, J. M.; Whitley, P. E., *Organometallics* **2013,** *32*, 1674-1686.

(206) Yang, M.; Tofan, D.; Chen, C.-H.; Jack, K. M.; Gabbaï, F. P., *Angew. Chem. Int. Ed.* **2018,** *57*, 13868-13872.

(207) Chang‐Hong, C.; P., G. F., *Angew. Chem. Int. Ed.* **2018,** *57*, 521-525.

(208) Hirai, M., Neutral and cationic organoantimony(V) Lewis acids as fluoride receptors and catalysts. Texas A&M University: Ph. D. Dissertation, 2016.

(209) McEwen, W. E.; Briles, G. H.; Giddings, B. E., *J. Am. Chem. Soc.* **1969,** *91*, 7079-7084.

(210) Winter, C. H.; Veal, W. R.; Garner, C. M.; Arif, A. M.; Gladysz, J. A., *J. Am. Chem. Soc.* **1989,** *111*, 4766-4776.

(211) Levason, W.; McAuliffe, C. A., *Inorg. Chim. Acta* **1974,** *11*, 33-40.

(212) Nunn, M.; Sowerby, D. B.; Wesolek, D. M., *J. Organomet. Chem.* **1983,** *251*, C45-C46.

(213) Whited, M. T.; Rivard, E.; Peters, J. C., *Chem. Commun.* **2006**, 1613-1615.

(214) Henry, M. C.; Wittig, G., *J. Am. Chem. Soc.* **1960,** *82*, 563-564.

(215) Levason, W.; McAuliffe, C. A.; Murray, S. G., *J. Organomet. Chem.* **1975,** *88*, 171-174.

(216) Baker, J. L.; Sudarsan, N.; Weinberg, Z.; Roth, A.; Stockbridge, R. B.; Breaker, R. R., *Science* **2012,** *335*, 233-235.

(217) Carton, R. J., *Fluoride* **2006,** *39*, 163-172.

(218) Aaseth, J.; Shimshi, M.; Gabrilove, J. L.; Birketvedt, G. S., *J. Trace Elem. Exp. Med.* **2004,** *17*, 83-92.

(219) Matsuo, S.; Kiyomiya, K.-i.; Kurebe, M., *Arch. Toxicol.* **1998,** *72*, 798-806.

(220) Zhou, Y.; Zhang, J. F.; Yoon, J., *Chem. Rev.* **2014,** *114*, 5511-5571.

(221) Wade, C. R.; Broomsgrove, A. E. J.; Aldridge, S.; Gabbaï, F. P., *Chem. Rev.* **2010,** *110*, 3958-3984.

(222) Jäkle, F., *Chem. Rev.* **2010,** *110*, 3985-4022.

(223) Hudnall, T. W.; Chiu, C.-W.; Gabbaï, F. P., *Acc. Chem. Res.* **2009,** *42*, 388-397.

(224) Hudson, Z. M.; Wang, S., *Acc. Chem. Res.* **2009,** *42*, 1584-1596.

(225) Cametti, M.; Rissanen, K., *Chem. Commun.* **2009**, 2809-2829.

(226) Adamo, C.; Barone, V., *J. Chem. Phys.* **1998,** *108*, 664-675.

(227) Yanai, T.; Tew, D. P.; Handy, N. C., *Chem. Phys. Lett.* **2004,** *393*, 51-57.

(228) He, R.; Wang, X.; Hashimoto, T.; Maruoka, K., *Angew. Chem. Int. Ed.* **2008,** *47*, 9466-9468.

(229) Yang, J.-L.; Wu, H.-L.; Li, Y.; Zhang, X.-H.; Darensbourg, D. J., *Angew. Chem. Int. Ed.* **2017,** *56*, 5774-5779.